

Faculty of Electrical Engineering and Communication

BRNO, 2020

BRNO UNIVERSITY OF TECHNOLOGY

HABILITATION THESIS

Author

MSc. Eric Daniel Głowacki, PhD

BRNO UNIVERSITY OF TECHNOLOGY

VYSOKÉ UČENÍ TECHNICKÉ V BRNĚ

FACULTY OF ELECTRICAL ENGINEERING AND COMMUNICATION

FAKULTA ELEKTROTECHNIKY A KOMUNIKAČNÍCH TECHNOLOGIÍ

DEPARTMENT OF BIOMEDICAL ENGINEERING

ÚSTAV BIOMEDICÍNSKÉHO INŽENÝRSTVÍ

PHOTOCAPACITIVE AND PHOTOFARADAIC ORGANIC SEMICONDUCTOR DEVICES FOR BIOELECTRONICS

FOTOKAPACITNÍ A FOTOFARADAICKÁ ORGANICKÁ POLOVODIČOVÁ
BIOELEKTRONICKÁ ZAŘÍZENÍ

HABILITATION THESIS

HABILITAČNÍ PRÁCE

AUTHOR
AUTOR PRÁCE

MSc. Eric Daniel Głowacki, PhD

BRNO 2020

Keywords: Bioelectronics, neuromodulation, organic semiconductors, photoelectrochemical cells, reactive oxygen species

Klíčová slova: Bioelektronika, neuromodulace, organické polovodiče, fotoelektrochemické články, reaktivní formy kyslíku

LIST OF COMMENTED PAPERS	3
1. INTRODUCTION AND MOTIVATION	4
2. KEY CONCEPTS	4
2.1 Organic thin film photovoltaics	4
2.2 Artificial neuromodulation and its applications	5
2.3 Electrochemistry: double layer formation and the oxygen reduction reaction	6
3. SCIENTIFIC NARRATIVE OF THE INCLUDED PAPERS	7
3.1 Photocapacitive devices (Papers 1, 2, 3, 4, 5)	7
3.1.1. First-generation semiconductor/cell interface concepts	7
3.1.2 The characterization of photothermal effects	9
3.1.3 Rethinking capacitive interfaces - second generation devices	10
3.1.4 Photocapacitive stimulation of electrophysiological model systems	11
3.1.5 Understanding the fundamentals of photocapacitive coupling	13
3.1.6 Increasing the interfacial capacitance of OEPCs	14
3.1.7 Differentiation between faradaic and capacitive currents	15
3.2 Photofaradaic devices (Papers 6, 7, 8)	17
3.2.1. Photocathodes and photoanodes in the context of organic semiconductors	17
3.2.2. Single-component organic semiconductor photocathodes for H ₂ O ₂ evolution	18
3.2.3. Optimized heterojunction devices for H ₂ O ₂ production	20
3.2.4. Photofaradaic “floating” pixels	20
4. CONCLUSIONS AND OUTLOOK	21
5. REFERENCES	22
6. INCLUDED PAPERS	24

List of commented papers

- (1) Sytnyk, M.; Jakešová, M.; Litviňuková, M.; Mashkov, O.; Kriegner, D.; Stangl, J.; Nebesářová, J.; Fecher, F. W.; Schöfberger, W.; Sariciftci, N. S.; Schindl, R.; Heiss, W.; **Głowacki, E.D.** Cellular Interfaces with Hydrogen-Bonded Organic Semiconductor Hierarchical Nanocrystals. *Nature Communications* **2017**, *8*, 91.
- (2) Rand, D.; Jakešová, M.; Lubin, G.; Vebraite, I.; David-Pur, M.; Đerek, V.; Cramer, T.; Sariciftci, N. S.; Hanein, Y.; **Głowacki, E.D.** Direct Electrical Neurostimulation with Organic Pigment Photocapacitors. *Advanced Materials* **2018**, *30*, 1707292.
- (3) Jakešová, M.; Ejneby, M. S.; Đerek, V.; Schmidt, T.; Gryszel, M.; Brask, J.; Schindl, R.; Simon, D. T.; Berggren, M.; Elinder, F.; **Głowacki, E.D.** Optoelectronic Control of Single Cells Using Organic Photocapacitors. *Science Advances* **2019**, *5*, eaav5265.
- (4) Ejneby, M. S.; Migliaccio, L.; Gicevic, M.; Jakešová, M.; Elinder, F.; **Głowacki, E.D.** Extracellular Photovoltage Clamp Using Conducting Polymer-Modified Organic Photocapacitors. *Advanced Materials Technologies* **2020**, *5*, 1900860.
- (5) Đerek, V.; Rand, D.; Migliaccio, L.; Hanein, Y.; **Głowacki, E.D.** Untangling Photofaradaic and Photocapacitive Effects in Organic Optoelectronic Stimulation Devices. *Frontiers Bioengineering and Biotechnology*. **2020**, *8*, 284.
- (6) Jakešová, M.; Apaydin, D. H.; Sytnyk, M.; Oppelt, K.; Heiss, W.; Sariciftci, N. S.; **Głowacki, E.D.** Hydrogen-Bonded Organic Semiconductors as Stable Photoelectrocatalysts for Efficient Hydrogen Peroxide Photosynthesis. *Advanced Functional Materials* **2016**, *26*, 5248–5254.
- (7) Gryszel, M.; Markov, A.; Vagin, M.; **Głowacki, E.D.** Organic Heterojunction Photocathodes for Optimized Photoelectrochemical Hydrogen Peroxide Production. *Journal of Materials Chemistry A* **2018**, *6*, 24709–24716.
- (8) Gryszel, M.; **Głowacki, E.D.** Organic Thin Film Photofaradaic Pixels for On-Demand Electrochemistry in Physiological Conditions. *Chemical Communications* **2020**, *56*, 1705–1708.

1. Introduction and motivation

Light absorption by semiconducting materials is exploited technologically in photodetectors and photovoltaic devices. Semiconductor absorbers are therefore vital for applications ranging from telecommunications to light-energy harvesting. While most traditional applications concern the semiconductor materials in “dry” conditions, illuminated semiconductors can also form “wet” interfaces with aqueous electrolytes. These are the conditions that prevail in biology. The motivation of the work in this thesis is to create functional optoelectronic biointerfaces with semiconductors. The goals, broadly defined, revolve around using light absorption in semiconductors to modulate the physiology and electrophysiology of living things, from the level of single cells up to tissues. The work in this thesis has two foci: 1) organic semiconducting structures for direct optoelectronic stimulation of neural cells, where impulses of light are transduced into electrolytic stimulation pulses that efficiently modulate cellular electrophysiology; 2) organic semiconducting systems for photoelectrochemical reduction of dissolved oxygen to hydrogen peroxide, an important reactive oxygen species implicated in numerous physiological pathways.

2. Key concepts

The science and engineering covered in this thesis spans across three disciplines: organic semiconductor device engineering, electrophysiology, and finally electrochemistry. Ideas from these fields are often combined to yield novel device concepts and functionality. However, to effectively move forward, it is critical to introduce the core of each of these fields: 1) Organic photovoltaics, 2) artificial neuromodulation, and finally, 3) electrochemistry of the oxygen reduction reaction. These concepts have intertwined to create a body of knowledge that has launched useful new directions in engineering of biomedical devices.

2.1 Organic thin film photovoltaics

The semiconducting properties of π -conjugated organic molecules and polymers has been recognized for many decades.¹ It was not until the groundbreaking discovery of the organic bilayer solar cell² and the organic light-emitting diode,³ in 1985 and 1986, respectively, that technological interest in organic electronic materials increased dramatically. Organic molecular semiconductors can transport electrical charge, however charge carriers are highly localized in molecular orbitals and intermolecular electronic coupling is weak. This causes a dominance of hopping transport with thermally-activated transport from localized states in organic materials.⁴ This leads to relatively low charge carrier mobility in organic materials, with the highest values in the range of 1 to 10 cm²/Vs.⁵ While transport properties are modest, organic materials have a major advantage over most inorganic counterparts in that they have high absorbance coefficients. Layers on the order of one hundred nanometers can absorb light more efficiently than most inorganic counterparts. This makes organic semiconductors theoretically promising materials for photovoltaics. This led to extensive exploration of organic materials for solar cell applications in the late 1970s and 1980s. However, power conversion efficiencies remained lower than 1%. The limiting factor is that upon photoexcitation, excitons with high binding energy (0.1 – 1 eV) are formed in organic molecular solids. The separation efficiency of such excitons is very low in the absence of a strong external field. An effective solution to this problem was introduced by Ching Tang in 1985, with his bilayer organic photovoltaic cell.² The principle of operation relies in creating a heterojunction between an

electron-donor and an electron-acceptor, where the energetic offset between the frontier molecular orbitals is larger than the exciton binding energy. In this way, excitons are generated in the donor layer, and diffuse to the interface with the acceptor, where the excitons are polarized into free carriers. This process is illustrated in Figure 1. Such structures can lead to power conversion efficiencies between 1-2.5% for solar energy conversion, while having monochromatic external quantum efficiencies as high as 80-90%.⁶

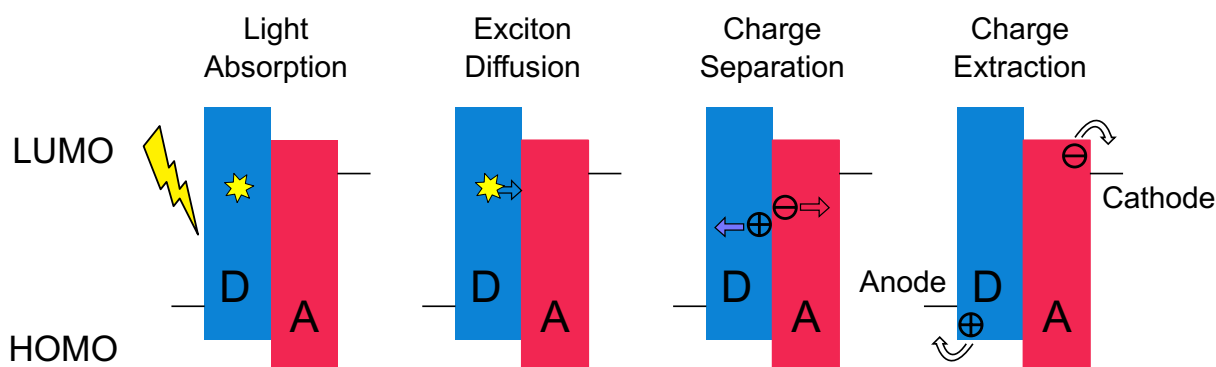


Figure 1. Donor-acceptor bilayer solar cells, consisting of sequentially-deposited organic films of a thickness roughly 10-100 nm. Light is absorbed primarily in the donor layer, producing an exciton. Excitons then diffuse to the donor-acceptor interface, where the energetic offset between the frontier molecular orbitals polarizes the exciton into free carriers. The carriers are separated due to the selective transport properties of the donor and acceptor materials, and collected at electrodes.

In the intervening decades, various innovations were introduced that dramatically increased the performance of organic solar cells. The bulk heterojunction concept represented the greatest jump in efficiency,⁷ and synthesis of rationally-designed organic absorbers further pushed efficiency upwards. Today, power conversion efficiencies are routinely reported in the range of 12-18%.⁸ Nevertheless, the original bilayer concept described by Tang in 1985 has a number of features which merits its reconsideration in the applications discussed in this thesis. Namely, the spatial directionality of charge separation between donor and acceptor will be shown to be important. The bilayers are extremely thin and consist of nanocrystalline pigments, which have high surface area and therefore can form relatively high capacitance interfaces with water. Most critically, the organic pigments used in these devices are industrial, cheap, and abundant pigments which are used in numerous commercial applications.^{9,10} They are recognized as nontoxic and belong to the lowest toxicity category for consumer products in the EU. For applications where stable and biocompatible operation is required at a biomedical interface, the “old” organic pigment bilayer concept holds interesting promise.

2.2 Artificial neuromodulation and its applications

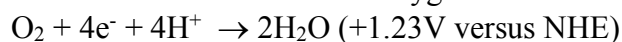
Excitable cells such as neurons and muscle cells have a negative resting membrane potential, maintained by active transmembrane transport which maintains an equilibrium where there is a lower concentration of cations inside of the cell, versus the outside. It is additionally important to note that the sodium-potassium pump maintains a gradient of high sodium concentration outside of the cell, and high potassium concentrations inside of the cell. The resting membrane potential of a neurons is typically around -70 to -60 mV. The fundamental signal transfer in neurons is the action potential (AP). The AP is a transient and localized positive perturbation of the membrane potential, where the normally negative resting membrane potential “depolarizes”. This depolarization travels down the axon bodies of neurons.¹¹ The generation and propagation of the AP occur due to the action of voltage-gated ion channels. Voltage-gated channels are transmembrane proteins that have a voltage-sensitive

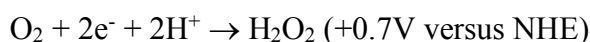
gate which selectively opens and closes as a function of membrane potential. They function as ionic diodes, with a characteristic conductivity/voltage relationship. AP is initiated normally when neurotransmitters cause ligand-gated channels to open and allow in a small amount of cations to go into the cell. Once the cell membrane potential is slightly depolarized, crossing a threshold potential, voltage-gate sodium channels open and allow sodium into the cell, leading to rapid repolarization. This increase in voltage causes potassium channels to open, and potassium ions exit the cell, thereby restoring the resting membrane potential. The timing of the opening of voltage-gated sodium and potassium channels accounts for the depolarization/repolarization cycle of the AP to last for about 4 milliseconds. Normally, this entire sequence is initiated by the action of neurotransmitters acting on ligand gated channels, causing the membrane potential to cross the threshold. Artificial neuromodulation relies on bypassing this mechanism, and depolarizing the cell directly by applying a pulse of electrolytic current.¹² For the purposes of this work, we consider only the case of an extracellular electrode injecting charge into the vicinity of the cell and causing depolarization. Extracellular neurostimulation electrodes are used in basic research and in medicine. Many examples exist of chronically-implanted electrode systems which stimulate neurons in the human body. Vagus nerve stimulation, deep-brain stimulation, spinal cord stimulators, etc are all examples of clinically-relevant applications of neuromodulation.^{13,14} All of these implant concepts belong to the category of bioelectronic medicine, one of the fastest growing areas in biomedicine.¹⁵ Next-generation bioelectronic medicine will benefit greatly from innovations leading to minimally-invasive solutions. Currently, the biggest problem is the long-term powering (batteries) and interconnecting wires inherent in all implanted stimulators. There is a great need for wireless solutions. In basic research, a similar need for wireless tools to stimulate a studied biosample are in demand. For this reason, we have focused on trying to use optoelectronic techniques to replicate many of the existing neurostimulation protocols, but using light and a minimalistic semiconductor transducer.

2.3 Electrochemistry: double layer formation and the oxygen reduction reaction

The physics of semiconductor-electrolyte systems varies significantly from that of completely solid-state devices. While in the solid-state electrons and holes function as charge carriers, in electrolytes, dissolved ions are the charge carriers. Any eventual transfer of electrons is limited to the nanoscale interface with the semiconductor surface. Another significant difference is the formation of electric fields. While at equilibrium fixed regions of electric field can exist in a solid-state semiconductor, in electrolytes electric field is screened by combined effect of the movement of ions and the high dielectric constant of water. The range over which an electrostatic field exists in solution is defined by the Debye length, and in aqueous electrolytes is on the order of a few nanometers. As ions and polar water molecules accumulate at a charged electrode surface, this region is called the electrolytic double layer – at equilibrium electric field only exists in this narrow region of electrolyte solution. Electric fields exist transiently in “bulk” solution only during charging and discharging of electrodes, and are therefore relevant under alternating current conditions. The action of electric fields over larger regions of electrolyte are needed for interfacing with cells, thus all the optoelectronic concepts discussed within this thesis for direct neuromodulation feature only AC operation.

Net DC current in electrolyte can only be sustained if the potential at an electrode surface is sufficient to cause an electron-transfer reaction to a species in solution. When charge is transferred from an electrode to a species in solution and a product is formed, this is referred to as a Faradaic reaction. The most familiar example is that of water electrolysis – where water can be reduced to form hydrogen gas, or oxidized to produce dioxygen. In this thesis, the electrochemistry we are most concerned with is the oxygen reduction reactions:





Oxygen can undergo a four-electron reduction to produce water as a product. This is the reverse reaction of water splitting, and is very well-known as a key reaction in hydrogen fuel cells, where oxygen is the final electron acceptor. The two-electron reduction of oxygen to hydrogen peroxide has received generally less attention than the four-electron process. It is thermodynamically less-favored, however it may in certain systems be kinetically favored as it preserves the oxygen-oxygen bond and features a lower multiplicity of electrons and protons transferred. In this work, the peroxide-forming oxygen reduction reaction will be considered in detail.

3. Scientific narrative of the included papers

3.1 Photocapacitive devices (Papers 1, 2, 3, 4, 5)

3.1.1. First-generation semiconductor/cell interface concepts: Our exploration of this field started at the beginning of 2015, where we put forth the goal of creating photoactive cell/semiconductor interfaces. At that time, there were a handful of works published where various nano and microparticle semiconductors were found to form close interfaces with cells, and various photoinduced physiological behaviors had been reported.¹⁶⁻¹⁹ The contemporary understanding of the possible mechanisms for these light-induced effects was poorly developed, and controversy existed in the literature. The possible mechanisms for cellular photostimulation with a semiconductor interface can be divided into three broad categories: 1) Photothermal, 2) Photocapacitive, or 3) Photofaradaic. These are schematized in figure 2 below, illustrating a phospholipid bilayer membrane at the intimate interface of a nanoscale semiconductor structure as we explored in **Paper 1**:

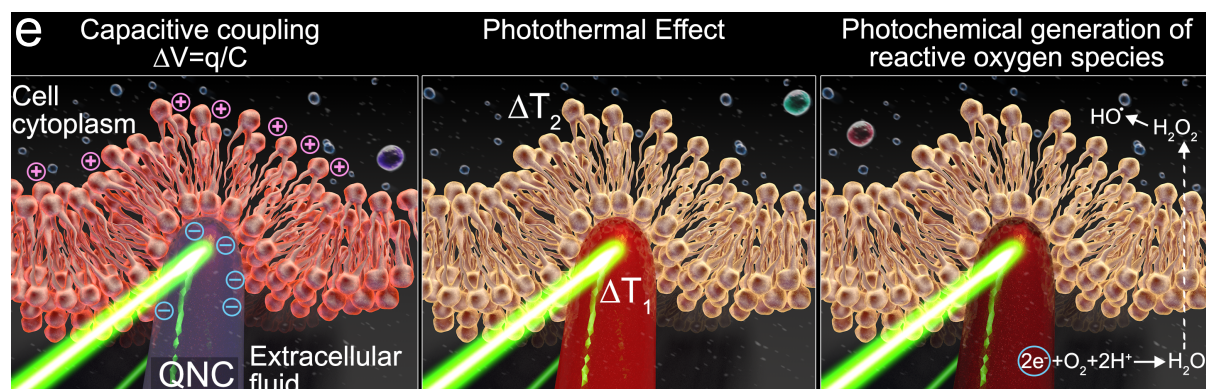


Figure 2. Three possible mechanisms for interaction of a semiconductor nanostructure at the interface with a cell membrane, shown for our materials quinacridone, QNC, explored in Paper 1. The leftmost panel illustrates idealized photocapacitive coupling, where the surface of the semiconductor acquires a negative charge, inducing a positive charge on the other side of the plasma membrane, thereby leading to depolarization which is necessary for stimulation of voltage-gated ion channels. This mechanism we finally were able to reproduce in papers 2-5. The central panel depicts photothermal heating, where the semiconductor absorbs light and increases its temperature, it can transfer heat to the cell membrane, triggering membrane conformation changes at fast time scales which transiently increase membrane capacitance (thermocapacitive coupling phenomenon) or simply increasing local temperature and triggering for example temperature-sensitive channels to open. This is what we have observed in Paper 1. The third mechanism, in the right panel, is the photochemical generation of reactive oxygen species in the form of hydrogen peroxide, which as an uncharged molecule can diffuse through the cell membrane and induce a number of different processes. Though we have not published

work showing cellular coupling using this mechanism, we have laid all the experimental groundwork for creating such devices (papers 6-8). Figure reproduced from Paper 1, under the Creative Commons license 4.0.

In paper 1, we designed and synthesized, using a novel colloidal-chemical technique, self-assembled colloidal particles consisting of the organic semiconductor quinacridone (QNC). QNC is a commercial pigment produced on a huge scale worldwide, and is used in various consumer products. Most famously, it is the magenta color in all printer ink cartridges. It is known to be safe and nontoxic, and an efficient and stable absorber of light. This is why from the beginning, in the design of optical biointerface devices, we have been committed to using well-known safe materials which are already approved for numerous commercial and cosmetic products. It had been established that to maximize the effectiveness of a bioelectronic interface, the semiconductor material should have high surface area in contact with the cell membrane.²⁰ Efforts should be taken to decrease the distance between the actual membrane and the semiconductor surface. These demands were met by our approach by creating hierarchically-arranged nanocrystals, which formed round microobjects resembling hedgehogs. These hedgehogs have a total diameter of around 10 μm , therefore making them on the same size-order as single cells. However, their surface has nanoneedles that have 30-50 nm tips. These are intended to penetrate through extracellular matrix and interface closely with the actual cell membrane. The QNC hedgehog structures are detailed in Figure 3.

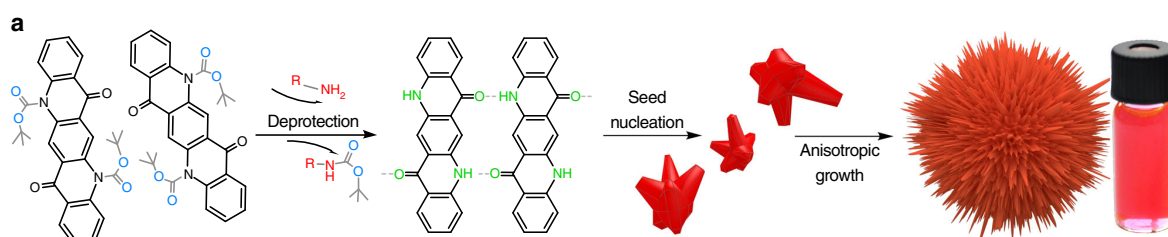


Figure 3. Hierarchical microstructures formed from colloidal nanocrystals of quinacridone, QNC, were the first “biomimetic” semiconductor structure designed by us for forming cell interfaces. The high roughness at the scale of tens of nanometers is known to promote cell adhesion, and the nanoneedles were modified with oleylamine, which is a hydrophobic ligand and thus interacts with the phospholipid bilayer membranes of cells. Figure adapted from Paper 1, under the Creative Commons license 4.0.

These micro-hedgehogs, despite their size, had good colloidal stability in organic solvents. Such colloids were spread on glass substrates, and were plated with cultured cells: rat basophilic leukemia (RBL) cells, or human embryonic kidney (HEK) cells. In a series of studies, we found excellent compatibility and viability of the cells on the QNC microhedgehogs. In control experiments with planar QNC substrates or other coatings on the glass substrates known to increase cell adhesion, we found that the cells showed a remarkable preference to grow on the hedgehog structures. We performed extensive electron microscopy studies to characterize these interfaces, finding a very high degree of interaction between the nanoneedles and the cell membranes (Figure 4). Combined with the successful cell viability tests, it was evident that we had achieved our goal of creating a unique and promising type of semiconductor/single cell interface.



d

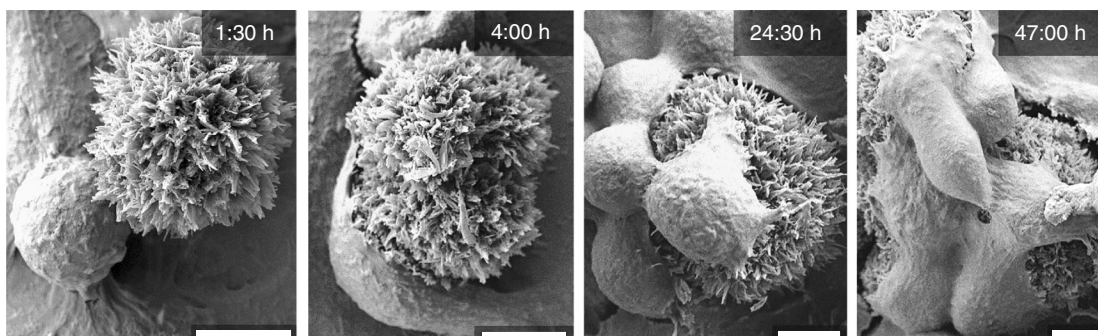


Figure 4. Scanning electron microscopy of cells cultured at the interface with QNC microhedgehogs. The false-colored image at the upper left shows rat basophilic leukemia (RBL) cells growing on the QNC structures, and are so colored to distinguish the two – the semiconductor structures indeed resemble the cells themselves. The remaining images display the intimate interface formation, clearly evidencing strong interaction between the QNC nanoneedles and the cell membranes. Cell viability and proliferation on these structures is good, and better than planar QNC controls. Figure reproduced from Paper 1, under the Creative Commons license 4.0.

3.1.2 The characterization of photothermal effects: Having established the formation of reliable cell/semiconductor interfaces, we launched into a period of single-cell electrophysiology studies. There we used established patch-clamp techniques to characterize the behavior of ion channels in the cells during illumination with various impulse sequences of light. Key results are summarized in the selection of panels in Figure 5. Several important conclusions were drawn from these experiments: 1) there are clear photoinduced changes in ion currents through K^+ inward rectifier ion channels, they feature a rapid capacitive charge/discharge component and higher steady-state current during illumination. 2) these changes in ion current occur only when the channels are open, i.e. the current/voltage curve does not shift, therefore the photoinduced changes to membrane potential are negligible. 3) The observed enhancement in ion currents could be attributed to efficient photothermal heating afforded by the close semiconductor particle in contact with the cell, increasing steady-state ion current. The final conclusion of photothermal heating was confirmed by an experiment featuring genetically transfecting HEK cells with TRPV1 channels, which are thermosensitive channels.²¹ There, we were able to clearly stimulate channel opening when the cell was held at resting membrane potential. All the evidence clearly pointed to photothermal heating effects and negligible capacitive or electrostatic coupling. While a significant step for us, and the field of semiconductor/cell interfaces, photothermal heating is not the preferred mechanism of coupling to electrophysiological processes. To achieve our goal of true capacitive coupling, with negligible thermal effects, we had to carefully reconsider our approach and engineer a different type of device.

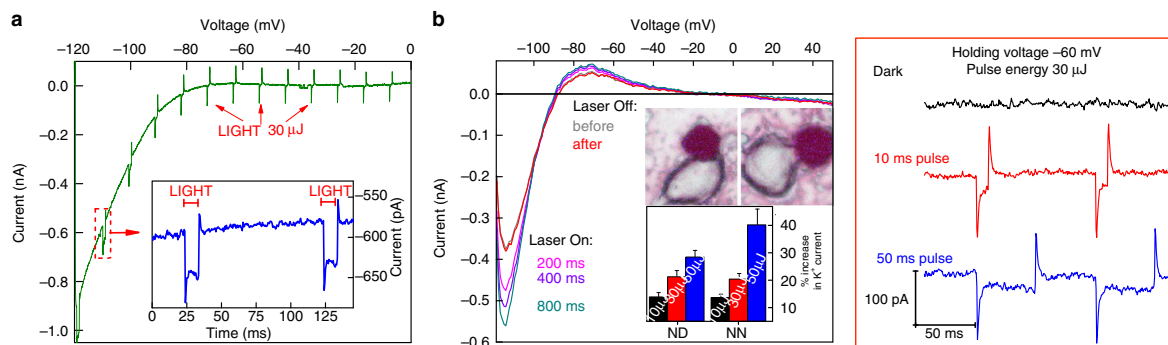


Figure 5. Voltage-clamp measurements of single cells interfacing with organic hierarchical nanocrystals. The leftmost and center panels show voltage-clamp $I(V)$ for potassium inward rectifier channels that are endogenous to RBL cells. Light pulse illumination of several ms up to tens of ms does not shift the gating voltage of the channel. What is observed is photoinduced increases in current, as well as relatively small capacitive spikes. Prolonged illumination with lower-intensity laser light (middle panel) does not shift the $I(V)$ characteristic either, only the potassium current through the open channels is 20-40% higher when illuminated, apparently the trivial effect of raised local temperature increasing diffusion. The panel on the right shows the data for HEK cells genetically-modified to express TRPV1 channels, known to be temperature sensitive. Here clearly illumination of the semiconductor results in channel opening when the cell is held at resting membrane potential, therefore implicating efficient photothermal heating as the dominant mechanism at play. Figure adapted from Paper 1, under the Creative Commons license 4.0.

3.1.3 Rethinking capacitive interfaces - second generation devices: The experience of paper 1 encouraged us to maximize the capacitive charge density produced by photoirradiation. A single semiconductor material without a clear energetic asymmetry could not create directional displacement currents to efficiently modulate the membrane potential of nearby cells. Our complete redesign led us to start with bilayer organic donor-acceptor heterojunctions. The p-n heterojunction enforces directionality of charge separation. An underlying metal conducting layer was selected to extend laterally around the PN pixel in order to close the electrolytic circuit. The two electrodes thus formed are the surface of the n-type layer (cathode) and the underlying metal electrode (anode), which is in contact with the surrounding solution (Figure 6). This new concept, termed the organic electrolytic photocapacitor (OEPIC), was introduced in **Paper 2**. The practical goal of a photocapacitor is to transduce a light pulse (pulse length in the range of 10 μ s – 10 ms) into electrolytic charging currents in surrounding solution which lead to depolarization of adjacent cells, thereby stimulating action potentials. Such a configuration is reproducing the well-established biphasic current pulses which are used to capacitively stimulate neurons and excitable tissues.²² In the second commented paper (2), the concept of OEPICs is explored for the first time and applied to successfully stimulate excitable cells using safe and practical light intensities. The target application in this paper is retinal prosthetic implants, for localized stimulation of retinal ganglion cells. For this reason, we devised the concentric pattern of a PN pixel surrounded by a circular return electrode in order to best localize the transient electric field and thus stimulate cells with the best possible spatial precision.

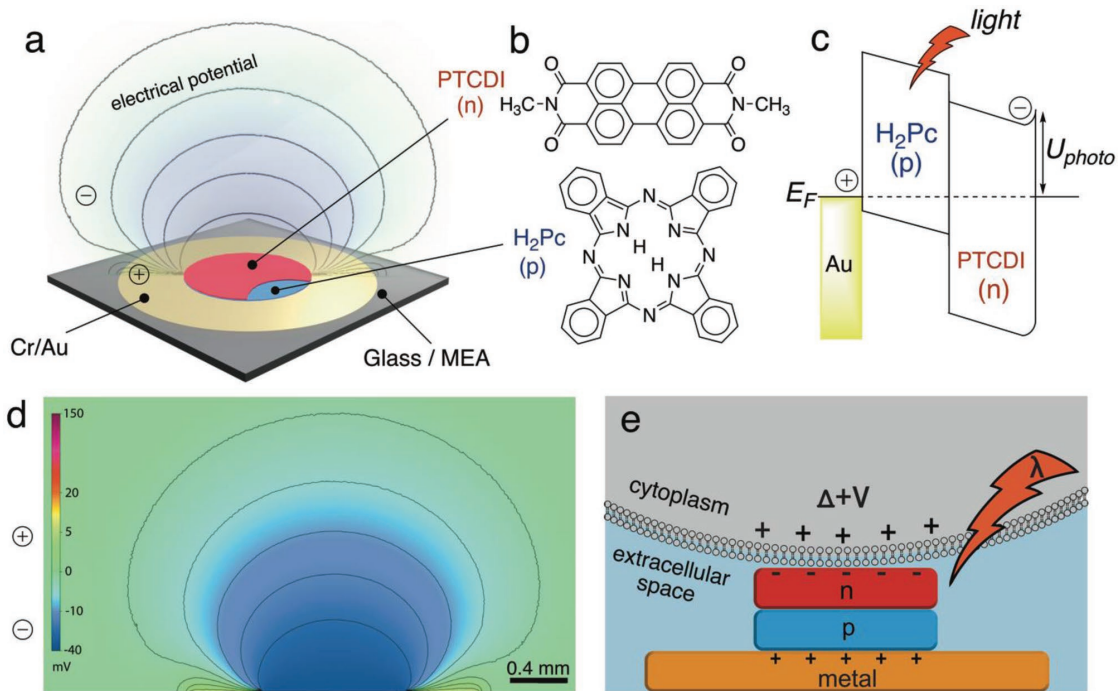


Figure 6. The organic electrolytic photocapacitor (OEPC). *a*) The concentric arrangement of the central PN charge-generating pixel surrounded by the metallic return electrode creates a localized transient voltage perturbation in solution. *b*) The organic donor-acceptor p- and n-type pigments are stable and cheap organic colorants, processed by vacuum sublimation. *c*) The band diagram of the device in short-circuit conditions under illumination. *d*) Electrostatic calculation for the electric field profile in solution while the device charges up. *e*) an idealized picture of the capacitive coupling of the OEPC with an adjacent cell and the associated depolarization of the cell membrane potential. Reproduced from Paper 2 within the Creative Commons 4.0 license.

3.1.4 Photocapacitive stimulation of electrophysiological model systems: Two types of models were tested in order to validate that the OEPCs worked: neuron cell cultures, and light-insensitive embryonic chicken retinas. Neurons were cultured on OEPC samples for periods of 2 weeks to 1 month, and calcium imaging experiments were performed to visualize action potentials. These experiments proved beyond reasonable doubt that cells could be efficiently stimulated (Figure 7). Moreover, these experiments showed that neurons cells adhered very well to the organic semiconductor surface, without needing any compatibilization layer. This remarkable result evidences good intrinsic biocompatibility of the organic pigment materials. It was likewise important that prolonged cell culture conditions did not degrade the performance of the OEPC devices. The OEPCs were found to be very robust, and survive for instance various sterilization treatments like bacteriocidal UV, ethanol wash, or autoclave heating. Having successfully validated that the OEPC can work to stimulate cells, we moved on to retinal stimulation experiments. The chosen model of embryonic chicken retinas provides a low-cost simple model of a blind retina. Between days 14 and 16 of embryonic development, the eye and retina of the chicken are essentially fully-formed, except for the photosensitive rod and cone cells – these are completely absent during this period. We integrated OEPC devices directly onto a commercial multielectrode recording array (MEA), and laminated the chicken retina tissue directly onto the MEA (Figure 8). This way, light pulses could be directed through a microscope objective onto a selected OEPC device, and any evoked action potentials could be recorded using the MEA. These experiments proved that direct capacitive neurostimulation was occurring, and OEPC pixels in size down to 100 μm diameter were able to evoke action potentials. This work was a milestone in the field, providing a completely new type of ultrathin

nanoscale device (< 100 nm thick) which could safely capacitively couple to cells. The work has since inspired extensive follow up by different groups, and was the launching off point for our continued work as well.

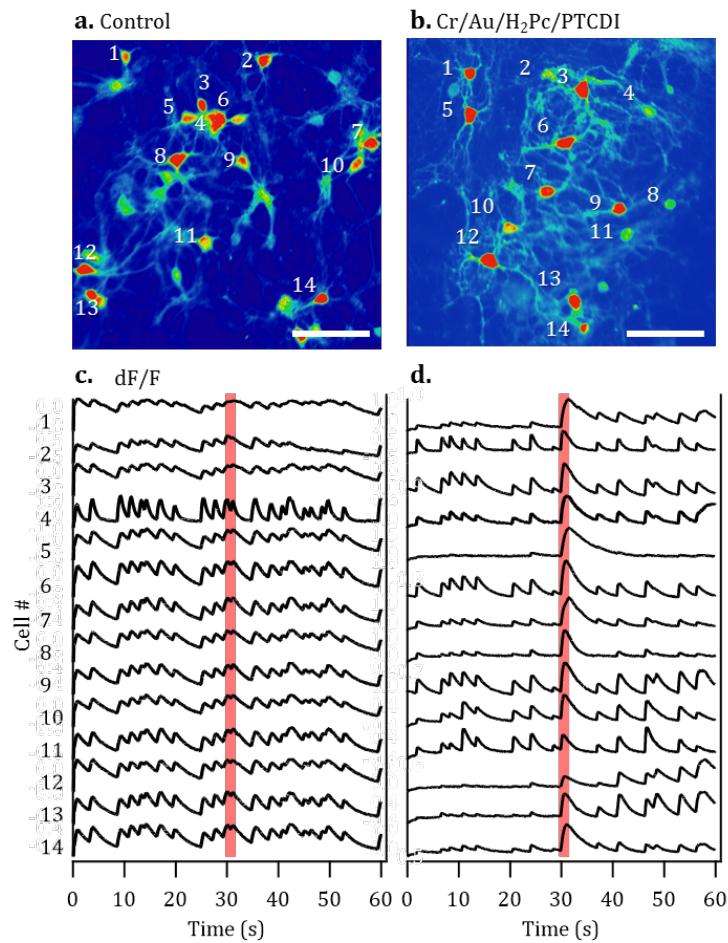


Figure 7. First experimental demonstration of successful photocapacitive stimulation of excitable cells. Neurons were cultured for 2-4 weeks on top of photocapacitive interface devices. Panels c and d show a non-photoactive control and the photocapacitor device, respectively. Illumination with red light pulses does not produce any response in the control, however on the photocapacitor sample, when illuminated, all neurons in the field of view fire an action potential at the same time. Reproduced from Paper 2 within the Creative Commons 4.0 license.

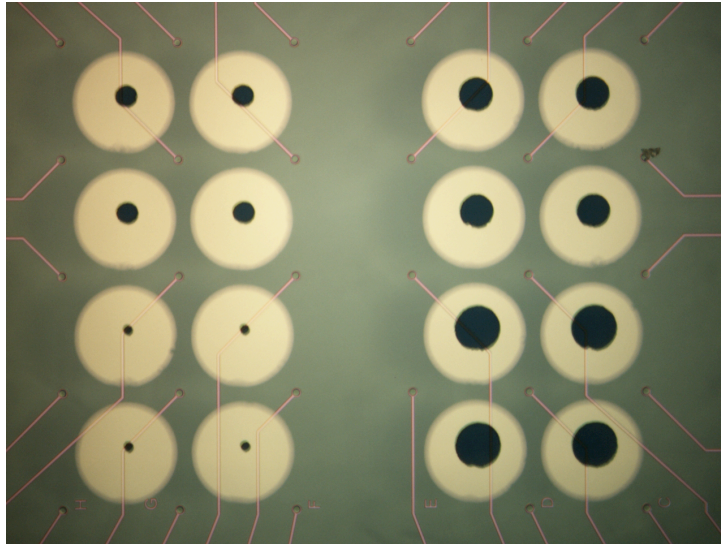


Figure 8. Test structures of multi-electrode arrays (underlying passivated traces with exposed microelectrodes) with OEPC devices patterned in the spaces in between. This way the retinal tissue could be placed on top of the array and OEPC pixels could be addressed individually through a microscope objective.

3.1.5 Understanding the fundamentals of photocapacitive coupling: While paper 2 demonstrated efficacy of neurostimulation using the organic thin film devices, and all the evidence pointed to a capacitive coupling mechanism, moving forward we wanted to quantify precisely this mechanism, and understand it at the single-cell level. Despite the extensive deployment of stimulation electrodes (usually of capacitive nature) in electrophysiological research and clinical practice, it was surprising that up to that time, studies of single-cell electrophysiology with capacitive extracellular stimulating electrodes were very rare. In fact, a series of papers by Schön and Fromherz, from the early 2000s were the only references on this topic. We set out to fully characterize the *photocapacitive* mechanism acting upon a single cell, and use experiment and numerical models to understand the benchmark parameters of how such photoelectrodes affect voltage-gated ion channels (**Paper 3**). We did this by measuring voltage-clamp electrophysiology on *xenopus laevis* oocytes. These oocytes are large single cells (1 mm \varnothing) that are perfectly spherical. They contain a very low density of endogenous ion channels, but can be easily genetically transfected to overexpress an ion channel of choice. In our experiments, the oocyte without any added channels provided the perfect reference model cell for understanding capacitive coupling.

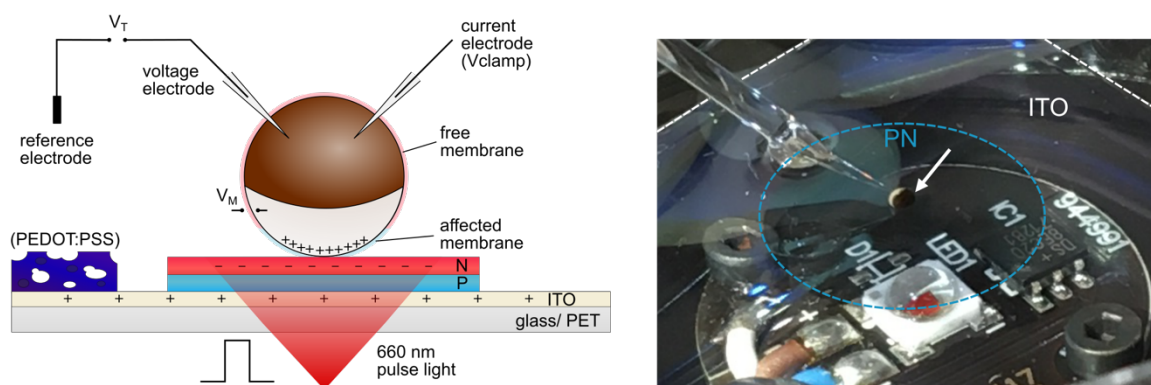


Figure 9. Single-cell electrophysiology experiments with *X. laevis* oocytes were performed to precisely characterize the nature of capacitive coupling between the photocapacitor and the cell membrane.

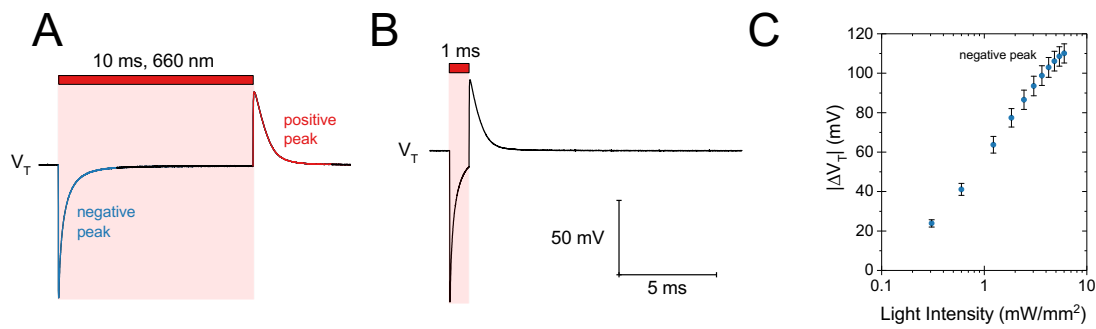


Figure 10. Intracellular transient voltages (V_T), showing the characteristic biphasic capacitive pulses delivered by the OEPC, shown for 10 or 1 ms long pulses of 660 nm light. The right panel plots the magnitude of the V_T as a function of incident light intensity. Adapted from paper 3, within the Creative Commons 4.0 license.

We were able to measure, using an intracellular voltage-follower electrode, the transient voltages induced by the device. Relatively high biphasic voltages were registered, in the range of several tens of millivolts to even over 100 mV. Importantly, the behavior appears fully capacitive. However, the important parameter that will affect voltage-gated channels in the membrane will be the transient voltage across the membrane at a given point. It is evident that the magnitude of that potential will vary based on position along the cell, i.e. the cell membrane closer to the semiconductor surface will experience a larger perturbation than areas of the membrane further away. We refer to this region as the “affected membrane”, as shown in Figure 9. The recording of intracellular voltage only quantifies the magnitude of the photoinduced voltage between a point inside of the cell and a reference electrode placed far away in the bath solution. To correlate this voltage (V_T) to different points along the cell membrane, V_M , a numerical model was necessary. Based on this model, the strongly-affected region of the bottom of the cell should experience a depolarization of around 20-40 mV. This is a large change that should easily open voltage-gated channels.

Voltage-clamp measurements on K^+ channels: To provide the direct experimental evidence for effective photoinduced depolarization, we performed two-electrode voltage-clamp measurements with the well-known Shaker K_V channel.²³ We were able to measure current-voltage and conductance-voltage curves for these channels in the “dark” and during 10 ms illumination pulses. The conductance curve shifted by 20-40 mV during illumination, beautifully correlating to calculated predictions. The observed changes in current were confirmed to be potassium-related by employing a channel blocker as a control. Moreover, we conducted experiments on a mutant channel which opens normally at around 40 mV more depolarized potentials relative to the wild-type channel. Cells with the mutant channels showed the same photoinduced shift in their conductance curve. These results, and accompanying numerical model, finally cemented the photocapacitive stimulation model to the community, and proved beyond reasonable doubt this new neuromodulation paradigm.

3.1.6 Increasing the interfacial capacitance of OEPCs: In the photocapacitor device, one of the most critical parameters is the electrolytic capacitance of the semiconductor/electrolyte interface. This capacitance will dictate how much charge per unit area can be injected into the surrounding system, and will change the RC time constant of the device, thereby significantly effecting the dynamics of the transient voltages produced. The impedance and charge injection capacity are the most important benchmark parameters that are considered in the

neuromodulation electrode field.²⁴ We were motivated to increase this capacitance in order to create long-lasting transient voltages which could be used to stimulate ion channel behavior which occurs only at longer time scales. In Paper 4, we were able to significantly increase the transient voltage magnitudes and time-scales by optimizing a hybrid electronic/ionic conducting polymer coating.

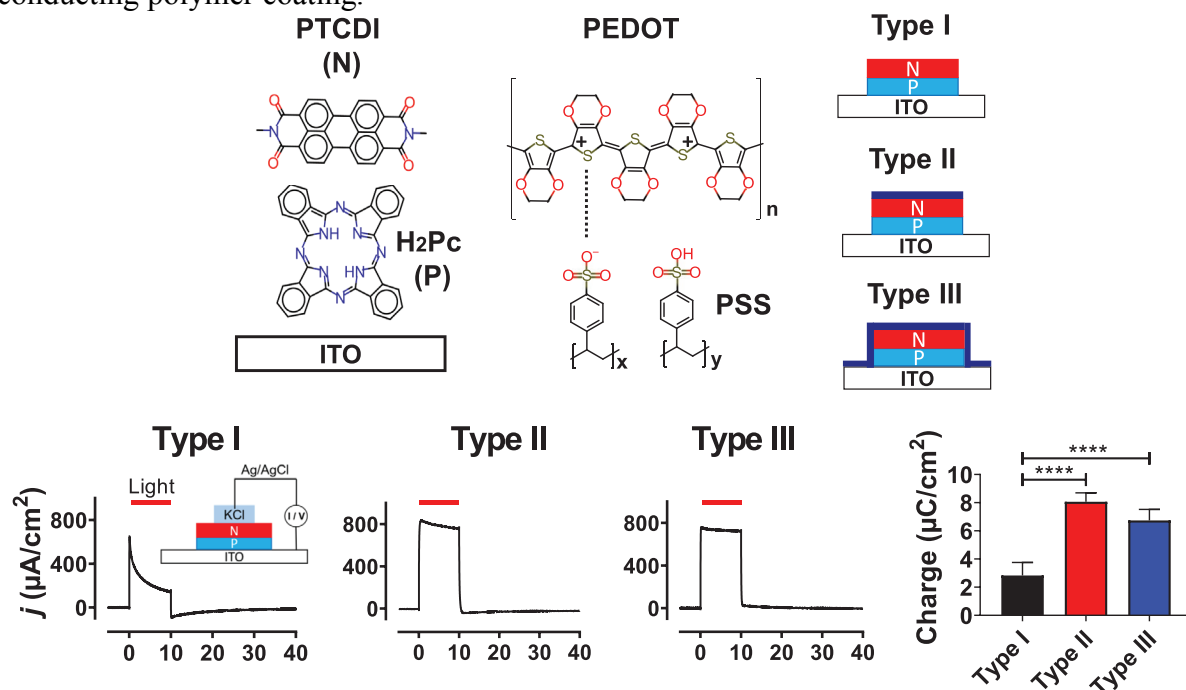


Figure 11. Conducting polymer-modified OEPCs. The conducting polymer PEDOT:PSS is a high-capacitance coating with hybrid electrical/ionic conductivity. We compared “Type II” and “Type III” modifications, involving coating only the PN surface or the whole device with a thin layer of PEDOT:PSS. The PEDOT-modified devices had higher and longer photocharging currents. The total electrolytic charge delivered by a 10 ms light pulse is plotted in the panel in the lower right corner. Adapted from paper 4, within the Creative Commons 4.0 license.

3.1.7 Differentiation between faradaic and capacitive currents: While a fully-capacitive mechanism is implicated in the electrophysiological findings discussed above, the question of a minor faradaic component remained open. In paper 5, we were motivated to have better understanding and methods to generally study faradaic versus capacitive processes in OEPC devices. In its final-use state, the OEPC is an electrically-floating device. It does not have any connection to an electrical ground and therefore the principle of charge neutrality must be strictly applied to the closed system of the OEPC, which is in electrical short circuit to itself via the electrolyte. To measure the photocurrents which actually flow through such a device, one should devise a way to integrate a low-impedance amperometer in series with the OEPC. To do this while still faithfully reproducing the actual structure in terms of component materials and size scale, we created a “split OEPC”, shorted externally by a low-impedance current amplifier. In essence this is a microfabricated photoelectrochemical cell.

Figure 13. Schematic summary of the different processes that can occur at “floating” semiconductor interfaces at the interface of a biological aqueous solution. In the diagrams above, each device is surrounded on all sides by an electrolyte solution. In A, only direct photochemical reactions are possible, or photothermal heat exchange. No net directional currents can flow. In B, the “buried conductor” case, charge separation can occur, but no electric field forms in the solution, the electric field is inside of the solid-state part of the device. The C case describes the structure disclosed by our group for the OEPC, where a photocapacitive regime could transition into a photofaradaic one if respective faradaic reactions are supported on both the semiconductor and the underlying metal contact. Both regimes can coexist if this requirement is fulfilled. Reproduced from Paper 5, within the Creative Commons 4.0 license.

3.2 Photofaradaic devices (Papers 6, 7, 8)

3.2.1. Photocathodes and photoanodes in the context of organic semiconductors

While the previous section dealt with a scenario where electrons accumulate at semiconductor/electrolyte interfaces to reversibly produce capacitive double-layers, a situation can be envisioned in which the potential across the semiconductor/electrolyte interface is high enough to support a charge transfer reaction. When charge is transferred into the electrolyte phase and a product is formed, this is referred to as a faradaic reaction. The most well-known faradaic reaction is that of water-splitting, where water can be oxidized to produce oxygen, or reduced, to yield hydrogen gas, H_2 . Of course, numerous other faradaic reactions in aqueous electrolytes exist, and are used in industrial processes. Photofaradaic devices based on light-absorbing semiconductors generate photocurrents by transferring photoexcited electrons, or holes, into solution. The respective opposite carrier, meanwhile, is transported through the semiconductor to an electrode, which is led to the opposite side of the electrolyte. At the opposite electrode, a complementary redox process must occur in order for faradaic currents to be sustained. A net faradaic reaction can only occur when a cathodic (reductive) and anodic (oxidative) process as paired in the same electrolyte. Charge neutrality must be conserved in such a system. Semiconductor photofaradaic electrodes can be divided into two distinct categories: photocathodes and photoanodes (Figure 14).²⁵ In photocathodes, photoexcited electrons are transferred into the solution (photoreduction), while the remaining hole in the photocathode is transported out to the underlying electrode. For this reason, photocathodes must support p-type transport and are always of p-type character. Photoanodes, on the other hand, afford photooxidation of species in solution by photogenerated holes, while electrons are transported to the underlying electrode. Therefore, n-type transport is critical.

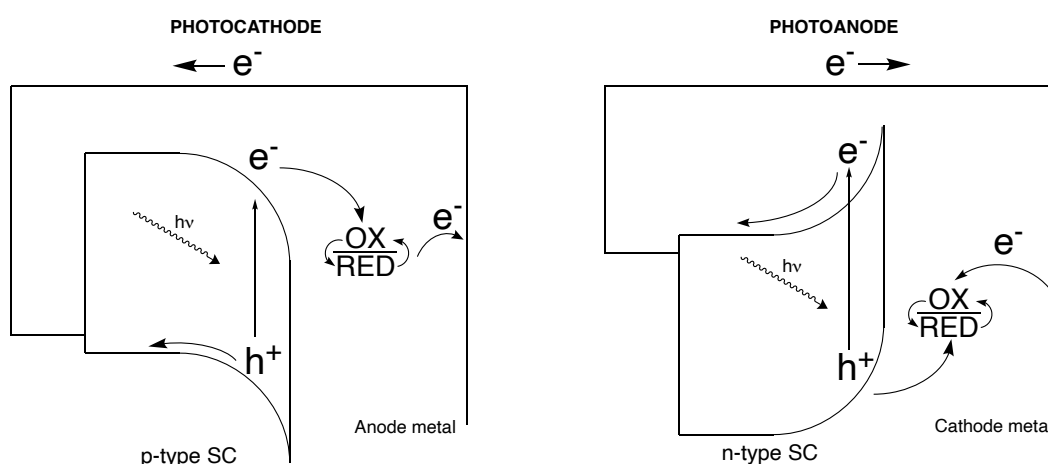
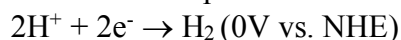


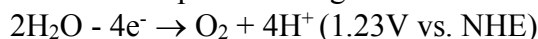
Figure 14. Semiconductor photocathodes comprise a p-type material, which transports holes to the underlying electrode while the photoexcited electrons reduce species in solution. Conversely,

semiconductor photoanodes oxidize species in solution, while photoexcited electrons are transported out to circuit. The p- and n-type materials are drawn with the appropriate band bending.

The archetypical and most-studied processes on photocathodes and photoanodes are water splitting reactions: Photocathodic reduction of protons to form H₂ gas:



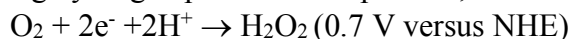
And photoanodic oxidation of water to produce O₂ gas:



Photocathodes and photoanodes based on inorganic semiconductors like silicon and metal oxides (TiO₂, ZnO, etc) are a topic that has been scientifically studied to a great depth, and found application in various industrial applications.^{26,27} Up until several years ago, however, photofaradaic processes on organic semiconductor photoelectrodes (both in a photocathodic or photoanodic configuration), remained almost unexplored.²⁸ There existed a few papers discussing the possibility of H₂ evolution at photocathodes and an example of photoanodes with organic semiconducting metal coordination compounds for O₂ evolution.²⁹ One of the primary reasons for this lack of exploration of this topic was that most of the organic semiconductors that had been extensively developed in the context of photovoltaic and organic-light emitting diode applications were regarded to be very fragile. Both water and oxygen were known to cause degradation, especially in the presence of light.

3.2.2. Single-component organic semiconductor photocathodes for H₂O₂ evolution

We began to explore the topic motivated by the knowledge that crystalline organic pigments belonging to the category of industrial colorants should in principle be much more stable (**Paper 6**). Since these materials were nontoxic and we wanted to explore them for biointerfacing applications as has been discussed in preceding sections, it made sense to evaluate their photoelectrochemical properties. The first organic materials that were tested were epindolidione and quinacridone.³⁰ Photoelectrodes are fabricated by starting with an underlying glass substrate with a conducting thin film (Au or ITO). Epindolidione or quinacridone are deposited by vacuum sublimation to form dense nanocrystalline thin-films (Figure 15). It became apparent that both materials showed clear photocathodic behavior, which was remarkably robust across the whole pH range from highly acidic to alkaline solutions. It became quickly apparent that essentially all (99%+) of the cathodic photocurrent corresponded to oxygen reduction. This could easily be proven by scrupulously excluding O₂ and performing electrochemistry experiments in inert conditions. By optimizing an enzyme-linked colorimetric assay,³¹ we effectively could characterize that all of the oxygen reduction photocurrent was producing hydrogen peroxide as a product, according to the reaction:



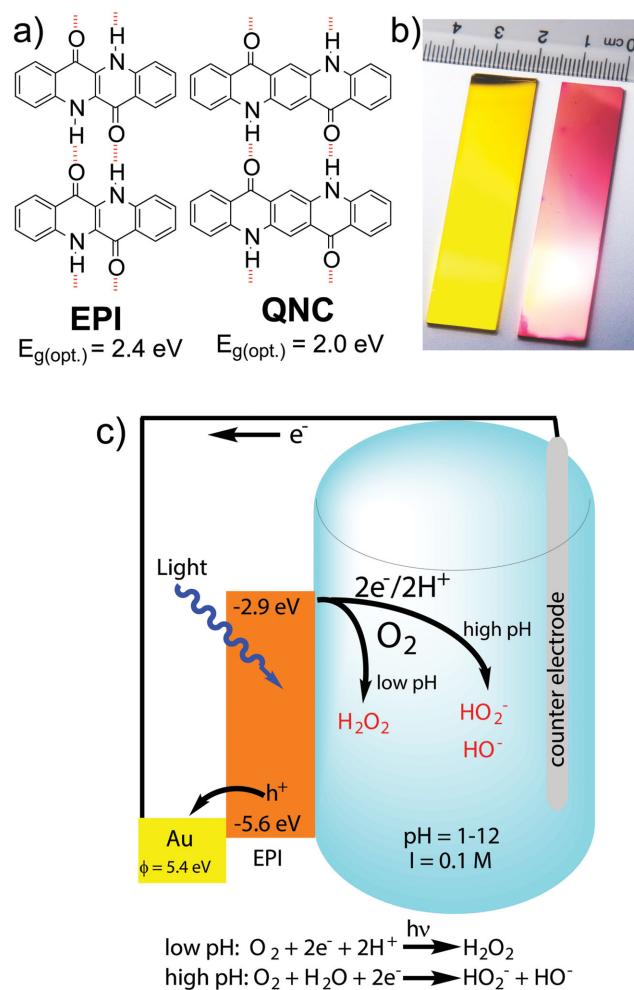
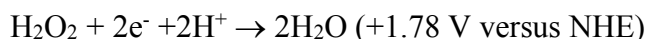


Figure 15. Organic semiconductor photocathodes with Epindolidione and Quinacridone, first published in 2016. These hydrogen-bonded small molecule pigments (a) form compact nanocrystalline films on gold-coated glass substrates (b). Upon illumination in water, measured in a three-electrode electrochemical cell, cathodic photocurrents are observed upon illumination in aqueous electrolytes of any pH (c). The dominant photocathodic process is the oxygen reduction reaction, generating hydrogen peroxide, H_2O_2 , with high faradaic yields exceeding 90%. Reproduced with permission from Paper 6, copyright Wiley-VCH GmbH.

The first remarkable outcome of Paper 6 was the stable faradaic operation of an organic semiconductor photoelectrode in aqueous environment. Experiments were performed under simulated solar irradiation from two to four days, continuously. That was a landmark result which proved that organic semiconductors can in fact be robust to degradation, and compete in a domain that belongs primarily to established oxide semiconductors. The second key finding of this work was that these photocathodes led to sustained accumulation of H_2O_2 in the cell. Hydrogen peroxide can easily be electrochemically further reduced to water, thereby leading to its disappearance:



Though thermodynamically favored, this process is apparently kinetically hindered at the organic semiconductor electrodes we explored. No intrinsic semiconductor photocathodes had been reported up to that time which showed this kind of behavior – we had produced a photoelectrolyzer device which could convert light energy, dissolved oxygen, and water, into the high-energy molecule hydrogen peroxide. The discovery of such a peroxide-generating photoelectrode generated interest in the field of sustainability research, as peroxide fuel cells

are a fast-emerging field. However, for our group this finding was exciting for its potential applications in biology. At high concentrations, hydrogen peroxide is toxic to living organisms. Applications ranging from bacteriostatic surfaces to devices for active killing of cancer cells come to mind. On the other hand, small quantities of peroxide, in the nM to μM concentration range, are implicated in a number of signaling pathways.³² At present, we have embarked on projects to explore primarily this second direction.

3.2.3. Optimized heterojunction devices for H_2O_2 production

Having created reliable and stable photocathodes based on epindolidione or quinacridone pigments, we set forth a goal to optimize this device concept in terms of increasing the photoelectrocatalytic current. With epindolidione electrodes illuminated with simulated solar light ($100 \text{ mW}/\text{cm}^2$) we were able to achieve around $100 \mu\text{A}/\text{cm}^2$ of photocurrent at a potential of 0 V versus Ag/AgCl. In **paper 7**, we asked ourselves how far this number can be increased while still preserving a high faradaic yield for hydrogen peroxide production. The most successful approach we found was to utilize the PN photovoltaic stack that had been optimized for the OEPC devices discussed in papers 2-5.

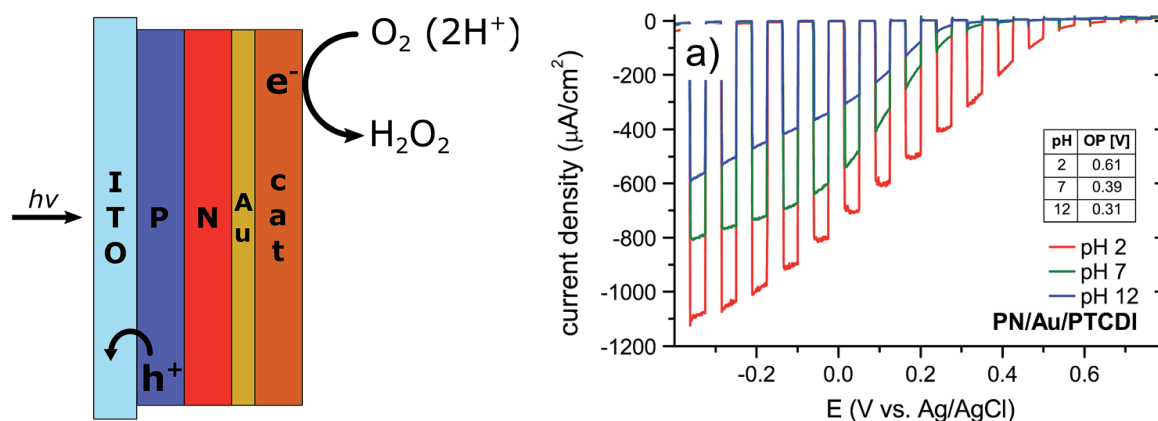


Figure 16. Organic heterojunction photocathodes based on a modification of the PN junction successful in OEPC applications. Under simulated solar irradiation, these photocathodes afford nearly one order of magnitude higher photocurrents compared to the best epindolidione-based photocathodes. The panel on the right shows a linear-scan voltammogram with chopped illumination. This experiment allows clear resolution of the open circuit photovoltages produced by the device (shown in the inset table), as well as the magnitude of dark/light current. Adapted from paper 7, figures originally distributed under the creative commons license 3.0.

These photocathodes rely on a 60+60 nm bilayer of the P and N materials, respectively. This is capped with a thin film of Au, which acts as an efficient charge collection layer. This is capped by a layer of organic pigment known to be an electrocatalyst for oxygen reduction to hydrogen peroxide. For this catalyst layer, we used either epindolidione or PTCDI, which we reported as an electrocatalyst in a paper that is not included in this thesis.³³ Such heterojunction photocathodes could achieve maximum current values at least six to eight times higher than the best single-material photocathodes reported earlier, while preserving faradaic yields of peroxide in excess of 80%. To-date, our report is the best performance photoelectrochemical system for hydrogen peroxide generation and accumulation.

3.2.4. Photofaradaic “floating” pixels

Paper 8 of this thesis represents a synthesis of the concepts of an electrically-floating PN pixel, like described in the sections about photocapacitive devices, and photofaradaic oxygen reduction to hydrogen peroxide. As established in our work on OEPC stimulators, there are negligible net faradaic reactions. This is because there is no anodic reaction at the anodic return electrode (in most cases Au). Therefore, even though the N layer in the PN stack can function as an electrocatalyst for oxygen reduction to peroxide, it does not, because the lack of

an accompanying anodic reaction violates charge neutrality – in other words, there is no source of electrons to sustain a reduction process. The electrocatalytic properties of the anode, therefore, are the gatekeeper of photofaradaic behavior. To create a photofaradaic pixel, we chose a suitable oxidizable target found in biological solutions: glucose. Gold, when prepared in specific ways, is known to show good catalytic properties for glucose oxidation. Photofaradaic devices were prepared as shown in Figure 17. Thin and semitransparent gold was deposited by vacuum evaporation, to create a conductor which was transparent to light. Next, the thin evaporated gold was modified with a thick layer of electrodeposited Au being patterned around the PN pixel. Au prepared in this way is known to have favorable glucose oxidation properties. The net result of our efforts was a stable photofaradaic configuration which cathodically reduces oxygen while simultaneously oxidizing glucose. This kind of device was benchmarked with light excitation at 660 nm, as this wavelength is within the tissue transparency window. The intention is to have photoactivated implantable devices that can modulate local peroxide concentration while simultaneously consuming oxygen (hypoxia) as well as reducing local glucose concentrations. We envision various biomedical applications for this novel concept, ranging from modulation of chronic inflammatory conditions to post-operative cancer therapy.

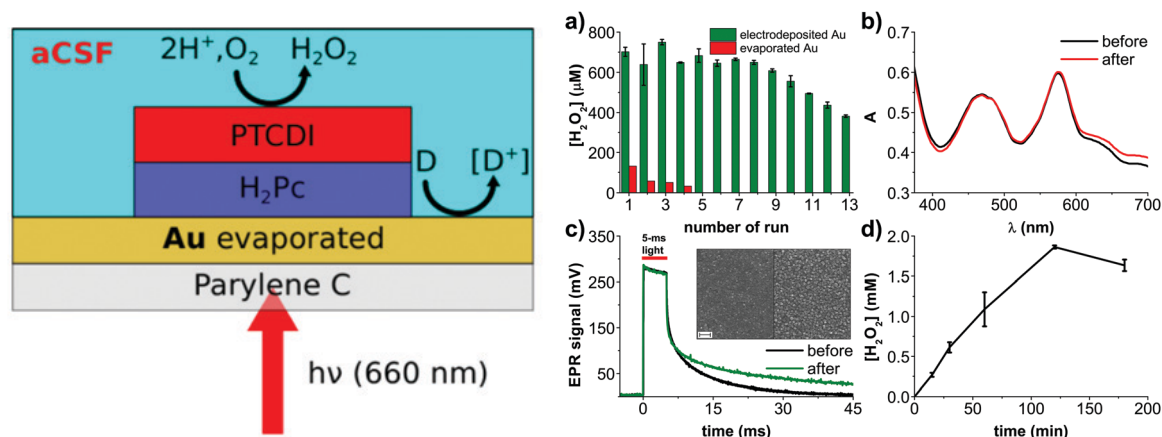


Figure 17. The photofaradaic pixel, for simultaneous light-driven hydrogen peroxide evolution, and oxidation of a sacrificial electron donor, D. In our work we have optimized the anode for oxidation of glucose as the donor. When tested in conditions of artificial cerebrospinal fluid and irradiation with tissue-penetrating red light, $[H_2O_2]$ in the range of 100-1500 μM was easily and reversibly achieved. Adapted from paper 8, figures originally distributed under the creative commons attribution 3.0 unported license.

4. Conclusions and outlook

The scientific work described in this thesis covers a set of directions for semiconductor-based optoelectronics in the “wet” environment of biology. Emerging research protocols and clinical applications alike all require less invasivity and wireless operation. The mechanical properties of soft organic materials, combined with their excellent optical absorbance coefficient, offer unique possibilities to make photoactivated biointerfaces unprecedentedly minimalistic and noninvasive. Organic materials offer also a better outlook for ultimate biocompatibility. In our work we have focused entirely on organic industrial pigments – materials well-known for excellent stability and nontoxicity. In this thesis, the outlined work shows how these “off the shelf” organic semiconductors can be interfaced with living cells, and optical impulses of light can be used to stimulate them. Substantial effort was made to understand the fundamentals of

the mechanisms involved, covering cell viability and the processes governing interaction of the photoexcited semiconductors with the cells: photothermal, photofaradaic, and photocapacitive processes. One of the main achievements of our efforts is the organic electrolytic photocapacitor, a thin film device that is minimalistic and stable and can stimulate excitable cells. These devices have been validated in stimulating single-cell models, neural cell cultures, and finally light-insensitive retinal tissues. Ongoing work is targeted at continuing to optimize these devices for retinal implants, while also focusing on *in vivo* stimulation of nerves accomplished through the actuation of tissue-penetrating deep red light. From the device physics point of view, key parameters to better understand and improve are interfacial capacitance and impedance of the organic semiconductor layers, and overall increasing of the charge injection capacity.

The other set of explorations of organic semiconductor materials in aqueous environments has been the discovery of an interesting photofaradaic process: namely oxygen reduction to hydrogen peroxide. This catalytic transformation is of great interest in industrial applications as well as biological ones, and it is remarkable to have a semiconductor photocathode able to accomplish this reaction and accumulate hydrogen peroxide. From the point of view of the organic semiconductor field, our findings are greatly enabling, because there had been a prevailing notion that all organic semiconductors are far too fragile and will degrade in such aqueous conditions. Our work opens up the area of aqueous photo(electro)catalysis with organic semiconductors.

Overall the future appears bright for organic semiconductor aqueous interfaces, and many opportunities exist for fundamental studies of these kinds of systems and devices, as well as practical applications, of which the most promising, in the opinion of the author, is neurostimulation.

5. References

- 1 Martin Pope and C. E. Swenberg, *Electronic Processes In Organic Crystals and Polymers*, Oxford University Press, Oxford, 2nd edn., 1999.
- 2 C. W. Tang, *Appl. Phys. Lett.*, 1986, **48**, 183–185.
- 3 C. W. Tang and S. a. VanSlyke, *Appl. Phys. Lett.*, 1987, **51**, 913.
- 4 V. Coropceanu, J. Cornil, D. a da Silva Filho, Y. Olivier, R. Silbey and J.-L. Brédas, *Chem. Rev.*, 2007, **107**, 926–952.
- 5 H. Klauk, 2018, **1700474**, 1–8.
- 6 P. Peumans, A. Yakimov and S. R. Forrest, *J. Appl. Phys.*, 2003, **93**, 3693.
- 7 S. E. Shaheen, C. J. Brabec, N. S. Sariciftci, F. Padinger, T. Fromherz and J. C. Hummelen, *Appl. Phys. Lett.*, 2001, **78**, 841.
- 8 D. Di Carlo Rasi and R. A. J. Janssen, *Adv. Mater.*, , DOI:10.1002/adma.201806499.
- 9 W. Herbst and K. Hunger, *Industrial Organic Pigments*, Wiley-VCH, Weinheim, 3rd edn., 2004.
- 10 K. Hunger, *Rev. Prog. Color. Relat. Top.*, 2005, **35**, 76–89.
- 11 B. Hille, *Ion Channels of Excitable Membranes*, Sinauer Associates Inc, Sunderland, Massachusetts, Third., 2001.
- 12 E. S. Krames, P. H. Peckham and A. R. Rezai, Eds., *Neuromodulation*, Academic Press, London, 2009.
- 13 K. Birmingham, V. Gradinaru, P. Anikeeva, W. M. Grill, V. Píkov, B. McLaughlin, P. Pasricha, D. Weber and K. Ludwig, *Nat. Rev. Drug Discov.*, 2014, **13**, 399–400.
- 14 S. Carrara and K. Iniewski, Eds., *Handbook of Bioelectronics*, Cambridge University

- Press, Cambridge, 2015.
- 15 E. Katz, Ed., *Implantable Bioelectronics*, Wiley-VCH, Weinheim, 1st edn., 2014.
 - 16 T. C. Pappas, W. M. S. Wickramanyake, E. Jan, M. Motamedi, M. Brodwick and N. a. Kotov, *Nano Lett.*, 2007, **7**, 513–519.
 - 17 M. G. Shapiro, K. Homma, S. Villarreal, C.-P. Richter and F. Bezanilla, *Nat. Commun.*, 2012, **3**, 736.
 - 18 J. L. Carvalho-de-Souza, J. S. Treger, B. Dang, S. B. H. Kent, D. R. Pepperberg and F. Bezanilla, *Neuron*, 2015, **86**, 207–217.
 - 19 US 2013/0184783 A1, 2013, 1.
 - 20 F. Santoro, S. Dasgupta, J. Schnitker, T. Auth, E. Neumann, G. Panaitov, G. Gompper and A. Offenhäusser, *ACS Nano*, 2014, **8**, 6713–6723.
 - 21 M. R. Antognazza, I. A. Aziz and F. Lodola, *Oxid. Med. Cell. Longev.*, 2019, **2019**, 2867516.
 - 22 S. B. Brummer, L. S. Robblee and F. T. Hambrecht, *Ann. NY Acad. Sci.*, 1983, **405**, 159–171.
 - 23 S. I. Börjesson, T. Parkkari, S. Hammarström and F. Elinder, *Biophys. J.*, 2010, **98**, 396–403.
 - 24 S. F. Cogan, *Annu. Rev. Biomed. Eng.*, 2008, **10**, 275–309.
 - 25 Rüdiger Memming, Ed., *Semiconductor electrochemistry*, Wiley-VCH, Weinheim, 2nd edn., 2016.
 - 26 Z. Chen, H. N. Dinh and E. Miller, *Photoelectrochemical Water Splitting Standards , Experimental Methods , and Protocols*, Springer, New York, 2013.
 - 27 S. N. Habisreutinger, L. Schmidt-Mende and J. K. Stolarczyk, *Angew. Chem. Int. Ed. Engl.*, 2013, **52**, 7372–408.
 - 28 S. Bellani, M. R. Antognazza and F. Bonaccorso, *Adv. Mater.*, 2018, **1801446**, 1801446.
 - 29 T. Abe, K. Nagai, S. Kabutomori, M. Kaneko, A. Tajiri and T. Norimatsu, *Angew. Chemie - Int. Ed.*, 2006, **45**, 2778–2781.
 - 30 E. D. Głowacki, M. Irimia-Vladu, M. Kaltenbrunner, J. Gąsiorowski, M. S. White, U. Monkowius, G. Romanazzi, G. P. Suranna, P. Mastroianni, T. Sekitani, S. Bauer, T. Someya, L. Torsi and N. S. Sariciftci, *Adv. Mater.*, 2013, **25**, 1563–1569.
 - 31 P. D. Josephy, T. Eling and R. P. Mason, *J. Biol. Chem.*, 1982, **257**, 3669–3675.
 - 32 C. R. Lee, J. C. Patel, B. O’Neill and M. E. Rice, *J. Physiol.*, 2015, **593**, 3431–3446.
 - 33 M. Warczak, M. Gryszel, M. Jakešová, V. Đerek and E. D. Głowacki, *Chem. Commun.*, 2018, **54**, 1960–1963.



6. Included Papers

ARTICLE

DOI: 10.1038/s41467-017-00135-0

OPEN

Cellular interfaces with hydrogen-bonded organic semiconductor hierarchical nanocrystals

Mykhailo Sytnyk^{1,2}, Marie Jakešová^{3,4,5}, Monika Litviňuková⁴, Oleksandr Mashkov^{1,2}, Dominik Kriegner⁶, Julian Stangl⁷, Jana Nebesářová⁸, Frank W. Fecher⁹, Wolfgang Schöfberger ¹⁰, Niyazi Serdar Sariciftci³, Rainer Schindl^{4,11}, Wolfgang Heiss^{1,2} & Eric Daniel Głowacki ^{3,5}

Successful formation of electronic interfaces between living cells and semiconductors hinges on being able to obtain an extremely close and high surface-area contact, which preserves both cell viability and semiconductor performance. To accomplish this, we introduce organic semiconductor assemblies consisting of a hierarchical arrangement of nanocrystals. These are synthesised via a colloidal chemical route that transforms the nontoxic commercial pigment quinacridone into various biomimetic three-dimensional arrangements of nanocrystals. Through a tuning of parameters such as precursor concentration, ligands and additives, we obtain complex size and shape control at room temperature. We elaborate hedgehog-shaped crystals comprising nanoscale needles or daggers that form intimate interfaces with the cell membrane, minimising the cleft with single cells without apparent detriment to viability. Excitation of such interfaces with light leads to effective cellular photostimulation. We find reversible light-induced conductance changes in ion-selective or temperature-gated channels.

¹Materials for Electronics and Energy Technology (i-MEET), Friedrich-Alexander-Universität Erlangen-Nürnberg, Martensstraße 7, 91058 Erlangen, Germany. ²Energie Campus Nürnberg (EnCN), Fürtherstraße 250, 90429 Nürnberg, Germany. ³Linz Institute for Organic Solar Cells (LIOS), Physical Chemistry, Johannes Kepler University, Altenbergerstraße 69, 4040 Linz, Austria. ⁴Institute for Biophysics, Johannes Kepler University, Gruberstraße 40, 4020 Linz, Austria. ⁵Laboratory of Organic Electronics, ITN Campus Norrköping, Linköpings Universitet, Bredgatan 33, 60221 Norrköping, Sweden. ⁶Department of Condensed Matter Physics, Charles University, Ke Karlovu 5, Prague 121162, Czech Republic. ⁷Institute of Semiconductor and Solid State Physics, University Linz, Altenbergerstraße 69, Linz 4040, Austria. ⁸Biology Centre of the Czech Academy of Sciences—Institute of Parasitology, Branišovská 31, České Budějovice 37005, Czech Republic. ⁹Bayerisches Zentrum für Angewandte Energieforschung (ZAE Bayern), Immerwahrstr. 2, 91058 Erlangen, Germany. ¹⁰Institute of Organic Chemistry, Johannes Kepler University, Altenbergerstraße 69, 4040 Linz, Austria. ¹¹Institute for Biophysics, Medical University of Graz, Harrachgasse 21/IV, 8010, Graz Austria. Mykhailo Sytnyk and Marie Jakešová contributed equally to this work. Correspondence and requests for materials should be addressed to R.S. (email: rainer.schindl@medunigraz.at) or to W.H. (email: wolfgang.heiss@fau.de) or to E.D.G. (email: eric.glowacki@liu.se)

Biology at the single-cell level is true nanomachinery¹. As we master new techniques for manipulating matter on the nanoscale, opportunities for interfacing with biological systems arise. Recently, nanomaterial interfaces at the cellular level have been demonstrated to achieve cell morphology control^{2–4}, cell fate determination^{5,6}, sensing^{7,8}, nano-injection^{9–11} and delivery of genetic material for transfection¹². In all of these applications, interrogation of intracellular events relies on sharp high-aspect ratio nanostructures^{9,13,14}. Artificial high-aspect nanostructures have similarly been a focus of interest for electronic interfacing with living cells, being sought after for applications in high-quality extracellular and intracellular electrophysiology^{7,15} recording and stimulation, and for providing a bridge into the cytosol for both delivery and intracellular sensing^{10,11}. Inorganic materials, especially silicon, and metals like platinum and gold predominate in all these applications. A common goal is getting as close an interface to the cell as possible, forming a minimal cleft, and ideally with large area^{13,15}. Optimising such structures is especially critical in the case of (opto)electronic interfaces, where the cleft between the cell and electronic element results in electric field screening and poor

coupling^{16–18}. Recently, close cellular interfaces with nanoscale amorphous silicon particles have been able to give reversible photostimulation of excitable cells¹⁹. Control of biology with light at the single-cell level is a concept with far-reaching consequences in both fundamental biological research and applied medicine. Optogenetics is widely considered to be one of the most significant development in neuroscience in the past decade, since it enables highly localised targeting at the single-cell level both in vitro and in vivo²⁰. Its reliance on genetic transfection introduces challenges and limitations, however, which has motivated extensive exploration of nongenetic means of optical control. Several reports have shown the possibility to achieve light-induced manipulation of cells, particularly excitable cells, either mediated by light-absorbing particles^{19,21,22}, or thin-films^{23–25}, or using direct near-infrared optical heating²⁶. In the past years, a growing spectrum of novel bioelectronics applications have been enabled by organic semiconductors, which have superior biocompatibility and mechanical properties, and novel functionality relative to silicon^{27–29}. These features, combined with their high optical absorbance coefficient, have made nanoscale thin films of organic semiconductors suitable for

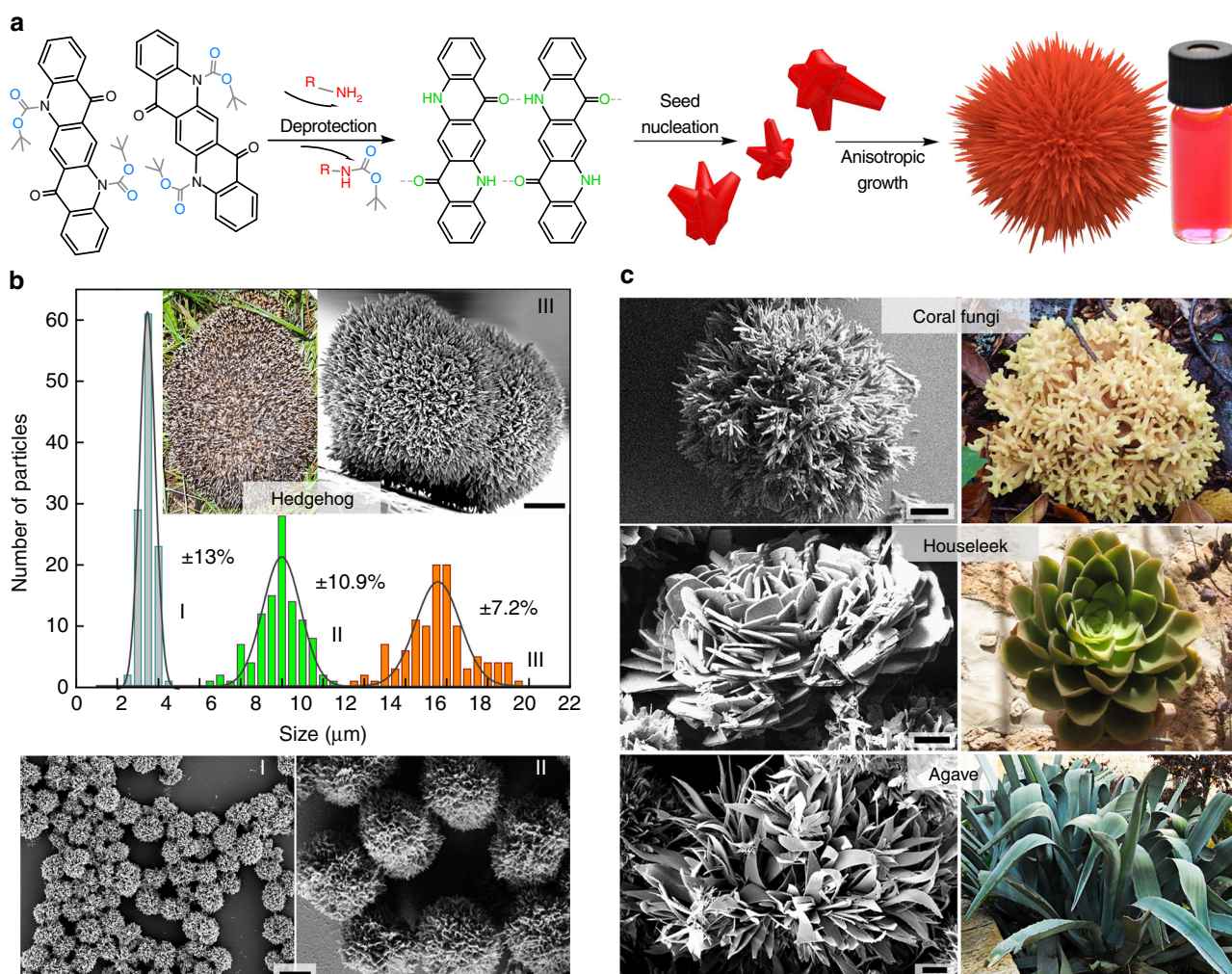


Fig. 1 Colloidal quinacridone hierarchical nanoarchitectures with bio-inspired shapes. **a** The synthesis proceeds when soluble *N,N'*-di(*t*-butoxycarbonyl)quinacridone (tBOC-QNC) is deprotected via an amine migration reaction, giving monomeric quinacridone (QNC) molecules that crystallise via an interplay of H-bonding and π - π stacking. These ligand-covered colloidal nanocrystals then assemble due to van der Waals forces into hierarchical colloidal assemblies. **b** The size of hedgehog crystals is determined by the starting concentration of tBOC-QNC, allowing narrow size distribution to be achieved. Three sizes—I, II and III are shown in the SEM micrographs. **c** Nanoarchitectures with shapes of various plants, given on the photos, are obtained by using different ligands. Scale bars on the electron micrographs = $4 \mu m$

optoelectronic photostimulation of single cells^{30–32} and retinal tissues^{25, 33}. The issue of the cell/semiconductor cleft still remains an obstacle for these organic devices, however.

The starting point of our work is the desire to create a new family of organic semiconductor structures that can by virtue of morphology form an intimate contact with the cell membrane. To this end, we develop a synthetic method to yield hierarchical colloidal architectures comprising organic semiconductor nanocrystals. We synthesise these using a ligand-mediated approach, not only to afford fine synthetic control of the structure, but also to yield a crystal surface modified with a ligand monolayer suitable for favourable interaction with lipid bilayer cell membranes. As an organic semiconductor suitable for biointerfacing, we choose quinacridone (QNC), a nontoxic magenta-coloured pigment industrially produced primarily for inks and paints³⁴. We present methods whereby QNC hierarchical assemblies form upon ligand-mediated QNC-precursor decomposition at room temperature followed by nucleation and assembly into hierarchical structures. By manipulation of conditions such as initial precursor concentration, reaction time, solvent, and chemical additives, we control size, shape, and crystalline polymorphism of the QNC structures, yielding spherical shapes consisting of high aspect-ratio nanocrystals with forms reminiscent of hedgehogs. These hedgehog colloidal semiconductors, with overall diameter similar to a eukaryotic cell (10 μm), can be used directly in cell culture. We find that two cultured cell lines used routinely in electrophysiology experiments, rat basophilic leukaemia (RBL), and human embryonic kidney (HEK) cells, grow preferentially on such hierarchical nanocrystal structures, forming close interfaces with minimal cleft after a few hours in culture. This occurs without apparent changes in cell viability. The hierarchical assembly has the auspicious property of being able to mechanically deform under the growing cell, resulting in an interface with a minimal cleft. This occurs because, though the constituent crystals are rigid, the hierarchical superstructure is held together by van der Waals forces and is thus plastic. These single cell/semiconductor nanostructure interfaces lend themselves to patch clamp electrophysiology experiments. Visible-light photoexcitation of the semiconductor nanostructures leads to reversible changes in ion conduction through ion-selective channels (K^+ rectifiers) and temperature-gated ion channels in cells growing on the hedgehogs. We see both rapid changes on the order of a few milliseconds as well as longer-scale ion conductivity increases, created by an interplay of rapid photoinduced changes in membrane capacitance and photothermal heating. Our work demonstrates a promising new platform for optoelectronic interfaces with living matter.

Results

Hierarchical nanoarchitecture syntheses. Nanocrystalline architectures of organics can be grown using various vapour or solution deposition/evaporation techniques^{35–37}. Colloidal techniques^{38, 39} are prevalent in the case of hierarchical inorganic materials^{40–44}. We have recently introduced the idea of ligand-mediated syntheses of colloidal organic monocrystals⁴⁵ using a range of hydrogen-bonded pigments. Here we make hierarchical crystals for cellular interfaces by designing a new colloidal synthetic method. As a molecular building block, we choose QNC. The hydrogen-bonded pigment QNC is particularly interesting in the context of biological applications due to reported nontoxicity⁴⁶ and presence of NH functional groups that enable direct bioconjugation reactions⁴⁷. Recently QNC, in the form of vacuum-evaporated thin films, has been reported as a promising semiconductor, with outstanding stability, ambipolar charge carrier mobility, and favourable optoelectronic⁴⁸ and

photocatalytic⁴⁹ properties. The multifunctionality and availability of QNC make it a good target for making organic semiconducting hierarchical nanostructures. Our chemical route (Fig. 1a) for QNC colloidal nanoarchitectures relies on first transforming the insoluble QNC pigment powder, obtained from a paint supplier, into a soluble dye, *N,N'*-di(*t*-butoxycarbonyl)quinacridone (tBOC-QNC), using the known amine protection reaction⁵⁰ with *t*-butoxycarbonyl (tBOC). QNC, due to interplay of intermolecular hydrogen bonding between carbonyl and amine functional groups and π - π stacking, is insoluble. By interrupting the hydrogen bonding with tBOC functionalisation of the NH group, a highly soluble dye is obtained^{45, 50}. The tBOC group can be removed by heat or strong acids⁵¹. To accomplish our crystal growth at room temperature and under mild conditions, we discovered a new deprotection reaction: the ability of carbamate esters to migrate between amine groups. The reaction can occur at room temperature, as the tBOC carbamate ester unit will favour migration to the amine that is the stronger nucleophile. Depending on the reactivity of the amine added to the tBOC-QNC, this reaction can go to completion in a few minutes (for highly reactive amines like methylamine) or even from hours to weeks (see Methods and Supplementary Table 1). We found that primary amines with long aliphatic chains interact at moderate rates with tBOC-QNC, resulting in reactions lasting several hours. Depending on the type of amine used, the starting concentration of tBOC-QNC, and the presence of solvents and chemical additives that selectively interact with the carbonyl or amine functionality on QNC, a range of hierarchical nanostructured microcrystals can be grown (Fig. 1b, c). When tBOC-QNC is reacted with oleylamine (acting as both solvent and reactive amine) at room temperature, 3D hierarchical structures with the shape of hedgehogs, consisting of self-assembled nanoneedles with diameters smaller than 50 nm (Fig. 1b) are reproducibly obtained. While such complex structures are relatively hard to synthesise in the case of inorganic materials, here we obtained them with narrow size dispersion in the range of $\pm 10\%$ by simply varying the starting concentration of tBOC-QNC. Changing the ligand species results in additional bio-inspired shapes of the final nano-architectures: while oleylamine provides hedgehogs, methylamine gives a coral fungi architecture consisting of dendritic nanocrystals (Fig. 1c). Mixtures of butylamine and di-methylaminopyridine give 2D nano-platelets arranging into nanoflower architectures, with a shape reminiscent of houseleek plants. Pure butylamine as ligand results in agave-shaped nanoarchitectures of approximately similar dimensions. In all cases, the microcrystals demonstrated outstanding colloidal stability when transferred to organic solvents (e.g. chloroform or chlorobenzene) due to extensive capping with alkylamine ligands. The structural integrity was found to be very robust in solution for several months, even after treatments by ultrasonication. Using X-ray diffraction, we can prove that all the QNC nanoarchitectures in Fig. 1c consist of differently sized and shaped nano-units having the same internal crystal structure (γ) (Supplementary Fig. 1), even though QNC pigments are known to crystallise in four polymorphs (α_1 , α_2 , β , γ)⁵².

The growth mechanism. In order to understand the mechanisms behind the anisotropic growth of the colloidal crystals, first the aspects of chemical reactivity were probed. A beautiful aspect of this reaction is that it can be easily monitored in situ by optical absorbance spectroscopy, thus the concentration of the constituents can be extracted via the Beer-Lambert law. Optical absorption measurements reveal three different stages linked to a chemical state of the QNC molecules (Supplementary Fig. 2): at the beginning of the reaction (stage 1) the QNC is

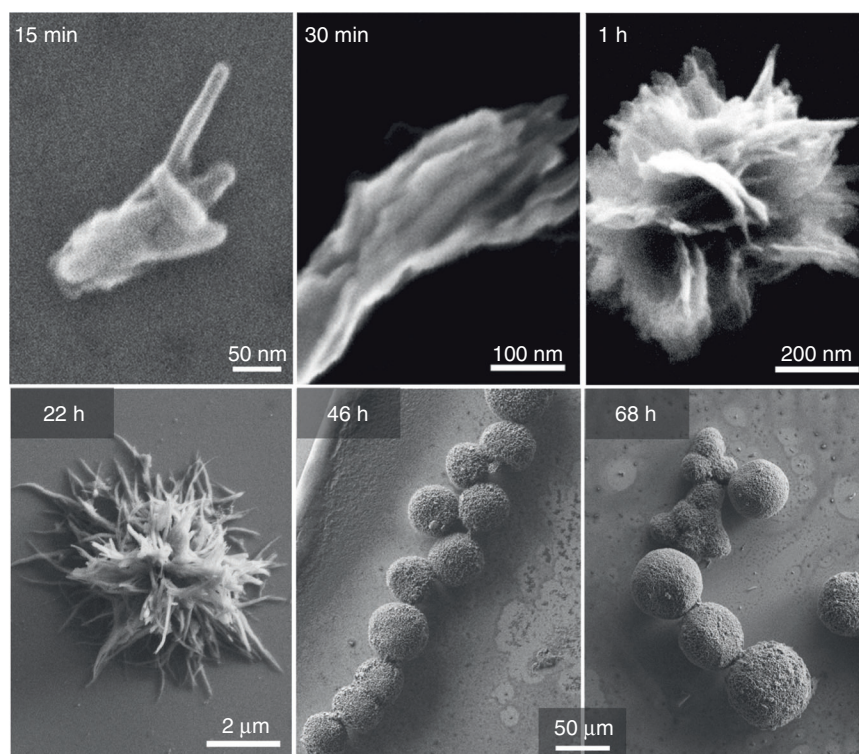


Fig. 2 SEM imaging of hierarchical crystal growth. Aliquots removed at different times during synthesis reveal the growth process of hierarchical crystals. Branching is occurring already at 15 min, and continues as the microstructures grow over 68 h. Monomeric quinacridone molecules precipitate onto exposed facets of the crystals, generating growth along this facet that progressively ceases to grow due to increased steric hindrance caused by attached alkylamine ligands. Repetition of this process maintains branched growth as the microstructures expand spherically

double-protected by tBOC, in stage 2 it is mono-tBOC protected and in stage 3 it is completely unprotected and in the monomeric state constituting the building block of crystals. The double-protected QNC shows an absorbance peak at 420 nm, the monoprotected at 470 nm and the unprotected at 520 nm. After stage 2 there is almost no signal from tBOC-QNC and the dominant species in solution is monomeric (peak at 510 nm). Based on these time-dependent optical measurements (Supplementary Note 1 and Supplementary Figs. 2–4), we conclude that the amine-induced deprotection of tBOC-QNC involves chemical migration of a tBOC group, via a pseudo-first-order chemical reaction in conditions where the concentration of the reactive amine is significantly greater than that of tBOC-QNC. The migration of the tBOC group to the reactive amine is confirmed by identifying *t*-butoxycarbonyl alkyl amide products with nuclear magnetic resonance spectroscopy (Supplementary Figs. 5 and 6). This amine-induced migration is significantly different from the well-established tBOC deprotection reactions, namely acid-catalysed and thermal, because in these two cases irreversible decomposition of the tBOC groups occurs. Those reactions are relatively harsh, requiring either strong acids like trifluoroacetic acid or temperatures in excess of 120 °C. A clear advantage of amine-induced deprotection is its occurrence at room temperature. The second advantage is a flexible control of the reaction kinetics by the tBOC-QNC concentration and reactivity of the amine and thus crystallisation and growth control of nanocrystals. To understand the growth over time, we removed aliquots from the reaction with oleylamine, which proceeds at a moderate rate, and imaged them using scanning electron microscope (SEM) (Fig. 2). It is clear that even at the earliest stages of the synthesis needle-like nanocrystallites branch off of nucleation points. Over time the branching continues, resulting in comb-like aggregates of nanocrystals that grow into spherical microstructures. The

spherical shape indicates that nucleation and growth occurs in colloidal solution rather than on a surface, as molecular monomers must nucleate from all sides of the microstructure to account for the spherical forms (Supplementary Figs. 7 and 8).

Polymorphism control. So far, we have discussed control of hierarchical structure shape by using different ligands while conserving the internal molecular crystal structure (γ). We further found that by manipulating reaction time and chemical additives, phase-pure samples of three polymorphs could be prepared: α_2 , β and γ (Fig. 3a, b). The three crystallisation routes are illustrated in Supplementary Fig. 9. The speed of crystal growth and coordination of QNC monomers determines the final crystal structure. Amine-induced deprotection lasting several hours reliably produces γ as described previously. The γ phase features a ‘criss-cross’ lattice of QNC molecules where each molecule forms single $\text{NH}\cdots\text{O}=\text{C}$ hydrogen bonds to four neighbours. Slowing down the reaction to last over several days (1–10 days) by using a noncoordinating solvent and a lower amine concentration gives the α_2 polymorph, qualitatively similar to γ but with closer spacing between chains of hydrogen-bonded QNC molecules and lower triclinic symmetry (Supplementary Fig. 10). Finally, by using a solvent that coordinates with amine groups, for example cyclohexanone, a completely different hydrogen-bonding pattern between QNC molecules is obtained, namely a linear-chain arrangement where each QNC molecule hydrogen bonds to only two neighbours, forming H-bonded sheets in the β polymorph (Supplementary Fig. 11). A major benefit of polymorphism control is that the different crystal structures lead to distinctive optical properties (Fig. 3c, d). We find that each polymorph is luminescent, with excitonic emission that is remarkably narrow compared to previous findings of solid state thin-film luminescence in QNC, which report coexistence or even dominance of

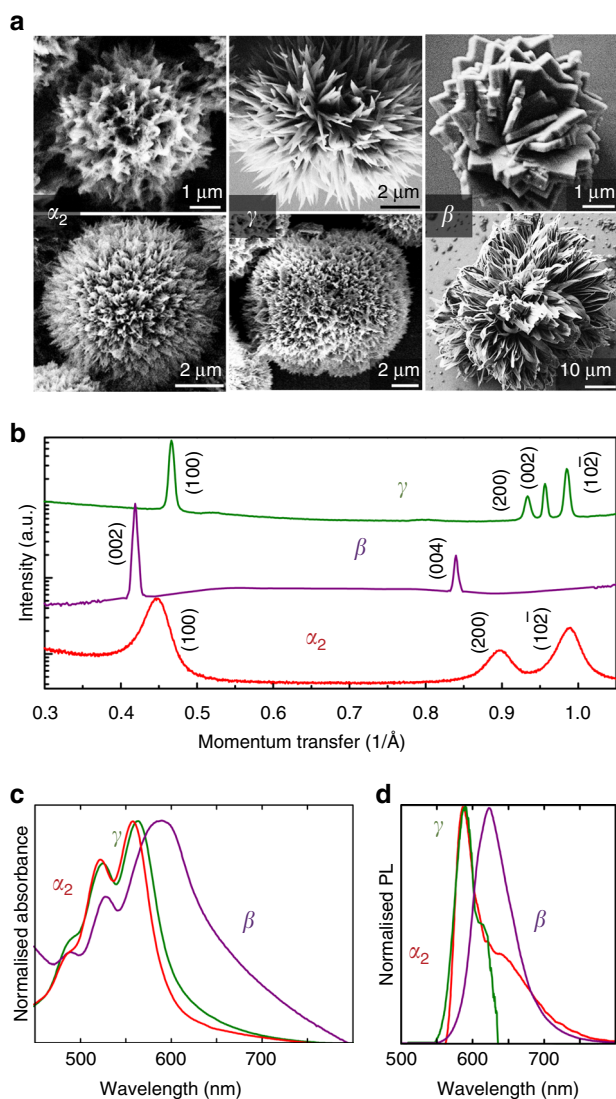


Fig. 3 Control of internal crystal structure. Polymorphism can be controlled by modulating reaction time and coordinating chemical additives. **a** SEM micrographs of α_2 , β and γ crystals. **b** X-ray diffraction, confirming the phase-pure quality of the colloidal samples, **c** absorbance and **d** luminescence of each sample. The upper row of SEM images shows the hierarchical nano-dagger modification, while the lower row shows hierarchical nanoneedle assemblies

broad defect state luminescence in the region of 700–850 nm^{48, 53}. This signifies that the crystalline semiconductor quality of the hierarchical crystals is high, and apparently far less defects are present than in vacuum-evaporated films. Two hierarchical hedgehog structural schemes could be observed for each polymorph: Shorter alkylamines like butylamine favour formation of nanodagger hedgehog crystals consisting of triangular units of tens to hundreds of nanometres in width tapering down to sharp tips (upper row of images in Fig. 3a). Using bulkier amines such as oleylamine result in hedgehogs consisting of nanoneedles (lower row of images in Fig. 3a).

Interfaces with single cells. From the outset of this study, we surmised that the organic needle-like hierarchical QNC hedgehogs should be capable of forming close and high surface-area contacts with cells. To evaluate this, we first drop-cast colloidal solutions of QNC hedgehogs on glass substrates suitable for cell culture. The two types of γ hedgehogs shown in Fig. 3a were used:

hierarchically assembled arrays of nanoneedles, while the second is the nanodagger modification, featuring nano-scale triangular daggers tapering down to a sharp 10–20 nm wide point. Drop-cast hedgehogs were found to adhere well to both hydrophobic octyltriethoxysilane (OTS)-modified, as well as hydrophilic (3-aminopropyl)triethoxysilane (APTES)-modified glass substrates, and did not delaminate in cell culture solutions, or after UV sterilisation. Rat basophilic leukemia (RBL) and human embryonic kidney (HEK) cells were chosen for culture due to their utility in electrophysiology experiments. Cell culture was carried out for up to 3 days, with samples removed for SEM imaging and cell viability assays. Glass substrates modified to be favourable for the given cell culture (OTS-modified glass for RBL cells and APTES-modified for HEK) were used for SEM imaging. The RBL cells were found to grow on the QNC planar films prepared by vacuum sublimation; however, HEK cells showed no attachment. On the other hand, we found that RBL and HEK cells readily attach to both types of hedgehogs. RBL cells form remarkably conformable interfaces with the nanostructured surface of hedgehog crystals already after 1.5 h in culture, apparent from SEM (Fig. 4). The cell/crystal interfaces can be conveniently viewed also by optical microscopy, where the crystals' luminescence allows fluorescence imaging of the semiconductor structures (Supplementary Fig. 12). From SEM imaging, it is apparent that the plasma membrane and extracellular matrix conforms to the nanoneedle structures, causing anchoring of cells onto the microhedgehog (Fig. 4). The evaluation of the true interface cleft distance in vivo is a question of current debate, as the fixation of cells for electron microscopy can produce a cleft morphology different from what is present in vivo^{15, 54}. The cleft distance has been determined to change as much as 10–50 nm following fixation in some cases, even where cryofixation methods are employed. In the case of SEM imaging of hedgehog/cell interfaces, the inevitable 'artefact problem' of cell shrinkage occurring during fixation actually yields interesting information: we observed frequent examples where the hedgehogs are actually pulled apart by cells, with cells extracting nanoneedles from the parent microstructure, or sometimes splitting the hedgehog structure between multiple cells (Fig. 4c, Supplementary Fig. 13). This indicates that the membrane/nanoneedle interaction can be stronger than the forces holding the hierarchical architecture together. Over longer times in culture, the cells are found to transition from a rounded shape to spread more extensively on the hedgehogs (Fig. 4d). Based on viability assays (CytoTox-Glo luminescence-based assay, Supplementary Fig. 14) we conclude that the cells remain viable while having such an extensive contact area with the crystals. Carried out over 3 days, the assay demonstrated no difference in viability between cells cultured with hedgehogs, planar or powder QNC and control samples. This experiment suggests that neither form of the QNC material is acutely cytotoxic. QNC itself, as a commercial pigment, has been studied with regards to consumer safety and determined to be nontoxic⁴⁶. Like RBLs, HEKs form a high interfacial area contact with hedgehog crystals, (Fig. 5), with occasional examples of engulfment-type processes¹⁵ clearly occurring (Fig. 5b). As mentioned before, HEK cells do not attach to planar evaporated QNC films. To discriminate the role of hierarchical nanostructure vs. QNC surfaces themselves, we prepared samples with hedgehogs drop-cast onto a glass slide, followed by sublimation of a uniform 80 nm thin film of QNC over the entire sample area, including on top of the hedgehogs. HEK cells were found to grow exclusively on the hedgehogs and not anywhere on the planar films (Fig. 5c, Supplementary Fig. 15). From this it is clear that hedgehog structures promote cell attachment and growth due to their nano-microstructure³. HEK cells progressively spread over hedgehog structures during

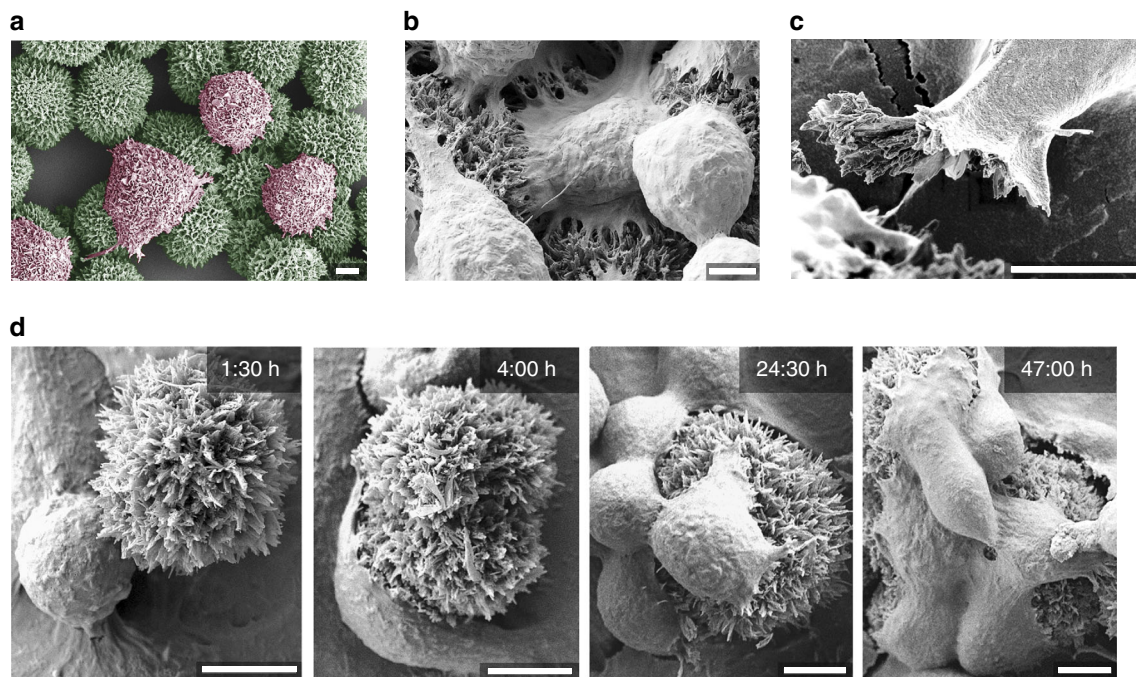


Fig. 4 SEM imaging of rat basophilic (RBL) cells cultured with quinacridone nanohedgehogs. **a** RBL cells cultured on 10- μ m-size nanoneedle hedgehogs, with cells false-coloured *pink* and hedgehogs false-coloured *green*. The image captures the cells when they are degranulating. **b** Tight interfaces between RBL cells and nanoneedle hedgehogs. **c** The cell membrane and extracellular matrix of RBL cells can rip nanoneedles out of the hierarchical microcrystal, demonstrating the strength of the cell/nanocrystals interaction. **d** RBL cell culture interrupted at different intervals (hours shown in image *upper right corners*), showing the progression of cell attachment, proliferation and morphology over time. Scale bars = 5 μ m

cell culture (Fig. 5d), with uncompromised viability verified by assays (Supplementary Fig. 14). Cross-sectional images revealing the cell/semiconductor interface were possible with HEK cells since, serendipitously, strain occurring during the fixation/dehydration procedure could lead to splitting of the cell/hedgehog pair, conveniently revealing the morphology of the interface (Fig. 6). It must be noted that since the fixation procedure leads to shrinkage in these samples, this imaging can only give us the lower limit for the actual cleft size. Keeping this in mind, two critical observations can be made: first, there appears to be no evidence that the nanocrystals penetrate through the cell membrane, rather, the cell membrane arranges flush with the nanocrystals, with extremely close contact and no distinguishable cleft. Second, the hierarchical nanocrystalline structure partially collapses, buckles and distorts to give way under the cell. Even though the extent of the distortions revealed by SEM is a result of fixation stresses, we find no examples of nanocrystallites breaking the integrity of the cell membrane. This leads us to conclude a unique mechanical advantage—the hierarchical structure has the mechanical freedom to move, and the constituent nanocrystallites can be rearranged by the growing cell. This interpretation is consistent with the observation discussed previously of RBL cells ripping nanocrystallites out of the hierarchical parent structures. This behaviour can easily be rationalised considering that the QNC molecules in the nanocrystals are held together by a strong interplay of π - π stacking and hydrogen-bonding, while the hierarchical arrangements are held together by much weaker van der Waals forces. These findings offer a new paradigm for organic semiconductors for bioelectronics—hierarchical architectures can show mechanical plasticity while being constituted of a rigid and stable material.

Photostimulation of ion channels. Having established stable and close, high-surface area cell/semiconductor interfaces, we used patch clamp electrophysiological techniques to probe the effect of

visible light irradiation (532 nm) on the cells. Our first electrophysiology measurements were on the endogenous potassium inward rectifier channels expressed in RBL cells (Fig. 7a). The K^+ inward rectifier channels are of general interest since they are responsible for maintaining the resting membrane potential of many types of cells in animals, bacteria and plants. In whole-cell voltage-clamp measurements, we delivered through-objective illumination to patched cells (532 nm, 10 ms pulses, with three energies 10, 30 and 50 μ J). The illuminated area had a 15 μ m diameter. The K^+ inward rectifier was selectively measured using a linear voltage-ramp protocol (Fig. 7a). Patched cells were recorded first in the dark and then with pulsed laser illumination (10 ms pulses). In the dark, reproducible rectifier current-voltage characteristics are obtained, indicating no non-specific membrane leakage. The integrity of patched cells was found to be identical for controls growing on plain glass (which show no photoinduced effects) in comparison with those on hedgehog structures. For cells growing on hedgehogs, application of light pulses generates depolarising currents at the beginning of the light pulse, with a corresponding spike in the opposite polarity at the end of the light pulse. This behaviour is visible at all voltage values along the sweep. At voltage values more negative than -80 mV, where the K^+ inward rectifier is open, following the transient current spike there is an increased inward current plateau (Fig. 7a, *inset*). After illumination, K^+ current returns to the baseline, dark, value. This net reversible increase in inward K^+ current scales with the light energy dose (Fig. 7b, *inset*) and is higher for nanoneedle-type hedgehogs compared with nanodagger ($n = 11$ – 13 cells). Control cells, growing on the same substrates but not in direct contact with hedgehogs, show no photoinduced changes whatsoever ($n = 20$ cells). Continuous wave (CW) illumination over longer time-scales comprising several whole voltage sweeps (hundreds of milliseconds with lower intensities of light, 5 mW/mm²) demonstrated that the K^+ rectifier curve does not change its current-voltage characteristics, only the net inward current peak

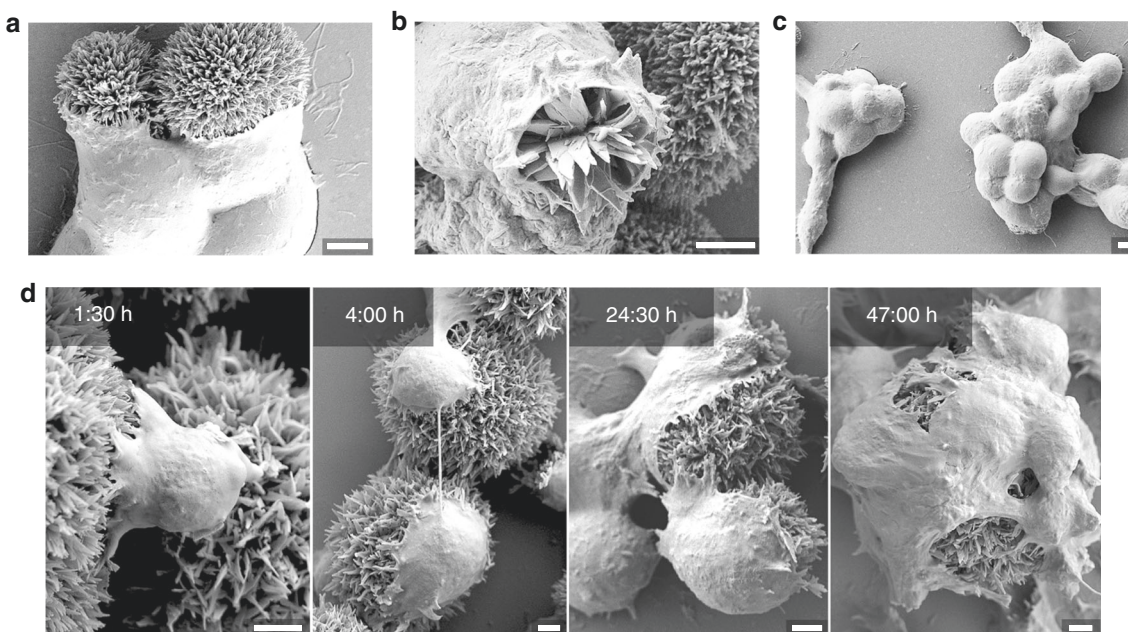


Fig. 5 SEM imaging of human embryonic kidney (HEK) cells cultured with quinacridone nanohedgehogs. **a** Close and highly conformal interfaces form after a few hours in culture. **b** Engulfment-like events are observable in the case of HEK cells, here a cell is imaged in the course of an endocytosis event with a nanodagger hedgehog. **c** HEK cells do not grow on evaporated quinacridone thin-films. Here cells are cultured on substrates with hedgehogs where the entire surface, including hedgehogs, is coated with a uniform sublimated quinacridone thin film, thus demonstrating that the nanostructure and not chemical nature of the substrate is critical for cell adhesion. **d** Interface contact between HEK cells and hedgehogs increases over cell culture time, and morphology transitions from rounded cells with a few attachment points to cells showing extensive spreading on the hedgehog structures. Scale bars = 2.5 μm

reversibly increases with illumination (Fig. 7b). We now consider the two separate light-induced observations: First, the rapid depolarising current spikes present throughout the trace, and second, the increased current ‘plateau’ region that is apparent for time-scales from 10 to 1000 ms. Our observation of depolarising current can be explained by a rapid photothermal or photocapacitive effect (Fig. 7e). Photocapacitive effects could arise from charging of the QNC surface with negative charges and capacitive coupling⁵⁵, resulting in transient depolarisation of the cell membrane. Recently the phenomenon of fast heating-induced capacitive currents induced by amorphous silicon microparticles in contact with the plasma membrane has been reported by Jiang et al.¹⁹. There, the photothermal capacitance change gives rise to transient depolarisation of the membrane. These findings were in line with earlier work that demonstrated that intense infrared pulsed illumination could lead to capacitive membrane depolarisation²⁶. Martino et al.³¹ in the case of polymeric thin films observed apparent photothermal depolarisation behaviour, but preceded by a more rapid photocapacitive depolarisation³¹. In principle, our observation of depolarising current spikes can be explained by a rapid photothermal or photocapacitive effect. Whatever the origin, the capacitive peaks cause only a passive membrane response and no clear effect on K^+ rectifier conductance. Considering the ‘plateau’ increase region: it is observable only in the voltage range where the K^+ channel is open, at both short and longer time scales, coupled with no observation in changes in current–voltage characteristics, suggesting that photothermal heating leads to increased ion diffusion rates and therefore higher current through the channels when they are open. This effect is reversible in both short (10 ms) and longer (hundreds of ms) time-scale regimes. With the evidence generally pointing towards the presence of photothermal heating, we elected to transfect HEK cells with a temperature-activated channel: the transient receptor potential vanilloid (TRPV1) ion channel, famous for its role in producing the ‘hot’ taste of chilli

peppers by being sensitive to capsaicin, and also transduction of pain caused by heat. Voltage-ramp measurements for TRPV1-transfected HEK cells grown on hedgehogs resulted in a more outward rectifying current–voltage relationship and gave qualitatively identical photoinduced behaviour as the K^+ channels, namely transient depolarising current spikes and increased plateau regions at voltages where the channel normally shows activity (Fig. 7c). At more positive voltage polarisations, the light-induced capacitive depolarisation becomes smaller, qualitatively similar to results found for rapid infrared photothermal cell excitation²⁶. One critical difference is apparent, however: at the cell resting potential (-60 mV) a reversible photoinduced cation influx current occurs (Fig. 7d). This demonstrates that temperature-gated channels can be directly and rapidly photo-stimulated in cells under normal physiological conditions. These results complement nicely recent findings of photoinduced stimulation of Ca^{2+} current in TRPV1 channels using nanoparticles of semiconducting polymers²². While that study demonstrates changes on the time scale of hundreds of milliseconds, using the patch clamp technique with our hedgehog crystals we are able to observe more rapid and reversible changes in TRPV1-mediated current. Finally, the picture that emerges is one where a photothermal mechanism can increase the ion flow through open channels without otherwise changing current–voltage characteristics, though there is a concurrent presence of faster depolarising current behaviour (Fig. 7e). Photothermal heating is unambiguously behind the light-modulated electrophysiology behaviour we observe in the potassium inward rectifier and in the temperature-gated TRPV1 channels. Rapid and localised heat transfer to cells has been targeted by various applications both in vitro and in vivo^{19, 26, 31}, and clinical applications of optical neural stimulation for neuroprosthetics are currently actively explored⁵⁶. The potential success of the hierarchical organic crystal architecture in this context may rely not only on the formation of the close and high surface-area

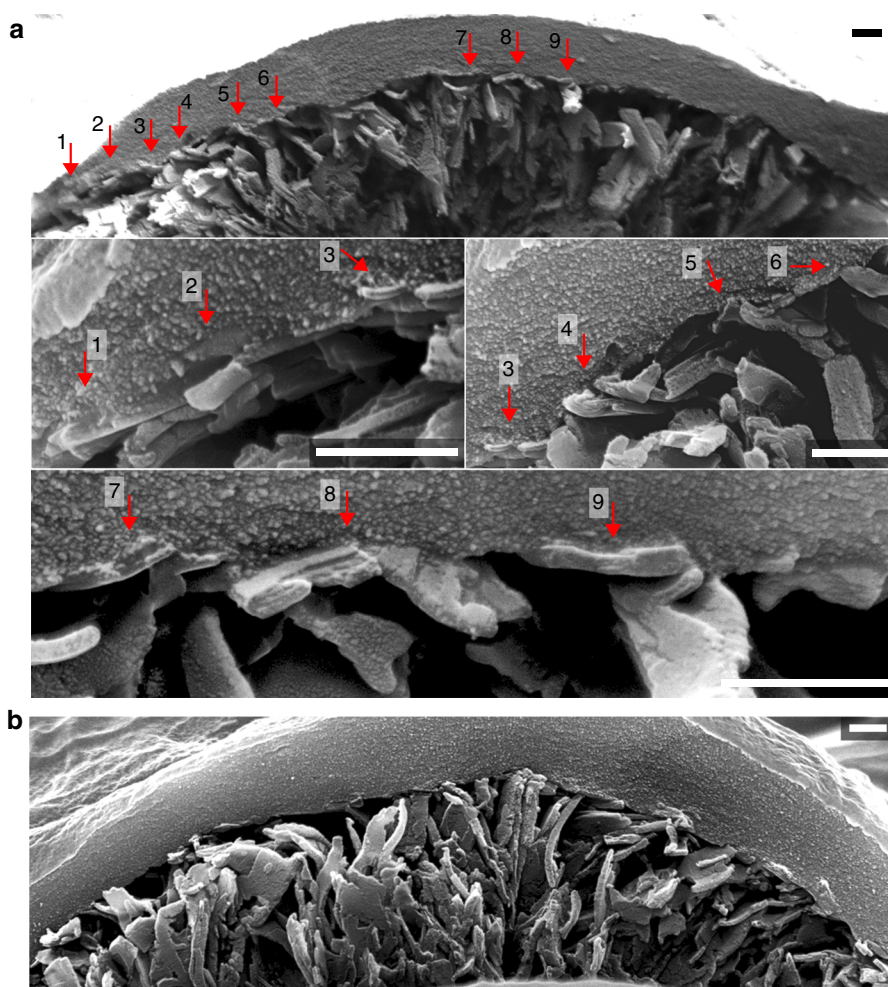


Fig. 6 Cross-sectional interface of cells and hedgehogs imaged with SEM. **a** An interface between a HEK cell and nanodagger hedgehog, with close contacts between cell membrane and nanocrystallites labelled and shown in higher magnification. **b** Cross-section overview of another HEK/nanodagger interface, clearly showing the extent of distortion and crumpling of the nanodagger assembly under the cell. Scale bars = 500 nm

interface, but also on the specific photothermal behaviour inherent for such structures. We simulated the photothermal heating of hedgehogs vs. spheres and planar films, using the known absorption coefficient for QNC and assuming only convective heat dissipation to surrounding water. The high aspect ratio needles of hedgehogs heat up to higher temperatures faster than the surface of a planar film or a similar micron-scale sphere (Supplementary Fig. 16). The hierarchical semiconductor nanoarchitectures shown here, by virtue of being of similar size and shape to single cells, function as a platform for inducing photoeffects in a highly local manner, providing means of stimulating cells without invoking the need for genetic modification with light-sensitive ion channels.

Discussion

In this work, we have introduced a room-temperature colloidal synthetic methodology for obtaining size-controlled and shape-controlled nanocrystalline hierarchical assemblies of the organic semiconducting building block QNC. These organic semiconductor hierarchical nanoarchitectures offer unique advantages for next-generation bioelectronics interfaces at the single-cell level. They feature the attractive properties of high aspect-ratio nanostructures that were to-date the domain of inorganic materials, notably silicon, but are mechanically much more pliable since the rigid nanocrystals are held together by van der

Waals forces. This enables very close interfaces with cells to form, with a minimal cleft. The minimisation of the cleft is a key parameter for several bioelectronics applications, especially electrophysiological recording and stimulation. QNC, as an organic semiconductor, has a high absorbance coefficient in the visible region, and we demonstrate that light irradiation of cells growing with a tight interface on QNC hierarchical nanocrystals results in photostimulation effects. Using pulsed irradiation, we are able to reversibly increase current flow through K^+ inward rectifier channels, at both millisecond and second time scales. A photothermal heating mechanism is implicated as most critical, as the hierarchical nanocrystals can efficiently and rapidly heat the interface with the cell. We exploit this feature by reversibly photostimulating the opening of temperature-gated channels (TRPV1) at normal physiological conditions. These demonstrations open up many potential research directions on this novel type of material. Future research should focus on establishing nanostructure-to-function relationships of how cellular function can be affected and controlled, and in particular should exploit the mechanical deformability of such assemblies. The details of such interfaces, as well as the occurrence of endocytosis-like processes, can be studied conveniently with optical means by leveraging the advantage of the strong luminescence of QNC combined with standard immunostaining procedures. Semiconductor-mediated optical stimulation of cells, despite encouraging seminal reports on the topic, remains largely

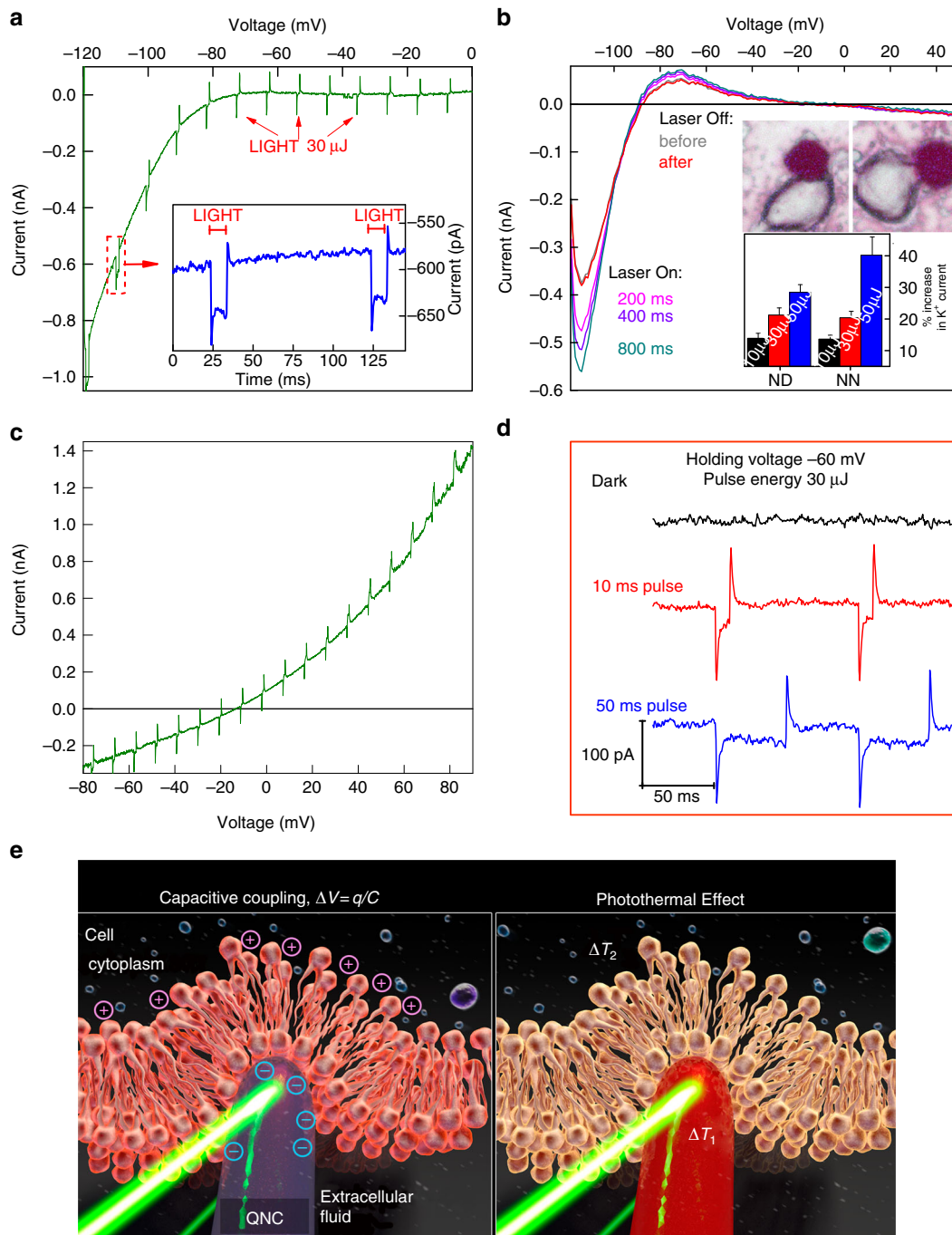


Fig. 7 Hedgehog-mediated photostimulation of ion channels. **a** Reversible photostimulation of the K^+ inward rectifier channel with 10 ms light pulses in an RBL cell grown on a 10- μm -size nanoneedle hedgehog apparent in voltage-clamp measurements in whole-cell configuration. Rapid (<1 ms time scale) light-induced depolarising currents are visible over the entire voltage sweep range, however only where the K^+ inward rectifier channel is open ($V < -80$ mV) are there photoinduced increases (+30%) in K^+ inward current. The inset shows the effects of light pulses, at a holding potential of -110 mV with the depolarising current spikes and a plateau region of K^+ current increase, the latter attributed to local photothermal heating and faster ion diffusion. **b** The K^+ rectifier in an RBL cell on hedgehog measured using CW illumination over 1 s, $5 \text{ mW}/\text{mm}^2$. The current-voltage characteristic remains the same, only the peak value of K^+ current increases reversibly with illumination. This is consistent with photothermal heating raising the local temperature of the cell, increasing the current of ions through the open channels. The inset shows statistics for photoinduced K^+ influx increase percentage (K^+ rectifier) of the illuminated RBL cells growing on nanoneedle-type and nanodagger-type hedgehogs. Error bars represent the standard error of the mean ($n = 11-14$). The photomicrograph shows how cells in contact with hedgehogs appear under the microscope. **c** Current-voltage relationship of cation current in temperature-sensitive TRPV1 channels overexpressed in HEK cells on hedgehogs. Depolarising current spikes are visible throughout the whole trace while increases in cation current are apparent in voltage ranges where the channel is open. **d** HEK cell with TRPV1 give rapid and reversible photoinduced stimulation of cation influx when measured at the cell resting potential, -60 mV. **e** Schematic illustration of the mechanisms possible at nanocrystal/cell interfaces. Photocapacitive membrane depolarisation can occur on a short time-scale (left) and rapid photothermal changes can lead to capacitive modulation at short time scales, while increases in through-channel conductance due to localised photothermal heating (right) can be observed on time scales from 10 ms up to 1000 ms

unexplored. We believe that the use of simple organic pigments as light-absorbing particles will allow many researchers to enter into this field. For *in vitro* electrophysiology, the interfaces presented here are already suitable and highly advantageous, since we obtain clear single-cell level reversible stimulation that is localised. Our finding of photostimulation of the cell/semiconductor interface yielding reversible electrophysiological responses should be built upon to enable devices that give stimulation via true electronic mechanisms. This can be achieved by creating a donor/acceptor core-shell structure, which can generate charge separation with high photovoltage and surface-charge density—the two key benchmark parameters urgently sought to enable true photocapacitive cellular stimulation. Using organic crystal engineering such structures should be accessible. Finally, for application in retinal implants, a colloidal solution of nanocrystal assemblies can be sub- or epiretinally injected, and their size and shape similarity with rod and cone cells combined with favourable cell adhesion and interface-forming properties can make them a potent artificial retinal implant technology. We argue that pigments like QNC are an obvious materials choice for a biocompatible organic semiconductor: a cheap pigment that we use today for cosmetics and printing inks can provide an interface between the information age and us.

Methods

Materials and characterisation. The commercially available QNC pigment was obtained from Kremer Pigmente or from TCI and was used as-received. All other chemicals were obtained from Sigma-Aldrich and used without additional purification. X-ray diffraction patterns were measured using synchrotron radiation at beamlines BM20/ESRF, Grenoble and powder diffraction beamline P02 at Hasylab Hamburg with 11.5 and 60 keV X-ray photons, respectively.

QNC latent pigment synthesis. tBOC-QNC was prepared by mixing QNC pigment powder (3.75 g, 12 mmol) in anhydrous tetrahydrofuran (600 ml) kept under nitrogen atmosphere at room temperature with di-*tert*-butyl dicarbonate (*t*-Boc₂O, 12.644 g, 58 mmol) and 4-dimethylaminopyridine (2.93 g, 24 mmol). This mixture was stirred for 48 h and monitored by thin layer chromatography. The crude solution was evaporated almost to dryness and filtrated in a chromatography column through a 80-fold amount of silica gel, with a 19/1 mixture of toluene/ethyl acetate (AcOEt) to obtain crystalline products in yields up to 60%. This product was further purified by recrystallisation from AcOEt prior to nanocrystal synthesis. Sample purity was verified by comparison to literature spectra⁴⁵.

Anisotropically grown nanoarchitectures. QNC nanoarchitectures were obtained by room-temperature decomposition of tBOC-QNC in the presence of primary amines. To yield the smallest hedgehogs shown in Fig. 1b, 20 mg (39 μmol) of tBOC-QNC was dissolved in 1 ml chloroform and then 1 ml oleylamine (OLA) was added. After 24 h, the decomposition was stopped by adding 3 ml of cyclohexane, and the nanoparticles were collected after a washing procedure, as described in the following section. To increase the size, instead of chloroform the same amount of pure OLA was used, or dimethylformamide was added. By replacing OLA with butylamine agave-shaped nanoarchitectures (Fig. 1c) were obtained. Butylamine/dimethylaminopyridine resulted in houseleek shape and using 33% methylamine/ethanol gave coral fungi shape (Fig. 1c). To get the beta phase with the shape of starflower (Fig. 3a, *top-right*), 10 mg of tBOC-QNC was dissolved in 2.5 ml cyclohexanone and then 2.5 ml butylamine was added. After 44 h the decomposition was quenched. By using 5-aminotetrazole (0.5 g) as a coordination ligand for both sides of QA molecules, with 3 ml of 5 mg/ml chloroform solution of tBOC-QNC chrysanthemum shaped (Fig. 3a, *bottom-right*) micronanostructures were obtained after 1 month of decomposition. Supplementary Table 1 summarises the reaction conditions for the different crystals. After synthesis, the organic pigment micronanocrystals were isolated by adding cyclohexane in a volume ratio of 3:1 to the crude colloidal solutions, followed by centrifugation (relative centrifugal force = 14,100g, 5 min) and redispersion in chloroform. The washing step was repeated four times before the micronanocrystals were stored in chloroform or in chlorobenzene. Instead of centrifugation, sedimentation for more than 1 h followed by decantation can be applied, yielding the same results.

Electrophysiological recordings. Details on cell culture, viability and SEM measurements of biological samples can be found in the Supplementary Methods. Untransfected RBL cells were used for the recording of the K⁺ inward rectifier. In these experiments the intracellular pipette solution contained 145 mM KCl, 1 mM MgCl₂, 10 mM Hepes, 10 mM glucose (pH 7.2) and the extracellular solution

contained 140 mM NaCl, 5 mM KCl, 2 mM CaCl₂, 1 mM MgCl₂, 10 mM Hepes, 10 mM glucose. Voltage ramps between -120 and +60 mV lasting for 100 ms (for long photostimulation in Fig. 7b) or 2 s (for short photostimulation in Fig. 7a) were applied from a holding potential of 0 mV. HEK 293 cells were transfected with 1 μg of YFP-TRPV1 DNA and 2 μl Transfectin reagent (Biorad). Electrophysiological experiments were performed 24–34 h after transfection using the patch-clamp technique in whole-cell recording configurations at 21 °C to 25 °C. An Ag/AgCl electrode was used as reference. For the study of the TRPV1 channel, voltage ramps were applied from a holding potential of 30 mV, covering a range of -100 to 100 mV over 2 s. The internal pipette solution included 145 mM cesium methanesulfonate, 20 mM EGTA, 10 mM Hepes, 8 mM NaCl, 3.5 mM MgCl₂ (pH 7.2). Standard extracellular solution consisted of 145 mM NaCl, 10 mM Hepes, 10 mM glucose, 5 mM KCl, 1 mM MgCl₂, 0.3 mM CaCl₂ (TRPV1), pH 7.4. Based on TRPV1 selectivity, inward currents of Na⁺ and Ca²⁺ are expected.

Data availability. The authors declare that the data supporting the findings of this study are available within the paper and its Supplementary Information files.

Received: 14 September 2016 Accepted: 5 June 2017

Published online: 21 July 2017

References

- Grzybowski, B. A. & Huck, W. T. S. The nanotechnology of life-inspired systems. *Nat. Nanotechnol.* **11**, 585–592 (2016).
- Stevens, M. M. & George, J. H. Exploring and engineering the cell surface interface. *Science* **310**, 1135–1138 (2005).
- Bettinger, C. J., Langer, R. & Borenstein, J. T. Engineering substrate topography at the Micro- and nanoscale to control cell function. *Angew. Chemie Int. Ed.* **48**, 5406–5415 (2009).
- Dalby, M. J., Gadegaard, N. & Oreffo, R. O. C. Harnessing nanotopography and integrin-matrix interactions to influence stem cell fate. *Nat. Mater.* **13**, 558–569 (2014).
- Trappmann, B. et al. Extracellular-matrix tethering regulates stem-cell fate. *Nat. Mater.* **11**, 742–742 (2012).
- Murphy, W. L., McDevitt, T. C. & Engler, A. J. Materials as stem cell regulators. *Nat. Mater.* **13**, 547–557 (2014).
- Cohen-Karni, T., Qing, Q., Li, Q., Fang, Y. & Lieber, C. M. Graphene and nanowire transistors for cellular interfaces and electrical recording. *Nano. Lett.* **10**, 1098–1102 (2010).
- Tian, B. et al. Three-dimensional, flexible nanoscale field-effect transistors as localized bioprobes. *Science* **329**, 830–834 (2010).
- Xie, X. et al. Mechanical model of vertical nanowire cell penetration. *Nano. Lett.* **13**, 6002–6008 (2013).
- Xu, A. M. et al. Quantification of nanowire penetration into living cells. *Nat. Commun.* **5**, 3613 (2014).
- Chiappini, C. et al. Biodegradable nanoneedles for localized delivery of nanoparticles *in vivo*: exploring the biointerface. *ACS Nano* **9**, 5500–5509 (2015).
- Elnathan, R. et al. Maximizing transfection efficiency of vertically aligned silicon nanowire arrays. *Adv. Funct. Mater.* **25**, 7215–7225 (2015).
- Kotov, N. A. et al. Nanomaterials for neural interfaces. *Adv. Mater.* **21**, 3970–4004 (2009).
- Tunuguntla, R. H., Allen, F. I., Kim, K., Belliveau, A. & Noy, A. Ultrafast proton transport in sub-1-nm diameter carbon nanotube porins. *Nat. Nanotechnol.* **11**, 639–644 (2016).
- Santoro, F. et al. Interfacing electrogenic cells with 3D nanoelectrodes: position, shape, and size matters. *ACS Nano* **8**, 6713–6723 (2014).
- Fromherz, P., Offenhäuser, A., Vetter, T. & Weis, J. A neuron-silicon junction: a Retzius cell of the leech on an insulated-gate field-effect transistor. *Science* **252**, 1290–1293 (1991).
- Schoen, I. & Fromherz, P. Activation of Na⁺ channels in cell membrane by capacitive stimulation with silicon chip. *Appl. Phys. Lett.* **87**, 1–3 (2005).
- Schoen, I. & Fromherz, P. The mechanism of extracellular stimulation of nerve cells on an electrolyte-oxide-semiconductor capacitor. *Biophys. J.* **92**, 1096–1111 (2007).
- Jiang, Y. et al. Heterogeneous silicon mesostructures for lipid-supported bioelectric interfaces. *Nat. Mater.* **15**, 1023–1030 (2016).
- Scanziani, M. & Häusser, M. Electrophysiology in the age of light. *Nature*. **461**, 930–939 (2009).
- Bareket, L. et al. Semiconductor nanorod-carbon nanotube biomimetic films for wire-free photostimulation of blind retinas. *Nano. Lett.* **14**, 6685–6692 (2014).
- Lyu, Y., Xie, C., Chechetka, S. A., Miyako, E. & Pu, K. Semiconducting polymer nanobioconjugates for targeted photothermal activation of neurons. *J. Am. Chem. Soc.* **138**, 9049–9052 (2016).

23. Pappas, T. C. et al. Nanoscale engineering of a cellular interface with semiconductor nanoparticle films for photoelectric stimulation of neurons. *Nano. Lett.* **7**, 513–519 (2007).
24. Migliori, B., Di Ventra, M. & Kristan, W. Photoactivation of neurons by laser-generated local heating. *AIP Adv.* **2**, 32154 (2012).
25. Ghezzi, D. et al. A polymer optoelectronic interface restores light sensitivity in blind rat retinas. *Nat. Photonics* **7**, 400–406 (2013).
26. Shapiro, M. G., Homma, K., Villarreal, S., Richter, C.-P. & Bezanilla, F. Infrared light excites cells by changing their electrical capacitance. *Nat. Commun.* **3**, 736 (2012).
27. Rivnay, J., Owens, R. M. & Malliaras, G. G. The rise of organic bioelectronics. *Chem. Mater.* **26**, 679–685 (2014).
28. Torsi, L., Magliulo, M., Manoli, K. & Palazzo, G. Organic field-effect transistor sensors: a tutorial review. *Chem. Soc. Rev.* **42**, 8612–8628 (2013).
29. Someya, T., Bao, Z. & Malliaras, G. G. The rise of plastic bioelectronics. *Nature* **540**, 379–385 (2016).
30. Ghezzi, D. et al. A hybrid bioorganic interface for neuronal photoactivation. *Nat. Commun.* **2**, 166 (2011).
31. Martino, N. et al. Photothermal cellular stimulation in functional bio-polymer interfaces. *Sci. Rep.* **5**, 8911 (2015).
32. Feyen, P. et al. Light-evoked hyperpolarization and silencing of neurons by conjugated polymers. *Sci. Rep.* **6**, 22718 (2016).
33. Gautam, V., Rand, D., Hanein, Y. & Narayan, K. S. A polymer optoelectronic interface provides visual cues to a blind retina. *Adv. Mater.* **26**, 1751–1756 (2014).
34. Zollinger, H. *Color Chemistry. Syntheses, Properties and Applications of Organic Dyes and Pigments* (Wiley-VCH, 2003).
35. Lei, T. & Pei, J. Solution-processed organic nano- and micro-materials: design strategy, growth mechanism and applications. *J. Mater. Chem.* **22**, 785–798 (2012).
36. Pan, L. et al. Hierarchical nanostructured conducting polymer hydrogel with high electrochemical activity. *Proc. Natl Acad. Sci. USA* **109**, 9287–9292 (2012).
37. Wang, Y. et al. Graphene-assisted solution growth of vertically oriented organic semiconducting single crystals. *ACS Nano* **9**, 9486–9496 (2015).
38. Talapin, D. V., Lee, J.-S., Kovalenko, M. V. & Shevchenko, E. V. Prospects of colloidal nanocrystals for electronic and optoelectronic applications. *Chem. Rev.* **110**, 389–458 (2010).
39. Kovalenko, M. V. et al. Prospects of nanoscience with nanocrystals. *ACS Nano* **9**, 1012–1057 (2015).
40. Ge, J., Lei, J. & Zare, R. N. Protein–inorganic hybrid nanoflowers. *Nat. Nanotechnol.* **7**, 428–432 (2012).
41. Noorduyn, W. L., Grinthal, A., Mahadevan, L. & Aizenberg, J. Rationally designed complex, hierarchical microarchitectures. *Science* **340**, 832–837 (2013).
42. Wegst, U. G. K., Bai, H., Saiz, E., Tomsia, A. P. & Ritchie, R. O. Bioinspired structural materials. *Nat. Mater.* **14**, 23–36 (2015).
43. Cai, W., Duan, G. & Li, Y. *Hierarchical Micro/Nanostructured Materials: Fabrication, Properties, and Applications* (CRC Press, 2014).
44. Ko, S. H. & Grigoropoulos, C. P. (eds) *Hierarchical Nanostructures for Energy Devices*. (Royal Society of Chemistry, 2015).
45. Sytnyk, M. et al. Hydrogen-bonded organic semiconductor micro- and nanocrystals: from colloidal syntheses to (Opto-)electronic devices. *J. Am. Chem. Soc.* **136**, 16522–16532 (2014).
46. Hunger, K. Toxicology and toxicological testing of colorants. *Rev. Prog. Color. Relat. Top.* **35**, 76–89 (2005).
47. Glowacki, E. D. et al. Bioconjugation of hydrogen-bonded organic semiconductors with functional proteins. *J. Mater. Chem. C* **3**, 6554–6564 (2015).
48. Glowacki, E. D. et al. Intermolecular hydrogen-bonded organic semiconductors—quinacridone versus pentacene. *Appl. Phys. Lett.* **101**, 23305 (2012).
49. Jakešová, M. et al. Hydrogen-bonded organic semiconductors as stable photoelectrocatalysts for efficient hydrogen peroxide photosynthesis. *Adv. Funct. Mater.* **26**, 5248–5254 (2016).
50. Zambounis, J. S., Hao, Z. & Iqbal, A. Latent pigments activated by heat. *Nature* **388**, 131–132 (1997).
51. Wuts, P. G. M. & Greene, T. W. in *Greene's Protective Groups in Organic Synthesis* 696–926 (Wiley and Sons, 2007).
52. Paulus, E. F., Leusen, F. J. J. & Schmidt, M. U. Crystal structures of quinacridones. *CrystEngComm* **9**, 131–143 (2007).
53. Rossi, L. et al. Ultrafast optical probes of electronic excited states in linear trans-quinacridone. *Chem. Phys. Lett.* **257**, 545–551 (1996).
54. Belu, A. et al. Ultra-thin resin embedding method for scanning electron microscopy of individual cells on high and low aspect ratio 3D nanostructures. *J. Microsc.* **263**, 78–86 (2016).
55. Abdullaeva, O. S. et al. Photoelectrical stimulation of neuronal cells by an organic semiconductor–electrolyte interface. *Langmuir* **32**, 8533–8542 (2016).
56. Richter, C.-P., Matic, A. I., Wells, J. D., Jansen, E. D. & Walsh, J. T. Jr. Neural stimulation with optical radiation. *Laser Photon. Rev.* **5**, 68–80 (2011).

Acknowledgements

We acknowledge financial support from the Austrian Science Fund FWF via the projects TRP 294-N19, FWF P28167-N34, and the Wittgenstein Prize for N.S.S.; as well as FWF Projects P26067 and P28701 to R.S. Support to E.D.G. from the Knut and Alice Wallenberg Foundation within the framework of the Wallenberg Centre for Molecular Medicine, Linköping University, is gratefully acknowledged. NMR spectrometers were acquired in collaboration with the University of South Bohemia (CZ) with financial support from the European Union through the EFRE INTERREG IV ETC-AT-CZ program (project M00146, 'RERI-uasb'). A part of the work was supported through the *Aufbruch Bayern* initiative of the state of Bavaria, and by the Czech Ministry of Education, Youth and Sports within the project Czech-BioImaging—LM2015062, and the Biological Chemistry cross-border Linz–České Budějovice study program.

Author contributions

W.H. and E.D.G. conceived the project. M.S. developed and carried out the syntheses of hierarchical nanocrystals, analytics and optical characterisation. M.S. and O.M. carried out the syntheses and purification of precursors. M.J. prepared all samples for biological experiments and imaging studies. M.S., M.J. and J.N. did all SEM imaging. M.J., M.L. and R.S. did the cell culture and electrophysiology experiments. D.K., M.S. and J.S. made XRD measurements and analysis. W.S. carried out NMR measurements. M.S. and F.W.F. did modelling and calculations. N.S.S., R.S., W.H. and E.D.G. supervised and coordinated the work. E.D.G. wrote the manuscript with input from all authors.

Additional information

Supplementary Information accompanies this paper at doi:10.1038/s41467-017-00135-0.

Competing interests: The authors declare no competing financial interests.

Reprints and permission information is available online at <http://npg.nature.com/reprintsandpermissions/>

Publisher's note: Springer Nature remains neutral with regard to jurisdictional claims in published maps and institutional affiliations.



Open Access This article is licensed under a Creative Commons Attribution 4.0 International License, which permits use, sharing, adaptation, distribution and reproduction in any medium or format, as long as you give appropriate credit to the original author(s) and the source, provide a link to the Creative Commons license, and indicate if changes were made. The images or other third party material in this article are included in the article's Creative Commons license, unless indicated otherwise in a credit line to the material. If material is not included in the article's Creative Commons license and your intended use is not permitted by statutory regulation or exceeds the permitted use, you will need to obtain permission directly from the copyright holder. To view a copy of this license, visit <http://creativecommons.org/licenses/by/4.0/>.

© The Author(s) 2017

Direct Electrical Neurostimulation with Organic Pigment Photocapacitors

David Rand, Marie Jakešová, Gur Lubin, Ieva Vėbraitė, Moshe David-Pur, Vedran Đerek, Tobias Cramer, Niyazi Serdar Sariciftci, Yael Hanein,* and Eric Daniel Głowacki*

Dedicated to Professor Ching Tang on occasion of his 70th birthday

An efficient nanoscale semiconducting optoelectronic system is reported, which is optimized for neuronal stimulation: the organic electrolytic photocapacitor. The devices comprise a thin (80 nm) trilayer of metal and p–n semiconducting organic nanocrystals. When illuminated in physiological solution, these metal–semiconductor devices charge up, transducing light pulses into localized displacement currents that are strong enough to electrically stimulate neurons with safe light intensities. The devices are freestanding, requiring no wiring or external bias, and are stable in physiological conditions. The semiconductor layers are made using ubiquitous and nontoxic commercial pigments via simple and scalable deposition techniques. It is described how, in physiological media, photovoltage and charging behavior depend on device geometry. To test cell viability and capability of neural stimulation, photostimulation of primary neurons cultured for three weeks on photocapacitor films is shown. Finally, the efficacy of the device is demonstrated by achieving direct optoelectronic stimulation of light-insensitive retinas, proving the potential of this device platform for retinal implant technologies and for stimulation of electrogenic tissues in general. These results substantiate the conclusion that these devices are the first non-Si optoelectronic platform capable of sufficiently large photovoltages and displacement currents to enable true capacitive stimulation of excitable cells.

devices in recent decades. Eliminating the need for wiring, optical stimulation is an alternative approach, which is inherently less invasive than electrodes.^[7] The motivation to achieve wireless access to electrophysiological processes has driven the field of optogenetics, involving genetic transfection of target cells with light-sensitive ion channels.^[8] Optogenetics is a relatively mature field, which showcases the high spatial and temporal resolution and minimal invasiveness afforded by light. Nevertheless, the reliance on genetic modification imposes many obstacles.

Nongenetic approaches to impart long-term photosensitivity to electrophysiological processes are highly desired for in vivo applications in humans, including peripheral or central nervous therapeutics, and implants such as retinal prostheses.^[9,10] Despite the clear need for nongenetic means to optically stimulate neurons, the range of available devices suitable to facilitate neuronal response under illumination is limited and silicon optoelectronics have been the primary platform in emerging Silicon photodiodes, which interconvert optical and electrical pulses, are reasonably efficient and mature technology at the crux of modern civilization that greatly benefits from extensive industrial infrastructure and know-how. Therefore, silicon-based devices were extensively studied for

Stimulation of neurons in a localized and safe manner is important both as an investigative tool and as a therapeutic means. Great progress in nano- and microengineered electrode platforms^[1–5] and ion delivery techniques^[6] for electrically communicating with neurons has enabled bioelectronic therapeutic

applications.^[9,11,12] Silicon photodiodes, which interconvert optical and electrical pulses, are reasonably efficient and mature technology at the crux of modern civilization that greatly benefits from extensive industrial infrastructure and know-how. Therefore, silicon-based devices were extensively studied for


Dr. D. Rand, G. Lubin, M. David-Pur, Prof. Y. Hanein
Tel Aviv University Center for Nanoscience and Nanotechnology,
and School of Electrical Engineering
Tel Aviv University
55 Haim Levanon St., Tel Aviv 699780, Israel
E-mail: yaelha@tauex.tau.ac.il

M. Jakešová, Dr. V. Đerek, Dr. E. D. Głowacki
Laboratory of Organic Electronics
Department of Science and Technology
Linköpings Universitet
Bredgatan 33, 60174 Norrköping, Sweden
E-mail: eric.glowacki@liu.se

I. Vėbraitė
Faculty of Agriculture
Food and Environment
Hebrew University of Jerusalem
POB 12, Rehovot 76100, Israel

Dr. V. Đerek
Center of Excellence for Advanced Materials and Sensing Devices
Ruđer Bošković Institute
Bijenička cesta 54, 10000 Zagreb, Croatia

Dr. T. Cramer
Department of Physics and Astronomy
University of Bologna
Viale Berti Pichat 6/2, I-40127 Bologna, Italy
Prof. N. S. Sariciftci
Linz Institute for Organic Solar Cells (LIOS)
Johannes Kepler University
Altenbergerstrasse 69, A-4040 Linz, Austria

 The ORCID identification number(s) for the author(s) of this article can be found under <https://doi.org/10.1002/adma.201707292>.

DOI: 10.1002/adma.201707292

neuronal stimulation applications and in particular for artificial retinal devices, some of which are in clinical trials or already on the market.^[12] Despite these clear advantages, silicon-based devices are not ideally suited to interface with soft and often very sensitive biological tissues. These devices are optimized to work in dry conditions, and electrical interconnects as well as many semiconductor materials corrode in a physiological setting, necessitating tightly sealed passivation and encapsulation. Moreover, these devices are hard and rigid, and create difficulties from mechanical mismatching, such as scar tissue formation.^[13–15] Silicon, as an indirect bandgap semiconductor, has a low absorbance coefficient, and therefore thickness of tens to hundreds of micrometers of silicon is necessary to absorb light efficiently, which sets a high lower-limit for the device thickness, further contributing to the overall rigidity, size, and relatively high weight.

Indeed, the motivation for finding novel materials with better properties for optical stimulation of cells was the focus of several recent studies involving organic semiconducting polymers,^[10,16,17] semiconducting nanocrystals,^[18–21] and amorphous silicon.^[22] Organic semiconducting polymers have shown the ability to photostimulate neurons^[16] and explanted retinas,^[10,17] and there is evidence that implanted films can impart light sensitivity to blind retinas *in vivo*.^[23] Semiconducting nanocrystals have also been successfully deployed for retinal stimulation.^[24] These systems boast ease of fabrication as well as flexibility, the ability to operate in a wet environment without extensive passivation/encapsulation, and biocompatibility. However, the stimulating mechanism underlying the observations of these new systems is often not fully elucidated, or the effects are primarily photothermal in nature. For example, photogenerated charge density values are too low ($<1 \mu\text{C cm}^{-2}$)^[25] to substantiate capacitive/electrical stimulation. Semiconducting polymer and inorganic nanocrystal systems can stimulate explanted retinas, however only delayed or latent responses are recorded.^[10,17,24] These observations have been rationalized by the slow (tens to hundreds of milliseconds) photocharging kinetics of these devices. Studies on the organic semiconductor-mediated electrophysiology of both excitable and nonexcitable cells suggest photothermal^[21,26–28] or thermocapacitive effects^[22,29] as dominant mechanisms in either depolarization or hyperpolarization of cells, rather than photocapacitive electrical stimulation.^[22,26] Though photothermal effects are appropriate for certain applications, direct electrical stimulation with short latency and high temporal resolution is required for most *in vivo* devices, especially chronic implants. Further, to avoid unwanted redox effects that may cause irreversible damage to cells as well as degradation of the device, electrical stimulation has to be truly capacitive in nature.^[30,31] There is a general consensus that capacitive coupling is the most safe and effective photostimulation mechanism.^[31,32] Thus, a fundamental requirement in designing photosensitive systems for neuronal stimulation is a high conversion efficiency of light into a capacitive displacement current sufficient for cell depolarization. Such a device should be biocompatible and ideally simple to fabricate in a scalable way with as small as possible dimensions and weight.

These requirements are the starting point for this work. Here we report on an efficient nanoscale semiconducting optoelectronic system optimized for neuronal stimulation:

the organic electrolytic photocapacitor. The devices comprise a thin (80 nm) tri-layer of metal and p–n semiconducting organic nanocrystals. When illuminated in physiological solution, these metal–semiconductor devices charge up, transducing light pulses into localized displacement currents that are strong enough to electrically stimulate neurons with safe light intensities, one hundred times below the safe ocular limit at 660 nm. The devices are freestanding, requiring no wiring or external bias, and are stable in physiological conditions. The semiconductor layers are made using ubiquitous and nontoxic commercial pigments via simple and scalable deposition techniques. We describe how, in physiological media, photovoltage and charging behavior depend on device geometry. To test cell viability and capability of neural stimulation, we show photostimulation of primary neurons cultured for three weeks on photocapacitor films. Finally, we demonstrate the efficacy of the device by achieving direct optoelectronic stimulation of light-insensitive retinal extracts in a similar manner to stimulation by current injection, proving the potential of this novel device platform for retinal implant technologies and for stimulation of electrogenic tissues in general. These results substantiate the conclusion that these devices are the first non-Si optoelectronic platform capable of sufficiently large photovoltages and displacement currents to enable a true capacitive stimulation of excitable cells.

The electrolytic photocapacitor we introduce here is a photodiode which produces electrical double layers upon illumination in water (Figure 1a). We hypothesized that the electrical potential difference induced in the surrounding electrolyte could affect the membrane potential of cells in the vicinity, even stimulating action potentials in excitable cells providing the voltage perturbation is large enough. The photocapacitors consist of a p–n heterojunction bilayer on top of a metallic back-contact. A surrounding physiological electrolyte is in contact with both the bottom metal and the top of the p–n junction (Figure 1a–c). Devices are fabricated by sequential physical vapor deposition through stencil masks, allowing control over geometries and compatibility with various substrates. For the photosensitive semiconductor p–n materials, we focused on hydrogen-bonded crystalline pigments owing to their favorable semiconducting properties combined with outstanding stability.^[33] The pigments used in this work are exploited industrially for high performance outdoor paints, printing inks, and cosmetics.^[34,35] In contrast to many semiconductor materials that are sensitive to water, hydrogen-bonded pigments are exceedingly stable in aqueous environments: they can be readily biofunctionalized using simple water-based chemistry^[36] and have recently been shown to be stable photoelectrocatalysts in a pH range from 1 to 12.^[37] The materials combination which emerged as most promising and was used throughout this study comprises a Cr/Au layer (2 nm/18 nm) followed by a 30 nm layer of metal-free phthalocyanine (H₂Pc) and 30 nm layer of *N,N'*-dimethyl perylene-3,4:9,10-tetracarboxylic diimide, PTCDI for short (Figure 1a,b). In an aqueous electrolyte, the device band diagram (shown at the beginning of the light pulse in Figure 1c) is that of a p–n donor–acceptor photodiode with the metal and the electrolyte forming the bottom and upper electrodes. Photogenerated excitons separate into free carriers at the donor–acceptor (p–n) interface.

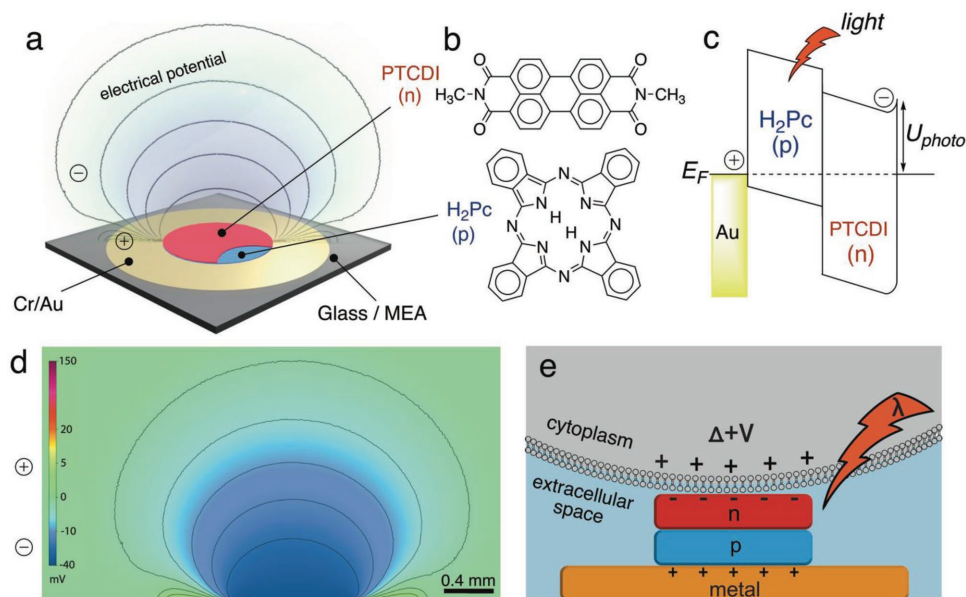


Figure 1. Organic photocapacitor devices. a) Schematic of the photocapacitor consisting of sequentially deposited Cr/Au and H₂Pc (p-type) and PTCDI (n-type). b) Molecular structures of the pigment semiconductors. Metal-free phthalocyanine (H₂Pc) functions as the primary light-absorbing layer and p-type electron donor, while *N,N'*-dimethyl perylenetetracarboxylic diimide (PTCDI) acts as the n-type electron-acceptor, which attains a negatively-charged surface upon illumination. c) Energy band illustration of a metal–p–n photocapacitor during the start of the illumination pulse when the capacitor charges. d) 2D slice of an electrostatic simulation of electrical potential distribution in electrolytic solution above a metal–p–n photocapacitor, at the point when the p–n junction charges to 250 mV. The positive potential is closely localized on the exposed metal film, while a negative potential “plume” extends from the top of the p–n layer. e) Mechanism of capacitive coupling of an illuminated photocapacitor with an adjacent cell.

The electrons accumulate in the n-type semiconducting layer and give rise to an oppositely charged double layer at the semiconductor–liquid interface. Photogenerated holes are injected into the metal and form an electrical double-layer with the surrounding electrolyte. The maximum possible photovoltage (U_{photo}) is given by the difference between the quasi-Fermi level at equilibrium and the conduction band edge of the n-type material. To understand the electrical potential in the surrounding aqueous environment, it is convenient to use electrostatic models. We calculated the charge and potential distribution for different charging voltages. The resultant distribution of electrical potential around a concentric photocapacitor device is plotted in Figure 1d. Perturbation of the potential has a magnitude of several tens of millivolts at tens of micrometers above the surface of the p–n layer. Therefore, the photo-induced voltage, which a cell in close contact with the photocapacitor will “feel”, can in principle be large enough to directly induce action potential generation via the capacitive coupling mechanism, as shown in Figure 1e. The choice of p–n, as opposed to n–p, gives a negative surface potential on the top of the organic layer, thereby leading to depolarization, as opposed to hyperpolarization, of the attached cell membrane. A further critical aspect of successful device design is the surface morphology of the p–n layer. Nanoscale structure allows for higher photocharge densities to be achieved. Our previous work with cell attachment on similar organic pigments showed that nanoscale roughening in the range of tens of nanometres played a key role in forming close interfaces with cells and cell attachment,^[21] which is in-line with other findings of nanomaterial/cell interfaces.^[38] Scanning electron microscopy revealed that 60 nm-thick p–n layers have a rough

truncated nanopillar-like morphology (Figure S1, Supporting Information) with relatively high surface area.

For photocapacitor characterization, we first fabricated 1.5×1.5 cm metallized (Cr/Au) glass slides with 1 cm^2 square p–n layer (denoted as type I samples). This arrangement was used to establish baseline parameters for photovoltage/photocurrent, spectral response, and stability. The gold electrode was wired (i.e., grounded) directly to the measurement equipment or floating in the electrolyte (Figure 2a). The spectral responsivity for photocathodic current was measured for wired samples, showing strong photocapacitive current generation in the red region of the visible spectrum, 700–600 nm, correlating closely with optical absorbance of the p–n stack (Figure 2b). Figure 2c shows photovoltage (V , trace 1) and photocurrent (I , trace 2) values of the photocapacitors measured between the Cr/Au layer versus reference electrode (Ag/AgCl) immersed in the solution, using pulsed illumination (5 ms, 660 nm). These results provide benchmark values for the photovoltages that the bilayer device can generate—around 280 mV (Figure 2c, trace 1). Corresponding displacement current values, I , are $400 \mu\text{A cm}^{-2}$ for light intensities of 60 mW cm^{-2} (Figure 2c, trace 2). The photocurrent profile has a capacitive transient shape, and by integrating charge of cathodic (charging) and anodic (discharging) phases, we obtain an equal value of charge, evidencing that the current is non-Faradaic in nature. We obtained more details on Type I devices using electrochemical impedance spectroscopy (EIS). In the dark, the p–n junction response is described by a geometric capacitance of 79.4 nF cm^{-2} that corresponds well to the layer thickness of the depleted n-type semiconductor ($d = \epsilon\epsilon_0 / C_g = 33 \text{ nm}$ with $\epsilon = 3$). Under illumination (620 nm, 0.81 mW cm^{-2}) the impedance drops as carriers

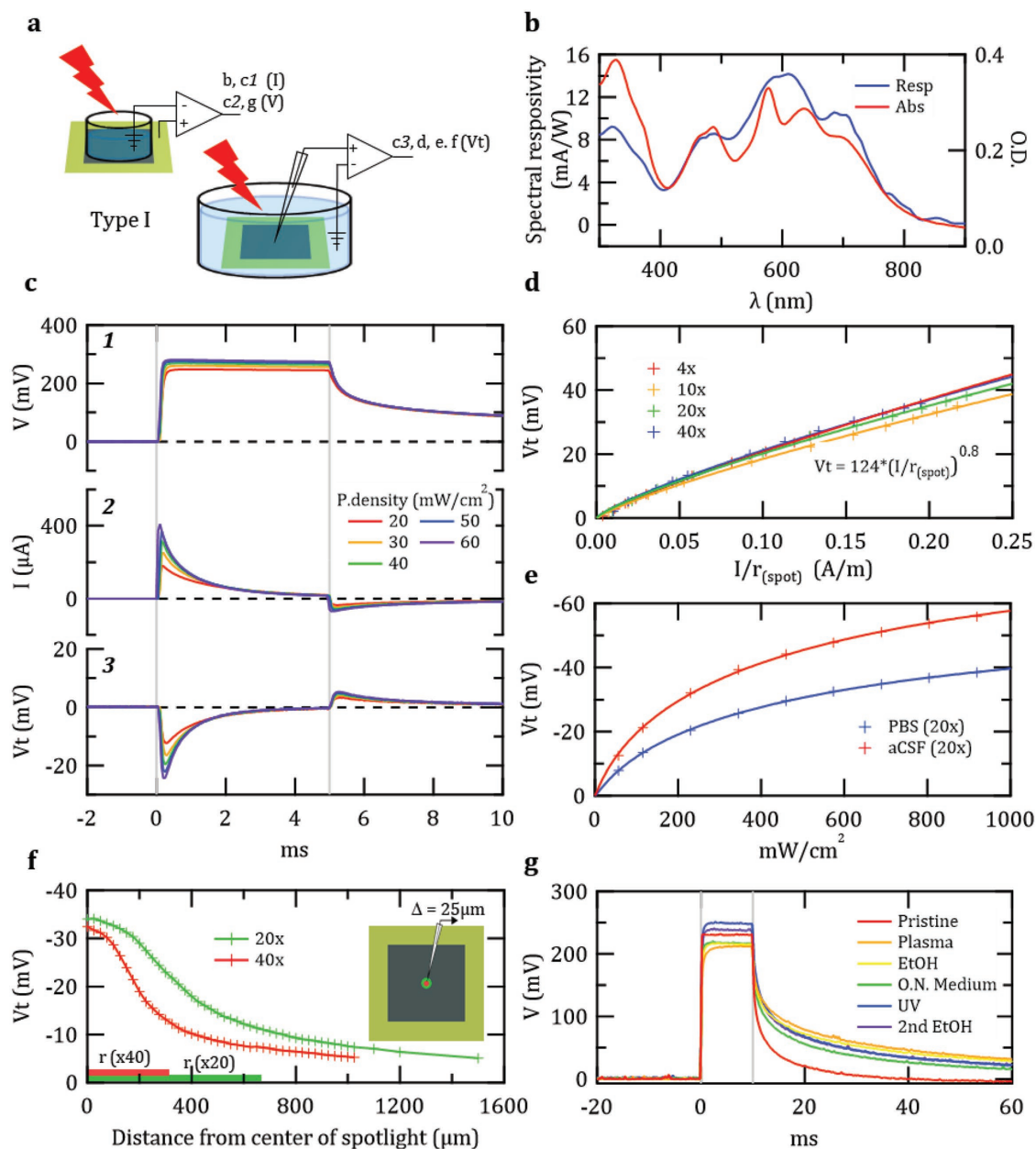


Figure 2. Photocapacitive charging of Cr/Au/H₂Pc/PTCDI film type I. a) Two photocapacitor measurement configurations for Type I samples (1 × 1 cm² p–n area on a 1.5 × 1.5 cm² gold coated glass slide): Grounded metal samples for voltage (V) and current (I) measurements, and “floating samples” for voltage transient (V_t) measurements. Numbers denote which figure panels show measurements in the given configuration. b) Optical absorbance overlaid with spectral responsivity of Type I photocapacitors. c) Photoelectric characterization. c1 and c2 are photovoltage (V) and photocurrent (I), respectively, measured between the bath electrode and the grounded p–n–metal device. c3 is the photovoltage transient (V_t) measured 10 μm above the p–n film, using a glass capillary electrode versus bath reference electrode. Vertical gray lines indicate onset and termination of the light pulses. The V_t follows the same dynamics as the capacitor charging current. d) Cathodic peak value of V_t (cpV_t) is a function of peak anodic current divided by the spot size radius r_(spot). e) cpV_t as a function of illumination intensity for two different electrolytes: phosphate-buffered saline and artificial cerebrospinal fluid. f) Lateral profile of cpV_t measured 10 μm above the surface for two different light spots that are significantly smaller than the p–n region. Measurements start from the center of the light spot and are measured laterally at 25 μm increments. Cathodic charging is strongest in the center of the spot, with V_t rapidly decaying outside of the directly illuminated region. g) Stress test results on grounded samples to evaluate the effects of different sterilization procedures. Measurement was done after sequential: oxygen plasma, triple treatment with absolute ethanol, storing overnight in buffer, UV sterilization, and second triple treatment with absolute ethanol.

are accumulated in the semiconducting layers. The EIS data allow us, on the basis of an equivalent circuit model (Figure S2, Supporting Information), to extract the capacitance between the

p–n layer and water ($C_{dl} = 3.8 \mu\text{F cm}^{-2}$) and the internal resistance of the illuminated p–n junction ($R_{int} = 1.2 \text{ k}\Omega \text{ cm}^{-2}$). The resistance in the dark, meanwhile, is very high ($\text{G}\Omega \text{ cm}^{-2}$) since

both p and n materials are intrinsic semiconductors. Photofaradaic processes that follow a purely resistive path through the junction have only a very small contribution in the impedance spectra and show charge-transfer resistances in darkness or under illumination of $R_{CT} > 1.1 \text{ M}\Omega \text{ cm}^{-2}$, evidencing that the photocurrent is indeed capacitive in nature.

We next evaluated the photovoltage buildup created in solution above the photocapacitor, we define this parameter as the transient voltage, V_t . This is measured with a glass micropipette electrode in solution mounted on a micromanipulator. All measurements were taken with the micropipette tip $10 \mu\text{m}$ above the pigment surface, versus a large Ag/AgCl bath reference electrode, to give a realistic impression of what voltage perturbations cells adhered to the devices will encounter (Figure 2c, trace 3). These V_t measurements are taken without the Cr/Au metal film being electrically grounded, the metal is instead in a direct contact with an electrolyte, allowing us to characterize the operation of the photocapacitors in a wireless, free-standing mode. This scenario reflects the working conditions of a standalone implantable device. The measured electrical potential is in the order of a few millivolts, up to 25 mV (to be contrasted with 280 mV under the same illumination conditions when measuring the grounded sample - Figure 2c, trace 1). V_t profile and intensity is positively correlated with current profile (Figure 2c, trace 2). We found that cathodic peak values of V_t (cpV_t) are a function of peak anodic current divided by the spot size radius, r_{spot} , consistent with classic electrostatics for potential above a disk of charge (Figure 2d). Thus, while a displacement current can be readily associated with a known injected charge value, V_t can also be associated with a corresponding charge value. To empirically link between V_t and electrophysiology-relevant charge injection values we recorded V_t as a function of distance (0–30 μm) from a standard TiN MEA electrode, during stimulation with known current values (using values above the critical threshold needed to achieve action potential stimulation in explanted retinas, $\approx 0.1 \text{ mC cm}^{-2}$)^[25] (Figure S3, Supporting Information). We then repeated the same experiment, this time recording the transient photogenerated potentials at $10 \mu\text{m}$ above the pigment as a function of light intensity, using 10 ms pulses. Photovoltage values were recorded in both phosphate-buffered saline (PBS) and artificial cerebrospinal fluid (aCSF), which mimics the electrolytic environment in the eye. The peak values (cathodic phase) are plotted in Figure 2e, which shows that photovoltages suitable for direct retinal stimulation can be generated already with illumination values around 100 mW cm^{-2} . We found that measuring type I samples while illuminating a limited area (through $\times 20$ and $\times 40$ objective), the photocathodic voltage is highest in the middle of the illumination spot and decays rapidly at the edges of the spotlight (Figure 2e). The lack of lateral “leakage current” in the semiconductor layer is due to its intrinsic nature. We know from impedance analysis that the resistance of the layer in the dark is in the gigaohm range.

For proper operation in electrophysiological applications, devices must be stable in aqueous environments and compatible with sterilization procedures. We measured samples over several days in PBS solution without noting decrease of recorded photovoltage. Accelerated stress test involving sequential treatment with oxygen plasma, ethanol, incubation in cell

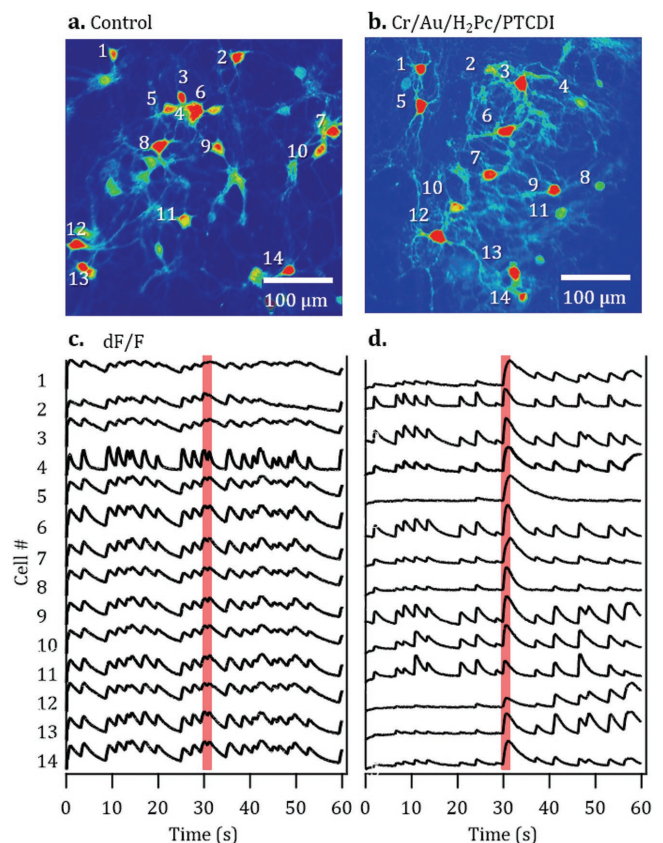


Figure 3. Photostimulation of neuronal cultures. a) Cortical primary neurons cultured on PDL-coated Petri dishes, control sample ($n = 4$). b) Cortical primary neurons cultured on type I devices ($n = 3$). c) Calcium imaging traces (dF/F) of neurons cultured on PDL-coated Petri dish. d) Ca imaging traces of neurons cultured on type I devices. Vertical red lines in (c) and (d) indicate a light stimulation of 100 consecutive pulses (600 nm , 480 mW cm^{-2} , pulse duration 5 ms, interpulse interval 10 ms).

culture medium, followed by UV sterilization treatment, and repeated ethanol rinsing, were performed to validate device stability (Figure 2g). In this study, we fabricated also devices from the well-known metal-containing phthalocyanine derivatives with copper and zinc, CuPc and ZnPc. These performed initially at a similar level as H₂Pc devices, however these devices were not stable with respect to delamination and failed during these stress-test experiments (Figure S4, Supporting Information). The Cr/Au/H₂Pc/PTCDI device configuration routinely passed the entire stress test sequence without significant loss in photovoltage or visible delamination.

Having established details on the relationships between device structure and photovoltage behavior, we proceeded to demonstrate stimulation of primary neuronal cultures (Figure 3). We compared dissociated mice cortical neurons cultured on type I sample (Cr/Au/H₂Pc/PTCDI, $n = 3$) with neurons cultured on standard Petri dishes coated with poly-D-lysine (PDL – a standard cell adhesion layer, $n = 3$). After 4 d in vitro (DIV) we infected the cultures with a viral vector for expressing the calcium indicator GCaMP6 and imaged neural activity at DIV 14. All cultures on both types of substrates developed into viable neural networks, exhibiting spontaneous

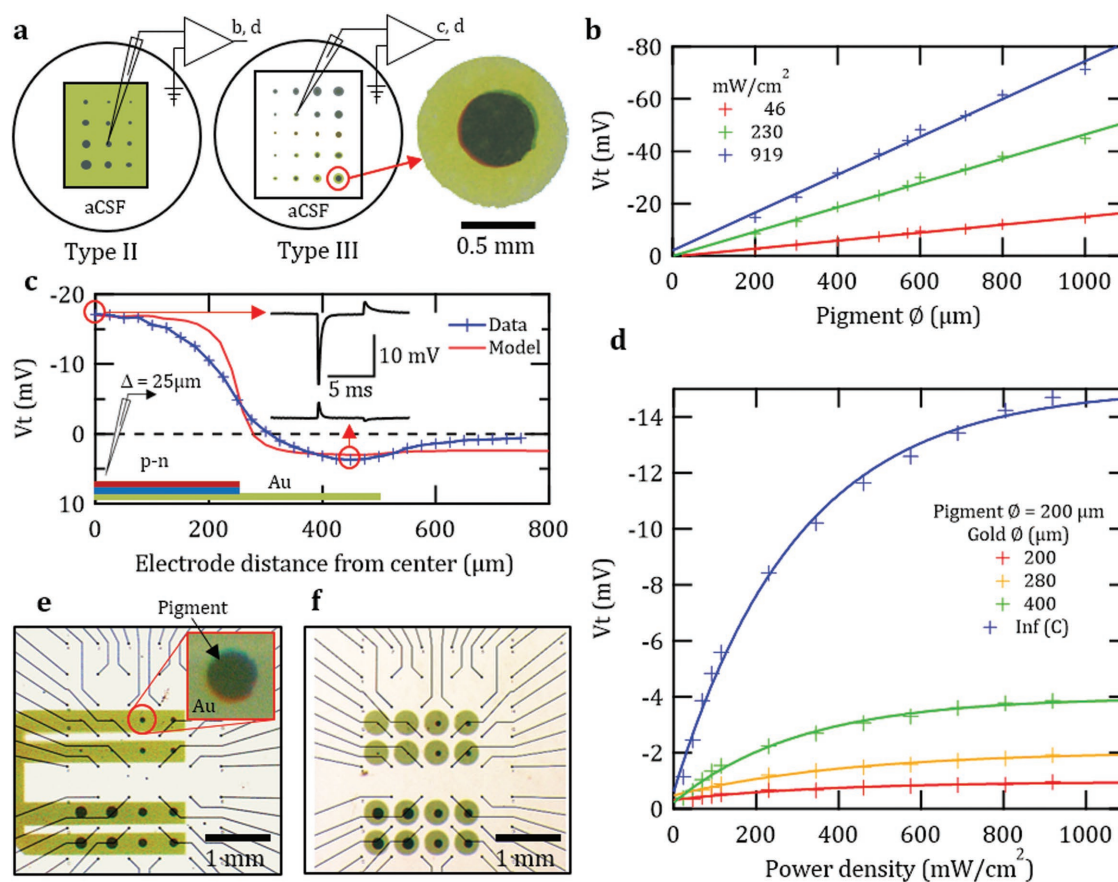


Figure 4. From films to pixels. a) Type II samples comprise p–n circular islands of varying size deposited on an “infinitely large” gold layer. Type III are devices where the size of both p–n islands and the underlying metal is varied. b) The effect of p–n island size. Cathodic peak values of voltage transients (cpV_t) from type II samples as a function of p–n island size for three different illumination intensities. V_t is measured 10 μm above the center of the p–n islands. Light spot size is larger than the maximal island size. c) Lateral cpV_t profile measured 10 μm above a type III sample, showing the maximum value of V_t in the center of the p–n island, with voltage changing sign above the metal film. Measurements are from the center of the p–n island and moving aside at 25 μm increments. d) The effect of gold size on V_t measured 10 μm above the p–n film in type III samples with constant p–n island size and variable metal size. e, f) p–n circular islands of varying size deposited in between the electrodes of multielectrode arrays with either “infinitely large” (e) or $\phi = 480 \mu\text{m}$ of circular (f) gold layer.

activity as indicated by the fluorescent calcium imaging (Figure 3a,b). Using a pulsed light stimulation, composed of 100 pulses of 600 nm, 480 mW cm^{-2} , 5 ms pulse duration, 10 ms inter-pulse interval, we were able to detect a clear response only in a neuronal network that was cultured on type I device samples (Figure 3d). A video of the experiment shown here is provided as Video S1 in the Supporting Information. It is important to note that the kinetics of the calcium indicators are relatively slow and do not show reliable single action-potential-associated calcium signals.^[39] Therefore, only a burst of activity that results from a train of pulses can accumulate into a detectable signal. In order to evidence the photocapacitive mechanism behind the observed action potential generation, we evaluated the contribution of photothermal heating (Figure S5, Supporting Information). We utilized a calibrated pipette conductometric technique^[40] to measure local heating at the p–n device surface. Using the same illumination protocol, with the pulse train of 5 ms pulses, we registered temperature increases of 0.28 $^{\circ}\text{C}$ over the timescale of 1.5 s. The magnitude of these temperature changes indicates that a photothermal effect cannot be

responsible for the action potential generation observed in these neuronal cultures. These calcium imaging studies show the potential of the organic photocapacitors to stimulate action potentials and the stability of the devices in physiological environment, and furnish preliminary evidence that the materials are not detrimental to cell viability.

While larger uniform films are appropriate for stimulating neurons, patterned pixels offer several possible advantages including integration with recording electrode arrays and stimulation localization. Decrease in the lateral dimensions of the device is also required for effective retinal implants or other applications requiring electrical stimulation. To design devices for effective stimulation using isolated islands, samples with p–n areas of different sizes, ranging from 200 to 1000 μm in diameter, on top of a large, (type II), or finite (type III) gold surface area were fabricated and their V_t was measured as described before (Figure 4a). We evaluated the dependence of cathodic photovoltage as a function of the sizes of both the p–n junction area and the underlying gold layer. First, we varied the size of p–n junction islands on a gold film that had

100-fold greater area than the p–n regions, which we refer to as the “infinite” gold condition (Figure 4a, device type II). We found that photocathodic voltage scales linearly with p–n junction diameter, and that p–n junction diameter of less than 150 μm is unlikely to yield effective stimulation (Figure 4b). By laterally scanning the micropipette electrode from the center of the p–n junction all the way to the exposed gold layer, it becomes clear that the sign of the recorded potential shifts from negative on top of the p–n junction to positive over the metal, and remains positive to around 250 μm away from the edge of the p–n layer (Figure 4c). The measured potential in solution closely follows the electrostatic model, plotted together with experimental data, for potential in the vicinity of disks of charge. To quantify the effect of exposed gold on performance, the p–n junction diameter was held constant 200 μm and we varied the underlying gold size (Figure 4a, device type III). It is apparent that the gold in contact with surrounding electrolyte is necessary for accommodating the positive charges photogenerated by the p–n junction. An increased area of exposed gold is a critical parameter to obtain higher photocathodic values (Figure 4d). Using these findings, we modified commercial multielectrode arrays (MEAs) with p–n pixels on large gold traces (Figure 4e) and on 470 μm diameter gold disks (Figure 4f), creating platforms for localized photostimulation and simultaneous neural recording.

The embryonic chick retina is a well-established model for the development of the visual system^[41] and the retina in particular.^[42] At embryonic day 14 (E14), retinal cells are in an early maturation stage,^[43,44] but the retina is not yet sensitive to light. Opsins mRNA only begins to appear in a small region by then,^[45] while photoreceptor electrical activity in response to light is not detected before E17.^[41] Thus, at this stage of development, the chick retina serves as a light insensitive retinal mode.^[24]

Retinas (E14) were placed on type II or type III device-modified MEAs (Figure 5a). Outer nuclear layer (Figure 5b) and the nerve fibre layer (Figure 5c) are readily apparent in visual inspection with a light microscope. The intrinsic light-insensitivity is always verified prior to further experiment, though E14 seldom show any light sensitivity. To provide an internal control, we used a single MEA electrode in the mode of typical electrical stimulation,^[25] delivering 8 μA over 300 μs , generating a direct action-potential response in the retina (Figure 5d). We find that the exact same direct responses are generated synchronously in ganglion cells and fibers at the vicinity of the illuminated photocapacitor device pixels by delivering a 2 ms light pulse through the objective (Figure 5e). In the chick retina, direct responses are easily recognized as they propagate in both directions along the nerve fibers (retrograde and anterograde). We have previously shown that these responses result from direct activation of ganglion cells, they can be suppressed by the presence of voltage-gated sodium channels blocker, tetrodotoxin,^[46] but not in the presence of synaptic transmission blockers.^[25] The latency of a direct response becomes larger when detected on electrodes that are further away from the stimulating electrode. Indeed, measured propagation direction (red and blue regression lines in Figure 5a) and speed of $0.33 \pm 0.045 \text{ m s}^{-1}$ (calculated from the latency of the response between two adjacent electrodes, 500 μm apart), correspond well with fiber layer alignment (Figure 5c) and known action potential propagation

speed in the chick retina.^[46] The photocapacitive pixels elicit the same direct response as current-injected MEA electrodes ($n = 4$ retinas), verifying that the devices are photocapacitively evoking direct retinal responses. Since these spikes are synchronized, they are summed into a large electrical signal that is superimposed on the stimulating signal. The amplitude of the recorded response is a function of the amount of recruited somas and nerve fibers that is directly correlated with the stimulus light intensity (Figure 5f). Both type II and type III MEA samples were found to evoke direct responses in retinas. Successful stimulations were made with all pixels of 100 μm diameter and above for pulse duration as short as 1 ms. The minimal intensities for detecting a response were 430 and 130 mW cm^{-2} for 100 and 200 μm diameter pixels, respectively. Our results unambiguously show deterministic and rapid action potential generation in light-insensitive retinas.

In this investigation we used ubiquitous organic semiconductor pigments with an extensive history: They have been used as photoconductors in xerographic applications^[47] since the 1960s, and indeed in the earliest heterojunction organic photovoltaic devices.^[48] Organic xerography is a direct inspiration for the physical concepts used in this work. The active materials we explored are cheap and nontoxic materials which constitute colorants used commercially in applications as various as printing inks, cosmetics, and automobile paints.^[34,35] We used these organic semiconductors to address several major challenges in the realm of optical stimulation of neuronal systems. Foremost is the ability to perform safe electrical stimulation mediated by a simple optoelectronic system. The devices we studied are free-standing (electrically floating structures) and are fabricated via scalable fabrication steps where the substrate remains at room temperature, which allows integration with arbitrary substrate materials. While silicon-based photo-diodes have so far played a dominant role in the realm of artificial photoelectrical stimulation of neurons, silicon devices have several shortcomings compared with organic pigment layers. First, pigment films have a higher absorbance coefficient, allowing them to efficiently absorb light. At 660 nm, used in this work, the absorbance coefficient of vacuum-evaporated H_2Pc is $3 \times 10^5 \text{ cm}^{-1}$, while silicon is $2.58 \times 10^3 \text{ cm}^{-1}$. This difference allows making thinner photoactive films much less invasive, as the devices can have thicknesses that are much smaller than single cells. Our devices are 500 times thinner than the thinnest state-of-the-art silicon diodes for retinal implants. Moreover, in our design, one has a nanostructured semiconductor surface in direct contact with the electrolytic medium/biological sample, there is no voltage drop on a passivation layer or on conducting interconnects in between. Silicon photocapacitive devices charge metal electrodes—here we have the semiconductor surface itself serving as the primary charge-carrying electrode. Secondary metal electrodes must be employed in the case of silicon since it is not stable in physiological aqueous media. It must be carefully encapsulated, and interconnects passivated using $\text{SiO}_2/\text{Si}_3\text{N}_4$ layers, for example. The organic p–n layers can make direct contact with the physiological environment due to their durability. Organic crystalline pigments like phthalocyanine and perylene diimide are famously indestructible in terms of chemical and photochemical stability.^[35] Further, the nontoxicity of both phthalocyanines and perylene pigments is

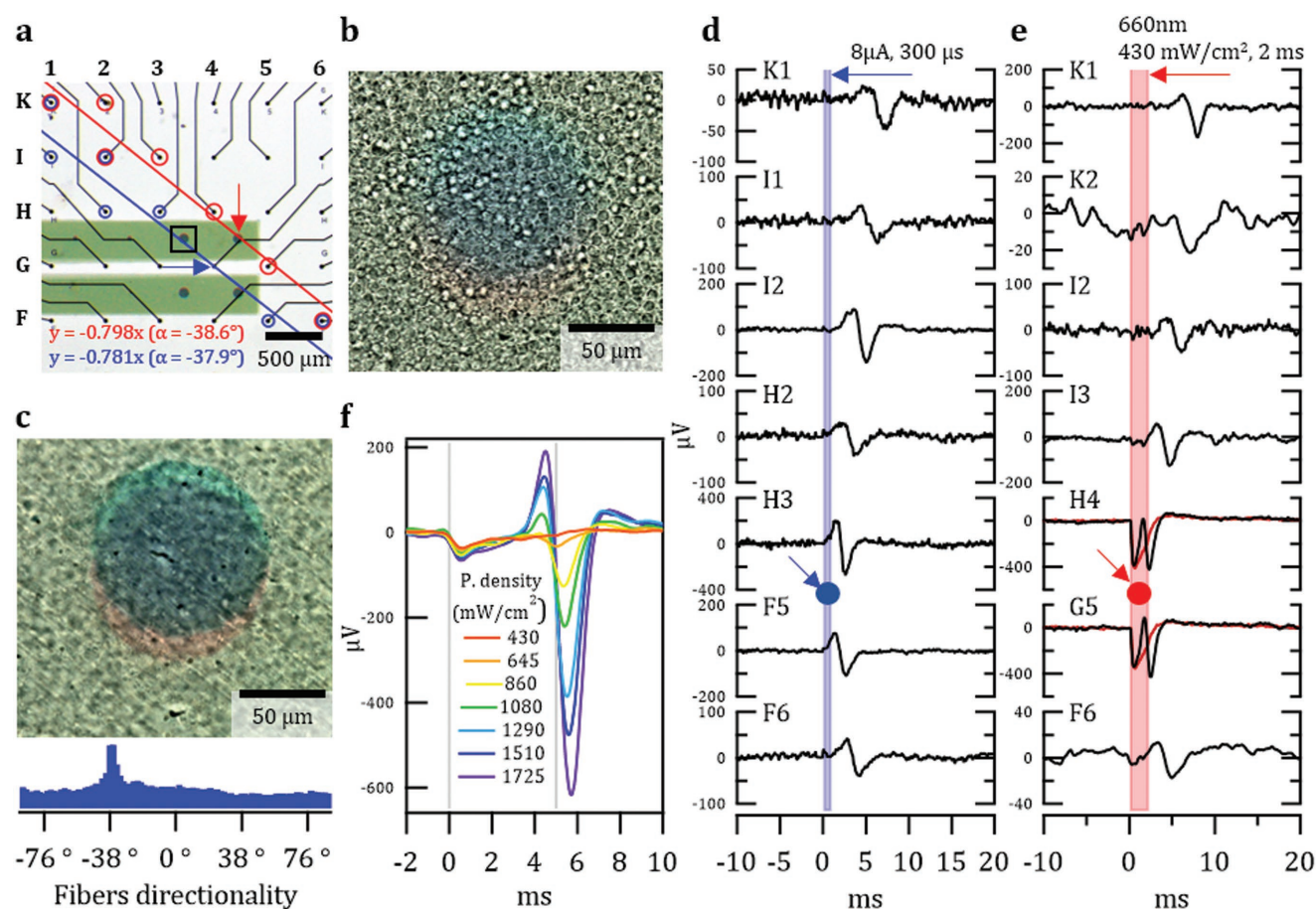


Figure 5. Direct responses of RGC in a light-insensitive retina. a) A piece of light insensitive embryonic chick retina was laid on the MEA shown in Figure 4e. Light pulses illuminated only a pigment bilayer of 100 μm marked by a red arrow using 40 \times objective. Electrical stimulation injected to electrode G4, marked by a blue arrow. Direct responses of the RGC were detected only in red-circled electrodes for light stimulation and blue-circled electrodes for electrical stimulation. Corresponding regression lines for these electrodes are shown and their linear equation, with a slope of 38 $^\circ$. b) An image of a retina placed on the MEA, with optical focus on the photoreceptor nuclear layer. The p-n island (marked with square in Figure 5a) is clearly visible beneath the retina. c) The same image as in (b) focused on the nerve fibre layer. The orientation of the fibers is clearly seen in the image, found to be 38 $^\circ$ by the fast Fourier transform directionality histogram. d) Current pulse stimulation of the retina. Relative location of the injected electrode, G4, is marked by a blue arrow and circle. The latency of the response is increased when recorded from more distant electrodes to the stimulating electrode. The stimulating pulse is not detected in the recording due to the operation of the amplifier's blanking circuit. This measurement serves as an internal control. e) Photostimulation of the retina. Relative location of the illuminated pigment is marked by a red arrow and circle. Electrodes H4 and G5, which are close to the source, record the electrical signal generated by the photocapacitor device. This signal, which can also be recorded from pulses that did not evoke retinal responses, is plotted in overlaid red traces. f) Direct responses to 5 ms light pulse of different intensities showing the intensity-response dependence. Vertical gray lines indicate onset and termination of the light pulses.

well-documented.^[49] These materials are used in cosmetics, medical products, and tattoos. They are commercial colorants which belong to the lowest category of hazard and toxicity for consumer approved materials in the EU.

Achieving temporal control over neural stimulation requires activation with short latency of the response. In the case of retinal stimulation, such short latency responses are attributed to directly activating the retinal ganglion cells (RGCs). Direct activation of RGCs means that each stimulation pulse produces short latency synchronized action potentials in several somas and axons of RGCs that are located at the vicinity of stimulating electrode.^[25,50,51] In contrast, stimulation of neurons presynaptic to the ganglion cells results in the generation of bursts of unsynchronized spikes in the RGCs with much longer latency,

due to synapse transmission.^[52,53] Therefore, a major challenge in neuronal activation, in particular with photosensitive nanostructures, is to understand and to control the mechanism by which the activation is achieved, aiming for a sufficient charge injection for obtaining direct electrical activation similar to that of the best-optimized silicon-based electronics. Moreover, such electrical stimulation should be capacitive, which is considered safe and can be used for extended duration, unlike faradaic stimulation and thermal activation that are not considered optimal and should be avoided.^[31]

The photoelectric transduction of our device is sufficient to stimulate the RGC layer in a direct electrical manner in safe light intensities. In terms of neuronal stimulation benchmark parameters, our ultrathin organic device reaches parity with the

state-of-the-art silicon diode-based technologies. We are able to evoke action potentials in retinas using the same light intensity range as triple-tandem silicon retinal stimulation diodes.^[9,54] The range of pulsed light intensities and durations we have used has been deemed two orders of magnitude below the safe limit for ocular stimulation.^[9] Moreover, 660 nm is within the biological tissue transparency window, which can enable different in vivo applications.

To conclude, we demonstrated a new and advantageous concept to photostimulate neurons. Primary neurons were cultured on our photocapacitor devices for three weeks, demonstrating viability of both the devices and the cells. The latter could readily be photostimulated using short impulses of light. We next integrated photocapacitors onto commercial MEAs, enabling simultaneous photoexcitation and recording. Using this platform, we demonstrated effective direct photostimulation of light-insensitive embryonic chicken retinas. The MEA allows us to make an in situ control of conventional electrical stimulation, thereby we verify that the photocapacitor arrays and the electrical stimulation have the exact same retinal response. We experimentally discount the presence of photothermal heating effects. The culmination of this work is stand-alone photocapacitors with organic pixels of 100 μm in diameter to locally and reproducibly evoke action potentials. Future research of this device concept should involve optimizing materials to afford higher responsivity and photovoltage, allowing smaller pixels and lower light intensities. Different nano- and microstructuring of the organic material must be explored to yield optimal coupling with cells. The technology is a new platform that can interact with living cells via a true capacitive coupling mechanism, thus enabling safe and versatile next-generation implant technologies, and already at the level demonstrated here is suitable for various in vivo applications in peripheral or central nervous system stimulation, for example, in the context of traumatic injury. Success in these efforts requires deployment of the devices on implantable and/or bioresorbable substrates, and evaluation of their stability and performance in vivo.

Experimental Section

Materials: Phthalocyanine H₂Pc (Alfa Aesar), ZnPc (BASF), and CuPc (BASF) were each purified by threefold temperature gradient sublimation in a vacuum of $<1 \times 10^{-3}$ torr. PTCDI, *N,N'*-dimethyl-3,4,9,10-perylene-tetracarboxylic diimide (BASF), was likewise purified thrice by sublimation.

Device Fabrication: Photocapacitor devices were fabricated using physical vapor deposition processes either on clean microscope slide glass or on commercial multielectrode arrays (Multichannel Systems GmbH), with both metal and organic regions defined by stainless steel shadow masks. Both glass and MEA substrates, after solvent cleaning, were treated with UV-generated ozone and a layer of chromium (2 nm) followed by gold (18 nm) was evaporated at a base pressure of $<1 \times 10^{-6}$ mbar at a rate of 0.2 and 3–5 $\text{\AA} \text{ s}^{-1}$, respectively. From previous work,^[55] it is known that following these fabrication procedures gives primarily Cr₂O₃ rather than metallic Cr. Following evaporation, the samples were exposed to UV-generated ozone for 15 min and then placed into a chamber held at 75 °C containing vapor of *n*-octyltriethoxysilane (OTS) for 2 h. Following OTS treatment the substrates were rinsed with acetone and water and placed in boiling acetone for 15 min to remove multilayers and excess silanization physioadsorbed on the Cr/Au or TiN electrodes (the latter in the case of MEA). The OTS layer was found to

improve the adhesion of the organic semiconductor layer and prevent delamination, and produced reliably higher photovoltage than bare Cr/Au. Following rinsing with isopropanol and water and drying under a nitrogen stream, the samples were placed with appropriate shadow masking in an organic materials evaporator. The pigment layers were evaporated at a rate of 0.5 $\text{\AA} \text{ s}^{-1}$ for the p-type layer and 5–6 $\text{\AA} \text{ s}^{-1}$ for the n-type at a base pressure of $<1 \times 10^{-6}$ mbar, to give a total thickness of 60 nm consisting of 30 nm of p- and n-type.

Photoresponse Characterization: Photocurrent and photovoltage characterization were done on 1.5×1.5 cm metallized (Cr/Au) glass slides with 1 cm^2 square p–n layer (type I sample). A glass chamber was placed on the p–n later coated area, leaving outside the exposed gold in the perimeter (left sample in Figure 2a). The chamber was filled with electrolyte, either PBS or modified Tyrode's solution (5×10^{-3} M KCl, 25×10^{-3} M NaHCO₃, 10×10^{-3} M glucose, 1.2×10^{-3} M MgSO₄, 1.2×10^{-3} M HEPES, 0.5×10^{-3} M glutamine, 2.5×10^{-3} M CaCl₂). A photogenerated response was measured between the underlying metal electrode and a reference electrode (either Au or Ag/AgCl) in the solution. The measurement unit consisted of a current amplifier (model 1212; DL Instruments) or voltage amplifier (model ELC-03XS, npi electronic GmbH). Photoresponse characterization was also done (for data in Figure 2g) on a simplified setup using a Techtronix TDS3000 oscilloscope, connecting the positive lead to the photocapacitor back electrode and the negative lead to a Ag/AgCl electrode immersed in electrolyte. Type I samples give large enough currents and voltages to be readily measured on an oscilloscope without any amplification. Measurement of voltage transients in electrolyte was done by immersing the entire samples of type I, II, or III in the electrolyte (right sample in Figure 2a for type I and Figure 4a for type II and III), and recording 10 μm above the surface using a micropipette electrode filled with 3M KCl, mounted on a computer motorized micromanipulator (model PatchStar, Scientifica) versus Ag/AgCl reference electrode in the electrolyte. The illumination unit, for all above experiments, consisted of a light-emitting diode with a peak wavelength of 660 nm (Thorlabs) mounted on an Olympus upright microscope (BX51WI) using a $4 \times$ or water immersion objectives of 10, 20, and 40 \times , resulting in illumination intensities within the range of 0.6–1725 mW cm^{-2} . A Xenon-Discharge Lamp and Czerny-Turner Monochromator were used as a light source to acquire the photocurrent spectra. The photocurrents were amplified using a Lock-in amplifier and chopper operated at 29 Hz. The current rms values were acquired as a function of wavelength and normalized for the light intensity as measured with a pyroelectric detector. Impedance spectra were acquired in 0.1 M KCl with a Metro-Ohm PGSTAT 204 at open-circuit potential conditions.

Electrostatic Modeling: Electric potential distribution of the device immersed in electrolyte was modeled using the Robin Hood Solver software package for complex 3D electrostatic problems using the Robin Hood calculation method.^[56] Charged photocapacitor devices were modeled as two concentric metal plates—larger bottom gold electrode fixed at 0 V potential, and the smaller top electrode which represented an equipotential surface at the top of the p–n junction, and which could be set at arbitrary potentials depending on the modeled electrode. The electrodes in the model were separated by a thin dielectric layer with relative permittivity of 3, characteristic to the organic semiconductors used here. The dielectric layer in the model represented the p–n junction region of the device. The space surrounding the device was modeled as a dielectric with relative permittivity of 80.1, representing a water-based electrolyte. All the dimensions in the model were true to the experimentally measured devices.

Neural Cultures: All mice were treated in accordance with the principles and procedures of the Israel National Institute of Health and the United States National Institutes of Health Guidelines for the Care and Use of Laboratory Animals. Protocols were approved by the Institutional Animal Care and Use Committee of the Tel Aviv University. Dissociated cortical cultures were prepared as follows: the entire cortices of SV129-mice, post-natal 0–1, were removed. Cortical tissue was digested with 0.065% trypsin (Biological Industries) in PBS for 15 min, followed by mechanical dissociation by trituration. Cells

were re-suspended in a modified essential medium without phenol red and glutamine, 5% horse serum, 50×10^{-3} M glutamine, 0.02×10^{-3} M glucose, 0.5% Pen-Strep, 2% B-27, and 0.75% glutamax (Gibco) and plated on either a poly-D-lysine (Sigma) covered Petri dish (control) or on type I samples (experiment) with a cell density of $3000 \text{ cells mm}^{-2}$ ($\approx 700 \times 10^3$ cells per dish). Cultures were maintained at 37°C with 5% CO_2 . Growth medium was partially replaced every 3–4 d. At 4 DIV, cultures were infected with AAV-CAG-GCaMP6s viral vector (prepared by the Tel Aviv University vector core facility).

Optical Recording via Calcium Imaging: Calcium imaging recordings were performed on 14 DIV in buffered mice artificial cerebrospinal solution (mice aCSF: 10×10^{-3} M HEPES, 4×10^{-3} M KCl, 1.5×10^{-3} M CaCl_2 , 0.75×10^{-3} M MgCl_2 , 139×10^{-3} M NaCl, 10×10^{-3} M D-glucose, adjusted with sucrose to an osmolarity of 325 mOsm, and with NaOH to a pH of 7.4). Images were acquired with an EMCCD camera (Andor Ixon-885) mounted on an Olympus upright microscope (BX51WI) using a $20\times$ water immersion objective (Olympus, LUMPLFL NA 0.4). Fluorescent excitation was provided via a 120 W mercury lamp (EXFO x-cite 120 PC) coupled to a GFP filter cube (Chroma T495LP). Images were acquired at 59 fps in 2×2 binning mode using Andor software data-acquisition card (SOLIS) installed on a personal computer, spooled to a high capacity hard drive and stored as uncompressed multipage tiff file libraries.

Electrical Recordings from Retinas: Direct retinal responses were recorded with $30 \mu\text{m}$ diameter TiN electrode MEAs. Coupling between the tissue and the electrodes was improved by placing a small piece of polyester membrane filter ($5 \mu\text{m}$ pores; Sterlitech) and a ring weight on the retina. The filter was removed before light stimulation to minimize scattering. Retinas were kept at physiological conditions, at a temperature of 34°C , and perfused ($2\text{--}5 \text{ mL min}^{-1}$) with oxygenated (95% O_2 , 5% CO_2) chick aCSF solution (5×10^{-3} M KCl, 25×10^{-3} M NaHCO_3 , 9×10^{-3} M glucose, 1.2×10^{-3} M MgSO_4 , 1.2×10^{-3} M HEPES, 0.5×10^{-3} M glutamine, 2.5×10^{-3} M CaCl_2). Neuronal signals were amplified with MEA1060-UP amplifier with a built-in blanking circuit that ground the electrodes during current injection (gain $\times 1100$; MultiChannel Systems), digitized using a 64-channel analogue to digital converter (MC_Card; MultiChannel Systems), and recorded (MC_Rack; MultiChannel Systems). In vitro epiretinal stimulation was carried out by injecting biphasic pulse of $300 \mu\text{s}$ to a single electrode of the MEA, using electrical stimuli generated by an external stimulator (STG4002; MultiChannel Systems) and a critical threshold for eliciting retinal responses of $0.4\text{--}1.4 \text{ mC cm}^{-2}$, similar to what has been reported in the literature, was found.

Supporting Information

Supporting Information is available from the Wiley Online Library or from the author.

Acknowledgements

No competing financial interests have been declared. The authors gratefully acknowledge the financial support from the Knut and Alice Wallenberg Foundation within the framework of the Wallenberg Centre for Molecular Medicine at Linköping University, the Austrian Science Fund FWF via the Wittgenstein Prize Solare Energie Umwandlung Z222-N19 for N.S.S., and the European Research Council under the European Community's Seventh Framework Program (FP7/2007-2013)/ERC grant agreement FUNMANIA-306707 for Y.H.. The authors thank Beatrice Fraboni for assistance with electrochemical impedance measurements, and Predrag Lazic for providing the electrostatic modelling software (Robin Hood Solver).

Conflict of Interest

The authors declare no conflict of interest.

Keywords

artificial retina, bioelectronics, neurostimulation, organic semiconductors

Received: December 14, 2017

Revised: March 4, 2018

Published online:

- [1] N. A. Kotov, J. O. Winter, I. P. Clements, E. Jan, B. P. Timko, S. Campidelli, S. Pathak, A. Mazzatenta, C. M. Lieber, M. Prato, R. V. Bellamkonda, G. A. Silva, N. W. S. Kam, F. Patolsky, L. Ballerini, *Adv. Mater.* **2009**, *21*, 3970.
- [2] P. Fattahi, G. Yang, G. Kim, M. R. Abidian, *Adv. Mater.* **2014**, *26*, 1846.
- [3] R. Green, M. R. Abidian, *Adv. Mater.* **2015**, *27*, 7620.
- [4] M. H. Histed, V. Bonin, R. C. Reid, *Neuroendocrinology* **2009**, *63*, 508.
- [5] M. D. Ferro, N. A. Melosh, *Adv. Funct. Mater.* **2017**, *28*, 1704335.
- [6] D. T. Simon, E. O. Gabriellson, K. Tybrandt, M. Berggren, *Chem. Rev.* **2016**, *116*, 13009.
- [7] S. H. Yun, S. J. J. Kwok, *Nat. Biomed. Eng.* **2017**, *1*, 1.
- [8] M. Scanziani, M. Häusser, *Nature* **2009**, *461*, 930.
- [9] K. Mathieson, J. Loudin, G. Goetz, P. Huie, L. Wang, T. I. Kamins, L. Galambos, R. Smith, J. S. Harris, A. Sher, D. Palanker, *Nat. Photonics* **2012**, *6*, 391.
- [10] D. Ghezzi, M. R. Antognazza, R. Maccarone, S. Bellani, E. Lanzarini, N. Martino, M. Mete, G. Pertile, S. Bisti, G. Lanzani, F. Benfenati, *Nat. Photonics* **2013**, *7*, 400.
- [11] E. Zrenner, K. U. Bartz-Schmidt, H. Benav, D. Besch, A. Bruckmann, V. Gabel, F. Gekeler, U. Grepmaier, A. Harscher, S. Kibbel, J. Koch, A. Kusnyerik, T. Peters, K. Stingl, H. Sachs, A. Stett, P. Szurman, B. Wilhelm, R. Wilke, *Proc. R. Soc. B* **2011**, *278*, 1489.
- [12] A. T. Chuang, C. E. Margo, P. B. Greenberg, *Br. J. Ophthalmol.* **2014**, *98*, 852.
- [13] D. Prodanov, J. Delbeke, *Front. Neurosci.* **2016**, *10*, 11.
- [14] T. D. Y. Kozai, A. S. Jaquins-Gerstl, A. L. Vazquez, A. C. Michael, X. T. Cui, *ACS Chem. Neurosci.* **2015**, *6*, 48.
- [15] A. Butterwick, P. Huie, B. W. Jones, R. E. Marc, M. Marmor, D. Palanker, *Exp. Eye Res.* **2009**, *88*, 22.
- [16] D. Ghezzi, M. R. Antognazza, M. Dal Maschio, E. Lanzarini, F. Benfenati, G. Lanzani, *Nat. Commun.* **2011**, *2*, 166.
- [17] V. Gautam, D. Rand, Y. Hanein, K. S. Narayan, *Adv. Mater.* **2014**, *26*, 1751.
- [18] T. C. Pappas, W. M. S. Wickramanyake, E. Jan, M. Motamedi, M. Brodwick, N. A. Kotov, *Nano Lett.* **2007**, *7*, 513.
- [19] L. Bareket, N. Waiskopf, D. Rand, G. Lubin, M. David-Pur, J. Ben-Dov, S. Roy, C. Eleftheriou, E. Sernagor, O. Cheshnovsky, U. Banin, Y. Hanein, *Nano Lett.* **2014**, *14*, 6685.
- [20] M. Zangoli, F. Di Maria, E. Zucchetti, C. Bossio, M. R. Antognazza, G. Lanzani, R. Mazza, F. Corticelli, M. Baroncini, G. Barbarella, *Nanoscale* **2017**, *9*, 9202.
- [21] M. Sytnyk, M. Jakešová, M. Litviňuková, O. Mashkov, D. Kriegner, J. Stangl, J. Nebesářová, F. W. Fecher, W. Schöfberger, N. S. Sariciftci, R. Schindl, W. Heiss, E. D. Głowacki, *Nat. Commun.* **2017**, *8*, 91.
- [22] Y. Jiang, J. L. Carvalho-de-Souza, R. C. S. Wong, Z. Luo, D. Isheim, X. Zuo, A. W. Nicholls, I. W. Jung, J. Yue, D.-J. Liu, Y. Wang, V. De Andrade, X. Xiao, L. Navrazhnykh, D. E. Weiss, X. Wu, D. N. Seidman, F. Bezanilla, B. Tian, *Nat. Mater.* **2016**, *15*, 1023.
- [23] J. F. Maya-Vetencourt, D. Ghezzi, M. R. Antognazza, E. Colombo, M. Mete, P. Feyen, A. Desii, A. Buschiazzo, M. Di Paolo, S. Di Marco, F. Ticconi, L. Emionite, D. Shmal, C. Marini, I. Donelli, G. Freddi, R. Maccarone, S. Bisti, G. Sambucetti, G. Pertile, G. Lanzani, F. Benfenati, *Nat. Mater.* **2017**, *16*, 681.

- [24] L. Bareket-Keren, N. Waiskopf, D. Rand, G. Lubin, M. David-Pur, J. Ben-Dov, S. Roy, C. Eleftheriou, E. Sernagor, O. Cheshnovsky, U. Banin, Y. Hanein, L. Bareket, N. Waiskopf, D. Rand, G. Lubin, M. David-Pur, J. Ben-Dov, S. Roy, C. Eleftheriou, E. Sernagor, O. Cheshnovsky, U. Banin, Y. Hanein, *Nano Lett.* **2014**, *14*, 6685.
- [25] C. Sekirnjak, P. Hottoway, A. Sher, W. Dabrowski, A. M. Litke, E. J. Chichilnisky, *J. Neurophysiol.* **2006**, *95*, 3311.
- [26] N. Martino, P. Feyen, M. Porro, C. Bossio, E. Zucchetti, D. Ghezzi, F. Benfenati, G. Lanzani, M. R. Antognazza, *Sci. Rep.* **2015**, *5*, 8911.
- [27] Y. Lyu, C. Xie, S. A. Chechetka, E. Miyako, K. Pu, *J. Am. Chem. Soc.* **2016**, *138*, 9049.
- [28] F. Lodola, N. Martino, G. Tullii, G. Lanzani, M. R. Antognazza, *Sci. Rep.* **2017**, *7*, 1.
- [29] M. G. Shapiro, K. Homma, S. Villarreal, C.-P. Richter, F. Bezanilla, *Nat. Commun.* **2012**, *3*, 736.
- [30] I. Schoen, P. Fromherz, *J. Neurophysiol.* **2008**, *100*, 346.
- [31] S. F. Cogan, *Annu. Rev. Biomed. Eng.* **2008**, *10*, 275.
- [32] I. Schoen, P. Fromherz, *Biophys. J.* **2007**, *92*, 1096.
- [33] E. D. Głowacki, G. Voss, N. S. Sariciftci, *Adv. Mater.* **2013**, *25*, 6783.
- [34] H. Zollinger, *Color Chemistry. Syntheses, Properties and Applications of Organic Dyes and Pigments*, Wiley-VCH, Weinheim, Germany **2003**.
- [35] *High Performance Pigments* (Eds: E. B. Faulkner, R. J. Schwartz), Wiley-VCH, Weinheim, Germany **2009**.
- [36] E. D. Głowacki, R. R. Tangorra, H. Coskun, D. Farka, A. Operamolla, Y. Kanbur, F. Milano, L. Giotta, G. M. Farinola, N. S. Sariciftci, *J. Mater. Chem. C* **2015**, *3*, 6554.
- [37] M. Jakešová, D. H. Apaydin, M. Sytnyk, K. Oppelt, W. Heiss, N. S. Sariciftci, E. D. Głowacki, *Adv. Funct. Mater.* **2016**, *26*, 5248.
- [38] F. Santoro, S. Dasgupta, J. Schnitker, T. Auth, E. Neumann, G. Panaitov, G. Gompper, A. Offenhäuser, *ACS Nano* **2014**, *8*, 6713.
- [39] C. Grienberger, A. Konnerth, J. Wu, T. Teramoto, Y. F. Chang, M. Nakano, A. S. Abdelfattah, M. Fujiwara, T. Ishihara, T. Nagai, R. E. Campbell, *Neuroendocrinology* **2012**, *73*, 862.
- [40] J. Yao, B. Liu, F. Qin, *Biophys. J.* **2009**, *96*, 3611.
- [41] J. Mey, S. Thanos, *Brain Res. Rev.* **2000**, *32*, 343.
- [42] M. N. Vergara, M. V. Canto-Soler, *Neural Dev.* **2012**, *7*, 22.
- [43] C. Prada, J. Puga, L. Perez-Mendez, R. Lopez, G. Ramirez, *Eur. J. Neurosci.* **1991**, *3*, 559.
- [44] S. Doh, H. Hao, S. C. Loh, T. Patel, H. Y. Tawil, D. K. Chen, A. Pashkova, A. Shen, H. Wang, L. Cai, *BMC Dev. Biol.* **2010**, *10*, 8.
- [45] S. L. Bruhn, C. L. Cepko, *J. Neurosci.* **1996**, *16*, 1430.
- [46] D. Raz-Prag, G. Beit-Yaakov, Y. Hanein, *J. Neurosci. Methods* **2017**, *291*, 20.
- [47] D. S. Weiss, M. Abkowitz, *Chem. Rev.* **2010**, *110*, 479.
- [48] C. W. Tang, *Appl. Phys. Lett.* **1986**, *48*, 183.
- [49] K. Hunger, *Rev. Prog. Color. Relat. Top.* **2005**, *35*, 76.
- [50] D. Boinagrov, J. Loudin, D. Palanker, *J. Neurophysiol.* **2010**, *104*, 2236.
- [51] M. Eickenscheidt, M. Jenkner, R. Thewes, P. Fromherz, G. Zeck, *J. Neurophysiol.* **2012**, *107*, 2742.
- [52] A. Stett, W. Barth, S. Weiss, H. Haemmerle, E. Zrenner, *Vision Res.* **2000**, *40*, 1785.
- [53] D. Tsai, S. Chen, D. A. Protti, J. W. Morley, G. J. Suaning, N. H. Lovell, *PLoS One* **2012**, *7*, e53357.
- [54] L. Wang, K. Mathieson, T. I. Kamins, J. D. Loudin, L. Galambos, G. Goetz, A. Sher, Y. Mandel, P. Huie, D. Lavinsky, J. S. Harris, D. V. Palanker, *J. Neural. Eng.* **2012**, *9*, 46014.
- [55] M. Kaltenbrunner, G. Adam, E. D. Głowacki, M. Drack, R. Schwödiauer, L. Leonat, D. H. Apaydin, H. Groiss, M. C. Scharber, M. S. White, N. S. Sariciftci, S. Bauer, *Nat. Mater.* **2015**, *14*, 1032.
- [56] P. Lazič, H. Štefančič, H. Abraham, *J. Comput. Phys.* **2006**, *213*, 117.

APPLIED PHYSICS

Optoelectronic control of single cells using organic photocapacitors

Marie Jakešová¹, Malin Silverå Ejneby², Vedran Đerek^{1,3}, Tony Schmidt⁴,
Maciej Gryszel^{1,3}, Johan Brask², Rainer Schindl⁴, Daniel T. Simon¹, Magnus Berggren¹,
Fredrik Elinder², Eric Daniel Głowacki^{1,3*}

Optical control of the electrophysiology of single cells can be a powerful tool for biomedical research and technology. Here, we report organic electrolytic photocapacitors (OEPCs), devices that function as extracellular capacitive electrodes for stimulating cells. OEPCs consist of transparent conductor layers covered with a donor-acceptor bilayer of organic photoconductors. This device produces an open-circuit voltage in a physiological solution of 330 mV upon illumination using light in a tissue transparency window of 630 to 660 nm. We have performed electrophysiological recordings on *Xenopus laevis* oocytes, finding rapid (time constants, 50 μ s to 5 ms) photoinduced transient changes in the range of 20 to 110 mV. We measure photoinduced opening of potassium channels, conclusively proving that the OEPC effectively depolarizes the cell membrane. Our results demonstrate that the OEPC can be a versatile nongenetic technique for optical manipulation of electrophysiology and currently represents one of the simplest and most stable and efficient optical stimulation solutions.

INTRODUCTION

Devices based on extracellular stimulation of nerve tissue have been deployed therapeutically for many neurological conditions. The growing field of neural prosthetics includes cochlear and artificial retina implants as well as brain stimulation electrodes for the treatment of Parkinson's disease, depression, etc. (1–3). As an alternative to conventional metal or semiconductor electrodes, light stimulation offers the potential of wireless, temporally and locally specific, minimally invasive manipulation of electrophysiological processes. Optical control can be achieved directly by using near-infrared light (4), through genetic manipulation (i.e., optogenetics) (5), by delivery of photosensitive pharmaceuticals (6), or by an optoelectronic device (7–9). Examples of semiconducting films (10–12) and semiconducting nanoparticles (13–17) that are used to alter the electrophysiology of cells have been elaborated in considerable detail (14, 18). In these cases, either photothermal (19), photothermocapacitive (4, 15), or photofaradaic mechanisms (13, 20, 21) are implicated behind the observed (electro)physiological effects. The suitability of different stimulation mechanisms varies by desired application, and deeper mechanistic understanding is a topic of extensive current study (22). Nevertheless, there is a widely accepted consensus that, to achieve effective extracellular stimulation, a given charge threshold has to be delivered to the cell (1, 23–25). Unfortunately, the realization of optoelectronic devices generating large electrolytic charge densities remains elusive. We are motivated to find an effective optoelectronic method that relies on capacitive coupling at the single-cell level. Pioneering research on the biophysics of capacitive stimulation was done by Fromherz and coworkers (26–28). They showed the possibility of modulating cellular electrophysiology through externally electrically controlled thin-film dielectric capacitors. In view of their findings, we introduce a wireless light-sensitive

version: the organic electrolytic photocapacitor (OEPC). In our earlier work on organic semiconductor/single-cell interfaces, we were able to stimulate via a photothermal mechanism and did not reach the charging threshold for capacitive stimulation (29). Learning from these studies, we designed the first version of the OEPC and we were successful in demonstrating stimulation of blind chick retinas (30). We found reproducible action potential generation in retinal ganglion cells. Capacitive coupling was implicated as the mechanism in that work. In parallel, organic heterojunction blends capped with insulating layers have also been recently reported to deliver increased charge density (31). Here, we have taken a reductive approach to understand this mechanism conclusively and use this knowledge to optimize OEPC devices at the level of single cells.

Our motivation for using organic semiconductors to construct high-performance light-to-capacitive current transducers arises from several facts. Organic conjugated molecules are very efficient absorbers. Thus, our nanometrically thin devices absorb the same light that a 100 \times thicker silicon wafer would. Therefore, organic devices can be fabricated to be thin and less mechanically invasive. Furthermore, the stability and nontoxicity of many organic pigments are established (32). Last, the specific combination of materials used in this study, metal-free phthalocyanine (H₂Pc; p-type) and *N,N'*-dimethylperylene-3,4:9,10-tetracarboxylic diimide (PTCDI; n-type) (Fig. 1A), allows operation in the 630- to 660-nm tissue transparency window, thereby widening the scope from the artificial retina to other *in vivo* applications such as peripheral nerve stimulation. Here, we study the performance and stability of the next-generation OEPC (Fig. 1, A and B) as well as its capacitive coupling with single cells (Fig. 1, C and D). As a model single cell, we study *Xenopus laevis* oocytes. These cells are large (1 mm ϕ) and have a vitelline envelope surrounding the cell membrane, roughly 3 μ m thick (33). The cleft between the membrane and the device surface is thus at least 3 μ m. They are therefore a challenging system to demonstrate effective capacitive coupling, which mimics more closely realistic conditions for applied neurostimulation rather than cultured cells, which can form clefts of 20 to 50 nm with the semiconductor surface (34). In

¹Laboratory of Organic Electronics, ITN Campus Norrköping, Linköping University, SE-60221 Norrköping, Sweden. ²Department of Clinical and Experimental Medicine, Linköping University, SE-58185 Linköping, Sweden. ³Wallenberg Centre for Molecular Medicine, Linköping University, SE-58185 Linköping, Sweden. ⁴Gottfried Schatz Research Center, Medical University of Graz, A-8010 Graz, Austria.

*Corresponding author. Email: eric.glowacki@liu.se

Copyright © 2019
The Authors, some
rights reserved;
exclusive licensee
American Association
for the Advancement
of Science. No claim to
original U.S. Government
Works. Distributed
under a Creative
Commons Attribution
NonCommercial
License 4.0 (CC BY-NC).

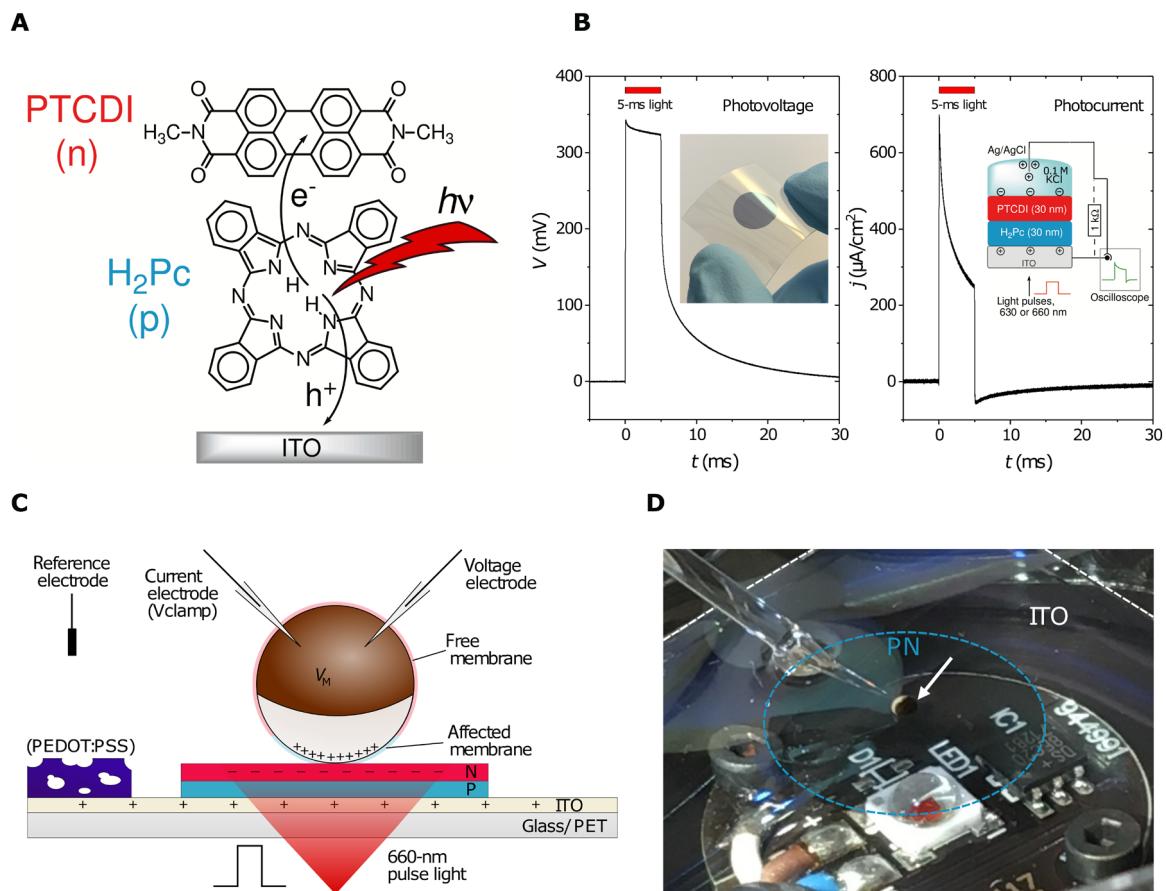


Fig. 1. The OEPC at the single-cell level. (A) The mechanism of action of OEPC devices relies on photoinduced charge transfer between H₂Pc (P-layer) as the electron donor and PTCDI (N-layer) as the electron acceptor. The conducting ITO layer plays a critical role in storing positive charge and serving as the return electrode in solution. (B) EPR measurements are used to characterize the photocharging dynamics of OEPC devices. Photovoltage is measured between the ITO and an Ag/AgCl reference electrode in solution, while the corresponding charging current is registered by measuring a voltage drop across a resistor. The insets show a photograph of an OEPC device on ITO-coated PET foil and a schematic of the EPR measurement configuration. (C) Cross-section of the OEPC device architecture, with an illustration of the capacitive coupling mechanism with an adjacent oocyte in the physiological electrolyte. Illustration shows the positive (+) and negative (−) charge density at the moment when photoinduced currents in the electrolyte have fully capacitively charged the oocyte. Single-cell electrophysiology experiments were carried out using one or two intracellular electrodes. The transient potential measured intracellularly by the voltage electrode is defined as V_T in this paper. The actual membrane potential across a given region of the cell membrane is defined as V_M . The sign of the induced V_M is represented in the illustration by the blue (positive) and red (negative) color of the cell membrane. In the vertical dimension, the thickness of the ITO/P/N structure is expanded for clarity. The thickness of the device layers is 110/30/30 nm, respectively. For voltage-clamp experiments where longer voltage transients are necessary, the capacitance of the device is boosted by adding a poly(3,4-ethylenedioxythiophene):polystyrene sulfonate (PEDOT:PSS) layer onto the ITO. (D) Photograph of the oocyte measurement setup with bottom LED illumination, with labeled PN region and ITO. The white arrow indicates the oocyte cell. Photo credit: E. D. Glowacki, Linköping University.

this work, we find that rapid and substantial changes of membrane potential are possible using the OEPC and unambiguously prove a capacitive coupling mechanism in achieving control of voltage-gated ion channels.

RESULTS AND DISCUSSION

Fabrication and stability of OEPCs

We introduced the concept of OEPCs in a previous study (30). The device comprises a conductive back electrode and a donor-acceptor junction of photosensitive organic semiconductor pigments, which, when immersed in electrolyte solution, form charged double layers upon illumination. We chose commercial indium tin oxide (ITO) on glass or poly(terephthalate) (PET) as a transparent conductor to serve as the bottom electrode in place of gold used in the original

study. ITO was favorable as it has a high overpotential for undesired faradaic processes (35), unlike gold, which can more easily catalyze various redox reactions. We found that OEPCs with gold photochemically produced reactive oxygen species, while ITO-based OEPCs did not (details in Supporting Note 1; fig. S1). The combination of donor-acceptor materials remained the same as previously described (i.e., 30 nm of H₂Pc and 30 nm of PTCDI). The organic layers were obtained through sequential physical vapor deposition using a stencil mask. The performance of the devices was investigated by measuring the electrical photoresponse (EPR). A set of typical traces is shown in Fig. 1B, with the schematic of the setup in the inset. In short, the photovoltage response to pulsed red light (630 nm) is measured between the ITO back electrode and an Ag/AgCl counter electrode immersed in 0.1 M KCl, which is in contact with the organic pixel only, using an oscilloscope. The photocurrent is obtained

by measuring the voltage drop over a 1-kilohm resistor. This measurement provides information on the maximum achievable voltage (330 mV) and current density (0.6 to 0.7 mA/cm²) of the device, as well as the associated charging/discharging dynamics. We used this technique to investigate the photostability of our devices as well as their endurance through sterilization. For *in vitro* and *in vivo* studies, sterilizability is an essential factor. The three sterilization procedures of choice were rinsing in 70% ethanol (EtOH), exposure to germicidal ultraviolet (UV) dose, or an autoclave cycle. The photostability test was accomplished by stressing the samples in the electrolyte with a constant pulsed illumination of 0.08 mW/mm² and 20-ms pulse with a 3.5% duty cycle (Fig. 2, A and B). All devices ($n = 20$, mean \pm SD) produced a peak photovoltage of 331 ± 9 mV and a peak photocurrent density of 670 ± 38 μ A/cm², as-fabricated when illuminated with a 630-nm red light-emitting diode (LED), giving an irradiance of 6 mW/mm². After sterilization ($n = 5$), the performance decreased by 5 to 10% for UV and EtOH treatments, while autoclaving resulted in a more substantial reduction. The parameters of UV- and EtOH-treated samples further declined after leaving the devices in an electrolyte (0.1 M KCl); however, the values were similar to those of unsterilized samples. To our surprise, the autoclaved samples recovered to higher performance than after fabrication. Afterward, the samples were exposed to continuous stress by pulsed illumination over 178 days (equivalent to around 27 million charge/discharge cycles). All samples remained functional, although performance declined slowly over time. Autoclaved samples overall kept the best performance. We hypothesized that the elevated performance was due to heat-induced recrystallization during the autoclave cycle (36). The autoclaved samples showed better-defined faceted crystals, providing evidence for heat-activated recrystallization

boosting performance (fig. S2). According to scanning electron microscopy (SEM) data, the nanoscale morphology difference between the as-fabricated samples (Fig. 2, C and D) and those exposed to stress over 178 days (Fig. 2E) evolves. All aged samples have a nanocrystalline morphology resembling autoclaved samples, implicating a surface recrystallization promoted by water. However, over longer periods of time (longer than 35 days), a process of progressive delamination of the organic layer at the edge was apparent (fig. S3). Erosion of the edge is observed, and redeposition of pieces of organic material both on the ITO layer and on top of the organic photoconductor nanocrystalline (PN) layer is clear. We hypothesize that adhesion of the PN layer to the conducting substrate over long periods of stress is the primary stability issue.

Photoinduced membrane potential modulation

After obtaining stable and well-characterized devices, we moved on to study the light-induced effects on the electrophysiology of single cells. As a model, we used *X. laevis* oocytes. An advantage of this model is the large cell size and easy handling. In addition, oocytes offer easy exogenous ion channel expression as well as a low level of endogenous ion channels. In our initial exploration of the OEPC (30), we reported stimulation of neurons or retinal ganglion cells tens of micrometers in size, using OEPCs with diameters in the range of 50 to 2000 μ m. For the relatively large oocytes (1 mm \varnothing), we use a correspondingly sized 12-mm \varnothing organic pixel. First, we established the magnitude of transient voltage, V_T , induced in the oocytes. In these intracellular measurements, the OEPC is placed in an electrolyte bath, and the oocyte is positioned directly on top of the device, as shown in Fig. 1 (C and D). Unlike in the EPR measurements, the OEPC device is not wired in any way and is therefore

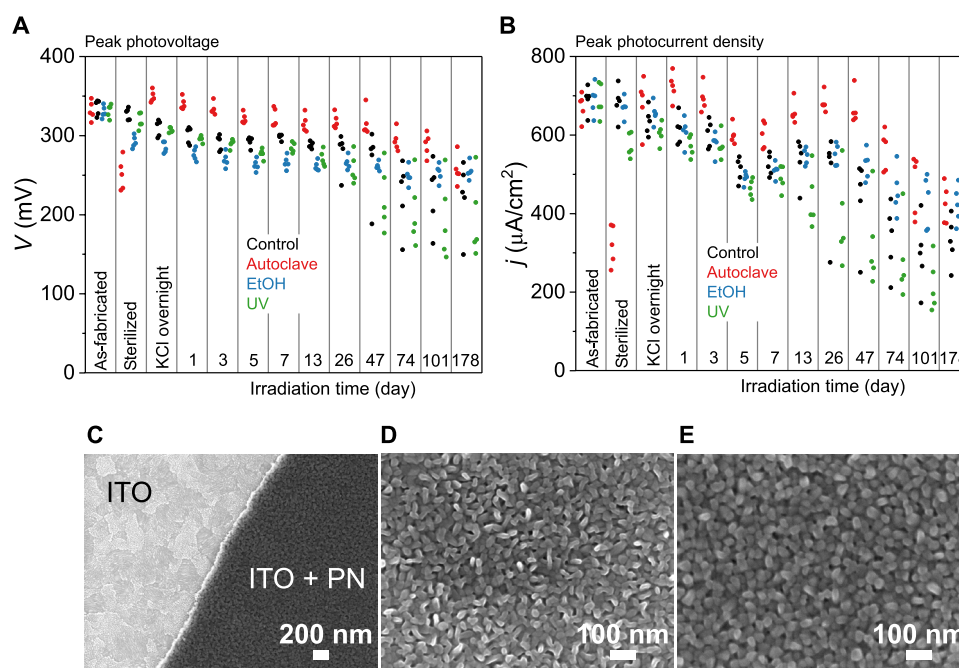


Fig. 2. Stability and nanomorphology of OEPC devices. (A) Peak photovoltage measured using the EPR of a series of devices subjected to a light stress test over 178 days. Three different sterilization conditions were applied, with autoclave yielding the most stable devices and UV resulting in faster performance decay. (B) Peak photocurrent of the same set of samples measured over the stress/stability test. (C) SEM micrograph of the edge of the organic PN layer on the ITO bottom electrode. This interface was stable for a month of stress but then began to experience delamination. (D) SEM of an as-fabricated organic PN layer and of a device (E) after 178 days of light pulse stress.

electrically floating. The recording is performed intracellularly, meaning that the voltage electrode is about 1 mm above the OEPC surface. The light pulse causes transient voltage peaks at the beginning and after the end of the pulse (10- and 1-ms pulses are shown in Fig. 3, A and B, respectively). The first negative peak had faster charging kinetics, while the second positive peak showed slower discharging corresponding to the discharging tail seen in the EPR measurement (Fig. 1B). The integrated area under both peaks was well balanced. The integration of the second peak gives $94.5 \pm 1.4\%$ of the value of the first peak. During the light pulse, the transient potential (V_T) typically returns to the resting membrane potential after ~ 3 ms. These positive-negative biphasic voltage peaks resemble transient potentials resulting from biphasic current pulses, which are typically used for electrical stimulation (30). We next studied the effect of light intensity on V_T . From Fig. 3C, it is evident that

with increasing light intensity, the magnitude of V_T increases and begins to saturate at the highest intensity values. At the highest intensity of 6 mW/mm^2 , the values were $110.1 \pm 4.9 \text{ mV}$ for the cathodic peak ($n = 12$, means \pm SEM). However, even the lowest probed intensity (0.3 mW/mm^2) delivered a V_T of $23.9 \pm 1.9 \text{ mV}$. For an excitable cell, this perturbation is above the threshold of what would be expected to elicit action potentials. To put the magnitude of these changes into context, we compare with recent studies of light-pulse irradiated organic donor-acceptor blends resulting in changes no higher than $\pm 1 \text{ mV}$ (18) or 80 mV , though this result was obtained with 72 mW/mm^2 (31). The efficiency of the capacitive coupling of our OEPC devices is therefore substantial.

When measured intracellularly in the oocyte, V_T corresponds to the potential difference that the voltage electrode registers between the upper intracellular region of the oocyte and the distant reference

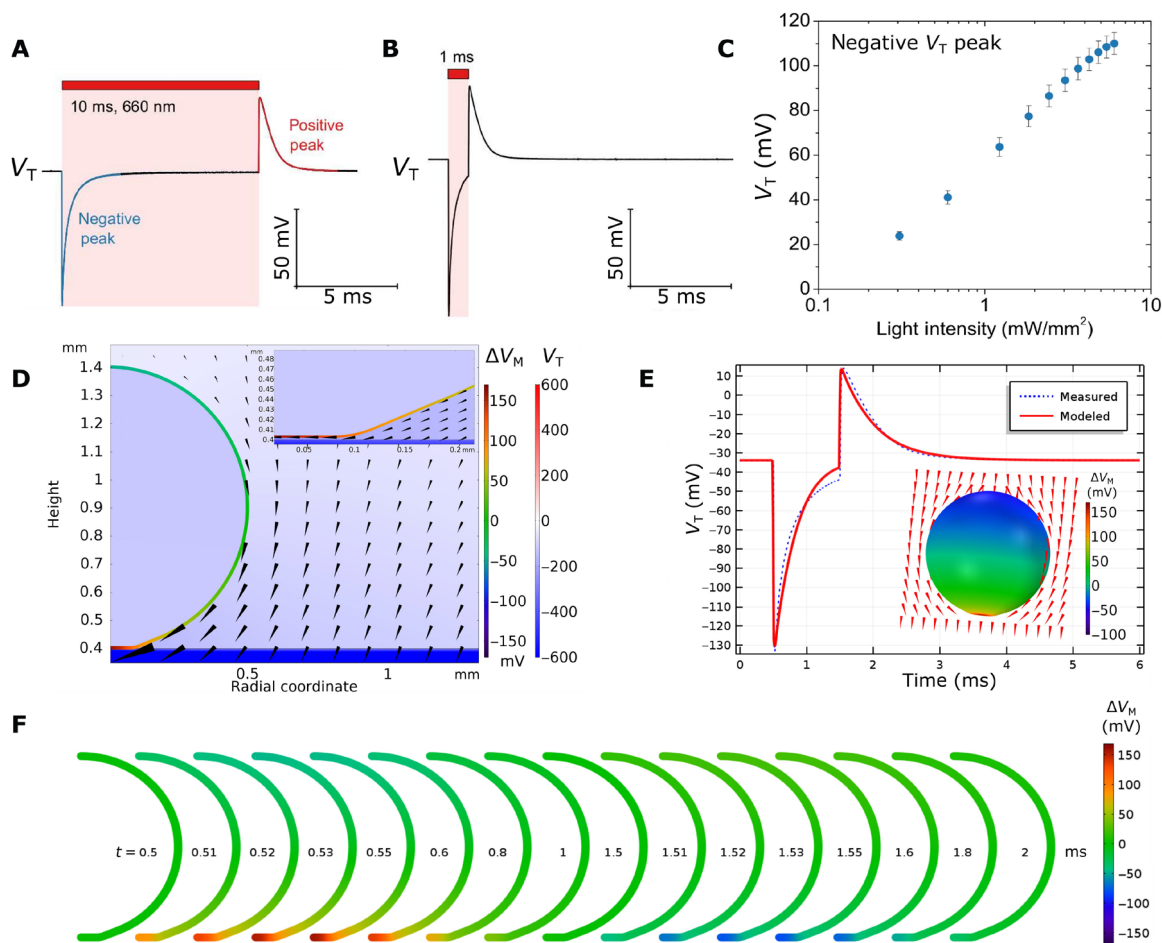


Fig. 3. Photoinduced transient voltages and their effect on oocyte membrane potential. (A) Photoinduced transient potential change measured intracellularly in an oocyte, showing the biphasic trace produced by a 10-ms illumination pulse. (B) V_T for 1-ms pulse length. (C) Peak cathodic V_T dependence on light intensity averages for 12 oocytes (pulse length, 250 μs). (D) Model of electrical potential during OEPC charging, showing both V_T and arrows indicating ionic current direction and magnitude. The cell membrane is colored with a different color scale representing the calculated induced membrane potential, ΔV_M . A resting membrane potential of -33 mV is assumed for all calculations. The bottom of the cell near the OEPC is depolarized, while the membrane on the top of the oocyte experiences a small hyperpolarization. A zoom of the cleft region showing the strongly depolarized region is given in the inset. A distance of $3 \mu\text{m}$ between the OEPC surface and the cell membrane is assumed for this calculation. Because of symmetry, only half of the oocyte is shown. (E) The calculated V_T for a 1-ms pulse in the upper intracellular region of the oocyte (red trace) corresponds to the experimentally measured V_T values (blue trace). The inset shows a three-dimensional (3D) projection of V_M in different regions of the oocyte at the time point ($50 \mu\text{s}$ after the light pulse is turned on) where the cathodic V_T is maximum. The red region at the bottom of the oocyte represents the strongly depolarized part of the membrane near the OEPC surface. (F) 2D projection showing the time evolution of the induced membrane potential over the course of a 1-ms light pulse (turned on at $t = 0.5 \text{ ms}$, turned off at $t = 1.5 \text{ ms}$) and subsequent discharging (i.e., anodic peak).

electrode. However, this V_T value is not equal in magnitude to the induced potential difference across the cell membrane, which would be felt by voltage-gated ion channels. To understand the magnitude of potential across different regions of the oocyte cell membrane, intra- versus extracellular, we applied a numerical model. Knowing the photocharging parameters of OEPCs from EPR measurements, electrolyte resistivity, and the areal capacitance of the oocyte ($1 \mu\text{F}/\text{cm}^2$), we constructed a numerical model to calculate the spatial and temporal evolution of V_T and the corresponding photoinduced membrane potential (V_M). V_M , V_T , and spatial capacitive currents at the time of the maximum perturbation ($t = 0.55 \text{ ms}$, 0.05 ms after the onset of light excitation) are plotted in Fig. 3D (see also figs. S4 and S5 for detailed conditions). In this model (details in Materials and Methods and Supporting Note 2), we assume a cleft distance of $3 \mu\text{m}$, given mostly by the relatively thick vitelline envelope present on the oocyte and a flattened region at the bottom of the oocyte, where it rests on the OEPC surface. When we apply a light pulse, the OEPC charges and ionic displacement currents in solution cause transductive extracellular potentials (37), which last only when the OEPC device is charging or discharging. From this numerical simulation, it is apparent that only the bottom region of the oocyte, which we will refer to as the affected membrane, experiences a large depolarization, while the free membrane becomes slightly hyperpolarized. The numerical model reproduces a $V_T(t)$ trace resembling closely the experimentally measured one (Fig. 3E). Using this model, we can understand the relevant voltage polarity and magnitude affecting different regions of the oocyte membrane. The V_M value for different phases of the photostimulation pulse is schematized in Fig. 3F and movie S1, showing the initial depolarization of the bottom part (affected membrane) of the oocyte when the light is turned on, followed by hyperpolarization of this region when the light is turned off. The validity of this model and electrophysiologically relevant photoinduced potential magnitudes will be evidenced experimentally in the following section concerning ion channel activation, where depolarization of the affected membrane is implicated.

Evaluating the possibility of photothermal effects is important. As a simple control, we fabricated dummy devices with an analogous absorber layer but that cannot electrically charge. For this purpose, we chose indigo as the organic pigment. The absorption spectrum of indigo overlaps that of H_2Pc relatively well. Upon excitation, indigo undergoes rapid tautomerization and thus dissipates >99% of the energy in the form of heat (38). With the same light intensity settings as before, we could not see any difference between an oocyte on the indigo substrate and a blank petri dish. There are no photoinduced changes in the absence of a full OEPC device. The rate of heating is apparently not enough to elicit thermocapacitive changes. We hypothesize that in this case, where the absorbing surface is several micrometers away from the cell membrane, the transfer of thermal energy from the semiconductor surface to the cell is not efficient, thus minimizing the expectation of photothermal effects. Therefore, we propose that in the case of the OEPC devices at the applied time scales, the capacitive coupling model holds true and photothermal effects are negligible.

Photoinduced ion channel opening

Once we established that the membrane potential could be perturbed by at least tens of millivolts, we went further to see whether we could use the OEPC device to evoke photoinduced activation of voltage-

gated ion channels. We chose a well-understood wild-type (WT) Shaker K_V channel expressed in *X. laevis* oocytes, and we measured the light-induced K^+ currents with the two-electrode voltage-clamp technique. These K_V channels are opened by depolarizing potentials. The action of an additional capacitive electrode can be regarded as an “external voltage-clamp.” If the proposed two-domain picture discussed above for capacitive coupling holds, we should expect photoinduced opening of the K_V channels located in the affected region of the cell membrane adjacent to the OEPC. Because of the slow dynamics of the channel relative to the capacitive response of the cell to the applied voltage, one can expect steady-state ion channel currents only after several milliseconds. Because of this fact, our original OEPC device was not ideal for this experiment, because the V_T perturbation decreases rapidly within milliseconds. To overcome this limitation, we tested two approaches. First, instead of a simple square pulse, we applied a light intensity ramp to prolong the charging of the OEPC. The other approach involved increasing the capacitance of the ITO back electrode, which allowed the OEPC system to accommodate more charge. We achieved this by partially coating the ITO with poly(3,4-ethylenedioxythiophene):polystyrene sulfonate (PEDOT:PSS) (as illustrated in Fig. 1C), a conducting polymer formulation known for its large electrolytic capacitance (39). Although the light intensity ramp made the residual V_T at the end of the light pulse larger (fig. S6), the effects of PEDOT:PSS were superior. At the end of a 5-ms light pulse, the PEDOT:PSS-modified OEPC kept a V_T value of up to 28 mV, while the unmodified sample decreased essentially to zero (Fig. 4A). The PEDOT:PSS-modified device has a larger time constant $\tau = RC$. Because the resistance has not changed, it is clear that the capacitance has increased and the OEPC can accommodate more charge over the whole course of the light pulse (Fig. 4A). Therefore, we continued all the voltage-clamp experiments with the PEDOT:PSS-modified samples only. As a point of reference, we studied the light pulse response to the voltage-clamp protocol on an uninjected oocyte with no exogenous ion channels present. Figure 4B shows that the light-induced capacitive response of the cell is independent of the applied command voltage. After expression of the Shaker K_V channel, the photoresponse follows the channel behavior (Fig. 4C). Between applied -100 and -70 mV , when all the channels are closed, the light-induced response is the same, similar to an uninjected oocyte. However, by -50 mV , all the channels are still closed in the dark condition, but the light current is already nonzero. This change is attributed to the external OEPC-induced depolarizing field, causing channels in the affected membrane to open at more negative command voltages. These voltage-clamp traces are consistent with external capacitive stimulation achieved on $K_V1.3$ channels with electrically controlled capacitors (27). When one extracts the dark current before the pulse and the light current at the end of the pulse (Fig. 4C), the $I(V)$ characteristic can be constructed, and channel conductance, G , is calculated to give $G(V)$. A result of such treatment is given in Fig. 4D. The data show that the light pulses cause channel opening at up to 40 mV more negative command voltages. To confirm that all light-induced effects in this measurement originate from the flow of K^+ , we applied the nonselective K_V current blocker 4-aminopyridine (4-AP) to the WT Shaker K_V channel. We observed inhibition of the light-induced effect in the $G(V)$ curves (Fig. 4D, green trace), with the raw voltage-clamp data resembling an uninjected oocyte. To further validate our proposed mechanism of photoinduced depolarization, we expressed a modified version of the Shaker K_V channel with a $G(V)$ characteristic

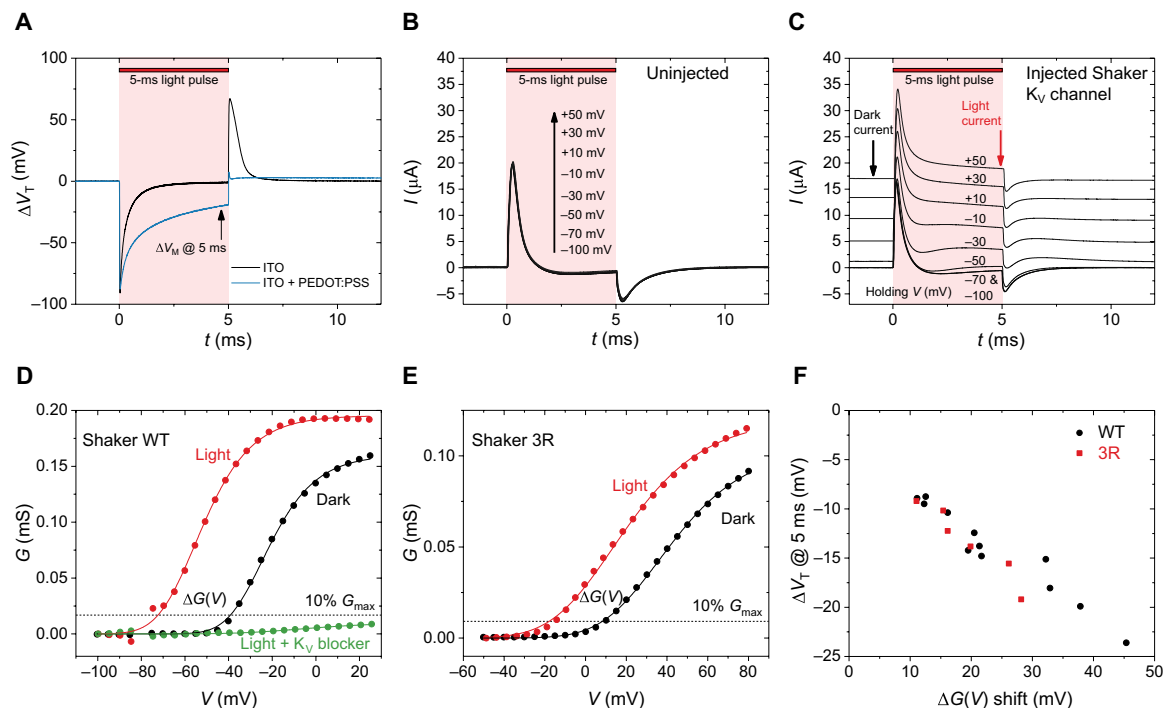


Fig. 4. Photostimulation effects on K_V Shaker-type channels in oocytes. (A) Voltage measurements on uninjected oocytes using a 5-ms light pulse in the case where the bare ITO is the back electrode and the ITO is modified with PEDOT:PSS. Because of the higher capacitance given by PEDOT:PSS, the photocapacitive charging currents are larger and are exhibited over longer time, thus applying higher transductive extracellular potentials. Maximizing V_T in a time scale of ≥ 2 ms is critical for observing effective stimulation of K_V channels. We use $V_T@5$ ms here as a convenient reference. (B) Voltage-clamp measurements at various voltage steps in uninjected oocytes, showing the voltage-independent capacitive response of the cell to the light pulse. (C) Voltage-clamp measurements of an oocyte transfected with the Shaker K_V channel, demonstrating the photoinduced increase in outward K^+ current. (D) $G(V)$ characteristic for WT Shaker K_V channels, for dark conditions (black trace) and during the light pulse (red trace). The green trace is for measurement after addition of the K_V channel blocker 4-AP. (E) $G(V)$ characteristics comparing dark conditions versus light pulses for 3R Shaker mutant channels. The onsets are shifted relative to WT. However, the photoinduced shift behavior is the same. (F) Correlation between the observed voltage shift in the light versus dark $G(V)$ and the transient voltage at the end of a 5-ms light pulse measured in the same cell. The higher transient voltage V_T corresponds to greater observed shifts in the $G(V)$ characteristics.

shifted toward more positive potentials, the 3R Shaker K_V channel (40). We saw the same photoinduced effect in the shifted 3R channel (Fig. 4E). To determine the relationship between the $G(V)$ curve shift and the performance of the OEPC in terms of the magnitude of photoinduced voltage change V_T , we constructed a correlation plot between the residual V_T at the end of a 5-ms light pulse and the ΔV shift of the Shaker $G(V)$ curves (Fig. 4F). The data show different cell cohorts of the WT and mutant K_V channels, and the light intensity applied was either 6 or 1.2 mW/mm². The correlation followed a clear trend, demonstrating that the V_T perturbation observed corresponds to the shift in the opening of the ion channel. In summary, the OEPC can perform analogously to a capacitive electrode acting as an extracellular voltage source.

CONCLUSIONS

In the present work, we have demonstrated efficient optical control of electrophysiology using a simple photocapacitive device based on organic semiconducting pigments, the OEPC. The motivation for developing OEPCs is to achieve a nongenetic, wireless, and minimally invasive analog to traditional electrodes, which are being used in fundamental research and medical applications treating neural dysfunction. In this work, we set out to understand the mechanism of action of OEPC at the single-cell level and see to what extent

capacitive coupling can be achieved. The OEPC can be regarded as an optoelectronic-to-ionic transducer. Photoexcitation of the donor-acceptor semiconductor junction produces electronic charges, which accumulate at the semiconductor/electrolyte and back electrode/electrolyte interfaces, producing oppositely charged electrolytic double layers. The electrolytic charging currents that result when short impulses of light are applied to the OEPC can be used to perturb the membrane potential in nearby cells. We found that capacitive coupling to oocytes was unexpectedly efficient, despite the relatively large effective cleft caused by the presence of the vitelline membrane on top of the oocyte's cellular membrane. The device can deliver voltage perturbations exceeding 100 mV intracellularly at the top of the oocyte, which is a distance of around 1 mm away from the OEPC surface. On the basis of numerical modeling, this perturbation translates to membrane potential changes on the level of tens to even over a hundred millivolts at different points of the cell. The values are well above levels necessary for action potential generation in excitable cells. This result validates why we were able to observe action potentials in the retinal ganglion cells we evaluated with the first version of the OEPC. One of the key findings of the study was the critical role of the back electrode not only in modulating the capacitance, and therefore dynamics, of the device but also as being the gatekeeper of photofaradaic processes. By boosting the capacitance of the back electrode through PEDOT:PSS modification, the

device RC time constant can be significantly increased and charging/discharging slowed down. The strongest evidence for the proposed mechanism of capacitive coupling is demonstrated by the opening of voltage-gated ion channels in a voltage-clamp measurement configuration, implicating effective optically induced membrane potential modulations of tens of millivolts. The OEPC here can be regarded as a light-activated external voltage-clamp electrode. This type of capacitive coupling experiment is rare and has been carried out in the case of electrically addressed capacitors only by Fromherz and coworkers in the past (28, 37). The goal of achieving optoelectronic coupling to single cells using semiconductor materials and devices has garnered attention for nearly a decade (9, 13, 14). The experiments here constitute the first conclusive demonstration of successful and substantial capacitive coupling using an organic electronic device. Subsequent work will focus on optimizing parameters for eliciting action potentials in single cells, as well as transfer of the device on flexible implantable platforms for in vivo applications. Although the OEPC withstands sterilization and shows relative photostability, the performance, stability, and biocompatibility in vivo have to be established. Once that goal is reached, integration of the OEPC devices with sophisticated implantable platforms (41) enables many devices to treat neural disorders in a safe and less invasive manner.

MATERIALS AND METHODS

Materials and OEPC device fabrication

H₂Pc (Alfa Aesar) and PTCDI (BASF) were used throughout this work. Both materials were purified three times by temperature gradient sublimation. ITO was used as a conducting layer on two different substrates: 125- μm -thick PET (Sigma-Aldrich) or 1.1-mm-thick borosilicate glass (Kintec). ITO substrates were cleaned by sequential sonication in acetone (only glass substrates), isopropanol, Hellmanex III detergent solution heated to 50°C, and deionized (DI) water. All samples were then exposed to UV/ozone treatment for 15 min and silanized in a vapor of *n*-octyltriethoxysilane (OTS) (TCI) at 90°C for 1 hour. Samples were sonicated in acetone (glass) or isopropanol (PET) and washed with water to remove any OTS multilayers. After OTS modification, substrates were moved to a multi-source organic deposition system and pumped down to 1×10^{-6} mbar. H₂Pc was evaporated at a rate of 1 to 2 Å/s to a thickness of 30 nm, and PTCDI was evaporated at a rate of 2 to 5 Å/s to a thickness of 30 nm. Rate control was verified using a quartz crystal microbalance, with previous thickness calibration using a Dektak contact profilometer cross-checked with absorbance measurements, which allowed comparison to optical density values for thin films reported in the literature. The indigo samples were prepared similarly, except the thickness of the absorber was 60 nm to compensate for the lower absorption coefficient. Patterning of the organic semiconductor layer was done using stencil shadow masking. For OEPC devices with an additional PEDOT:PSS layer added to the ITO back contact, the procedure was modified slightly. During the OTS vapor-phase deposition, the edges of the ITO were protected with a stencil tape. This effectively masked the OTS deposition and left the protected areas hydrophilic. The sample was then spin-coated with a commercial PEDOT:PSS formulation (PH1000, Heraeus GmbH). The PH1000 mixture was modified by adding 1% (by volume) dimethyl sulfoxide (DMSO) and 1 volume % (3-glycidylxypropyl)trimethoxysilane (GOPS). GOPS was added to provide good adhesion to the ITO, while DMSO was an additive that increased the PEDOT:PSS conduc-

tivity. The modified PH1000 mixture was spin-coated from freshly made solutions at 1500 rpm for 30 s, following a 2-s spreading step at 800 rpm. Coated samples were baked on a hotplate at 120°C for 10 min. PEDOT:PSS was found to stick only to the hydrophilic edges and did not deposit on the OTS modified area in the center of the substrate. The SEM images were obtained on a ZEISS Sigma 500 FE-SEM using an in-lens secondary electron detector and with an acceleration voltage of 3 kV.

EPR measurements

EPR data were collected using a high-resolution 15-bit two-channel PicoScope 5243B oscilloscope. Measurements were conducted inside a dark faraday cage. Light excitation was achieved with a 630-nm red LED placed behind a transparent glass window below the sample stage, giving an irradiance of 6 mW/mm² at the sample position on the stage. Contact to the transparent conductor back electrode of the devices was established with a needle probe, while the electrolyte contact was achieved with an AgCl-coated silver wire placed in a syringe containing 0.1 M KCl electrolyte. The electrode-containing syringe was positioned above the device using a holder with the screw-controllable *z* axis. The level of the electrolyte in the electrode-containing syringe was controlled manually by adjusting the pressure with an empty syringe connected by flexible tubing to the electrode-containing syringe. In this way, the top electrolyte contact to the devices was accomplished without mechanical contact by a drop of the electrolyte from the syringe. The EPR voltage measurements were taken directly with an oscilloscope, while the current measurements were obtained by measuring the voltage drop over a 1-kilohm resistor shorting the electrolyte contact and the back contact to the devices or by using a low-impedance (50-ohm) low-noise current amplifier (FEMTO DLPCA-200). The devices (15 mm by 15 mm ITO, 8 \varnothing mm organic pixel) were sterilized in three different ways: They were either washed three times in 70% EtOH for 5 s with rinses of DI water in between, exposed to UV irradiation (8000 $\mu\text{W s/cm}^2$), or autoclaved at 121°C for 20 min (Tuttnauer, Elara 9i). The samples were measured 2 hours after the sterilization process. The irradiation stress was performed by exposing the OEPCs immersed in 0.1 M KCl to a high-density LED light source (626 nm, 0.08 mW/mm²) pulsed at 20 ms with a 550-ms interval. Before measurement, the samples were washed with DI water and dried under a stream of nitrogen. Samples measured for 178 days were allowed to rest for 4 hours before the final measurement.

Electrophysiology with *X. laevis* oocytes

The Shaker H4 channel (42) containing $\Delta(6-46)$ deletion to suppress fast inactivation (43), referred to as the WT Shaker K_V channel, and its modification with two introduced arginine residues (M356R, A359R, R362), referred to as the 3R Shaker K_V channel (40), were used throughout this study. Mutagenesis, oocyte preparation, storage, complementary RNA (cRNA) synthesis, and injection followed the procedures described previously (44, 45). Animal experiments were approved by the local Animal Care and Use Committee at Linköping University. All chemicals were purchased from Sigma-Aldrich if not stated otherwise. Experiments were performed with a GeneClamp 500B amplifier (Axon Instruments) and pClamp 10 software (Molecular Devices) and were digitized with a Digidata 1440A converter (Molecular Devices) at 4 μs per point. For the two-electrode voltage-clamp data, the amplifier's leak compensation was used, and the currents were low pass-filtered at 10 kHz. All experiments

were done at room temperature (20° to 23°C). The extracellular solution was composed of 88 mM NaCl, 1 mM KCl, 15 mM Hepes, 0.4 mM CaCl₂, and 0.8 mM MgCl₂ with pH adjusted to 7.4 with NaOH. The intracellular electrodes were prepared from borosilicate glass capillaries (World Precision Instruments) using an electrode puller (Narishige) to obtain a resistance of 0.5 to 2.0 megohms when filled with 3 M KCl. The measurement chamber was a 50-mm petri dish, with the OEPC device (25.4 by 25.4 mm ITO, 13 mm Ø organic pixel) placed centrally on a mounted LED (660 nm, 0.06 to 6 mW/mm², operated with DC2200 High-Power LED Driver, Thorlabs). The oocyte was positioned in the center of the organic pixel. For the V_T experiment, the voltage electrode was inserted into an oocyte (voltage follower amplifier), and the reference electrode was placed in the bath next to the OEPC device. The changes in potential upon pulsed light were measured. For the two-electrode voltage-clamp experiments, an additional electrode was used. The holding voltage was set to -100 mV (WT Shaker K_V) or -70 mV (3R Shaker K_V), and steady-state currents were measured between -100 and +50 mV for the WT Shaker K_V channel and between -70 and +80 mV for the 3R Shaker K_V channel with 5-mV steps, each for 150 ms. For the light experiments, a 3- to 10-ms light pulse was applied at 100 ms of the voltage step. All the shown voltage-clamp experiments were performed with the PEDOT:PSS-modified OEPCs, which were soaked in an electrolyte for at least 1 day before measurements. The blocking experiments were measured by adding 10 mM 4-AP (Alomone Labs) into the bath solution, yielding a final concentration of ~2 mM. The channel $G(V)$ curves were constructed according to $G_K(V) = I_K/(V - V_{rev})$, where I_K is the steady-state current before the light pulse (dark) and 100 μ s before the end of the 5-ms light pulse (light). The light ionic current was corrected for the light-induced capacitive current by subtracting I_K at the most negative applied potential, where all ion channels are closed, V is the absolute membrane potential, and V_{rev} is the reversal potential for the K channel, here set to -80 mV. The light-induced shift in the $G(V)$ curve was estimated at 10% level of the maximum dark conductance. For this purpose, $G(V)$ was fitted with a Boltzmann equation raised to the fourth power $G(V) = A/(1 + \exp((V_{50} - V)/s))^4$, where A is the amplitude, V_{50} is the midpoint, and s is the slope factor, as described previously (44).

Numerical modeling

The time-dependent electrical behavior of the photocapacitor/electrolyte/oocyte system was numerically modeled in a pseudo-three-dimensional (3D) axisymmetric geometry using a finite element analysis software (COMSOL Multiphysics version 5.3a, COMSOL Inc.). The effect of the photocapacitive excitation on the system was represented by a 4-mm-diameter conductive disc with infinite contact resistivity to replicate the nonfaradaic nature of the excitation. The disc was put in an electrically conductive medium (a circular right cylinder 5 mm in diameter and 3.5 mm in height, electric conductivity of 1.25 S/m, grounded on the top and the sides) representing the electrolyte used in the oocyte experiments. The oocyte cell was modeled as a 1-mm-diameter truncated sphere, with a 200- μ m-diameter truncated flat zone at the bottom, representing the contact area with the photocapacitor. The model cell was placed at a distance of 3 μ m from the model photocapacitor, a distance that we believe accurately represents the cleft width in the modeled system. The model cell was given an infinite surface resistance, representing the lack of endogenous ion channels, a surface capacitance of 1 μ F/cm², and a resting potential of -34 mV. A 1-ms

constant voltage pulse starting at 0.5 ms was applied to the disc, resulting in capacitive spatial currents in the electrolyte and the oocyte. To faithfully model the charging and discharging dynamics of the system due to the differing properties of the photocapacitor in the light versus dark phase, the disc bulk conductivity and contact capacitance were fitted separately during the light excitation phase and the “dark” part of the time-dependent study. The disc bulk conductivity, surface capacitance, and excitation voltage were initially set to match the measured injected current density (200 to 600 μ A/cm²) by the photocapacitor under the light intensity used in the experiment. The photocapacitor/electrolyte interface capacitance was set to the value (3 to 4 μ F/cm²) previously determined by electrochemical impedance spectroscopy (30). The parameters were further refined to match as closely as possible the measured intracellular voltage transient V_T from the inside of the oocyte (Fig. 3, A and E). The response of the modeled system (capacitive currents, resulting transient voltages, and changes in the cell membrane potential) to the voltage pulse representing the light excitation are shown in Fig. 3 and movie S1. Further details can be found in Supporting Note 2.

SUPPLEMENTARY MATERIALS

Supplementary material for this article is available at <http://advances.sciencemag.org/cgi/content/full/5/4/eaav5265/DC1>

Supporting Note 1. Photofaradaic reactions: Quantification of H₂O₂ production.

Supporting Note 2. Numerical modeling of the OEPC/oocyte interface.

Table S1. Results of H₂O₂ photogeneration.

Fig. S1. Illustration of photocapacitive versus photofaradaic behavior in OEPCs.

Fig. S2. SEM micrographs comparing control samples of ITO/H₂Pc/PTCDI.

Fig. S3. SEM micrographs of samples subjected to 178 days of light pulse stress.

Fig. S4. 2D representation of the electrolyte/oocyte/photocapacitor system.

Fig. S5. A 3D representation of the oocyte/photocapacitor model.

Fig. S6. Comparison of voltage transients in the case of light intensity ramps with a standard square light pulse.

Movie S1. Animation of evolution of transient potentials and membrane potentials during a 1-ms illumination pulse for an oocyte on top of an OEPC.

REFERENCES AND NOTES

1. S. F. Cogan, Neural stimulation and recording electrodes. *Annu. Rev. Biomed. Eng.* **10**, 275–309 (2008).
2. N. Pour Aryan, H. Kaim, A. Rothermel, *Stimulation and Recording Electrodes for Neural Prostheses* (Springer, 2015).
3. T. Someya, Z. Bao, G. G. Malliaras, The rise of plastic bioelectronics. *Nature* **540**, 379–385 (2016).
4. M. G. Shapiro, K. Homma, S. Villarreal, C.-P. Richter, F. Bezanilla, Infrared light excites cells by changing their electrical capacitance. *Nat. Commun.* **3**, 736 (2012).
5. M. Scanziani, M. Häusser, Electrophysiology in the age of light. *Nature* **461**, 930–939 (2009).
6. W. A. Velema, W. Szymanski, B. L. Feringa, Photopharmacology: Beyond proof of principle. *J. Am. Chem. Soc.* **136**, 2178–2191 (2014).
7. D. Palanker, A. Vankov, P. Huie, S. Baccus, Design of a high-resolution optoelectronic retinal prosthesis. *J. Neural Eng.* **2**, S105–S120 (2005).
8. K. Mathieson, J. Loudin, G. Goetz, P. Huie, L. Wang, T. I. Kamins, L. Galambos, R. Smith, J. S. Harris, A. Sher, D. Palanker, Photovoltaic retinal prosthesis with high pixel density. *Nat. Photonics* **6**, 391–397 (2012).
9. F. Benfenati, G. Lanzani, New technologies for developing second generation retinal prostheses. *Lab. Anim.* **47**, 71–75 (2018).
10. D. Ghezzi, M. R. Antognazza, R. Maccarone, S. Bellani, E. Lanzarini, N. Martino, M. Mete, G. Pertile, S. Bisti, G. Lanzani, F. Benfenati, A polymer optoelectronic interface restores light sensitivity in blind rat retinas. *Nat. Photonics* **7**, 400–406 (2013).
11. V. Gautam, D. Rand, Y. Hanein, K. S. Narayan, A polymer optoelectronic interface provides visual cues to a blind retina. *Adv. Mater.* **26**, 1751–1756 (2014).
12. L. Ferlauto, M. J. I. Airaghi Leccardi, N. A. L. Chenais, S. C. A. Gilliéron, P. Vagni, M. Bevilacqua, T. J. Wolfensberger, K. Sivula, D. Ghezzi, Design and validation of a foldable and photovoltaic wide-field epiretinal prosthesis. *Nat. Commun.* **9**, 992 (2018).
13. T. C. Pappas, W. M. S. Wickramanyake, E. Jan, M. Motamedi, M. Brodwick, N. A. Kotov, Nanoscale engineering of a cellular interface with semiconductor nanoparticle films for photoelectric stimulation of neurons. *Nano Lett.* **7**, 513–519 (2007).

14. L. Baret-Keren, Y. Hanein, Novel interfaces for light directed neuronal stimulation: Advances and challenges. *Int. J. Nanomedicine* **9**, 65–83 (2014).
15. Y. Jiang, J. L. Carvalho-de-Souza, R. C. S. Wong, Z. Luo, D. Isheim, X. Zuo, A. W. Nicholls, I. W. Jung, J. Yue, D.-J. Liu, Y. Wang, V. de Andrade, X. Xiao, L. Navrazhnykh, D. E. Weiss, X. Wu, D. N. Seidman, F. Bezanilla, B. Tian, Heterogeneous silicon mesostructures for lipid-supported bioelectric interfaces. *Nat. Mater.* **15**, 1023–1030 (2016).
16. R. Parameswaran, B. Tian, Rational design of semiconductor nanostructures for functional subcellular interfaces. *Acc. Chem. Res.* **51**, 1014–1022 (2018).
17. M. Zangoli, F. di Maria, E. Zucchetti, C. Bossio, M. R. Antognazza, G. Lanzani, R. Mazzaro, F. Corticelli, M. Baroncini, G. Barbarella, Engineering thiophene-based nanoparticles to induce phototransduction in live cells under illumination. *Nanoscale* **9**, 9202–9209 (2017).
18. O. S. Abdullaeva, M. Schulz, F. Balzer, J. Parisi, A. Lützen, K. Dedek, M. Schiek, Photoelectrical stimulation of neuronal cells by an organic semiconductor–electrolyte interface. *Langmuir* **32**, 8533–8542 (2016).
19. N. Martino, P. Feyen, M. Porro, C. Bossio, E. Zucchetti, D. Ghezzi, F. Benfenati, G. Lanzani, M. R. Antognazza, Photothermal cellular stimulation in functional bio-polymer interfaces. *Sci. Rep.* **5**, 8911 (2015).
20. C. Tortiglione, M. R. Antognazza, A. Tino, C. Bossio, V. Marchesano, A. Bauduin, M. Zangoli, S. V. Morata, G. Lanzani, Semiconducting polymers are light nanotransducers in eyeless animals. *Sci. Adv.* **3**, e1601699 (2017).
21. R. Parameswaran, J. L. Carvalho-de-Souza, Y. Jiang, M. J. Burke, J. F. Zimmerman, K. Koehler, A. W. Phillips, J. Yi, E. J. Adams, F. Bezanilla, B. Tian, Photoelectrochemical modulation of neuronal activity with free-standing coaxial silicon nanowires. *Nat. Nanotechnol.* **13**, 260–266 (2018).
22. Y. Jiang, X. Li, B. Liu, J. Yi, Y. Fang, F. Shi, X. Gao, E. Sudzilovsky, R. Parameswaran, K. Koehler, V. Nair, J. Yue, K. Guo, Y. Fang, H.-M. Tsai, G. Freyermuth, R. C. S. Wong, C.-M. Kao, C.-T. Chen, A. W. Nicholls, X. Wu, G. M. G. Shepherd, B. Tian, Rational design of silicon structures for optically controlled multiscale biointerfaces. *Nat. Biomed. Eng.* **2**, 508–521 (2018).
23. S. B. Brummer, L. S. Robblee, F. T. Hambrecht, Criteria for selecting electrodes for electrical stimulation: Theoretical and practical considerations. *Ann. N. Y. Acad. Sci.* **405**, 159–171 (1983).
24. D. R. Merrill, M. Bikson, J. G. R. Jefferys, Electrical stimulation of excitable tissue: Design of efficacious and safe protocols. *J. Neurosci. Methods* **141**, 171–198 (2005).
25. E. S. Krames, P. H. Peckham, A. R. Rezaei, *Neuromodulation* (Academic Press, 2009).
26. I. Schoen, P. Fromherz, Activation of Na⁺ channels in cell membrane by capacitive stimulation with silicon chip. *Appl. Phys. Lett.* **87**, 193901 (2005).
27. M. H. Ulbrich, P. Fromherz, Opening of K⁺ channels by capacitive stimulation from silicon chip. *Appl. Phys. A* **81**, 887–891 (2005).
28. I. Schoen, P. Fromherz, The mechanism of extracellular stimulation of nerve cells on an electrolyte-oxide-semiconductor capacitor. *Biophys. J.* **92**, 1096–1111 (2007).
29. M. Sytnyk, M. Jakešová, M. Litviňuková, O. Mashkov, D. Kriegner, J. Stangl, J. Nebesářová, F. W. Fecher, W. Schöffberger, N. S. Sariciftci, R. Schindl, W. Heiss, E. D. Glowacki, Cellular interfaces with hydrogen-bonded organic semiconductor hierarchical nanocrystals. *Nat. Commun.* **8**, 91 (2017).
30. D. Rand, M. Jakešová, G. Lubin, I. Věbraité, M. David-Pur, V. Đerek, T. Cramer, N. S. Sariciftci, Y. Hanein, E. D. Glowacki, Direct electrical neurostimulation with organic pigment photocapacitors. *Adv. Mater.* **30**, 1707292 (2018).
31. O. S. Abdullaeva, F. Balzer, M. Schulz, J. Parisi, A. Lützen, K. Dedek, M. Schiek, Organic photovoltaic sensors for photocapacitive stimulation of voltage-gated ion channels in neuroblastoma cells. *Adv. Funct. Mater.* **2018**, 1805177 (2018).
32. K. Hunger, Toxicology and toxicological testing of colorants. *Rev. Prog. Color. Relat. Top.* **35**, 76–89 (2005).
33. V. Kiessling, S. Vassanelli, Potassium channel gating in adhesion: From an oocyte-silicon to a neuron-astrocyte adhesion contact. *Eur. Biophys. J.* **34**, 113–126 (2005).
34. F. Santoro, S. Dasgupta, J. Schnitker, T. Auth, E. Neumann, G. Panaitov, G. Gompfer, A. Offenhäuser, Interfacing electrogenic cells with 3D nanoelectrodes: Position, shape, and size matter. *ACS Nano* **8**, 6713–6723 (2014).
35. J. D. Benck, B. A. Pinaud, Y. Gorlin, T. F. Jaramillo, Substrate selection for fundamental studies of electrocatalysts and photoelectrodes: Inert potential windows in acidic, neutral, and basic electrolyte. *PLOS ONE* **9**, e107942 (2014).
36. M. Warczak, M. Gryszel, M. Jakešová, V. Đerek, E. D. Glowacki, Organic semiconductor perylene-tetracarboxylic diimide (PTCDI) electrodes for electrocatalytic reduction of oxygen to hydrogen peroxide. *Chem. Commun.* **54**, 1960–1963 (2018).
37. I. Willner, E. Katz, *Bioelectronics* (Wiley-VCH, Weinheim, 2005).
38. E. D. Glowacki, G. Voss, N. S. Sariciftci, 25th anniversary article: Progress in chemistry and applications of functional indigos for organic electronics. *Adv. Mater.* **25**, 6783–6800 (2013).
39. C. M. Proctor, J. Rivnay, G. G. Malliaras, Understanding volumetric capacitance in conducting polymers. *J. Polym. Sci. Part B Polym. Phys.* **54**, 1433–1436 (2016).
40. N. E. Ottosson, S. I. Liin, F. Elinder, Drug-induced ion channel opening tuned by the voltage sensor charge profile. *J. Gen. Physiol.* **143**, 173–182 (2014).
41. D. Khodagholy, J. N. Gelinas, Z. Zhao, M. Yeh, M. Long, J. D. Greenlee, W. Doyle, O. Devinsky, G. Buzsáki, Organic electronics for high-resolution electrocorticography of the human brain. *Sci. Adv.* **2**, e1601027 (2016).
42. A. Kamb, L. E. Iverson, M. A. Tanouye, Molecular characterization of Shaker, a *Drosophila* gene that encodes a potassium channel. *Cell* **50**, 405–413 (1987).
43. T. Hoshi, W. N. Zagotta, R. W. Aldrich, Biophysical and molecular mechanisms of shaker potassium channel inactivation. *Science* **250**, 533–538 (1990).
44. S. I. Börjesson, T. Parkkari, S. Hammarström, F. Elinder, Electrostatic tuning of cellular excitability. *Biophys. J.* **98**, 396–403 (2010).
45. N. E. Ottosson, X. Wu, A. Nolting, U. Karlsson, P.-E. Lund, K. Ruda, S. Svensson, P. Konradsson, F. Elinder, Resin-acid derivatives as potent electrostatic openers of voltage-gated K channels and suppressors of neuronal excitability. *Sci. Rep.* **5**, 13278 (2015).

Acknowledgments: We are grateful to K. Tybrandt for helpful support with calculations and D. Rand and Y. Hanein for inspiring discussions. **Funding:** The authors are grateful to the Knut and Alice Wallenberg Foundation for support, especially within the framework of the Wallenberg Centre for Molecular Medicine (WCMM) at Linköping University, the Swedish Foundation for Strategic Research (SSF), and the Swedish Research Council (Vetenskapsrådet, 2018-04505). **Author contributions:** M.J., F.E., R.S., and E.D.G. conceived the research idea. D.T.S., M.B., F.E., and E.D.G. supervised and coordinated the research. M.J. fabricated all devices. M.J., V.Đ., M.G., and E.D.G. performed optoelectronic measurements and physical characterization. M.J., M.S.E., T.S., and J.B. conducted electrophysiology measurements and analyzed the electrophysiology data. V.Đ. carried out the numerical modeling. M.J. and E.D.G. wrote the manuscript with input from all authors. **Competing interests:** The authors declare that they have no competing interests. **Data and materials availability:** All data needed to evaluate the conclusions in the paper are present in the paper and/or the Supplementary Materials. Additional data related to this paper may be requested from the authors.

Submitted 25 September 2018

Accepted 12 February 2019

Published 5 April 2019

10.1126/sciadv.aav5265

Citation: M. Jakešová, M. Silverà Ejneby, V. Đerek, T. Schmidt, M. Gryszel, J. Brask, R. Schindl, D. T. Simon, M. Berggren, F. Elinder, E. D. Glowacki, Optoelectronic control of single cells using organic photocapacitors. *Sci. Adv.* **5**, eaav5265 (2019).

Extracellular Photovoltage Clamp Using Conducting Polymer-Modified Organic Photocapacitors

Malin Silverå Ejneby, Ludovico Migliaccio, Mindaugas Gicevičius, Vedran Đerek, Marie Jakešová, Fredrik Elinder, and Eric Daniel Głowacki*

Optoelectronic control of physiological processes accounts for new possibilities ranging from fundamental research to treatment of disease. Among nongenetic light-driven approaches, organic semiconductor-based device platforms such as the organic electrolytic photocapacitor (OPEC) offer the possibility of localized and wireless stimulation with a minimal mechanical footprint. Optimization of efficiency hinges on increasing effective capacitive charge delivery. Herein, a simple strategy to significantly enhance the photostimulation performance of OPEC devices by employing coatings of the conducting polymer formulation poly(3,4-ethylenedioxythiophene):poly(styrene sulfonate), or PEDOT:PSS is reported. This modification increases the charge density of the stimulating photoelectrodes by a factor of 2–3 and simultaneously decreases the interfacial impedance. The electrophysiological effects of PEDOT:PSS-derivatized OPECs on *Xenopus laevis* oocyte cells on membrane potential are measured and voltage-clamp techniques are used, finding an at-least twofold increase in capacitive coupling. The large electrolytic capacitance of PEDOT:PSS allows the OPEC to locally alter the extracellular voltage and keep it constant for long periods of time, effectively enabling a unique type of light-controlled membrane depolarization for measurements of ion channel opening. The finding that PEDOT:PSS-coated OPECs can remain stable after a 50-day accelerated ageing test demonstrates that PEDOT:PSS modification can be applied for fabricating reliable and efficient optoelectronic stimulation devices.

research to bioelectronic medical implants, which positively affect the lives of over a million patients worldwide.^[2–4] In the clinical setting, electrical neural prostheses can modulate, restore, or bypass nerves, with the aim to restore sensory,^[5] motor, or autonomic functions of the diseased or damaged nervous system.^[4,6] There are several neuronal prostheses used on a large scale, such as cochlear implants, deep brain stimulators, and a variety of peripheral nerve stimulators for treating inflammatory disorders and chronic pain.^[7] At present, the scope of new applications of bioelectronic medicine is expanding at a rapid pace.^[8] Despite the diversity of application, all neuromodulation devices comprise a controllable power supply, pulse generator, electrodes in contact with the tissue, and interconnecting wires. The necessity of an implanted power supply and accompanying wiring represents a formidable obstacle, and has led many researchers to explore wireless technologies. Optical stimulation, leveraging highly mature and efficient solid-state light emitting technologies, has been one of the most promising avenues.^[9–12] The tissue transparency

window between 620–800 nm allows efficient and safe transmission of light through skin, tissue, and even bone.^[13] Optoelectronic devices, which convert light impulses into electrical signals, offer the potential of localized, wireless, and minimally invasive stimulation of cells and tissues.^[11,14] Optoelectronic

1. Introduction

Neuromodulation devices artificially regulate neural processes by delivering controlled electrical stimulation.^[1] The applications of these techniques are manifold, ranging from fundamental

Dr. M. Silverå Ejneby, Dr. L. Migliaccio, M. Gicevičius, Dr. V. Đerek, M. Jakešová, Dr. E. D. Głowacki
Laboratory of Organic Electronics
Linköping University
Bredgatan 33, 602 21 Norrköping, Sweden
E-mail: eric.glowacki@liu.se

 The ORCID identification number(s) for the author(s) of this article can be found under <https://doi.org/10.1002/admt.201900860>.

© 2020 The Authors. Published by WILEY-VCH Verlag GmbH & Co. KGaA, Weinheim. This is an open access article under the terms of the Creative Commons Attribution License, which permits use, distribution and reproduction in any medium, provided the original work is properly cited.

DOI: 10.1002/admt.201900860

Dr. M. Silverå Ejneby, Dr. L. Migliaccio, M. Gicevičius, Dr. V. Đerek, Dr. E. D. Głowacki
Wallenberg Centre for Molecular Medicine
Linköping University
SE-58185 Linköping, Sweden
Dr. M. Silverå Ejneby, Dr. F. Elinder
Department of Clinical and Experimental Medicine
Linköping University
SE-58185 Linköping, Sweden
M. Gicevičius
Faculty of Chemistry and Geosciences
Vilnius University
Naugarduko st. 24, LT-03225 Vilnius, Lithuania
Dr. E. D. Głowacki
Warsaw University of Technology
Faculty of Chemistry
00-664 Warsaw, Poland

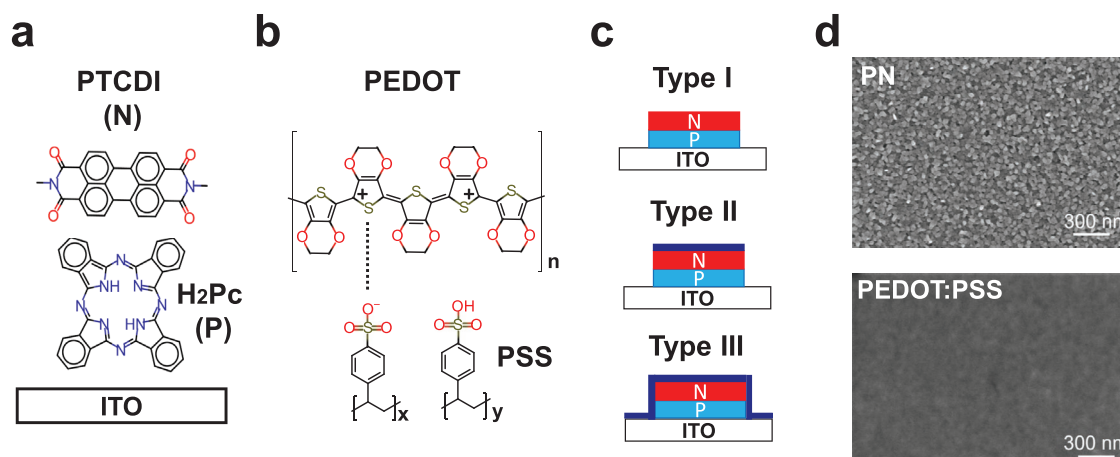


Figure 1. The OEPC device structure. a) Schematic drawing of the OEPC device, with the molecular structures of H₂Pc (light absorber and electron-donor, P) and PTCDI (electron-acceptor, N). PN layers consisting of 30 nm of each material are produced by vacuum sublimation through a shadow mask. b) Molecular structure of PEDOT:PSS. c) Schematic drawing of the three types of OEPCs devices compared in this work. The blue capping layer in Type II and III represents PEDOT:PSS coating. d) Scanning electron microscopy images of the PN surface before and after modification with PEDOT:PSS by spin-coating (5000 rpm = 55 nm thickness).

neuromodulation is of interest for biomedical applications, however it can also enable new in vitro research tools in electrophysiology^[15] that are normally too difficult on account of complex wiring.

We have recently introduced the organic electrolytic photocapacitor (OEPC) as a simple thin-film device for cellular photostimulation.^[16,17] It is fabricated from metal-free phthalocyanine (H₂Pc; p-type) and *N,N'*-dimethylperylene-3,4:9,10-tetracarboxylic diimide (PTCDI; n-type), deposited and patterned on top of a conductive back electrode. (Figure 1a,c; Type I device). The efficacy of OEPCs in neuromodulation was shown for cultured neurons and explanted retinal tissues where OEPCs stimulate direct action potentials in retinal ganglion cells of blind chick retinas.^[16] More recently, the potential of OEPCs was validated by measuring large depolarizations of the membrane potential of *Xenopus laevis* oocytes, and accompanying opening of voltage-gated channels.^[17] Advantages of the OEPC include that they are fabricated from biocompatible and nontoxic components, and are ultrathin, in the range of tens to hundreds of nanometers. The low thickness is possible because organic semiconductors can absorb deep red light efficiently. The *Xenopus laevis* oocyte model provides a robust test platform for new device concepts and for understanding the fundamentals of capacitive coupling behavior at the level of ion channel electrophysiology. Moreover, its round shape and 1 mm diameter provides a convenient model of a peripheral nerve. Peripheral nerves are one of the most important clinical neuromodulation targets.

To improve the efficiency of OEPCs, for both neuromodulation and extracellular stimulation of cells, two key parameters should be improved: electrolytic charge injection capacity and interfacial impedance. These two parameters apply generally to all stimulation electrode/microelectrode systems. To achieve these goals, in this work we turn to the conducting polymer poly(3,4-ethylenedioxythiophene):poly(styrene sulfonate) (Figure 1b, PEDOT:PSS). PEDOT:PSS belongs to the category of materials which are hybrid electronic and ionic conductors.^[18] In aqueous

environment, PEDOT:PSS swells with water, and has extremely high volumetric electrolytic capacitance.^[19] PEDOT:PSS has recently emerged as one of the highest performance electrode materials for neuromodulation, excelling in the application of flexible multielectrode recording arrays.^[20,21] The low impedance as well as stability PEDOT:PSS are key to its success.^[22] PEDOT:PSS as a modification for stimulation electrodes has been explored less than for recording, however there are indications that high capacitance and low impedance could also cause PEDOT:PSS to be a good stimulation electrode material.^[23] Herein we have explored PEDOT:PSS modification of the OEPC architecture and find that the performance of OEPCs is vastly enhanced in terms of capacitance and impedance. These conspire to increase the stimulation efficacy of OEPCs, which we benchmark using photoelectrochemical measurements, as well as single-cell electrophysiology in *Xenopus laevis* oocytes. The high capacitance afforded by PEDOT:PSS modification allows precise operation of the OEPC to act as an external capacitive voltage clamp electrode. This leads us to introduce a new concept of photovoltage clamp (without feedback circuit) for single-cell electrophysiology measurements—photovoltaic transductive extracellular potential (PVTEP) clamp.

2. Results and Discussion

2.1. Fabrication and Testing of PEDOT:PSS-Modified OEPCs

As a substrate for OEPC devices, we chose indium tin oxide (ITO) modified with octyltriethoxysilane as a hydrophobization layer which promotes good adhesion of the subsequent organic semiconducting layers. H₂Pc (30 nm, P) and PTCDI (30 nm, N) bilayers were processed by vacuum evaporation through a shadow mask (Figure 1a). This heterojunction, referred henceforth to as “PN”, is responsible for photocharge generation in the OEPC. A commercial high-conductivity formulation of PEDOT:PSS (Figure 1b) could then be spin-coated

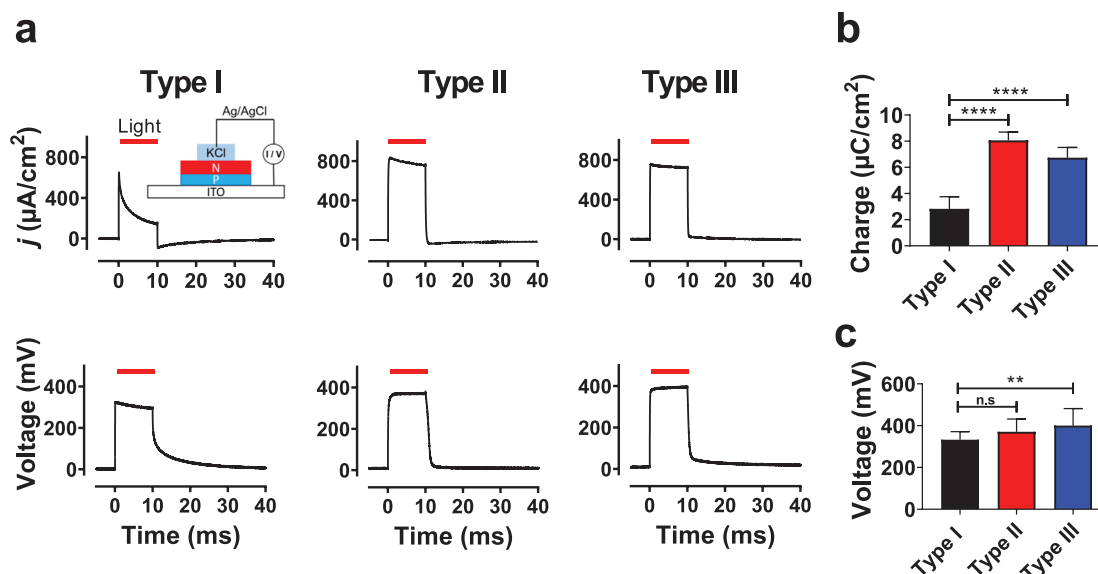


Figure 2. Electrophotoreponse (EPR) characteristics. a) EPR measurements of photocurrent density and photovoltage for Type I, II, and III devices (0.33 mW mm^{-2}). The inset shows a schematic of the EPR setup (see the Experimental Section). b) Photocharge density produced by a 10 ms light pulse. Charge density is at least two times higher for PEDOT:PSS-modified samples. **** = $p < 0.0001$. c) Maximal photovoltage. ** = $p < 0.01$. (b,c) Type I ($n = 18$), Type II ($n = 13$), Type III ($n = 18$).

on top of the device, followed by annealing. This resulted in a $55 \pm 2 \text{ nm}$ PEDOT:PSS layer, measured in the dry state. We compared three types of devices (Figure 1c): Type I – an unmodified OEPC as control, Type II – with PEDOT:PSS patterned only on top of the organic PN region, and Type III – with PEDOT:PSS covering the organic PN and surrounding ITO. To evaluate the coverage of the PEDOT:PSS on the PN layer and the morphology, we conducted scanning electron microscopy (SEM) imaging (Figure 1d). The PN layer alone has a distinctive nanocrystalline morphology, where crystallites which are tens of nanometers in size pack to form dense layers. The PEDOT:PSS, however, results in a conformal coating, which covers completely the underlying morphology, producing a smooth and defect-free coating. It should be noted that we attempted different spin speeds between 3000 and 6000 rpm, and found essentially the same performance of all these PEDOT:PSS-modified samples. Therefore, the whole study was conducted with 5000 rpm spin speed/55 nm thick PEDOT:PSS. Electropolymerization was also considered, but we found it too difficult to implement since the PN layers are photoconductors, and are highly insulating in the dark.

The performance of the OEPC devices was investigated by measuring the electrical photoresponse (EPR, schematized in Figure 2a inset). EPR gives information on the achievable photovoltage, current/charge density, and the charging/discharging dynamics of the device. EPR was performed at an irradiance of 0.33 mW mm^{-2} (Figure 2a). In EPR, voltage and current are measured between the back electrode (ITO) and an Ag/AgCl electrode immersed in 0.1 M KCl electrolyte, which is confined to a defined area above the device. For Type I devices, the photocharge density was $2.8 \pm 0.2 \mu\text{C cm}^{-2}$ (using a 10 ms long light pulse), and the maximal photovoltage was $333 \pm 10 \text{ mV}$ ($n = 18$) (Figure 2b,c). The introduction of PEDOT:PSS into the structure of organic electrolytic photocapacitor device resulted

in an increased photocharge density for Type II and III devices, and photovoltage for Type III devices (Figure 2b,c). The charge density and maximal photovoltage for Type II and III devices, respectively, were $8.1 \pm 0.2 \mu\text{C cm}^{-2}$ and $371 \pm 17 \text{ mV}$ ($n = 13$), and $6.7 \pm 0.2 \mu\text{C cm}^{-2}$ and $400 \pm 19 \text{ mV}$ ($n = 18$). The remarkable increase in current can be attributed to the electrolytic capacitance of PEDOT:PSS. The electrolytic capacitance of PEDOT:PSS is known to be outstanding, and due to its 3D hydrogel network, PEDOT:PSS has been referred to as a “volumetric capacitor”. The increased interfacial capacitance afforded by PEDOT:PSS manifests itself also in the charging dynamics. A Type I device charging current peaks within tens of microseconds and then rapidly declines. For Type II and III devices, over a 10 ms light pulse, a persistent photocharging current is measured. Based on the transient charging behavior shown in Figure 2a, one can conclude that the PEDOT significantly increases (pseudo)capacitance as over 10 ms the charging current is essentially a plateau. An additional distinction is the lack of the anodic discharge peak apparent in Type I devices when illumination is turned off. This must be rationalized based on the actual electrochemical reactions taking place in this system: In a normal OEPC, negative charge carriers accumulate in the PTCDI layer at the interface with water, where corresponding cations create an electrolytic double layer. When light is turned off, these electrons in PTCDI recombine with holes in the PN junction, resulting in the anodic discharge peak. Due to slow recombination kinetics in the PN junction, as previously established, this anodic peak has slower kinetics than the cathodic rising current.^[16] Upon modification of the OEPC with PEDOT:PSS, the behavior at the PTCDI/PEDOT interface is different. PEDOT:PSS is p-doped under normal conditions. During illumination, photogenerated electrons are presumably injected from PTCDI into the PEDOT layer, resulting in reduction of p-doped PEDOT to PEDOT⁽⁰⁾. The capacity of

PEDOT:PSS to accommodate this reaction is indeed high, and over the course of the light pulse clearly current is injected at a nearly constant value. When light is turned off, however, there is no injection of charge carriers from the PEDOT⁽⁰⁾ back into the PTCDI. For this reason, no anodic peak in EPR is visible. We hypothesize that the critical aspect in restoring and preserving the PEDOT:PSS function in such OEPCs is the presence of O₂, which will serve to oxidize the unstable PEDOT⁽⁰⁾ back to PEDOT⁺. It should further be noted that PEDOT:PSS on ITO itself does not show any photoeffects, as can be expected based on the fact that PEDOT:PSS is a degenerately doped semiconducting system.

Frequency-dependent electrochemical impedance response of illuminated organic electrolytic photocapacitor devices modified with PEDOT:PSS was registered in 0.1 M KCl solution at closed-circuit conditions versus a low-impedance, large-surface area Pt counterelectrode. In the dark, the PN layer is highly insulating, and PEDOT does not impact impedance. However, in illuminated devices, a clear difference is present. It is evident from electrochemical impedance spectra of PN and PN/PEDOT:PSS devices given in **Figure 3** that at low frequencies (1 Hz) conducting polymer-modified devices exhibit electrochemical impedance that is ten times lower than that of unmodified devices. These findings align well with studies of PEDOT:PSS-modified recording and stimulation electrodes, where similar trends have been reported.^[23–25] The increase in the interfacial capacitance and associated impedance drop have been ascribed to the volumetric capacitance effect of PEDOT:PSS formulations, recently elaborated by Proctor et al.^[19]

2.2. Photoinduced Membrane Potential Modulation and Ion Channel Opening

2.2.1. Intracellular Transient Voltage (V_T) Changes

We have previously described *Xenopus laevis* oocytes as a useful model for studying stimulation with extracellular OEPCs. Briefly, an oocyte is placed on top of an OEPC device (13 mm ϕ), surrounded by electrolyte, and irradiation by 660 nm light pulses is delivered from below (**Figure 4a**). The stimulation performance of OEPCs can be characterized using voltage-follower and voltage-clamp techniques. This allows quantification of intracellular transient voltage changes (V_T) and validation of effective photostimulation by measuring the activation of ion channels. Since Type II and III devices have a higher charge density and higher capacitance, we hypothesized that these modified OEPCs will generate larger changes in the membrane potential of *Xenopus laevis* oocytes, and/or have longer-lasting effects when compared with Type I controls.

In the first set of measurements, we characterized OEPC effects on uninjected oocytes. These cells express very few endogenous ion channels and the effect of OEPC devices on membrane potential can then be evaluated without interference from ion channel opening/closing. Intracellular transient voltage changes (V_T), measured from Type I, II, and III devices, during a light pulse of 10 ms (6 mW mm⁻², 660 nm) are shown in **Figure 4b**. The potential difference is measured between the

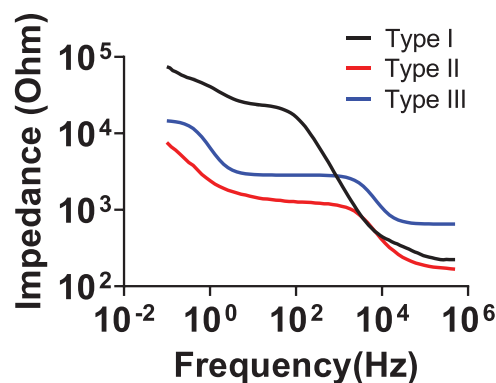


Figure 3. Electrochemical impedance of illuminated Type I, II, and III devices, measured under short-circuit conditions. These conditions mimic true operating conditions of the device. PEDOT:PSS leads to lowering of interfacial impedance in OEPC devices. Type III devices, which have PEDOT:PSS also on the ITO back contact, are measured to have higher impedance than Type II. This effect is due to the fact that the probe tip employed in the measurements to contact the device contacts ITO/PEDOT in the case of Type III, resulting in an additional in-series resistance.

voltage electrode (at the upper intracellular region of the oocyte) and a distant reference electrode (**Figure 4a**). As described in our previous paper,^[17] the measured V_T does not correspond, in magnitude or sign, to the membrane voltage, V_M , of the oocyte since the effect on the membrane voltage is dependent on the distance from the OEPC device, not the reference electrode. However, this cathodic transient voltage at the beginning of the light pulse (**Figure 4b**) is characteristic of OEPC devices, and as previously reported, this phase of the pulse leads to light-induced membrane depolarization. The depolarization is strongest at the interface of the bottom part of the oocyte where it contacts the surface of the OEPC.^[17] An increased V_T correlates to an increased membrane depolarization, and the interplay of V_M and V_T are further discussed in Section 2.2.2. Both Type II and Type III devices increased the magnitude of the V_T at the maximal light intensity (6 mW mm⁻², 660 nm) from 116 ± 15 mV (Type I devices, $n = 4$), to 217 ± 10 mV (Type II devices, $n = 4$) and 280 ± 15 mV (Type III devices, $n = 5$). The maximum V_T as a function of light intensity for all three types of devices is plotted in **Figure 4c**. Type III devices overall performed better than Type II devices. At maximum light intensity, where one can assume that photogeneration is not a limiting factor, the magnitude of V_T increased by a factor of 2 for PEDOT:PSS-modified devices. This corresponds well with findings from EPR measurements, where charge density of PEDOT:PSS-modified devices was at least twice as high as Type I devices.

Aside from the obvious increasing V_T with PEDOT:PSS, the devices with PEDOT:PSS (Type II and Type III devices) also had longer-lasting effects on the membrane potential (**Figure 4b,d,e**). At the maximal light intensity (6 mW mm⁻², 660 nm), a Type I control device induces a V_T which decays within 3 ms. Type II devices decay over 20 ms, while Type III holds a transient potential over 200–300 ms (**Figure 4d,e**). When the light intensity was lowered (0.6 mW mm⁻²) the V_T lasted even longer (**Figure 4e**). Lower light intensity corresponds to slower charging of the OEPC structure due to lower

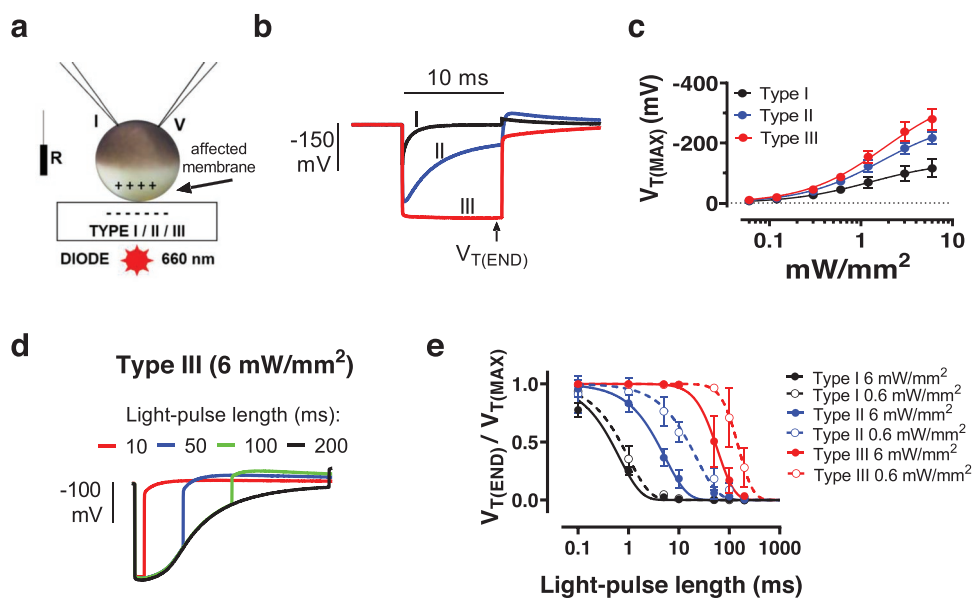


Figure 4. Intracellular transient voltage changes (V_T) in uninjected *Xenopus laevis* oocytes. a) Schematics of the OPEC/oocyte experiment. The oocyte is placed on top of an OEPC device, surrounded by electrolyte, and irradiation by 660 nm light pulses is delivered from below. The OEPC produces a transient perturbation in the potential, V_T , which is registered using a voltage-follower intracellular electrode (V) versus a reference electrode (R), placed in extracellular solution far away from the OEPC. b) V_T during a 10 ms light pulse (6 mW mm^{-2} , 660 nm) for Type I, II, and III devices. c) Maximal V_T at different light intensities. Mean \pm SEM ($n = 4-5$). Maximal V_T and $I_{(1/2)}$ (Equation (1)) were $-140 \pm 12 \text{ mV}$ and $1.3 \pm 0.3 \text{ mW mm}^{-2}$ (Type I), $-281 \pm 12 \text{ mV}$, and $1.7 \pm 0.2 \text{ mW mm}^{-2}$ (Type II), $-372 \pm 18 \text{ mV}$ and $1.8 \pm 0.3 \text{ mW mm}^{-2}$ (Type III). d) Change in V_T for a Type III device using different light-pulse lengths. e) Relative V_T at the end of the light-pulse, at different light-pulse lengths, and light intensities (6 and 0.6 mW mm^{-2}). Data fitted with Equation (2). (Type I and II, $n = 1$, Type III 6 mW mm^{-2} $n = 2.3$, Type III 0.6 mW mm^{-2} , $n = 3.8$). Mean \pm SEM, $n = 4$.

photogeneration of carriers. While the OEPC charges, there is a persistent displacement current in surrounding solution, resulting in a constant depolarizing transductive potential felt across the cell membrane. By dramatically increasing the capacitance of an OEPC using PEDOT:PSS, it is therefore possible to create a photoelectrode that can shift extracellular potential locally over long periods, thereby also extending the duration of effective membrane depolarization (Figure 4e). Taken together, the introduction of the conducting polymer PEDOT:PSS into the structure of the OEPC resulted in larger and long-lasting transient voltage effects on the membrane potential of *Xenopus laevis* oocytes.

2.2.2. Photovoltage Clamp Using an OEPC–Potassium Channel Opening

Given that Type III devices can afford a large and controllable perturbation of the membrane potential for relatively long periods of time (10+ ms), we tested if Type III devices could mimic the effect of a voltage clamp, in a way that you can shift the holding voltage by adjusting the light intensity. To test this, we first verified if Type III devices could depolarize the membrane sufficiently to trigger opening of the 3R Shaker K_V channel. We used the 3R mutant instead of wild-type since the 3R channel opens at more positive potentials from the resting potential. This allows us to use a higher light intensity range. The measured magnitude of V_T in 3R channel-expressing oocytes was 25% lower compared to uninjected oocytes, possibly due to the current leakage when ion

channels open (Figure 5a). Nevertheless, the Type III devices had a long-lasting effect on the membrane potential (10+ ms), and there was no obvious effect on the light intensity dependence (Figure 5a). This confirms that channel-expressing oocytes respond similarly to the external OEPC as the uninjected oocytes. Knowing that the OEPC is delivering V_T in a similar way, we could move on to voltage-clamp tests to measure ion currents through the 3R K_V channels. During a voltage-clamp step protocol we applied 10 ms light pulses to the OEPC (0.3 mW mm^{-2} , 660 nm). Clearly, the Type III device depolarized the oocyte and increased the K^+ current (Figure 5b). The shift of the conductance versus voltage ($G(V)$) curve was $-26 \pm 3 \text{ mV}$ ($n = 4$) and $-62 \pm 7 \text{ mV}$ ($n = 3$), at a light-intensity of 0.3 and 0.6 mW mm^{-2} , respectively (Figure 5c,d). The device-induced $G(V)$ shift equaled around 65% of the V_T measured for uninjected oocytes discussed in Section 2.2.1 (Figure 5d).

Given this observation, we postulated that the light-intensity could be swept in order to produce a result analogous to a current–voltage curve. To test this, we conducted voltage-clamp measurements of oocytes expressing 3R Shaker K_V channels while holding the potential of the voltage clamp electrode constant (-100 mV) and sweeping the light intensity incident on the OEPC from 0.12 up to 3 mW mm^{-2} . K^+ currents measured from an oocyte during this photovoltage-clamp, compared with a conventional voltage-clamp protocol, are shown in Figure 5e. It is evident that a light-intensity sweep produced a result closely mimicking a conventional voltage-clamp protocol. However, the membrane potential around the oocyte during the “photovoltage-clamp” is likely not uniform, since a relatively larger membrane depolarization is expected at the OEPC/oocyte

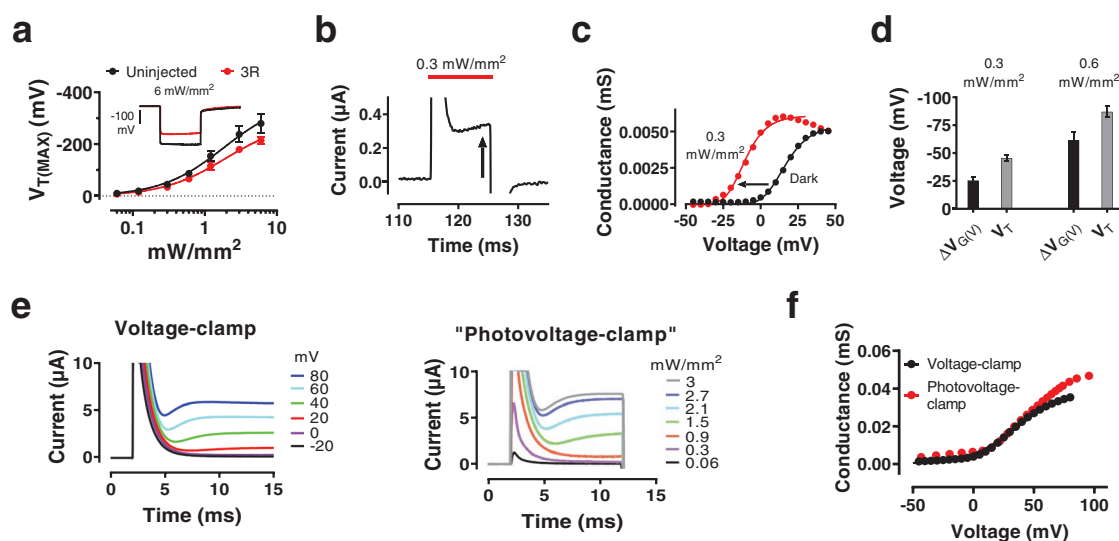


Figure 5. Type III devices used as an external photovoltage-clamp electrode. a) V_T values as a function of light intensity for uninjected oocytes (black) and oocytes expressing 3R K_V channels (red). The V_T in 3R channel-expressing oocytes is consistently 75% of the value of uninjected oocytes. V_T and $I_{(1/2)}$ (Equation (1)); -372 ± 18 and 1.8 ± 0.2 mW mm^{-2} (uninjected), -286 ± 11 mV and 1.9 ± 0.2 mW mm^{-2} (3R). Mean \pm SEM, $n = 4-5$. Inset shows V_T traces during a 10 ms applied light pulse at 6 mW mm^{-2} . b) 3R Shaker K_V channel, K currents at -100 mV. Red line: light on for 10 ms (0.3 mW mm^{-2} , 660 nm). c) $G(V)$ curves in dark and light conditions. Shift = -25.4 mV. d) Device-induced $G(V)$ shift (3R Shaker K_V channel) and V_T measured from uninjected oocytes at corresponding light-intensity. e) K^+ currents from the same oocyte during a conventional voltage-clamp protocol, holding potential $V_h = -100$ mV (left), or with the photovoltage-clamp protocol (right), where V_h is left at a constant -100 mV and light intensity is swept. f) $G(V)$ curve for the 3R Shaker K_V channel using a conventional voltage-clamp protocol, and estimated $G(V)$ curve (using Equation (3), see the Experimental Section) for the photovoltage-clamp protocol.

interface.^[17] A rough quantification of the average membrane potential for the whole oocyte, at a given light intensity, was calculated by estimating the average membrane depolarization to 65% of the measured V_T , from a holding potential of -100 mV, according to Equation (3) (see the Experimental Section). With this estimation a $G(V)$ curve could be plotted for the photovoltage-clamp protocol, together with a conventional voltage-clamp $G(V)$ curve (Figure 5f). There was no significant increase in the maximal conductance using the photovoltage clamp protocol estimation, and $\Delta V_{1/2}$ varied with ± 20 mV for the tested oocytes, compared to conventional voltage clamp $G(V)$ curves.

2.3. Stability of OEPC Devices—Accelerated Aging Test

Long-term stability is important for a number of potential applications of OEPCs, and establishing in vitro robustness is a prerequisite for moving forward with potential chronic implant devices. We conducted aging tests on Type I, II, and III devices by storing them in electrolyte solution 0.1 KCl and periodically measuring EPR over the course of 50 days. One group of devices was kept in the dark at room temperature, while the second was heated at 40°C and subjected to a light pulse stress of continuous charge/discharge cycles (a total of 8 million cycles over 50 days). The results for EPR currents and voltages are shown in Figure 6. It can be said that generally over time all devices give a decrease in performance parameters of voltage and current. Of Type I and Type II devices, not a single device failed, and all retain performance with current and voltage always more than half of the original value. Overall, Type II devices gave the best stability, superior to Type I controls. Type III

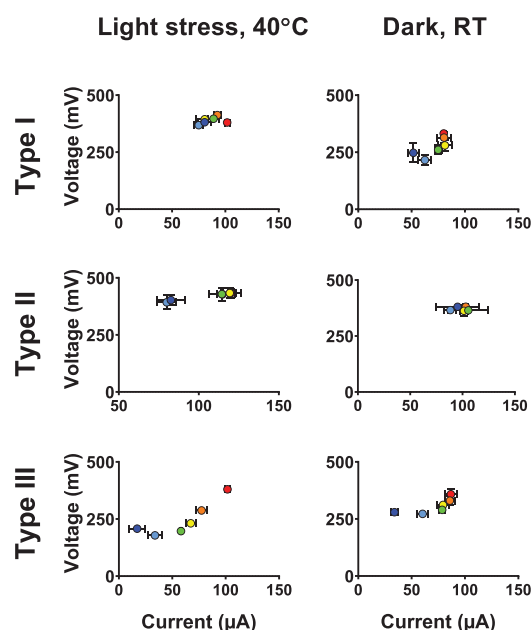


Figure 6. Stability of PEDOT:PSS-modified OEPC devices over 50 days in terms of EPR photovoltage (y -axes) and photocurrent (x -axes). Data on the left are from an accelerated ageing test in 0.1 m KCl, at 40°C , under constant light-pulse stress (628 nm , 20 ms light pulses, 550 ms period = total of 8 million charge/discharge cycles over 50 days); data on right are for samples stored in 0.1 m KCl in the dark at room temperature. All devices show gradual drop in EPR performance in terms of photovoltage and current, though no devices show complete failure. The best performance stability was shown by Type II devices. Type III devices suffered from delamination of PEDOT:PSS from the ITO, clearly visible regardless of whether the samples were stressed or kept in dark at room temperature.

devices suffered from more substantial stability problems after two weeks. Interestingly, both light-stressed and devices kept in dark showed almost the same decline. Visual inspection as well as SEM investigation elucidates that the problem is delamination of the PEDOT:PSS from the ITO layer, and random redeposition of pieces of the delaminated film across the sample. PEDOT:PSS is also known, due to its locally acidic nature, to etch ITO. From this it can be concluded that PEDOT:PSS on the PN itself appears to be stable, and does not affect the device stability appreciably one way or the other. The adhesion and interface of PEDOT:PSS on ITO in such devices is a problematic point and in the future this combination should be avoided. It should also be stated that this test is primarily designed to establish stability under the stress of continuous operation in the form of charge–discharge cycles, nevertheless stability in an actual physiological environment may differ considerably due to adsorption of proteins or other factors. Future success of this device technology approach must hinge on stability assessment using *in vitro* or *in vivo* tests.

3. Conclusions

Here we report a strategy to significantly enhance the photostimulation performance OEPC devices by coating with PEDOT:PSS. The PEDOT:PSS modification enhances the performance of the OEPC device by increasing the charge density delivered by the electrode, due to increase in device capacitance, while simultaneously decreasing the impedance. Using *Xenopus laevis* oocytes at least a twofold increase in the stimulation efficacy of the PEDOT:PSS coated devices can be seen. The large capacitance of PEDOT:PSS allowed the OEPCs to depolarize the oocyte for a longer period of time (10+ ms). In turn, Type III devices could be used as a unique type of external, wireless, photovoltage-clamp, analogous to conventional voltage-clamp. It can mimic the effect of a voltage clamp, in a way that you can shift the holding voltage by adjusting the light intensity. As a general name for this concept, we would define it as PVTEP clamp. PVTEP can be used to wirelessly manipulate the membrane potential of adjacent cells for applications in electrophysiological research. An accompanying wireless readout of membrane currents would afford a fully wireless electrophysiology platform. PN PEDOT:PSS-coated OEPCs (Type II devices) can remain stable after a 50 days ageing test with 8 million charge/discharge cycles. These results suggest the elaboration of OEPCs for novel electrophysiology measurement tools, and also pave the way for OEPC use in wireless *in vivo* neuromodulation applications, like peripheral nerve stimulation. The current level of efficiency of OEPCs at the millimeter scale demonstrates that such photoelectrodes can operate on-par with similar-sized wired electrodes as are used for *in vivo* stimulation. Due to their size they do not operate at a highly localized cellular level such as some emerging nanoscale-based photostimulation approaches.^[26] However, they operate at orders-of-magnitude lower light intensity than those cellular-level stimulation devices. Intensities of several mW mm⁻² can easily and safely be transmitted through even ten to twenty mm of tissue or bone.^[13] With continued optimization of photovoltage while keeping the electrolytic

impedance low by employing methods like PEDOT:PSS modification, OEPC platforms can shrink further to also perform neurostimulation in a highly localized manner.

4. Experimental Section

Materials: Phthalocyanine H₂Pc (Alfa Aesar) and *N,N'*-dimethyl-3,4,9,10-perylenetetracarboxylic diimide, PTCDI (BASF) were purified by threefold temperature-gradient sublimation. For the preparation of the PEDOT:PSS films, 20 mL of aqueous dispersion (CLEVIOS PH 1000) was mixed with 1 wt% of dimethyl sulfoxide, and 2 wt% of 3-glycidioxypropyltrimethoxysilane (as a crosslinker), and the resulting dispersion was spin-coated. ITO-coated glass (Kintec) 15–20 Ohm sq⁻¹ was used as a substrate. The ITO area under the organic layers of H₂Pc/PTCDI was modified with *n*-octyltriethoxysilane (Alfa Aesar).

Device Fabrication: 1 × 1 in. square ITO slides were cleaned by consecutive ultrasonication for 5 min in acetone, 2-propanol, and 2% Hellmanex III cleaning solution. The substrates were then rinsed with DI water and dried under a N₂ stream. The solvent cleaning was followed by 5 min O₂ plasma treatment (100 W) and coating the surface of the ITO with a monolayer of *n*-octyltriethoxysilane (OTS) by placing the samples in an OTS-vapor saturated chamber heated to 80 °C for 1 h. This improves the adhesion of organic PN layers to the ITO substrate. Excess of physioadsorbed OTS was removed by sonicating the samples in acetone for 5 min followed by rinsing twice with DI water and drying under N₂ stream. The organic pigment layers were formed by thermal evaporation deposition through a shadow mask at a base pressure of <2 × 10⁻⁶ Torr using a rate of 0.1–0.5 nm s⁻¹. 30 nm of P-type H₂Pc and 30 nm of N-type PTCDI were successively deposited resulting in the organic device (PN) of 60 nm thickness. The PN pixel was a 13 mm diameter circle in the center of the substrate. The modification of PN devices with PEDOT:PSS was performed by spin-coating at 5000 rpm at 1000 rpm s⁻¹ acceleration for 60 s to obtain a well-adhered PEDOT:PSS coating (55 nm ± 2 nm, measured using scanning stylus profilometry). The films were subsequently baked at 140 °C for 1 h and were immersed in 0.1 M KCl to remove any excess low-molecular weight compounds as well as to allow the PEDOT:PSS to take up water and swell. All samples were then stored in 0.1 M KCl for 20 h before further use.

Electrophotoreponse EPR: Measurements of photovoltage and charging current of OEPC devices was performed according to previously described methods.^[17] Briefly, the backside ITO of the OEPC was contacted with a probe electrode connected to the positive terminal of an oscilloscope. Meanwhile, the negative terminal was connected to an Ag/AgCl electrode in 0.1 M KCl electrolyte, making contact to the top of the organic layer of the OEPC device. An LED (630 nm) with intensity of 0.33 mW mm⁻² was used.

Impedance Measurements: Impedance measurements of OEPCs were carried out in 0.1 M KCl in the frequency range 500 kHz to 0.1 Hz, using a BioLogic SP-300 Bipotentiostat. Two-electrode configuration was exploited for this characterization measuring in short-circuit condition at 0 V working electrode versus counterelectrode. Short-circuit condition was realized shorting the reference electrode (Ag/AgCl) to the counterelectrode (large surface area Pt electrode) and measuring at 0 V working electrode versus counterelectrode. Impedance was measured during illumination (630 nm, 33 mW cm⁻²).

Electrophysiology: Oocyte (*Xenopus laevis*) preparation, storage, and RNA injection were done as described previously.^[27,28] Animal experiments were approved by the local Animal Care and Use Committee at Linköping University. The 3R Shaker K_v channel, a modified wt Shaker K_v channel (M356R/A359R) with removed N-type inactivation, was used throughout the study.^[29] The 3R Shaker K_v channel opens at more positive membrane voltages compared to wt Shaker K_v channel (V_{1/2} = -21 mV (wt), V_{1/2} = 25 mV 3R.^[30] Therefore, higher light intensities could be used with the 3R. Electrophysiological measurements were done 1–4 days after RNA injection, or 1 day after oocyte harvesting from uninjected oocytes. The measurements were

performed with a GeneClamp 500B amplifier (Axon Instruments), pClamp 10 software (Molecular Devices) and a Digidata 1440A converter (Molecular Devices), as described previously.^[17] For K currents, the amplifier leak compensation was used. The extracellular bath solution contained (in mM): 88 NaCl, 1 KCl, 15 HEPES, 0.4 CaCl₂, and 0.8 MgCl₂, pH was set to 7.4 with NaOH (all chemicals purchased from Sigma-Aldrich). All recordings were done in room temperature (20–23 °C). Briefly, the OEPC device was placed centrally above a light-emitting diode (660 nm, Thorlabs, 0.06–6 mW mm⁻², operated with a high-power LED Driver, DC2200 Thorlabs), in a petri dish filled with extracellular bath solution, and the oocyte in the middle, on top, of the OEPC PN pixel (see Figure 4a). All PEDOT:PSS-modified OEPC devices were stored in 0.1 M KCl for at least 2 days prior to measurements and washed with deionized water before being placed into the petri dish filled with extracellular bath solution.

Data Analysis: The transient voltage, V_T , is defined as the voltage change between resting membrane potential (dark conditions) and the intracellular potential during the light pulse. Potential is always relative to a distant reference electrode. To quantify the light-intensity dependence for the maximal V_T the following equation was used

$$V_{T(\text{MAX})} = A / (1 + I_{1/2} / I) \quad (1)$$

where A is amplitude of the curve, I is the light intensity and $I_{1/2}$ is the light intensity as which half-maximal response occurs.

For fitting the relative V_T change at the end of a light-pulse with increasing light-pulse length, a single-phase exponential decay curve was used

$$V_{T(\text{END})} / V_{T(\text{MAX})} = 1 - (1 - \exp(-t/\tau))^n \quad (2)$$

where $V_{T(\text{END})} / V_{T(\text{MAX})}$ is the relative V_T at the end of a light-pulse, t is the light-pulse length, and τ is the time constant (in ms), and n is an exponent for better curve fitting due to the sigmoidal shape of the V_T decay for Type III devices. For Type I and II devices, on the other hand, n is set to 1.

When the photovoltage-clamp protocol was used, the holding potential was set to -100 mV, and the light-intensity was increased in 0.12 mW mm⁻² steps up to 3 mW mm⁻² (to avoid excessive depolarization and opening of endogenous ion channels). The average membrane potential of the whole oocyte, at each light intensity ($V_{m(\text{light})}$) was then estimated accordingly

$$V_{m(\text{light})} = f * \left(V_h - \left(A / (1 + I_{(1/2)} / I) \right) \right) \quad (3)$$

where f is the relative ratio of membrane depolarization compared to the V_T measured for uninjected oocytes (estimated to 0.65, Figure 5c), V_h is the holding potential (set to -100 mV), A is the amplitude in the V_T versus light intensity curve (-371.7 , Type III Figure 4c), I is the light intensity and $I_{(1/2)}$ is the light-intensity at which half-maximal response occurs (1.818 , Type III Figure 4c).

The K conductance was calculated as

$$G_K(V) = I_K / (V_m - V_K) \quad (4)$$

where I_K is the steady-state current in dark, or in the end of a 10 ms light-pulse (the ionic current during a light-pulse was corrected for the light-induced capacitive current as described previously,^[17] V_m the absolute membrane potential (or estimated membrane potential using the photovoltage-clamp protocol, Equation (3)), and V_K the reversal potential (set to -100 mV). The data were then fitted to a modified Boltzmann curve

$$G_K(V) = A / \left(1 + \exp\left(\frac{(V_{1/2} - V)}{s} \right) \right)^n \quad (5)$$

where A is the amplitude of the curve, $V_{1/2}$ is the midpoint when $n = 1$, s is the slope, and n is an exponent for better curve fitting (set to 4).

Statistics: Average values are expressed as means \pm SEM. When comparing device-induced responses a two-tailed unpaired t -test was used. A two-tailed one-sample t -test (mean value set to a hypothetical value of 1) was used to analyze changes in the maximal conductance. $P < 0.05$ was considered significant.

Acknowledgements

The authors gratefully acknowledge the financial support from the Knut and Alice Wallenberg Foundation within the framework of the Wallenberg Centre for Molecular Medicine at Linköping University, the Swedish Research Council (Vetenskapsrådet, 2018–04505), and the Swedish Foundation for Strategic Research (SSF).

Conflict of Interest

The authors declare no conflict of interest.

Keywords

cellular photostimulation, electrophysiology, organic bioelectronics, organic photovoltaics, PEDOT:PSS

Received: September 30, 2019

Revised: November 22, 2019

Published online:

- [1] *Neuromodulation* (Eds: E. S. Krames, P. H. Peckham, A. R. Rezai), Academic Press, London **2009**.
- [2] I. Willner, E. Katz, *Bioelectronics*, Wiley-VCH, Weinheim, Germany **2005**.
- [3] *Implantable Bioelectronics* (Ed: E. Katz), Wiley-VCH, Weinheim, Germany **2014**.
- [4] *Handbook of Bioelectronics* (Eds: S. Carrara, K. Iniewski), Cambridge University Press, Cambridge **2015**.
- [5] L. Ferlauto, M. Jole, I. Airaghi, N. Aurelia, L. Chenais, S. Charles, A. Gilliéron, P. Vagni, M. Bevilacqua, T. J. Wolfensberger, K. Sivula, D. Ghezzi, *Nat. Commun.* **2018**, *9*, 992.
- [6] H. Acarón Ledesma, X. Li, J. L. Carvalho-de-Souza, W. Wei, F. Bezanilla, B. Tian, *Nat. Nanotechnol.* **2019**, *14*, 645.
- [7] A. S. Caravaca, A. L. Gallina, L. Tarnawski, K. J. Tracey, V. A. Pavlov, Y. A. Levine, P. S. Olofsson, O. David, E. K. Ross, K. J. Otto, *Front. Neurosci.* **2019**, *13*, 877.
- [8] K. Birmingham, V. Gradinaru, P. Anikeeva, W. M. Grill, V. Pikov, B. McLaughlin, P. Pasricha, D. Weber, K. Ludwig, *Nat. Publ. Gr.* **2014**, *13*, 399.
- [9] M. Scanziani, M. Häusser, *Nature* **2009**, *461*, 930.
- [10] A. Canales, S. Park, A. Kiliyas, P. Anikeeva, *Acc. Chem. Res.* **2018**, *51*, 829.
- [11] J. F. Zimmerman, B. Tian, *ACS Nano* **2018**, *12*, 4086.
- [12] Y. Jiang, R. Parameswaran, X. Li, J. L. Carvalho-de-Souza, X. Gao, L. Meng, F. Bezanilla, G. M. G. Shepherd, B. Tian, *Nat. Protoc.* **2019**, *14*, 1339.
- [13] S. L. Jacques, *Phys. Med. Biol.* **2013**, *58*, 5007.
- [14] M. Sytnyk, M. Jakešová, M. Litviňuková, O. Mashkov, D. Kriegner, J. Stangl, J. Nebesářová, F. W. Fecher, W. Schöfberger, N. S. Sariciftci, R. Schindl, W. Heiss, E. D. Glowacki, *Nat. Commun.* **2017**, *8*, 91.
- [15] Y. Jiang, B. Tian, *Nat. Rev. Mater.* **2018**, *3*, 473.

- [16] D. Rand, M. Jakešová, G. Lubin, I. Vebráite, M. David-Pur, V. Ďerek, T. Cramer, N. S. Sariciftci, Y. Hanein, E. D. Głowacki, *Adv. Mater.* **2018**, *30*, 1707292.
- [17] M. Jakešová, M. S. Ejneby, V. Ďerek, T. Schmidt, M. Gryszel, J. Brask, R. Schindl, D. T. Simon, M. Berggren, F. Elinder, E. D. Głowacki, *Sci. Adv.* **2019**, *5*, eaav5265.
- [18] B. D. Paulsen, K. Tybrandt, E. Stavrinidou, J. Rivnay, *Nat. Mater.* **2019**, *19*, 13.
- [19] C. M. Proctor, J. Rivnay, G. G. Malliaras, *J. Polym. Sci., Part B: Polym. Phys.* **2016**, *54*, 1433.
- [20] M. Sessolo, D. Khodagholy, J. Rivnay, F. Maddalena, M. Gleyzes, E. Steidl, B. Buisson, G. G. Malliaras, *Adv. Mater.* **2013**, *25*, 2135.
- [21] D. Khodagholy, J. N. Gelinás, Z. Zhao, M. Yeh, M. Long, J. D. Greenlee, W. Doyle, O. Devinsky, G. Buzsáki, *Sci. Adv.* **2016**, *2*, e1601027.
- [22] S. Inal, J. Rivnay, A. O. Suiu, G. G. Malliaras, I. McCulloch, *Acc. Chem. Res.* **2018**, *51*, 1368.
- [23] R. A. Green, P. B. Matteucci, R. T. Hassarati, B. Giraud, C. W. D. Dodds, S. Chen, P. J. Byrnes-Preston, G. J. Suaning, L. A. Poole-Warren, N. H. Lovell, *J. Neural Eng.* **2013**, *10*, 016009.
- [24] D. Khodagholy, T. Doublet, M. Gurfinkel, P. Quilichini, E. Ismailova, P. Leleux, T. Herve, S. Sanaur, C. Bernard, G. G. Malliaras, *Adv. Mater.* **2011**, *23*, H268.
- [25] A. Schander, T. Teßmann, S. Strokov, H. Stemmann, A. K. Kreiter, W. Lang, *Conf. Proc. of the IEEE Engineering in Medicine and Biology Society*, IEEE, Sweden **2016**, p. 6174.
- [26] R. Parameswaran, J. L. Carvalho-De-Souza, Y. Jiang, M. J. Burke, J. F. Zimmerman, K. Koehler, A. W. Phillips, J. Yi, E. J. Adams, F. Bezanilla, B. Tian, *Nat. Nanotechnol.* **2018**, *13*, 260.
- [27] S. I. Börjesson, T. Parkkari, S. Hammarström, F. Elinder, *Biophys. J.* **2010**, *98*, 396.
- [28] N. E. Ottosson, X. Wu, A. Nolting, U. Karlsson, P.-E. Lund, K. Ruda, S. Svensson, P. Konradsson, F. Elinder, *Sci. Rep.* **2015**, *5*, 13278.
- [29] N. E. Ottosson, S. I. Liin, F. Elinder, *J. Gen. Physiol.* **2014**, *143*, 173.
- [30] M. Silverå-Ejneby, X. Wu, N. E. Ottosson, E. P. Mürger, I. Lundström, P. Konradsson, F. Elinder, *J. Gen. Physiol.* **2018**, *150*, 731.



Untangling Photofaradaic and Photocapacitive Effects in Organic Optoelectronic Stimulation Devices

Vedran Đerek^{1,2,3,4}, David Rand⁵, Ludovico Migliaccio^{1,2}, Yael Hanein⁵ and Eric Daniel Glowacki^{1,2,6*}

¹ Laboratory of Organic Electronics, Campus Norrköping, Linköping University, Norrköping, Sweden, ² Wallenberg Centre for Molecular Medicine, Linköping University, Linköping, Sweden, ³ Department of Physics, Faculty of Science, University of Zagreb, Zagreb, Croatia, ⁴ Center of Excellence for Advanced Materials and Sensing Devices, Ruđer Bošković Institute, Zagreb, Croatia, ⁵ Tel Aviv University Center for Nanoscience and Nanotechnology, School of Electrical Engineering Tel Aviv University, Tel Aviv, Israel, ⁶ Faculty of Chemistry, Warsaw University of Technology, Warsaw, Poland

OPEN ACCESS

Edited by:

Maria Rosa Antognazza,
Centro per la Scienza e la Tecnologia
Nano, IIT, Italy

Reviewed by:

Fulvio Ratto,
Italian National Research Council, Italy
Michele Di Lauro,
Italian Institute of Technology (IIT), Italy

*Correspondence:

Eric Daniel Glowacki
eric.glowacki@liu.se

Specialty section:

This article was submitted to
Nanobiotechnology,
a section of the journal
Frontiers in Bioengineering and
Biotechnology

Received: 24 October 2019

Accepted: 18 March 2020

Published: 17 April 2020

Citation:

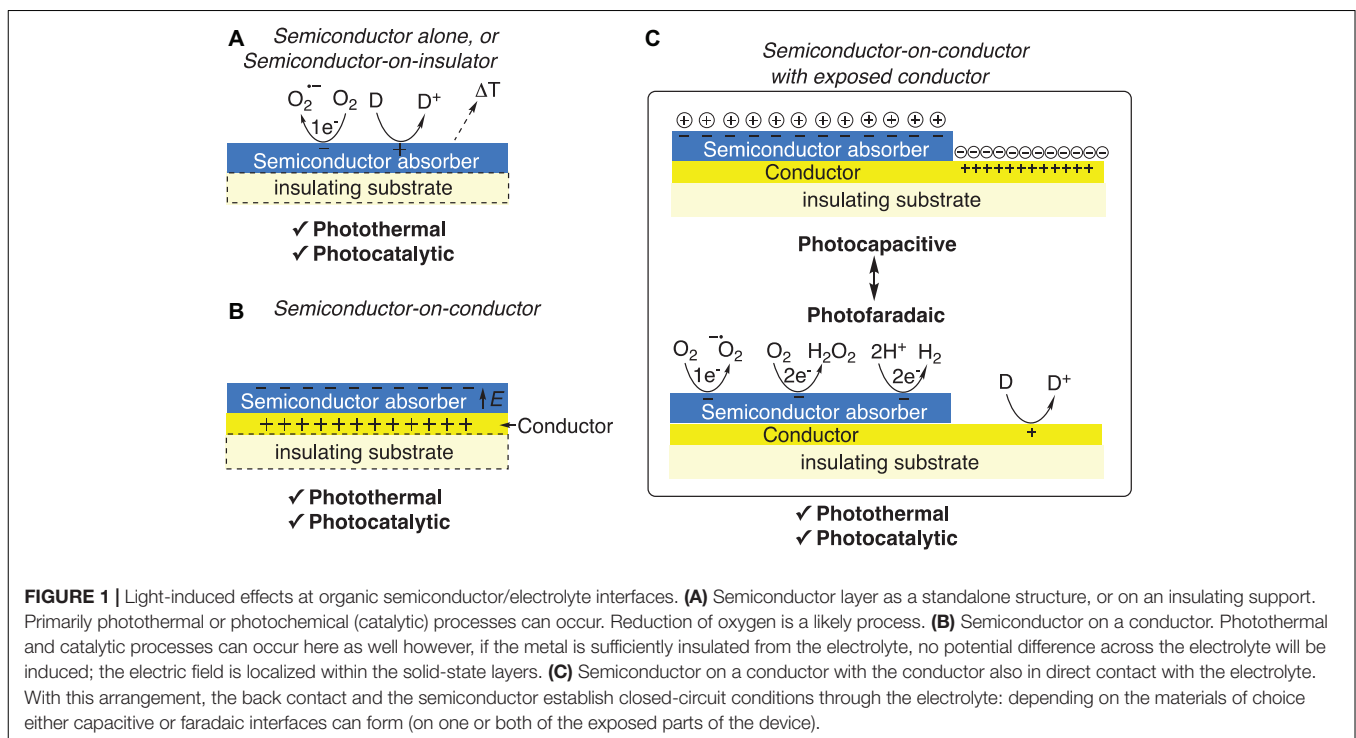
Đerek V, Rand D, Migliaccio L,
Hanein Y and Glowacki ED (2020)
Untangling Photofaradaic
and Photocapacitive Effects
in Organic Optoelectronic Stimulation
Devices.
Front. Bioeng. Biotechnol. 8:284.
doi: 10.3389/fbioe.2020.00284

Light, as a versatile and non-invasive means to elicit a physiological response, offers solutions to problems in basic research as well as in biomedical technologies. The complexity and limitations of optogenetic methods motivate research and development of optoelectronic alternatives. A recently growing subset of approaches relies on organic semiconductors as the active light absorber. Organic semiconductors stand out due to their high optical absorbance coefficients, mechanical flexibility, ability to operate in a wet environment, and potential biocompatibility. They could enable ultrathin and minimally invasive form factors not accessible with traditional inorganic materials. Organic semiconductors, upon photoexcitation in an aqueous medium, can transduce light into (1) photothermal heating, (2) photochemical/photocatalytic redox reactions, (3) photocapacitive charging of electrolytic double layers, and (4) photofaradaic reactions. In realistic conditions, different effects may coexist, and understanding their role in observed physiological phenomena is an area of critical interest. This article serves to evaluate the emerging picture of photofaradaic vs. photocapacitive effects in the context of our group's research efforts and that of others over the past few years. We present simple experiments which can be used to benchmark organic optoelectronic stimulation devices.

Keywords: bioelectronics, neurostimulation, organic electronics, photoelectrochemistry, photostimulation

INTRODUCTION

Light illumination of a semiconducting material (or heterostructure thereof) immersed in an electrolyte solution, with an energy greater than its band gap energy, can induce several different processes. What happens after light absorption depends on semiconductor material properties and heterostructure details. In **Figure 1**, we summarize a breakdown of three distinct device architectures, and the possible associated mechanisms of photophysiological coupling each can offer. In the following paragraphs, we describe these key photoeffects basing on literature examples.



Photothermal Heating Effects

Organic semiconducting materials can be highly efficient light absorbers (Lin et al., 2012). Under the right conditions, this absorbed light can be converted into heat. In photovoltaic and photodiode technologies this conversion is highly undesired and band-gap engineering is used to avoid such processes. However, photothermal heating can also produce interesting and useful effects. For illumination timescales on the order of hundreds of milliseconds to seconds, light absorption causes a rise in local temperature that may have a physiological response. Heat-sensitive ion channels, such as the TRPV-family of ion channels, can be reversibly stimulated in this way (Albert et al., 2012). Human embryonic kidney (HEK) cells transfected with TRPV1 ion channels could be locally photothermally stimulated by irradiating (tens to hundreds of milliseconds) thin films of the polymeric semiconductor poly(3-hexylthiophene), P3HT (Lodola et al., 2017). In another example, organic nano-crystalline structures made from the material quinacridone also proved to be efficient, local, photothermal heaters (Sytnyk et al., 2017). These nano-structures form close and high surface-area interfaces with cultured cells. Local photothermal heating results in higher ion currents through open channels (potassium inward rectifier) which was demonstrated in irradiated rat basophilic leukemia cells growing on quinacridone nano-structures (5 mW/mm^2 , 100–800 ms) (Sytnyk et al., 2017). Photoactivation of cation influx through TRPV1 channels in HEK cells held at resting membrane potential was also shown for quinacridone/cell interfaces ($30 \mu\text{J}$ pulses) (Sytnyk et al., 2017). With high intensities of light at short timescales below a few ms, rapid heating can trigger a completely different mechanism: the local rise in temperature transiently increases

cell membrane capacitance, generating a depolarizing current. The thermocapacitive stimulation effect was discovered and studied in detail by Shapiro, Bezanilla, and coworkers (Shapiro et al., 2012; Carvalho-de-Souza et al., 2015; Jiang et al., 2016). The magnitude of cell depolarization depends on the rate of temperature change $\Delta T/t$ (not on the absolute rise in temperature). Therefore, even though very high light intensities were used, they produced only harmless transient temperature changes. Shapiro et al. (2012) first detailed thermocapacitance for the case of NIR light around $1.5 \mu\text{m}$ wavelength, where water absorbs light and is heated directly. The thermocapacitive mechanism can be far more local and controlled when nano or microscale semiconducting particles located near a given cell can lead to selective stimulation of cells (Carvalho-de-Souza et al., 2015; Jiang et al., 2019). The effect can be achieved using a wide range of semiconductors (Zimmerman and Tian, 2018). A disadvantage of the method, however, is the necessity for powerful light sources. For chronic implants, the approach may be considered safe when short light pulses lead to low total dissipated energy. However, harnessing such high-power light intensities may prove challenging in many clinical applications.

Photochemical Reactions

The next possible phenomenon of illuminated organic semiconductors in a physiological environment is the elicitation of a photochemical reaction. Photochemical reactions are precipitated by photogenerated electrons and holes. The former lead to the reduction of suitable electron-acceptors in solution, while the latter oxidize electron-donors. Possible reducible acceptors in physiological solutions are protons,

dissolved dioxygen, or certain organic moieties such as quinone-containing molecules (Chowdhury et al., 2016). In the case of organic semiconductors (without suitable cocatalysts like Platinum), H₂ evolution has proven to be inefficient (Bellani et al., 2018), and no evidence for H₂ in a physiological context have been found. Oxygen reduction reactions, on the other hand, have been discovered to be highly favored on organic semiconductors (Bellani et al., 2015). The single-electron reduction of O₂ to superoxide (Suppes et al., 2013; Gryszel et al., 2019) or the two-electron reduction to produce hydrogen peroxide (Jakešová et al., 2016; Węclawski et al., 2017; Gryszel et al., 2018b), H₂O₂, were demonstrated to proceed efficiently for several organic semiconductors. Both oxygen reduction reactions are thermodynamically more favorable than hydrogen evolution, with the two-electron peroxide reaction being 700 mV lower than H₂ production. The dominance of the oxygen reduction reaction with organic semiconductors was shown in electrochemical (Warczak et al., 2018; Mitraka et al., 2019), photoelectrochemical (Jakešová et al., 2016; Gryszel et al., 2018a), and photochemical experiments (Gryszel et al., 2018b, 2019) for a wide range of organic semiconductors, including polythiophenes like P3HT, the biopolymer melanin (Migliaccio et al., 2018), and various carbonyl pigments (Gryszel et al., 2018a). The oxygen reduction products are considered reactive oxygen species (ROS) and have numerous physiological effects ranging from toxicity at high concentrations (Huang et al., 2013) to ion channel modulation (Gamper et al., 2006) and signaling effects (Lim et al., 2016) at low concentrations. In photochemistry involving photogenerated carriers, both electrons and holes must be consumed in order to sustain the process. In organic semiconductors, the fate of the photogenerated holes is often the critical element. Gryszel et al. have shown that various molecules can serve as sacrificial electron donors, such as oxalate, ethanol, and glucose (Gryszel et al., 2018b, 2019). In some cases where the highest occupied molecular orbital (HOMO) is sufficiently deep, oxidation of water as the donor is possible. Unfortunately, often self-oxidation of the organic semiconductor itself will serve to complete the photochemical cycle and lead to irreversible corrosion of the organic semiconductor (Gryszel et al., 2018b; Migliaccio et al., 2018). It was experimentally found that the deeper the HOMO, the more stable the semiconductor is with respect to self-oxidation. Quantifying the semiconductor oxidation degree, to benchmark the stability/degradation, is an important consideration. Gryszel et al. report a reliable method based on the redissolution of the semiconductor into a suitable solvent to obtain solutions that follow the Beer-Lambert law in UV-Vis absorbance (Gryszel et al., 2018b). It is then possible to calculate, based on the absorbance of such solutions, the quantity of degraded material. Registering absorption of the semiconductor in the solid state can give misleading results, as the optical density of a solid-state sample may remain high. An interesting example case is P3HT. Upon illumination in physiological solutions, P3HT thin films or colloidal particles have been demonstrated to photochemically reduce oxygen to produce ROS, ultimately yielding H₂O₂ as a metastable and easily quantifiable product. The ROS generation by P3HT has been exploited by Antognazza et al. to yield

light-induced physiological effects in both *in vitro* (Moros et al., 2018; Antognazza et al., 2019; Lodola et al., 2019) and *in vivo* models (Tortiglione et al., 2017). When evaluated by UV-V spectroscopy, P3HT throughout these experiments affords a negligible drop in solid-state absorbance, suggesting that the P3HT is stable under these conditions. However, using the Beer-Lambert method, whereby photochemically-aged films are redissolved and measured in chlorobenzene, it is possible to detect quantifiable degradation. Indeed, catalytic turn-over number (TON) of mol H₂O₂ produced divided by mol P3HT degraded is ≤ 1 . Meaning that for every equivalent of ROS produced, a monomer of P3HT is consumed (Gryszel et al., 2018b). Various organic semiconductors have been tested for their TON under similar conditions, and compounds with deeper HOMO levels achieve TON of 10²–10³ range. However, this indicates that the irreversible oxidation of organic semiconductors is an issue that requires careful consideration. The fate of the oxidation products should be evaluated as this may also have important physiological consequences.

Photocapacitive and Photofaradaic Currents

Photoinduced charges can charge the surface of the semiconductor resulting in an electrolytic double-layer effect. Alternatively, this charge can be transferred to the solution to generate a product in a faradaic reaction. The photocapacitive effect is important for effective and safe coupling to cells, avoiding some of the chemical processes mentioned above. To generate substantial charging of the surface, an energetic asymmetry in the semiconductor structure is needed. If a semiconductor heterostructure has a built-in spatial asymmetry (resulting from doping or a Schottky contact) then photoexcitation can result in carrier generation followed by their spatial separation, leading to a gradient of potential across the surface of the semiconductor (Willner and Katz, 2005). The spatial separation of charges within the device is critical to generate a potential difference that will affect the surrounding medium. To achieve this, careful engineering of a particle or a film must be carried out; otherwise, no electric potentials in the solution can develop. Utilizing conductor/organic semiconductor structures drastically affects charge separation and localization. Conductor/organic interface devices can be divided into two categories: (1) buried conductor, where the conductor does not make contact with the electrolyte (**Figure 1B**) and (2) extended and exposed metal (**Figure 1C**). In the former case, the presence of the conductor can drive charge separation and localization. On the other hand, if the conductor is passivated from the electrolyte by the semiconductor layer, upon illumination, the electric field is localized inside of the device, making capacitive coupling to the surrounding electrolyte impossible. It should be noted that the term “conductor” can often be used interchangeably with “metal,” however, it may be a highly-doped semiconductor (indium tin oxide for example), or a conducting polymer—therefore we use the general term “conductor” here.

In extended/exposed architectures, as shown in **Figure 1C**, the lateral separation of the metal from the organic layer

dictates the localization of the current flow that is generated across the electrolytic solution. The semiconductor/electrolyte interface is the charge-generating electrode, while the exposed metal/electrolyte interface acts as the return electrode. As in the case of a traditional wired stimulation electrode, optoelectronic stimulation devices must consider both the stimulation and the return electrodes. The terms *return electrode* or *reference electrode* often appear in the neuromodulation literature, though these terms do not mean the same thing as in the electrochemical literature. Return or reference electrode refers to the electrode with respect to which a given potential or current at the primary stimulation electrode is applied, therefore for most purposes, this term identifies the electrical ground. In the case of self-contained optoelectronic devices, the concept of the return electrode must be carefully considered, as due to the limited size/geometry of such devices, the electrochemical current induced will be spatially confined by the two electrodes. Such optoelectronic devices with a two-electrode architecture can be either capacitive, where the photocarriers generated by the semiconductor component lead to the build-up to two oppositely-charged electrical double layers or photofaradaic where both electrodes of the device catalytically support faradaic reactions (Figure 1, bottom). The latter case resembles the “artificial leaf” concept developed by Reece et al. (2011) and Surendranath et al. (2012). For a sustained faradaic current to be present, both cathode and anode of the device must be suitably catalytic to support the given reactions, and the total photovoltage generated by the semiconductor component introduces the fundamental thermodynamic constraint on what faradaic reactions will be possible or not. Thus, it must be considered that a sustained photoelectrocatalytic cycle is not that likely due to limited voltage and non-ideal catalytic interfaces. The final aspect in determining faradaic vs. capacitive phenomena is dynamics—a sustained photocurrent at long time scales must be attributed to a faradaic reaction, but it may remain obscured by capacitive behavior for durations shorter than several capacitive time constants. In the neurostimulation field, the key figure of merit is the electrochemical charge density, defined as the integral of current density over a phase of a stimulus waveform (McCreery et al., 1990). Reports give threshold values of charge density for reproducible generation of action potentials (APs). For *in vivo* stimulation of APs on peripheral nerves, charge densities in the range of 2–50 $\mu\text{C}/\text{cm}^2$ are used (McCreery et al., 1990; Cogan et al., 2017; Günter et al., 2019). Generally, the larger the stimulation electrode, the lower the necessary charge density for eliciting AP generation will be. For retinal stimulation, smaller area microelectrodes are desired to achieve a high spatial resolution of stimulation. For retinal ganglion cell stimulation with microelectrodes, action potential stimulation thresholds have been reported in the range of 0.05 mC/cm^2 to roughly 1 mC/cm^2 , with thresholds declining for larger electrode sizes (Sekirnjak et al., 2006). While seemingly counterintuitive, this is due to current being injected over a larger area producing a transient voltage perturbation over a larger region of solution, thereby being able recruit more cells into a response.

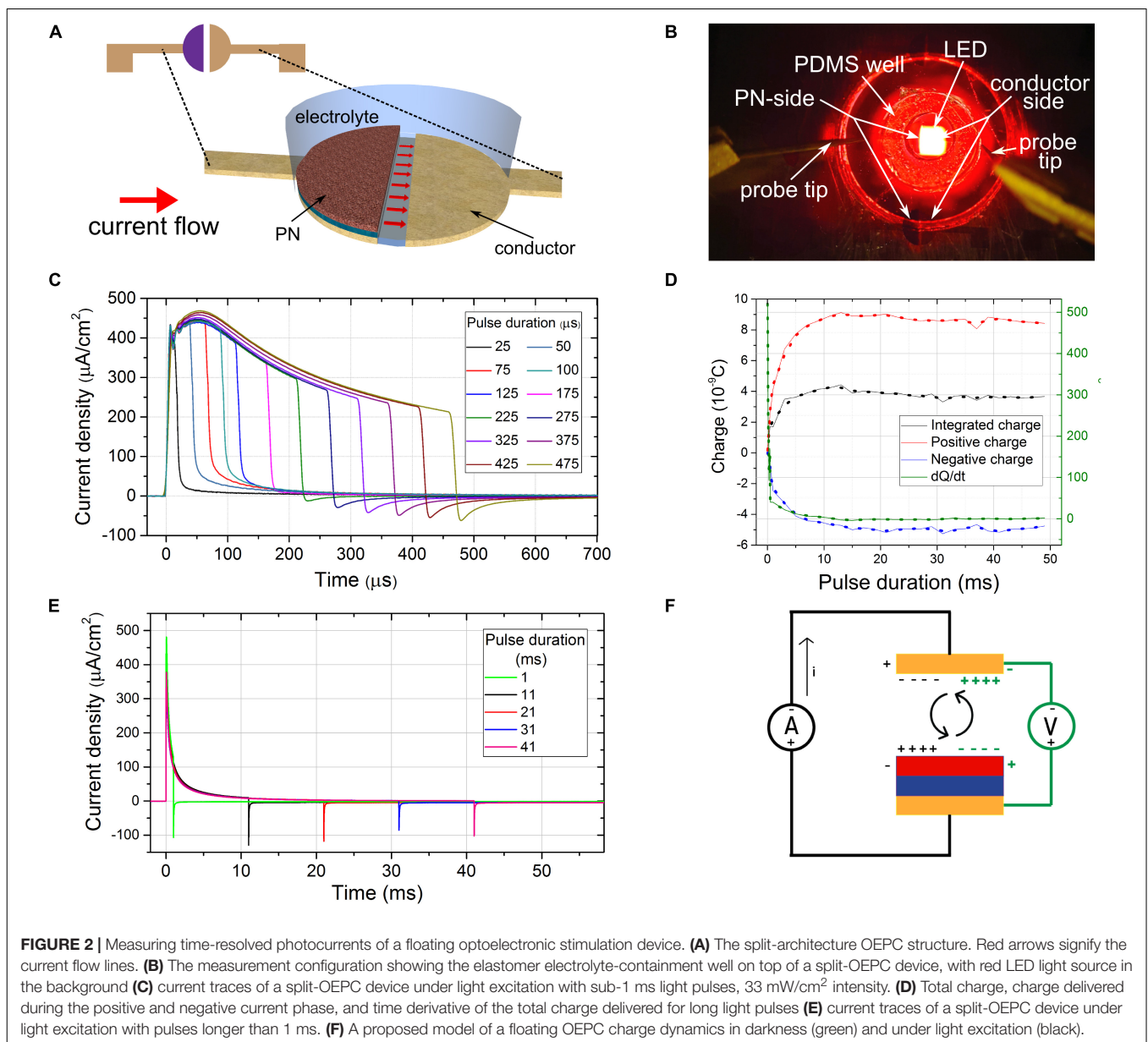
QUANTIFYING PHOTOCAPACITIVE VS. PHOTOFARADAIC CURRENT

It is not immediately clear how to benchmark the performance of autonomous “Type C” devices designed for optoelectronic stimulation. Two- or three-electrode photoelectrochemical measurements of the conductor/semiconductor device stack can be useful to evaluate the electrolytic capacitance of the photoelectrode, photocurrent magnitude, and possibility of faradaic reactions. However, such measurements do not faithfully reproduce conditions where the device itself is wireless and electrically floating. Conventional electrochemical characterization techniques utilizing potentiostats are also not ideal considering that light pulses for neurostimulation are intended to last in the range 0.05–10 ms, showing relatively fast dynamics. Accordingly, we have as a rule adopted measuring this dynamic electrochemistry with an oscilloscope, measuring between the rear electrode and an electrolytic solution contacted with an Ag/AgCl electrode. Such a measurement can correctly resolve the charging/discharging dynamics. Nevertheless, this configuration still does not reflect the realistic “floating” conditions. Here we present a method to interrogate the photocurrents between the primary photoelectrode and rear conductor directly.

The device we test is an organic optoelectronic stimulator our group has recently introduced, called the organic electrolytic photocapacitor (OEPC). The OEPC was designed as a “Type C” device (see Figure 1C), employing a small-molecule evaporated semiconductor donor/acceptor (*a.k.a.* P/N) bilayer as the photocharge generation component. OEPC devices have been demonstrated to successfully generate action potentials in cultured neurons and in explanted embryonic chicken retinas, using red light (660 nm) pulses of 1–5 ms length. We have recently evaluated more optimized OEPC devices where it was possible to measure the photoinduced activation of K^+ channels in single-cell voltage-clamp experiments (Jakešová et al., 2019). These experiments clearly show the strong depolarization in the range of 20–40 mV which OEPC devices can induce in cell membranes at a distance of several micrometers away from the semiconductor-electrolyte interface. Such large membrane voltage perturbations substantiate findings of action potential generation using the OEPC platform. In our previous published studies a photocapacitive mechanism was hypothesized on the basis of charge balance between cathodic and anodic charging pulses when measuring photocharging between the back electrode and a non-polarizable electrode in solution; the transient nature of these currents, which decay within a few ms of the pulse onset without displaying a sustained faradaic current, and the observation of reproducible and stable stimulation.

Split-Electrode Photocurrent Response Measurement Method

To measure the photocurrent in a realistic “floating” OEPC device, we created a split bottom electrode architecture (Figure 2A). One conductor layer has the PN semiconductor layer on it, while the other is the blank back conductor.



The “counter electrode” is 100 microns away from the “photoelectrode.” For these measurements, we fabricated a device consisting of a semitransparent gold back electrode topped by a PN charge-generating layer [30 nm metal free phthalocyanine (H_2PC)/30 nm N,N' -dimethyl perylenetetracarboxylic diimide (PTCDI)]. An elastomer (PDMS, Sylgard 184) block with a well confines the electrolyte above the two electrodes, while with the help of microprobes, the two electrodes are short-circuited externally by a low-impedance high-bandwidth current amplifier (**Figure 2B**). The device was optically excited with a 630 nm LED driven light pulses. Temporally-resolved currents generated by the OEPC during the light pulse and delivered to the conductor back-electrode were measured to help resolve the nature of the processes taking place. If both the conductor/PN and the bare conductor electrodes can sustain respective cathodic/anodic

faradaic reactions, a faradaic current should persist over long periods. In case the electrodes are fully capacitive and cannot sustain faradaic reactions, the current should exhibit a capacitive peak and decay once the electrical double layers fully charge. At the end of the light pulse, the double layers will discharge. The charge delivered during charging and discharging, i.e., time integrals under the current trace, for times significantly longer than the stimulation duration, should cancel out. If in fact both electrodes can support a low level of faradaic reactions, current traces will show a capacitive charging peak upon initiation of the light pulse followed by a sustained non-zero photocurrent. This current can only originate if faradaic processes are present on both of the split electrodes. Thus, the total current delivered by a photocapacitor can have both capacitive and a faradaic component. By integrating the current measured from the

beginning of the light stimulation until a time significantly longer than the capacitive time constant τ after the end of the light pulse, we can test for charge conservation. The closer the charge is to zero, the more capacitive the device is. If there is any unaccounted charge left after the integration, the missing charge can be associated with faradaic reactions:

$$\begin{aligned}\int_0^{T \gg \tau} i(t) dt &= \int_0^{T \gg \tau} i_F(t) + i_C(t) dt \\ &= \int_0^{T \gg \tau} i_F(t) dt + \int_0^{T \gg \tau} i_C(t) dt = Q_F + 0\end{aligned}$$

Overall current will be limited by the higher impedance electrode. Faradaic reactions will be controlled by the overpotential (i.e., kinetic barrier) of the given electrode, meaning that the capacitive vs. faradaic nature of the device can be tuned by the selection of the materials comprising the electrodes. Another important consideration is the open-circuit photovoltage of the PN structure. If the conductor chosen for a back electrode does not support electrochemical reactions within the open-circuit potential window of the OEPC, faradaic process on the charge-generating conductor/PN electrode may also not take place, since the redox processes on the two electrodes could not be balanced. On the other hand, if a perfectly non-polarizable electrode such as Ag/AgCl in Cl^- containing electrolyte is used for a back electrode, the faradaic reactions on the photocharge-generating electrode will not be hindered.

RESULTS AND DISCUSSION

The device was exposed to a series of light pulses of durations between 25 μs and 50 ms to study the charging dynamics (Figure 2C). A 1 s off time was held between consecutive pulses to make sure that the devices have enough time to reestablish the thermodynamic equilibrium. For each pulse duration, a current trace was measured and integrated during the light pulse duration and the following discharge time. Before each measurement, a dark current was recorded for the same duration, averaged, and the current zero offset was adjusted. For each pulse duration, a total integrated charge Q , as well as the charge delivered over positive (Q_+) and the negative (Q_-) phase of the current were evaluated. The rate of change of the total, un-accounted charge left after the integration of the current traces of different durations, dQ/dt (Figure 2D), was plotted as well. This value can tentatively be attributed to the faradaic component of the total current delivered by the photocapacitor.

In the case of pulses lasting longer than 10 ms (Figure 2E) capacitive charge and discharge pulses are clearly evident, with the capacitive time constant $\tau = RC$ of about 1 millisecond. Even though the total integrated charge Q does not completely cancel out, there is no sustained faradaic current dQ/dt for longer time durations. However, in the case of pulses significantly shorter than the time constant τ , a negative current discharge pulse was not observed at all (Figure 2C). A progressively more-pronounced discharge pulse was observed for pulse durations between 200 μs and 1 ms. This may lead one to believe that

the faradaic process is present for short pulses, while for longer pulses the process is more capacitive in nature. While this may be the case, it appears that this is a measurement artifact. Voltage pulses significantly shorter than the time constant $\tau = RC$ of a RC circuit and thus possessing a significant high frequency content can pass through the capacitor acting as a high-pass filter virtually unchanged, without eliciting a pronounced capacitive discharge peak. During the short duration of the pulse of the order of 0.1 RC, the photocapacitor doesn't have the time to charge up significantly, even though the charging current can be of significant magnitude. This small amount of charge discharges after the end of the light stimulation, but following the dynamics of the RC circuit—thus it takes $5RC$ for > 99% of the charge to be discharged, which can be > 50 times the stimulation pulse duration, meaning that the discharge current can be extremely small, and present over a long time. This presents an experimental difficulty, since it is necessary to measure the current trace both with high temporal and current resolution, and to eliminate the measurement offset completely. Even though we used a high bandwidth current amplifier, and high dynamic range and high-speed oscilloscope, with paying attention to zero the offset before every measurement, it is likely that a significant portion of the discharge current was lost in the measurement noise, which thus yielded a false faradaic current as a result. For verification, a “dry” photodiode device was manufactured, with the same device architecture as a $\text{H}_2\text{PC}/\text{PTCDI}$ photocapacitor, but with added top titanium metal contact. A 47 nF ceramic capacitor was connected in series with this photodiode and the current traces were measured with light pulses of different length. Qualitatively the same behavior as in a “wet” photocapacitor was observed, with sub-0.1RC pulses showing no or negligible discharge current. Therefore this is an important artifact that should be taken into consideration when measuring dynamic electrochemical currents.

Another contribution to the short-time scale non-balanced current effect may be the “dark charging” of the double layers between the light pulses. In darkness after the thermodynamic equilibrium is established, the gold/PN electrode was observed to have a positive potential vs. the bare gold electrode (measured using an electrometer), while the opposite polarity was observed in short-circuit conditions during the excitation by a light pulse. This leads to the possible conclusion that in the dark the double layers of the device are charged slowly while establishing the thermodynamic equilibrium, and the device enters the light-pulse cycle pre-charged. The charge generation during the light pulse lowers the impedance of the PN junction by 3–4 orders of magnitude (Rand et al., 2018), and the charges at the opposite device electrodes can discharge, leading to the observed non-balanced current pulse at short times and the reversal of the polarities of the electrodes. The equilibrium during which the electrical double layers get charged is established over relatively long times, on the order of seconds. These low “dark” charging currents, however, are below the amplifier's noise limit, so they cannot be reliably measured over such long-time spans.

This shows that the measured charge dynamics of the floating photocapacitor corresponds to the case of a RC circuit, charged by a photovoltaic PN element. In our model, the process is capacitive

in nature, even for the short pulses, and shows that the device can get a boost in delivered current from its pre-charged state in case of short light pulses separated by much longer durations of darkness, as is typically the case in electrical neuro-stimulation.

From the split-electrode measurement, it is possible to resolve the dynamics of the photocurrents and conclusively establish that the OEPC devices do not source stable faradaic current. An unexpected phenomenon observed at the shortest measured time scales of tens of microseconds, may be explained by the photogeneration process first discharging two preexisting double layers of the opposite polarity, which are the result of the thermodynamic equilibrium of the device/electrolyte structure in the dark.

FUTURE OUTLOOK FOR ORGANIC OPTOELECTRONIC STIMULATION DEVICES

Organic semiconductors hold the promise to enable ultrathin and biocompatible bio-interfacing devices for cellular photostimulation. At present this field is still in its infancy. Success depends on several critical factors. The first is photocurrent optimization and the resulting charge density. If the goal is to mimic and replace conventional electrical stimulation protocols, organic semiconductor devices must be engineered to deliver charge densities in the range of $> 1 \mu\text{C}/\text{cm}^2$ over timescales of 100–5,000 μs . The second is operational robustness and long-term safety. Promising indications for biocompatibility and stability for organic devices exist, however long-term stability and efficacy must be established. Finally, photochemical and photofaradaic reactions remain to be fully understood. The recent reports on reactive oxygen species generation by organic semiconductors represent on one hand a caveat for deployment of such stimulation devices, on the other hand there are also many opportunities for on-demand ROS delivery. Therefore, moving forward demands careful characterization

of the photochemical, photofaradaic, and photocapacitive properties of organic materials and devices. In this perspective, we attempted to bring these concepts to the forefront and to offer a measurement strategy to resolve the photofaradaic vs. photocapacitive issue in realistic conditions.

DATA AVAILABILITY STATEMENT

All datasets generated for this study are included in the article/supplementary material.

AUTHOR CONTRIBUTIONS

EG and VÐ conceived the research idea. EG and YH supervised and coordinated the research. VÐ fabricated and tested all the devices, with fabrication and measurement assistance from LM and DR. EG wrote the first draft of the manuscript. VÐ, EG, DR, and YH wrote sections of the manuscript. All authors contributed to manuscript revision, read and approved the submitted version.

FUNDING

This work has been supported in part by Croatian Science Foundation under the project UIP-2019-04-1753. We gratefully acknowledge the financial support from the Knut and Alice Wallenberg Foundation within the framework of the Wallenberg Centre for Molecular Medicine at Linköping University, the Swedish Research Council (Vetenskapsrådet, 2018-04505), and the Swedish Foundation for Strategic Research (SSF).

ACKNOWLEDGMENTS

We are grateful to Marie Jakesova for support in device fabrication.

REFERENCES

- Albert, E. S., Bec, J. M., Desmadryl, G., Chekroud, K., Travo, C., Gaboyard, S., et al. (2012). TRPV4 channels mediate the infrared laser-evoked response in sensory neurons. *J. Neurophysiol.* 107, 3227–3234. doi: 10.1152/jn.00424.2011
- Antognazza, M. R., Aziz, I. A., and Lodola, F. (2019). Use of exogenous and endogenous photo-mediators as efficient ROS modulation tools: results & perspectives for therapeutic purposes. *Oxid. Med. Cell. Longev.* 2019, 1–24. doi: 10.1155/2019/2867516
- Bellani, S., Antognazza, M. R., and Bonaccorso, F. (2018). Carbon-based photocathode materials for solar hydrogen production. *Adv. Mater.* 31:1801446. doi: 10.1002/adma.201801446
- Bellani, S., Ghadirzadeh, A., Meda, L., Savoini, A., Tacca, A., Marra, G., et al. (2015). Hybrid organic/inorganic nanostructures for highly sensitive photoelectrochemical detection of dissolved oxygen in aqueous media. *Adv. Funct. Mater.* 25, 4531–4538. doi: 10.1002/adfm.201500701
- Carvalho-de-Souza, J. L., Treger, J. S., Dang, B., Kent, S. B. H., Pepperberg, D. R., and Bezanilla, F. (2015). Photosensitivity of neurons enabled by cell-targeted gold nanoparticles. *Neuron* 86, 207–217. doi: 10.1016/j.neuron.2015.02.033
- Chowdhury, P., Fortin, P., Suppes, G., and Holdcroft, S. (2016). Aqueous photoelectrochemical reduction of anthraquinone disulfonate at organic polymer films. *Macromol. Chem. Phys.* 217, 1119–1127. doi: 10.1002/macp.201500440
- Cogan, S. F., Ludwig, K. A., Welle, C. G., Takmakov, P., Clinic, M., Spring, S., et al. (2017). Tissue damage thresholds during therapeutic electrical stimulation. *J. Neural Eng.* 13:021001. doi: 10.1088/1741-2560/13/2/021001
- Gamper, N., Zaika, O., Li, Y., Martin, P., Hernandez, C. C., Perez, M. R., et al. (2006). Oxidative modification of M-type K⁺ channels as a mechanism of cytoprotective neuronal silencing. *EMBO J.* 25, 4996–5004. doi: 10.1038/sj.emboj.7601374
- Gryszel, M., Markov, A., Vagin, M., and Głowacki, E. D. (2018a). Organic heterojunction photocathodes for optimized photoelectrochemical hydrogen peroxide production. *J. Mater. Chem. A* 6, 24709–24716. doi: 10.1039/C8TA08151D
- Gryszel, M., Rybakiewicz, R., and Głowacki, E. D. (2019). Water-soluble organic dyes as molecular photocatalysts for H₂O₂ evolution. *Adv. Sustain. Syst.* 3:1900027. doi: 10.1002/adsu.201900027
- Gryszel, M., Sytnyk, M., Jakesova, M., Romanazzi, G., Gabrielson, R., Heiss, W., et al. (2018b). General observation of photocatalytic oxygen reduction to hydrogen peroxide by organic semiconductor thin films and colloidal crystals. *ACS Appl. Mater. Interfaces* 10, 13253–13257. doi: 10.1021/acsami.8b01295

- Günter, C., Delbeke, J., and Ortiz-Catalan, M. (2019). Safety of long-term electrical peripheral nerve stimulation: review of the state of the art. *J. Neuroeng. Rehabil.* 16:13. doi: 10.1186/s12984-018-0474-8
- Huang, Y. Y., Nagata, K., Tedford, C. E., Mccarthy, T., and Hamblin, M. R. (2013). Low-level laser therapy (LLLT) reduces oxidative stress in primary cortical neurons in vitro. *J. Biophotonics* 6, 829–838. doi: 10.1002/jbio.201200157
- Jakešová, M., Apaydin, D. H., Sytnyk, M., Oppelt, K., Heiss, W., Sariciftci, N. S., et al. (2016). Hydrogen-bonded organic semiconductors as stable photoelectrocatalysts for efficient hydrogen peroxide photosynthesis. *Adv. Funct. Mater.* 26, 5248–5254. doi: 10.1002/adfm.201601946
- Jakešová, M., Ejneby, M. S., Đerek, V., Schmidt, T., Gryszel, M., Brask, J., et al. (2019). Optoelectronic control of single cells using organic photocapacitors. *Sci. Adv.* 5:eav5265. doi: 10.1126/sciadv.aav5265
- Jiang, Y., Carvalho-de-Souza, J. L., Wong, R. C. S., Luo, Z., Isheim, D., Zuo, X., et al. (2016). Heterogeneous silicon mesostructures for lipid-supported bioelectric interfaces. *Nat. Mater.* 15, 1023–1030. doi: 10.1038/nmat4673
- Jiang, Y., Parameswaran, R., Li, X., Carvalho-de-Souza, J. L., Gao, X., Meng, L., et al. (2019). Nongenetic optical neuromodulation with silicon-based materials. *Nat. Protoc.* 14, 1339–1376. doi: 10.1038/s41596-019-0135-9
- Lim, J. B., Langford, T. F., Huang, B. K., Deen, W. M., and Sikes, H. D. (2016). A reaction-diffusion model of cytosolic hydrogen peroxide. *Free Radic. Biol. Med.* 90, 85–90. doi: 10.1016/j.freeradbiomed.2015.11.005
- Lin, Y., Li, Y., and Zhan, X. (2012). Small molecule semiconductors for high-efficiency organic photovoltaics. *Chem. Soc. Rev.* 41, 4245–4272. doi: 10.1039/c2cs15313k
- Lodola, F., Martino, N., Tullii, G., Lanzani, G., and Antognazza, M. R. (2017). Conjugated polymers mediate effective activation of the Mammalian ion channel transient receptor potential vanilloid 1. *Sci. Rep.* 7:8477. doi: 10.1038/s41598-017-08541-6
- Lodola, F., Rosti, V., Tullii, G., Desii, A., Tapella, L., Catarsi, P., et al. (2019). Conjugated polymers optically regulate the fate of endothelial colony-forming cells. *Sci. Adv.* 5:eav4620. doi: 10.1126/sciadv.aav4620
- McCreery, D. B., Agnew, W. F., Yuen, T. G. H., and Bullara, L. (1990). Charge density and charge per phase as cofactors in neural injury induced by electrical stimulation. *IEEE Trans. Biomed. Eng.* 37, 996–1001. doi: 10.1109/10.102812
- Migliaccio, L., Gryszel, M., Đerek, V., Pezzella, A., and Glowacki, E. D. (2018). Aqueous photo(electro)catalysis with eumelanin thin films. *Mater. Horizons* 5, 984–990. doi: 10.1039/C8MH00715B
- Mitraka, E., Gryszel, M., Vagin, M., Jafari, M. J., Singh, A., Warczak, M., et al. (2019). Electrocatalytic production of hydrogen peroxide with Poly(3,4-ethylenedioxythiophene) electrodes. *Adv. Sustain. Syst.* 3:1800110. doi: 10.1002/advs.201800110
- Moros, M., Lewinska, A., Onorato, G., Antognazza, M. R., Di Maria, F., Blasio, M., et al. (2018). Light-triggered modulation of cell antioxidant defense by polymer semiconducting nanoparticles in a model organism. *MRS Commun.* 155, 1–8. doi: 10.1557/mrc.2018.104
- Rand, D., Jakešová, M., Lubin, G., Vebrat, I., David-Pur, M., Đerek, V., et al. (2018). Direct electrical neurostimulation with organic pigment photocapacitors. *Adv. Mater.* 30:1707292. doi: 10.1002/adma.201707292
- Reece, S. Y., Hamel, J. A., Sung, K., Jarvi, T. D., Esswein, A. J., Pijpers, J. J. H., et al. (2011). Wireless solar water splitting using silicon-based semiconductors and earth-abundant catalysts. *Science* 334, 645–648. doi: 10.1126/science.1209816
- Sekirnjak, C., Hottoway, P., Sher, A., Dabrowski, W., Litke, A. M., and Chichilnisky, E. J. (2006). Electrical stimulation of mammalian retinal ganglion cells with multielectrode arrays. *J. Neurophysiol.* 95, 3311–3327. doi: 10.1152/jn.01168.2005
- Shapiro, M. G., Homma, K., Villarreal, S., Richter, C.-P., and Bezanilla, F. (2012). Infrared light excites cells by changing their electrical capacitance. *Nat. Commun.* 3:736. doi: 10.1038/ncomms1742
- Suppes, G., Ballard, E., and Holdcroft, S. (2013). Aqueous photocathode activity of regioregular poly(3-hexylthiophene). *Polym. Chem.* 4, 5345–5350. doi: 10.1039/c3py00143a
- Surenranath, Y., Bediako, D. K., and Nocera, D. G. (2012). Interplay of oxygen-evolution kinetics and photovoltaic power curves on the construction of artificial leaves. *Proc. Natl. Acad. Sci. U.S.A.* 109, 15617–15621. doi: 10.1073/pnas.1118341109
- Sytnyk, M., Jakešová, M., Litviouková, M., Mashkov, O., Kriegner, D., Stangl, J., et al. (2017). Cellular interfaces with hydrogen-bonded organic semiconductor hierarchical nanocrystals. *Nat. Commun.* 8:91. doi: 10.1038/s41467-017-00135-0
- Tortiglione, C., Antognazza, M. R., Tino, A., Bossio, C., Marchesano, V., Bauduin, A., et al. (2017). Semiconducting polymers are light nanotransducers in eyeless animals. *Sci. Adv.* 3:e1601699. doi: 10.1126/sciadv.1601699
- Warczak, M., Gryszel, M., Jakešová, M., Đerek, V., and Glowacki, E. D. (2018). Organic semiconductor perylenetetracarboxylic diimide (PTCDI) electrodes for electrocatalytic reduction of oxygen to hydrogen peroxide. *Chem. Commun.* 54, 1960–1963. doi: 10.1039/C7CC08471D
- Węclawski, M. K., Jakešová, M., Charyton, M., Demitri, N., Koszarna, B., Oppelt, K., et al. (2017). Biscoumarin-containing acenes as stable organic semiconductors for photocatalytic oxygen reduction to hydrogen peroxide. *J. Mater. Chem. A* 5, 20780–20788. doi: 10.1039/C7TA05882A
- Willner, I., and Katz, E. (2005). *Bioelectronics*. Weinheim: Wiley-VCH.
- Zimmerman, J. F., and Tian, B. (2018). Nongenetic optical methods for measuring and modulating neuronal response. *ACS Nano* 12, 4086–4095. doi: 10.1021/acsnano.8b02758

Conflict of Interest: The authors declare that the research was conducted in the absence of any commercial or financial relationships that could be construed as a potential conflict of interest.

Copyright © 2020 Derek, Rand, Migliaccio, Hanein and Glowacki. This is an open-access article distributed under the terms of the Creative Commons Attribution License (CC BY). The use, distribution or reproduction in other forums is permitted, provided the original author(s) and the copyright owner(s) are credited and that the original publication in this journal is cited, in accordance with accepted academic practice. No use, distribution or reproduction is permitted which does not comply with these terms.

Hydrogen-Bonded Organic Semiconductors as Stable Photoelectrocatalysts for Efficient Hydrogen Peroxide Photosynthesis

Marie Jakešová, Doğukan Hazar Apaydin, Mykhailo Sytnyk, Kerstin Oppelt, Wolfgang Heiss, Niyazi Serdar Sariciftci, and Eric Daniel Głowacki*

Research on semiconductor photocatalysts for the conversion of solar energy into chemical fuels has been at the forefront of renewable energy technologies. Water splitting to produce H₂ and CO₂ reduction to hydrocarbons are the two prominent approaches. A lesser-known process, the conversion of solar energy into the versatile high-energy product H₂O₂ via reduction of O₂ has been proposed as an alternative concept. Semiconductor photoelectrodes for the direct photosynthesis of H₂O₂ from O₂ have not been applied up to now. Photoelectrocatalytic oxygen reduction to peroxides in aqueous electrolytes by hydrogen-bonded organic semiconductor is observed photoelectrodes. These materials have been found to be remarkably stable operating in a photoelectrochemical cell converting light into H₂O₂ under constant illumination for at least several days, functioning in a pH range from 1 to 12. This is the first report of a semiconductor photoelectrode for H₂O₂ production, with catalytic performance exceeding prior reports on photocatalysts by one to two orders of magnitude in terms of peroxide yield/catalyst amount/time. The combination of a strongly reducing conduction band energy level with stability in aqueous electrolytes opens new avenues for this widely available materials class in the field of photo(electro) catalysis.

1. Introduction

Oxygen reduction reactions (ORR) of dissolved O₂ in water are important in biology, fuel cells, other energy conversion

devices, and many industrial processes.^[1–4] ORR can be a single-electron reduction to the oxygen radical anion, a two-electron reduction to hydrogen peroxide, H₂O₂, or finally a four-electron reduction to H₂O. Of these, H₂O₂ represents a versatile, high energy^[5] product, capable of participating in numerous further redox reactions and is an active species in a plethora of biological processes.^[6] Conversion of solar irradiation to hydrogen peroxide has been proposed for energy storage.^[5,7] Hydrogen peroxide is a preferred “green” oxidant for industrial chemistry, as its only products are H₂O and O₂. The incumbent anthraquinone oxidation industrial process for H₂O₂ synthesis, however, is far from green, employing high temperatures, noble metal catalysts, high-pressure hydrogenation with H₂, and large volumes of organic solvents. This motivates research to develop alternative processes for H₂O₂ synthesis.^[8] Some inorganic semiconductors in colloidal form (notably ZnO and

CdS) are known photocatalysts for photochemical O₂ reduction to H₂O₂ (in the presence of a sacrificial electron donor).^[9–12] Recently, graphitic carbon nitrides (g-C₃N₄) have been found to photocatalyze reduction of O₂ to H₂O₂ with concurrent ethanol oxidation^[13] or water oxidation.^[14] Observation of photocatalytic generation of H₂O₂ by a semiconductor photocathode has never been reported. This approach is advantageous as it is a truly heterogeneous catalysis that is accompanied by the generation of photocurrent which can do additional work, thereby allowing the photocathode to be incorporated into a photoelectrochemical cell. In this paper, we have successfully demonstrated that an emerging class of organic semiconductors, hydrogen-bonded pigments, is suitable as catalytic semiconductor photocathodes for selective ORR to produce hydrogen peroxides in an unprecedented pH range with nearly two orders of magnitude higher catalytic activity compared with the best known H₂O₂-producing photocatalysts. Organic semiconductors, which have evolved over the past decades to be established materials for xerography^[15] and light-emitting diodes,^[16] are also promising for photovoltaics.^[17,18] Due to limited stability in aqueous environments, especially under photoirradiation, they have been largely unexplored in aqueous (photo)electrochemistry applications. Aqueous photocathode behavior of the

M. Jakešová, D. H. Apaydin, Prof. N. S. Sariciftci, Dr. E. D. Głowacki
Linz Institute for Organic Solar Cells (LIOS)
Physical Chemistry
Johannes Kepler University
Altenbergerstrasse 69, A-4040 Linz, Austria
E-mail: eric_daniel.glowacki@jku.at



Dr. M. Sytnyk, Prof. W. Heiss
Materials for Electronics and Energy Technology (i-MEET)
Friedrich-Alexander-Universität Erlangen-Nürnberg
Martensstrasse 7, D-91058 Erlangen, Germany
Dr. M. Sytnyk, Prof. W. Heiss
Energie Campus Nürnberg (EnCN)
Fürtherstrasse 250, D-90429 Nürnberg, Germany
Dr. K. Oppelt
Institute of Inorganic Chemistry
Johannes Kepler University
Altenbergerstrasse 69, A-4040 Linz, Austria

DOI: 10.1002/adfm.201601946

archetypal organic semiconductor poly(3-hexylthiophene), or P3HT, was first reported in 1996 and attributed to the hydrogen evolution reaction (HER).^[19] These results were later elaborated in 2013,^[20] however it has recently been contended that in fact HER does not occur, but instead ORR dominates.^[21] A single-electron reduction to produce O_2^- radical was postulated as a mechanism.^[21] P3HT is known to react reversibly with oxygen generating charge-transfer species, but also does degrade irreversibly especially when absorbing photons with $\lambda < 500$ nm.^[22] Bulk heterojunction blends^[23] of semiconducting polymers with a C_{60} fullerene acceptor were recently reported as being photoelectrochemically active for ORR, with application for oxygen sensing in aqueous solutions.^[24] Reduction products were not evaluated, however.^[19,20,24] Aside from these reports, organic semiconductors have not been explored as photocathodes for ORR. Herein we have found promising aqueous photocathodic properties of polycrystalline thin films of hydrogen-bonded organic pigments of the epindolidione (EPI) and quinacridone (QNC) family (Figure 1a). These materials are low-cost and robust organic semiconductors, and are mass-produced as colorants for inks. They are known to be nontoxic and environmentally benign,^[25,26] and appear to be biocompatible. EPI and QNC are ambipolar organic semiconductors^[27,28] with charge carrier mobility in the range $0.1\text{--}1\text{ cm}^2\text{ V}^{-1}\text{ s}^{-1}$, and are capable of efficient photocarrier generation (EQE $\approx 10\%$) in the absence of a classic donor–acceptor heterojunction.^[29,30] Recently thin-film transistors with EPI as an active material were found to be stable while operating in contact with aqueous solutions in a pH range from 2 to 10.^[28] These results encouraged us to explore the (photo)electrochemistry of EPI and QNC in aqueous electrolytes.

2. Results and Discussion

2.1. Selective Photocathodic Oxygen Reduction Reaction to Hydrogen Peroxide

EPI and QNC semiconductor electrodes were prepared by vacuum evaporation of polycrystalline films onto thin-film Au electrodes deposited on glass (Figure 1b). Details on sample preparation can be found in the experimental section. Photoelectrochemical measurements were conducted using a configuration as shown in the schematic in Figure 1c. Cyclic voltammetry and chronoamperometry experiments were carried out using a potentiostat, with the semiconductor-modified Au as the working electrode, a Pt wire as the counter electrode, and an Ag/AgCl quasi-reference electrode. A scan rate of 25 mV s^{-1} was used throughout. The electrodes were illuminated with a tungsten halogen lamp equipped with a fluorine-doped tin oxide coated glass to function as an IR and UV-blocking filter. The photoelectrodes were measured in aqueous electrolyte consisting of HCl (or NaOH for $\text{pH} > 7$) with Na_2SO_4 added to keep the ionic strength of the electrolyte constant at 0.1 M as the pH was changed. Cyclic voltammograms in the dark and under illumination for EPI and QNC at pH 1 and 7 are shown in Figure 2a,b. A photocathodic effect was observed in all cases, and was measured up to pH 12. We compared both oxygenated and deoxygenated (O_2 -bubbled, N_2 -purged)

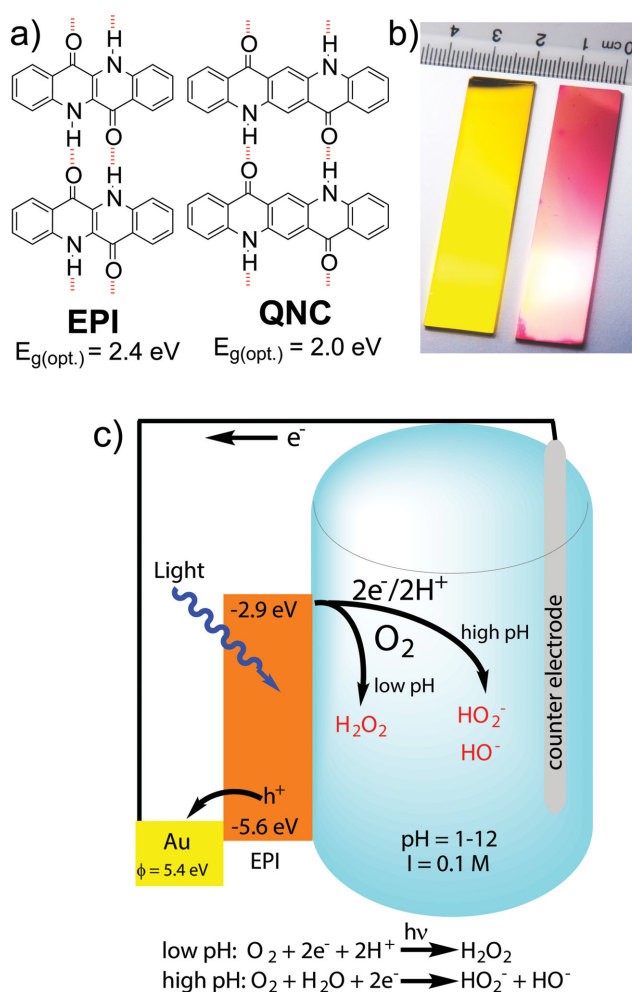


Figure 1. a) Hydrogen-bonded pigment semiconductors epindolidione (EPI) and quinacridone (QNC), with dashed red lines indicating intermolecular hydrogen bonding. Frontier orbital energy values (optical and electrochemical) are from Ref. [28] b) EPI (left) and QNC (right) photoelectrodes, consisting of polycrystalline films evaporated on Au-coated glass slides c) Photoelectrochemical measurement configuration with EPI semiconductor electrode shown. Aqueous electrolytes in the pH range 1–12 were used. ORR reactions at low and high pH values occur via the different equations shown.

conditions, concluding that the photocurrent magnitude scales with the oxygenation of the electrolyte (Figure S1–S3, Supporting Information). Thoroughly deoxygenated electrolytes gave photocurrents 10–20 times lower than measurements in air, signaling that ORR is the dominant photocathodic process. The remaining photocurrent may originate from HER, as suggested in previous work with organic photocathodes.^[21] In ambient conditions, illuminated photoelectrodes gave ORR photocurrent densities up to $12\text{--}15\ \mu\text{A cm}^{-2}$ at pH 1 with an illumination intensity of 60 mW cm^{-2} at 0 V vs. Ag/AgCl . Under these conditions oxidation of chloride to chlorine as well as reoxidation of ORR reduction products occurs at the counter electrode. Photocathodic on/off transient currents at 0 V , pH 1, are shown in the inset of Figure 2 for both EPI and QNC. Rapid rise and fall times with stable photocurrent under

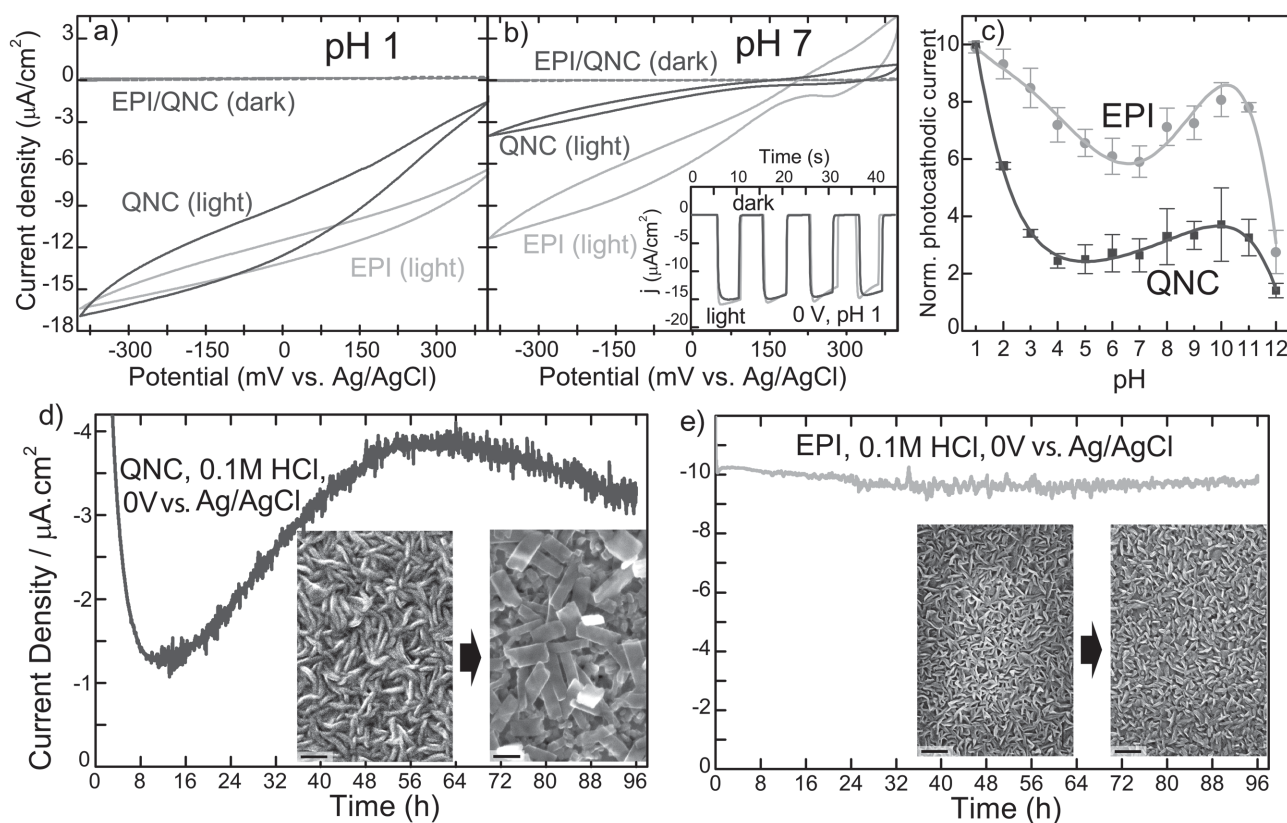


Figure 2. a) Cyclic voltammograms of EPI and QNC photocathodes at pH 1. Dashed gray curves are measured in the dark, while solid lines are under 60 mW cm^{-2} irradiation; b) photocathodes in dark and under illumination in pH 7 electrolytes. Inset shows current transients for light on/off at pH 1 and 0 V. c) Normalized photocathodic current at 0 V vs. Ag/AgCl for EPI and QNC photocathodes as a function of electrolyte pH. d) QNC photocathode measured at 0 V over 96 h in pH 1 electrolyte under illumination with intensity of 60 mW cm^{-2} . Photocathodic current drops as oxygen in the cell is consumed, reaching a steady state. Then photocurrent increases, corresponding to a recrystallization as evident in the SEM images (inset) of the QNC film taken before and after (20 h) operation at pH 1. All scale bars = 100 nm. e) EPI photocathode measured for 96 h under the same conditions. After initial decline due to consumption of O_2 , a steady-state photocurrent remains stable for the rest of the measurement period. SEM revealed no significant morphology changes.

illumination were observed. Photocurrent magnitude was proportional to pH, for both QNC and EPI (Figure 2c). The photocurrent decreases as pH is increased from 1 to ≈ 7 , however it again increases at $\text{pH} > 7$, giving a peak at $\text{pH} 10$, before falling at higher pH values. It is important to note that in the pH range 1–12, considering the effects of dissolved ions, there are negligible changes in the solubility of O_2 , so the effect of changes in O_2 concentration must be discounted.^[31] The presence of low- and high-pH cathodic processes already hints that the mechanism is peroxide formation and not another ORR process, since peroxide evolution occurs at both a low- and high-pH regimes. First, we consider the photocathodic process occurring at low pH: Taking into account the known $2\text{e}^-/2\text{H}^+$ electrochemical behavior of indigo-like hydrogen-bonded pigments,^[32] $2\text{e}^-/2\text{H}^+$ coupled redox reactions are expected: namely the reduction of O_2 to hydrogen peroxide according to the equation in Figure 1c. To test for the evolution of hydrogen peroxide, we used the tetramethyl benzidine/horseradish peroxidase (TMB/HRP) assay well known from biological applications (details in Experimental Section).^[33] Aliquots were taken from the photoelectrolysis solution after 10 min at 0 V vs. Ag/AgCl and measured spectrophotometrically using TMB/HRP.

Based on the TMB/HRP assay, we found a H_2O_2 concentration of $0.1 \times 10^{-3} \text{ M}$ and could calculate a Faradaic efficiency for H_2O_2 formation of $62 \pm 5\%$ for EPI and $80 \pm 5\%$ for QNC at pH 1. From this, we can conclude that ORR to peroxide is the dominant process. Under these conditions, the Faradaic efficiency calculation is an underestimation, as peroxide is being reoxidized at the counter electrode back to O_2 . As pH increases, photocurrent decreases (Figure 2c), because the $2\text{e}^-/2\text{H}^+$ mechanism becomes less probable and the second reaction shown in Figure 1c predominates, correlating with a rise in photocurrent as pH is increased from 7 to 10. These two mechanisms are discussed in detail in Section 2.3. To put these results in context with the reported ORR photocathode behavior of P3HT, we conducted experiments using regioregular P3HT films on Au. In direct comparison with EPI and QNC, optimized P3HT showed cathodic photocurrents 20 to 30 times lower than either hydrogen-bonded pigment material (Figures S4–S9, Supporting Information), and no H_2O_2 was measurable using the TMB/HRP assay. Previous studies assigned the photocathodic behavior of P3HT to single-electron reduction to the oxygen radical anion.^[21] While based on our results at low pH values ORR to H_2O_2 is the dominant photoelectrochemical reaction

for EPI and QNC, the occurrence of HER cannot be completely excluded, however. We attempted to measure the presence of H_2 in the cell headspace by gas chromatography (GC) using photoelectrodes irradiated for several days under deoxygenated conditions, using a sealed H-cell—but no H_2 could be detected (details in Experimental Section). Additional cathodic polarization up to -200 mV combined with illumination did not yield measurable H_2 either. As reference, the plain Au electrode yielded only HER (as verified by GC) and no ORR (Figure S10, Supporting Information).

2.2. Photocatalytic Stability and Efficiency

2.2.1. Photocurrent Stability in a Single-Compartment Cell Measured Potentiostatically

Organic semiconductors are typically notorious for stability and degradation problems, especially in contact with water and oxygen. We tested the photocathodic current stability for EPI and QNC over 4 d under continuous illumination with 60 mW cm^{-2} (Figure 2d,e). Though both pigments continuously operated under these conditions, there were marked differences. In the case of QNC, photocurrent was found to increase over several hours, before leveling off (Figure 2d). Examination of QNC using scanning electron microscopy shows that the films underwent a recrystallization, where the original rod-like crystallites transformed into rectangular platelets (Figure 2d, inset), though the internal crystal structure is preserved, as concluded by XRD analysis (Figure S11, Supporting Information). It is likely that this leads to an increase of photocatalytically active crystallite surface. EPI photoelectrodes measured under these conditions give constant photocurrent for at least 96 h and do not significantly change morphology (Figure 2e). QNC after 3–4 d began to show steadily decreasing photocurrents, accompanied by some eventual bleaching of the pigment. EPI photocathodes, however, were found to be remarkably robust, and several samples were subjected to repeated measurements and performance was retained. We concluded that EPI had superior stability to QNC.

2.2.2. Photoelectrochemical Cells with EPI

Since these conditions did not degrade the EPI photoelectrodes, we attempted a more drastic experiment with a photoelectrochemical cell (PEC) comprising an EPI photoelectrode and a Pt counter electrode (pH 1), measured using a source meter. The PEC was irradiated with a 500 W Xe lamp, with a substantial UV component. The PEC generated a J_{sc} of $2.9 \mu\text{A cm}^{-2}$ and V_{oc} of 300 mV, degrading to around $1 \mu\text{A cm}^{-2}$ after 55 h of continuous operation (Figure S12, Supporting Information). Examination of the photoelectrode under a microscope showed that these intense conditions had led to delamination and recrystallization of the gold electrode, while the EPI pigment remained intact, as evidenced by fluorescence microscopy (Figure S12, Supporting Information). We found that P3HT electrodes under the same conditions gave no measurable photocurrent at short circuit. Measuring with a cathodic bias of -300 mV gave a $\approx 1 \mu\text{A cm}^{-2}$

photocurrent that degraded within 2 h. These results highlight the outstanding robustness of this materials class. Since gold electrodes degrade under these conditions, we substituted them with carbon felt. Photocathodes were fabricated by evaporation of 200 nm of EPI onto the carbon felt electrode. This PEC gave stable photocurrent for at least 11 d (Figure S13, Supporting Information), which demonstrates the usefulness of such photocathodes in a photoelectrochemical cell.

2.2.3. Photoluminescence Quenching

It is difficult to estimate an upper limit for how high photocurrent densities can theoretically be for photocathodic H_2O_2 evolution, due to unknowns about the kinetics of the diffusion and adsorption of dissolved O_2 ($[O_2] \approx 10\text{--}20 \times 10^{-3} \text{ M}$ at room temperature) onto our electrode. With optimization photocurrents in the mA cm^{-2} range should be possible, as a point of reference noble metal catalyst electrodes for electrocatalytic ORR can achieve current densities up to $5\text{--}6 \text{ mA cm}^{-2}$.^[4] In order to better understand the mechanism and limitations behind the photocathodic ORR process, we measured photoluminescence of the EPI and QNC semiconductor electrodes at pH 1 vs. pH 7, and as a function of negative polarization. Both EPI and QNC showed photoluminescence quenching at pH 1 vs. pH 7, as well as quenching as the electrode was cathodically polarized (Figures S14,S15, Supporting Information). The overall quenching effect was small, especially in the case of QNC. The luminescent decay pathway still remains highly efficient, showing that few excitons lead to photoelectrochemistry.

2.2.4. Photosynthesis of H_2O_2 Using a Two-Compartment Electrochemical Cell

Due to its superior stability, we chose to use EPI as a photocatalyst for continuous H_2O_2 photosynthesis. In order to maximize the peroxide yield in the working electrolyte solution, it is critical to saturate the electrolyte with O_2 and to isolate the anodic reaction chamber from the cathodic one to prevent reoxidation of peroxide back to O_2 . For this purpose, we utilized a two-compartment H-cell separated by a glass frit. We were not able to detect measurable H_2O_2 permeating through the frit. We used a working electrode of 200 nm of EPI on Au, with a graphite rod and Ag/AgCl (3 M KCl) serving as the counter and reference electrodes, respectively. Figure 3 shows the results of H_2O_2 photosynthesis (at 0 V vs. Ag/AgCl) in the H-cell setup employing 0.1 M HCl as electrolyte with continuous bubbling of O_2 . The same tungsten halogen lamp was used for irradiation with an intensity of 60 mW cm^{-2} . We found that in a two-compartment cell, the calculated Faradaic efficiency for ORR to H_2O_2 is significantly higher than in a one-compartment configuration, and was found to be more than 95%. The studies to date on semiconductor photocatalysts for ORR to H_2O_2 have relied on illumination of powdered or nanocrystalline particles in colloidal dispersion, with oxidation of a sacrificial donor providing the electrons for the photoreduction of O_2 to H_2O_2 . In order to compare the catalytic activity of these systems with the photocathodes reported in this paper, we utilize

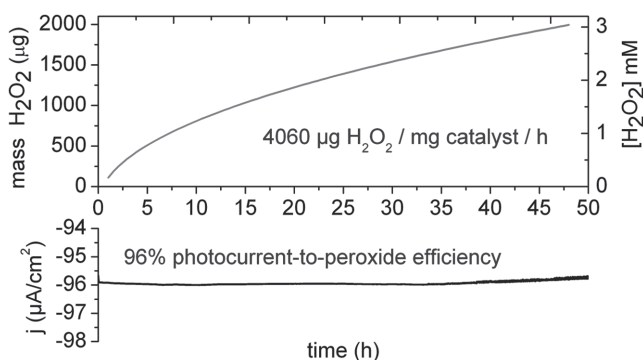


Figure 3. Photocathodic hydrogen peroxide evolution over 48 h in O_2 -purged 0.1 M HCl electrolyte with a 200 nm EPI on Cr/Au working electrode. An H-cell was used, with the cathode chamber illuminated with 60 mW cm^{-2} light from a halogen bulb. The working electrode was held at a potential of 0 V vs. Ag/AgCl. The oxidation of chloride to Cl_2 occurred in the anode chamber. Measurable quantities of H_2O_2 did not permeate into the anode chamber.

the metric of amount of peroxide per amount of catalyst per time ($\mu\text{g mg}_{\text{cat}}^{-1} \text{ h}^{-1}$) as well as the reported steady-state peroxide concentration achieved in the working solution. For the most optimal EPI photoelectrodes, we achieved a value of $4060 \mu\text{g mg}_{\text{cat}}^{-1} \text{ h}^{-1}$ with a concentration of $3 \times 10^{-3} \text{ M}$. This compares favorably with the best reported values from other semiconductor systems: CdS and ZnO powders gave $10\text{--}180 \mu\text{g mg}_{\text{cat}}^{-1} \text{ h}^{-1}$, with a working concentration up to $\approx 1 \times 10^{-3} \text{ M}$.^[10] Nanocrystalline colloidal ZnO under UV illumination was reported to give $21 \mu\text{g mg}_{\text{cat}}^{-1} \text{ h}^{-1}$.^[12] Graphitic C_3N_4 materials gave values of 4.25 ^[13] and 0.7 ^[14] $\mu\text{g mg}_{\text{cat}}^{-1} \text{ h}^{-1}$, with working concentrations in the range of a few millimolar. Table 1 shows a comparison of performance of semiconductor photocatalysts for H_2O_2 evolution. Adapting this photoelectrochemical method to potential larger-scale industrial synthesis would require maximizing the photocathode surface area and likely adopting a similar biphasic arrangement as is implemented in the current anthraquinone method, whereby synthesized H_2O_2 is extracted constantly out of the working solution to prevent back reactions. Alternatively, the hydrogen peroxide can be completely separated by distillation from aqueous solution. Nevertheless the stable and consistent generation of the concentrations reported here ($\approx 1\text{--}3 \times 10^{-3} \text{ M}$) is enough for certain applications, notably antiseptics, as such concentrations are cytotoxic to bacteria and fungi.^[6]

Table 1. Comparison of semiconductor photocatalysts for oxygen reduction to hydrogen peroxide.

Material	Sacrificial e^- donor	$\mu\text{g } H_2O_2/\text{mg catalyst/h}$	Maximum $[H_2O_2]$ [mM]	Year [Refs.]
ZnO	Formate, oxalate	180	0.9	1953 ^[9]
CdS	Phenol	25	3–4	1955 ^[10]
ZnO NCs	Formate	21	1.2	1994 ^[12]
g- C_3N_4	Ethanol	4.25	3	2014 ^[13]
g- C_3N_4	Water	0.7	1.6	2014 ^[14]
EPI	–	4060	3	2016 [this work]

2.3. Mechanistic Considerations

Two key materials properties shared by these hydrogen-bonded organic semiconductors enable ORR to H_2O_2 : (1) the combination of energetically high-lying and thus strongly reducing conduction band energy (-2.9 eV , $\approx -1.6 \text{ V}$ vs. NHE) with photochemical stability. Most organic semiconductors with similar conduction band energies are known to be photochemically and electrically unstable in O_2 and/or H_2O containing environments;^[34] (2) Proton-coupled two-electron redox chemistry. The electrochemistry of such pigments is known to resemble the quinone/hydroquinone system,^[32,35,36] and the two-electron redox behavior of the pigment indigo, for example, is probably the oldest electrochemical process exploited by humankind.^[37] The two-electron proton-coupled redox properties of such pigments are critical, in contrast to materials such as P3HT where single-electron electrochemistry dominates in aqueous conditions.^[22,24] Mechanistically, based on known electrochemical and excited-state properties of indigoid-like H-bonded pigments, the low-pH reaction proceeds as shown in Figure 4. Step (1) involves the generation of a photoexcited molecule at the aqueous interface. The excited state of H-chromophore pigments such as QNC and EPI features highly basic carbonyl groups, several orders of magnitude more basic than in the ground state.^[36,38] These are protonated, following photoreduction by the bulk semiconductor to create the reduced *enol* state^[39,40] on the surface (2). This molecule initiates nucleophilic attack on dissolved O_2 , resulting in a tetrahedral intermediate (3) analogous to the one postulated for the industrial anthraquinone peroxide process.^[6,41] This tetrahedral intermediate collapses, yielding a peroxide anion which abstracts a proton from the second *enol* unit, thereby restoring the ground-state EPI pigment and generating one H_2O_2 molecule (4). Other plausible mechanisms can be conceived, which include the NH proton of the pigment, however we discount this based on measurements of photocathodes comprising *N,N'*-dimethylepindolidione (Figures S16, S17, Supporting Information). Though inferior in performance and stability to hydrogen-bonded EPI, we found that the dimethyl derivative also gives ORR, indicating the NH proton cannot be participating in the ORR mechanism. The high-pH ORR should proceed via analogous mechanism to the low-pH one (Figure S18, Supporting Information), where photoreduction generates a reduced *enolate* at the surface (1), which initiates nucleophilic attack on O_2 (2) giving a similar tetrahedral intermediate which in turn decomposes with the loss of a peroxide anion accompanied by one hydroxide ion (3). The efficiency of ORR is in either case dependent on the quantity of accessible surface sites featuring carbonyl moieties. It is known that for quinacridones, the crystal facets with dangling NH and C=O bonds are small compared to the π -stacking and aromatic edge-on “hydrophobic contact” facets.^[38,42] This property leads to the high aspect-ratio nanocrystallite rods common for QNC pigments.

3. Conclusions

Aqueous photocatalysts based on hydrogen-bonded organic pigments represent an attractive avenue due to their wide-scale low-cost availability (thousands of tons per annum produced,

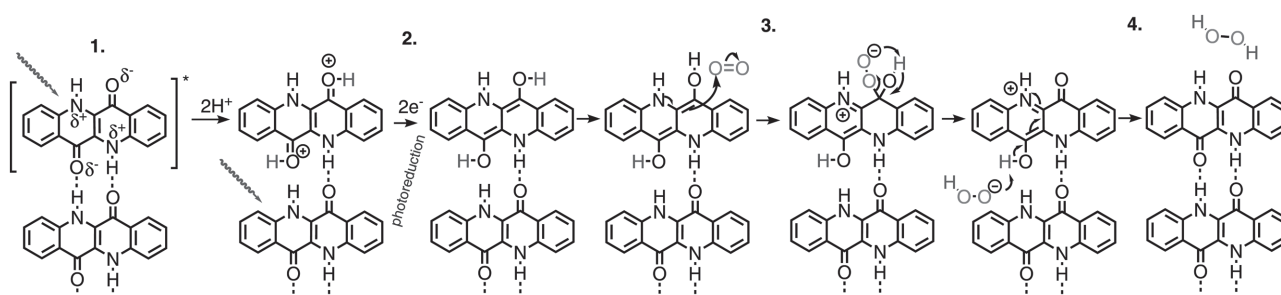


Figure 4. $2e^-/2H^+$ photoreduction mechanism of O_2 to H_2O_2 occurring at low pH.

costs around ≈ 0.2 – 0.5 $\text{\$ g}^{-1}$) and very low toxicity. Herein we have found their capability of affording stable photoelectrochemical ORR to peroxides in a pH range of 1–12. Moreover, hydrogen peroxide is a high-energy density product for chemical energy storage^[5] and is relevant for biochemistry. Besides generating H_2O_2 for various applications, we have shown that the photocathodes can be a component of a photoelectrochemical cell—an air/water battery, which generates electrical power while consuming water and O_2 . EPI was found to have excellent stability and give higher catalytic photocurrents. Based on photoluminescence quenching, EPI appears to be more efficient than QNC. Inorganic semiconductors (ZnO, CdS, etc.) known to photoreduce O_2 to H_2O_2 are only stable in a narrow pH range around 7, meanwhile the wide pH range accessible for the H-bonded pigments is an impressive advantage. The finding of stable photoelectrochemistry in aqueous environments is remarkable for organic semiconductors, and suggests the hydrogen-bonded pigment family as highly promising for photo(electro)catalysis applications.

4. Experimental Section

Sample Fabrication: Semiconductor-modified electrodes consisted of the structure glass/Cr/Au/semiconductor. 1.1 mm thick microscope slides were used as substrates. They were cleaned by sequential ultrasonication in acetone, isopropanol, detergent, and DI water. After drying under a stream of N_2 , the slides were treated with O_2 plasma for 5 min. Next the slides were transferred to a vacuum evaporation system (1×10^{-6} mbar) for deposition of chromium at a rate of 0.5 – 1 \AA s^{-1} (total thickness ≈ 3 nm), followed by gold at a rate of 1 – 2 nm s^{-1} . (total thickness ≈ 80 nm). Substrates were rotated during evaporation to ensure uniform thickness across the slides. Next the samples were treated with O_2 plasma again and transferred into a sealed, dry, glass container containing n-octyltrichlorosilane (OTS) vapor. Following vapor-phase silanization at 90 $^\circ\text{C}$ with OTS for ≈ 12 h, the samples were taken out, rinsed with isopropanol and DI water, then ultrasonicated in toluene for 15 min to remove any OTS on the gold electrode area and desorb any OTS multilayers. Samples were then rinsed with isopropanol and DI water again and dried. The OTS layer thus makes the glass surface hydrophobic, which is critical as otherwise water can seep through the polycrystalline semiconductor layer and lead to delamination of the semiconductor film. Adhesion of the polycrystalline film on Au is very good, however erosion of the pigment layer from the glass without OTS typically leads to partial delamination at the Au/glass edges. Next, the OTS-treated Cr/Au slides were transferred to a custom organic evaporation system (Vakis R&D) utilizing resistively heated alumina crucibles for deposition of the EPI or QNC layer. QNC (Kremer Pigmente, Germany) and EPI (synthesized according to ref. [28]) were both purified by $\times 2$ temperature-gradient sublimation prior to loading in the evaporation system. EPI and QNC were

evaporated at a rate of 2 – 6 \AA s^{-1} on substrates held at room temperature. QNC films of around 80 nm typically gave best performance while thicker EPI films, around 200 nm, were more optimal. Poly(3-hexylthiophene) (P3HT) was used for comparative purposes. A regioregular fractionated sample ($M_w > 100$ 000) was used. A 1.5 w% solution in chlorobenzene was prepared and spin-casted at 2000 rpm onto gold electrodes, followed by annealing at 140 $^\circ\text{C}$ for 10 min. The films had a thickness of ≈ 30 nm. Thicker films did not perform better.

Gas Chromatography Measurements: For the analysis of gaseous products, especially H_2 , a ThermoScientific Trace Ultra GC equipped with a thermal conductivity detector was used. 2 mL of sample was taken with a gas-tight glass syringe from the headspace of the electrolysis cell and was injected to GC. Electrolysis with plain Au electrodes was used to verify that H_2 gas could be measured in the headspace. Photocathodic current in EPI and QNC was found to never produce any measurable H_2 .

Horseradish Peroxidase/3,3',5,5'-Tetramethylbenzidine H_2O_2 Quantification: The quantification of the produced hydrogen peroxide was done spectrophotometrically by following the oxidation of TMB^[33] at 653 nm using PerkinElmer UV/VIS/NIR Spectrometer Lambda 1050. Electrolysis at 0 V vs. Ag/AgCl was performed on semiconductor-modified working electrodes under constant illumination. Aliquots of the electrolyte solution (14 μL) were afterwards added into a stirred mixture of 30 $\mu\text{g mL}^{-1}$ TMB (Sigma-Aldrich) and 0.750 ng mL^{-1} HRP (Sigma-Aldrich) in 0.1 M citrate-phosphate buffer pH 6.0, giving a volume of 1 mL. Quantification of the produced H_2O_2 was determined using extinction coefficient values^[33] for the TMB dimer and cross-checked with a calibration curve made by measuring solutions of known H_2O_2 (Merck) concentration.

Supporting Information

Supporting Information is available from the Wiley Online Library or from the author.

Acknowledgements

No competing financial interests have been declared. The authors acknowledge financial support from the Austrian Science Fund FWF via the projects TRP 294-N19, I-958-N20, and the Wittgenstein Prize for N.S. Sariciftci. A part of the work was supported by founding through the *Aufbruch Bayern* initiative of the state of Bavaria. The authors thank G. Romanazzi of the University of Bari, Italy, for supplying Epindolidione.

Received: April 19, 2016
Published online: May 24, 2016

- [1] K. Rajeshwar, P. Singh, J. DuBow, *Electrochim. Acta* **1978**, *23*, 1117.
[2] A. J. Bard, *Science* **1980**, *207*, 139.

- [3] C. Song, J. Zhang, in *PEM Fuel Cell Electrocatalysts and Catalyst Layers, Fundamentals and Applications* (Ed: J. Zhang) **2008**, p. 89, Springer, London, UK JiuJun Zhang.
- [4] L. Dai, Y. Xue, L. Qu, H.-J. Choi, J.-B. Baek, *Chem. Rev.* **2015**, *115*, 4823.
- [5] R. S. Disselkamp, *Energy Fuels* **2008**, *22*, 2771.
- [6] G. Goor, J. Glenneberg, S. Jacobi, in *Ullmann's Encyclopedia of Industrial Chemistry*, **2012**, Wiley-VCH, Weinheim.
- [7] S. Kato, J. Jung, T. Suenobu, S. Fukuzumi, *Energy Environ. Sci.* **2013**, *6*, 3756.
- [8] J. M. Campos-Martin, G. Blanco-Brieva, J. L. G. Fierro, *Angew. Chem., Int. Ed.* **2006**, *45*, 6962.
- [9] T. R. Rubin, J. G. Calvert, G. T. Rankin, W. MacNevin, *J. Am. Chem. Soc.* **1953**, *75*, 2850.
- [10] R. E. Stephens, B. Ke, D. Trivich, *J. Phys. Chem.* **1955**, *59*, 966.
- [11] T. Freund, W. P. Gomes, *Catal. Rev.: Sci. Eng.* **1970**, *3*, 1.
- [12] A. J. Hoffman, E. R. Carraway, M. R. Hoffmann, *Environ. Sci. Technol.* **1994**, *28*, 776.
- [13] Y. Shiraishi, S. Kanazawa, Y. Sugano, D. Tsukamoto, H. Sakamoto, S. Ichikawa, T. Hirai, *ACS Catal.* **2014**, *4*, 774.
- [14] Y. Shiraishi, S. Kanazawa, Y. Kofuji, H. Sakamoto, S. Ichikawa, S. Tanaka, T. Hirai, *Angew. Chem., Int. Ed.* **2014**, *53*, 13454.
- [15] D. S. Weiss, M. Abkowitz, *Chem. Rev.* **2010**, *110*, 479.
- [16] C. W. Tang, S. A. VanSlyke, *Appl. Phys. Lett.* **1987**, *51*, 913.
- [17] C. W. Tang, *Appl. Phys. Lett.* **1986**, *48*, 183.
- [18] G. Dennler, M. C. Scharber, C. J. Brabec, *Adv. Mater.* **2009**, *21*, 1323.
- [19] O. A. El-Rashiedy, S. Holdcroft, *J. Phys. Chem.* **1996**, *100*, 5481.
- [20] G. Suppes, E. Ballard, S. Holdcroft, *Polym. Chem.* **2013**, *4*, 5345.
- [21] G. M. Suppes, P. J. Fortin, S. Holdcroft, *J. Electrochem. Soc.* **2015**, *162*, H551.
- [22] S. Bellani, D. Fazzi, P. Bruno, E. Giussani, E. V. Canesi, G. Lanzani, M. R. Antognazza, *J. Phys. Chem. C* **2014**, *118*, 6291.
- [23] S. Günes, H. Neugebauer, N. S. Sariciftci, *Chem. Rev.* **2007**, *107*, 1324.
- [24] S. Bellani, A. Ghadirzadeh, L. Meda, A. Savoini, A. Tacca, G. Marra, R. Meira, J. Morgado, F. Di Fonzo, M. R. Antognazza, *Adv. Funct. Mater.* **2015**, *25*, 4531.
- [25] K. Hunger, *Rev. Prog. Color. Relat. Top.* **2005**, *35*, 76.
- [26] W. Herbst, K. Hunger, *Industrial Organic Pigments*, Wiley-VCH, Weinheim, Germany **2004**.
- [27] E. D. Głowacki, M. Irimia-Vladu, M. Kaltenbrunner, J. Gąsiorowski, M. S. White, U. Monkowius, G. Romanazzi, G. P. Suranna, P. Mastroilli, T. Sekitani, S. Bauer, T. Someya, L. Torsi, N. S. Sariciftci, *Adv. Mater.* **2013**, *25*, 1563.
- [28] E. D. Głowacki, G. Romanazzi, C. Yumusak, H. Coskun, U. Monkowius, G. Voss, M. Burian, R. T. Lechner, N. Demitri, G. J. Redhammer, N. Sünger, G. P. Suranna, S. Sariciftci, *Adv. Funct. Mater.* **2015**, *25*, 776.
- [29] D. Weiss, M. Burberry, *Thin Solid Films* **1988**, *158*, 175.
- [30] E. D. Głowacki, L. Leonat, M. Irimia-Vladu, R. Schwödiauer, M. Ullah, H. Sitter, S. Bauer, N. Serdar Sariciftci, *Appl. Phys. Lett.* **2012**, *101*, 023305.
- [31] R. Battino, T. R. Rettich, T. Tominaga, *J. Phys. Chem. Ref. Data* **1983**, *12*, 163.
- [32] E. D. Głowacki, G. Voss, N. S. Sariciftci, *Adv. Mater.* **2013**, *25*, 6783.
- [33] P. D. Josephy, T. Eling, R. P. Mason, *J. Biol. Chem.* **1982**, *257*, 3669.
- [34] A. Facchetti, *Chem. Mater.* **2011**, *23*, 733.
- [35] H. Zollinger, *Color Chemistry. Syntheses, Properties, and Applications of Organic Dyes and Pigments*, Wiley-VCH, Weinheim, Germany **2003**.
- [36] S. S. Labana, L. L. Labana, *Chem. Rev.* **1967**, *67*, 1.
- [37] M. Seefelder, *Indigo in Culture, Science, and Technology*, Ecomed, Landsberg, Germany **1994**.
- [38] *High Performance Pigments* (Eds: E. B. Faulkner, R. J. Schwartz), Wiley-VCH, Weinheim, Germany **2009**.
- [39] J. S. S. de Melo, R. Rondão, H. D. Burrows, M. J. Melo, S. Navaratnam, R. Edge, G. Voss, *ChemPhysChem* **2006**, *7*, 2303.
- [40] M. Dittmann, F. F. Graupner, B. Maerz, S. Oesterling, R. de Vivie-Riedle, W. Zinth, M. Engelhard, W. Lüttke, *Angew. Chem., Int. Ed. Engl.* **2014**, *53*, 591.
- [41] T. Kamachi, T. Ogata, E. Mori, K. Iura, N. Okuda, M. Nagata, K. Yoshizawa, *J. Phys. Chem. C* **2015**, *119*, 8748.
- [42] G. Lincke, *Dyes Pigm.* **2000**, *44*, 101.



Cite this: DOI: 10.1039/c8ta08151d

Received 21st August 2018
Accepted 20th November 2018

DOI: 10.1039/c8ta08151d

rsc.li/materials-a

Organic heterojunction photocathodes for optimized photoelectrochemical hydrogen peroxide production†

Maciej Gryszel,^{ID}*^{ab} Aleksandr Markov,^{ID}^{ab} Mikhail Vagin^{ID}^{ac}
and Eric Daniel Głowacki^{ID}^{ab}

Solar-to-chemical conversion of sunlight into hydrogen peroxide as a chemical fuel is an emerging carbon-free sustainable energy strategy. The process is based on the reduction of dissolved oxygen to hydrogen peroxide. Only limited amounts of photoelectrode materials have been successfully explored for photoelectrochemical production of hydrogen peroxide. Herein we detail approaches to produce robust organic semiconductor photocathodes for peroxide evolution. They are based on evaporated donor–acceptor heterojunctions between phthalocyanine and tetracarboxylic peryleneimide, respectively. These small molecules form nanocrystalline films with good operational stability and high surface area. We discuss critical parameters which allow fabrication of efficient devices. These photocathodes can support continuous generation of high concentrations of peroxide with faradaic efficiency remaining at around 70%. We find that an advantage of the evaporated heterojunctions is that they can be readily vertically stacked to produce tandem cells which produce higher voltages. This feature is desirable for fabricating two-electrode photoelectrochemical cells. Overall, the photocathodes presented here have the highest performance reported to date in terms of photocurrent for peroxide production. These results offer a viable method for peroxide photosynthesis and provide a roadmap of strategies that can be used to produce photoelectrodes with even higher efficiency and productivity.

Photoelectrochemical conversion of solar energy into chemical fuels is a key emerging sustainable energy approach. Water splitting to generate H₂ has been up to now the most popular approach; however, storage and transport of H₂ gas present challenges. An alternative concept of storing energy in the form

of hydrogen peroxide (H₂O₂) has been proposed for decades,^{1,2} yet a few key findings in recent years have allowed this concept to evolve from theory to practice. The first critical finding is the single-compartment peroxide fuel cell, introduced in 2008 and being optimized since.^{3,4} Peroxide fuel cells have a theoretical efficiency on a par with hydrogen fuel cells. The advantages of H₂O₂ fuel cells over hydrogen fuel cells are that peroxide is an aqueous solution, promising easier storage and handling, and that they do not require a membrane separator.

The concept of solar energy conversion to hydrogen peroxide in most of the reports is based on photochemical reduction of oxygen to hydrogen peroxide, catalysed by inorganic semiconductors, for example ZnO,^{5,6} TiO₂,⁷ and CdS.⁸ In brief, while the oxygenated suspension of an inorganic catalyst is irradiated with an appropriate light source, photogenerated electrons occupying the semiconductor conduction band reduce oxygen, leading to the formation of hydrogen peroxide. The same phenomenon was also shown for materials based on carbon nitride,^{9,10} and organic semiconductors, recently by our group.¹¹ As the reductive part of the photochemical process is efficient enough to lead to the accumulation of hydrogen peroxide up to a few mM, the major challenge is its oxidative part, necessary for closing the redox cycle. In most cases the energy level of the semiconductor valence band lies too high to enable water oxidation by the photoinduced hole. It can not only limit the system performance towards H₂O₂ evolution but also significantly affects the catalyst stability, as it can undergo self-oxidation.¹¹ Although the possibility of a full redox cycle leading to photoinduced oxygen reduction to hydrogen peroxide with simultaneous water oxidation was reported for some of the wide-bandgap semiconductors,^{12,13} the most common practice is the addition of sacrificial electron donors (*e.g.* oxalate and formate) to the reaction system. The oxidation potentials of these compounds are much lower than that of water, which allows the process to occur even for lower-bandgap semiconductors, such as polythiophene. Another possibility of overcoming the water oxidation limitation is photoelectrocatalysis. The field, first explored in 1972 by Fujishima

^aLaboratory of Organic Electronics, Linköping University, ITN Campus Norrköping, 60221, Norrköping, Sweden. E-mail: maciej.gryszel@liu.se

^bWallenberg Centre for Molecular Medicine (WCMM), Linköping University, Linköping, Sweden

^cDepartment of Physics, Chemistry and Biology, Linköping University, SE-581 83 Linköping, Sweden

† Electronic supplementary information (ESI) available. See DOI: 10.1039/c8ta08151d



and Honda¹⁴ using a TiO₂ based photoanode for water oxidation with hydrogen evolution on a platinum counter electrode, has developed significantly since that time. In comparison to photocatalysis, a photoelectrochemical cell allows one to separate reduction and oxidation processes to two different materials, each optimized for the intended electrochemical transformation. The possible application of a voltage bias can also facilitate the process and overcome the thermodynamic and kinetic barriers related to water oxidation. Although many examples of photocathodes^{15–17} and photoanodes^{18,19} enabling water splitting to H₂ and O₂ were published, the concept of a photocathode for hydrogen peroxide remains relatively unexplored. In the first report of such a device, Jakešová *et al.* showed that an organic semiconductor, the yellow pigment epindolidione (EPI), deposited on a gold substrate, is able to promote H₂O₂ photosynthesis, giving a stable photocurrent of approx. 100 $\mu\text{A cm}^{-2}$ over the course of 48 h with 96% faradaic efficiency.²⁰ This work was followed by a similar report on devices based on biscoumarin-containing acenes.²¹ Recently, photocathodes based on porphyrins,^{22,23} chemically polymerized eumelanin,²⁴ polymeric metal salen-type complexes,²⁵ and dye-sensitized NiO were reported.²⁶ Despite high faradaic yields achieved by these devices, a key parameter, photocurrent density, should be improved in order to achieve a H₂O₂ evolution rate sufficient enough for effective solar energy harvesting. While top-performing photocathodes for hydrogen evolution, biased at 0 V *vs.* Ag/AgCl, achieve photocurrent densities of up to 22 mA cm⁻² under 1 sun irradiation,²⁷ the abovementioned photocathodes for H₂O₂ photosynthesis give a much lower photocurrent density (around 0.1 mA cm⁻²) under these conditions; therefore there is a possibility of progress in this field. The realistic upper limit for the photocurrent in such a cell is limited by the concentration and diffusion of dissolved O₂; however values of several mA cm⁻² should be possible.

Herein we present our work on photocathodes for H₂O₂ synthesis based on an organic donor–acceptor heterojunction (referred to hereafter as the PN junction) made by evaporation of metal-free phthalocyanine (H₂Pc) and *N,N'*-dimethyl perylenetetracarboxylic bisimide (PTCDI), respectively (Fig. 1). This is the first example of H₂O₂ evolving photoelectrodes based on an organic PN junction, despite wide utilization of this concept in photovoltaics and photoelectrocatalysis for hydrogen evolution.^{28,29} The concept of the H₂Pc/PTCDI photocathode was based on previous findings by our group. Organic PN junctions made from these materials were recently reported as showing the ability to be charged upon excitation with pulsed red light (≤ 5 ms) in an electrolytic environment, producing stable devices for neuronal stimulation.³⁰ Although this process was proved to be non-faradaic in nature under these conditions, the PN junction behaviour under constant irradiation with white light was not investigated. In a parallel study, we also proved that if PTCDI films are polarized cathodically in an oxygenated electrolyte, they are able to electrochemically produce H₂O₂, being completely stable despite hundreds of hours of operation at high current density.³¹ As the PTCDI on Au system cannot be used as a photocathode due to the very low p-type conductivity of this semiconductor, the H₂Pc/PTCDI heterojunction,

ambipolar as a whole, gives the opportunity to obtain the photocathode which utilises favourable catalytic properties of the PTCDI towards the O₂ to H₂O₂ reduction.

We first evaluated the photoelectrochemical properties of the H₂Pc/PTCDI junction. This we fabricated by subsequent vacuum evaporation of both pigments on indium tin oxide (ITO) substrates modified with *n*-octyltriethoxysilane (OTS), resulting in the 60/60 nm double layer organic heterojunction with a nanocrystalline morphology. For comparison, H₂Pc on ITO and EPI on ITO were investigated as well. These samples were electrochemically characterized by cyclic voltammetry and chronoamperometry in a three-electrode system with a Ag/AgCl reference electrode (Fig. 2a and b), using an electrochemical H-cell as shown in Fig. S1.† The measurements were performed either under a tungsten halogen lamp illumination of 100 mW cm⁻² intensity or without illumination. All details of the sample preparation and electrochemical characterization can be found in the ESI.† As expected, the H₂Pc/PTCDI photocathode (hereinafter PN photocathode), biased at 0 V *vs.* Ag/AgCl under chopped illumination with 15 s amplitude, showed a pulsed photocurrent response of a constant value, proving the existence of a photofaradaic process. The system performance turned out to be similar to that of a reference EPI photocathode, prepared and measured in the same way. As the optical characteristics of the PN allow for far superior light absorption compared with EPI and it is known that PTCDI is a good catalyst for the O₂ to H₂O₂ reduction, the limited performance of the PN photocathode suggests that charge carrier recombination limits the performance. To suppress this process, we decided to deposit a thin layer of Au as an electron accepting layer on top of the PN photocathode. Besides being a good ohmic contact for electrons of PTCDI, Au at the same time can be a good catalyst for O₂/H₂O₂ reduction.^{32–34} The PN/Au photocathode showed an impressive, roughly twenty-fold photocurrent increase, to over 800 $\mu\text{A cm}^{-2}$ at 0 V *vs.* Ag/AgCl bias, stable for at least 2 h (black traces, Fig. 2a and b). However, under these conditions (pH 2) the faradaic yield was low (32.5–18.3%), regardless of the Au layer thickness used. Apparently, the gold structure obtained by vacuum evaporation does not favour the selective oxygen reduction to hydrogen peroxide under these conditions. The faradaic yield is lowered by the 4e⁻ reduction of O₂ to H₂O, 2e⁻ reduction of H₂O₂ to H₂O, or competition from H₂ evolution. In the next step of the photocathode optimization, we deposited a more selective electrocatalyst for H₂O₂ electrosynthesis on the PN/Au structure. There are many examples of such catalysts in the literature;^{35–37} nevertheless, based on our previous studies, we chose to fabricate two different PN photocathodes with organic pigments as catalysts for H₂O₂ electrosynthesis: PTCDI and EPI. The structures of the final photocathodes discussed in this work, PN/Au/PTCDI and PN/Au/EPI, are illustrated in Fig. 1b. It is worth noting that in the case of the PN/Au/PTCDI photocathode there are two layers of PTCDI which play different roles. The first one, deposited directly on H₂Pc, works as an n-type semiconductor in the organic PN junction. The second, final PTCDI layer is the electrocatalyst for the H₂O₂ synthesis. Compared with the PN/Au photocathode, the PN/Au/PTCDI, and PN/Au/EPI photocathodes showed significantly



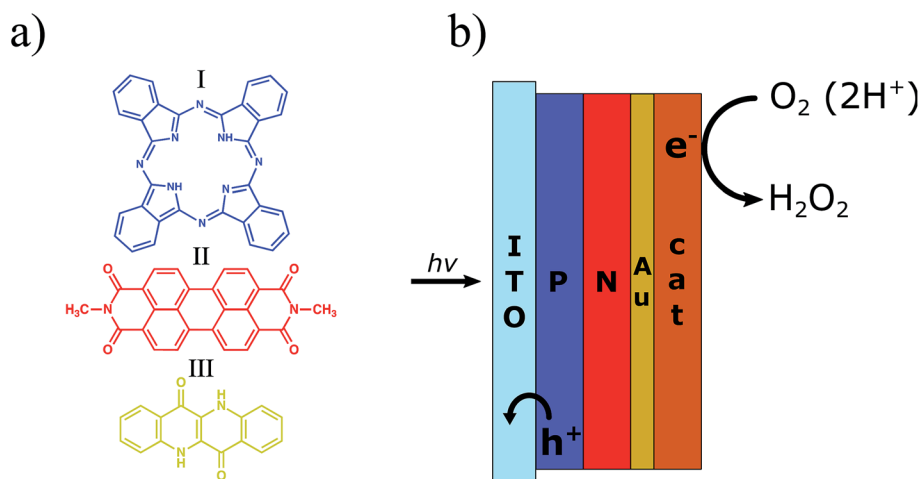


Fig. 1 (a) Chemical structure of the organic semiconducting pigments used in this work for fabrication of photocathodes: I – metal-free phthalocyanine (H₂Pc), II – *N,N'*-dimethyl perylene-3,4,9,10-tetracarboxylic diimide (PTCDI), and III – epindolidione (EPI). The outline colour corresponds to the approximate colour of the pigment. (b) Schematic of the PN/Au/catalyst photocathodes. H₂Pc (P), PTCDI (N) and Au are used as the organic donor, the organic acceptor, and electron transporting layer, respectively. The catalyst layer is either PTCDI or EPI. The thicknesses of the layers in the best performing devices characterized herein were as follows: 60/60/5/30 nm for the PN/Au/PTCDI photocathode and 30/30/5/100 nm for the PN/Au/EPI photocathode.

improved faradaic yields without almost any drop in photocurrent, giving stable photoelectrodes having the characteristic shown in Fig. 2c and d. The cyclic voltammetry experiments proved that both systems demonstrate high activity towards photoelectrochemical reduction of oxygen within a wide pH (pH = 2, 7, and 12) and bias potential range. For both photocathodes, the highest photocurrent was registered for the acidic electrolyte, what is consistent with previous findings for the PTCDI on Au electrode³¹ and EPI on Au photoelectrode.²⁰

Chronoamperometry experiments at 0 V vs. Ag/AgCl bias with 15 s light on/off cycles show excellent carrier transport dynamics, with a constant current value within the whole 15 s cycle. Lack of transient peaks on the $I = f(t)$ plot proves that these systems do not suffer from the occurrence of trap states (Fig. 2b, green and red traces).

To get a more detailed picture of the performance of the photoelectrochemical system, we performed linear sweep voltammetry with 15 s light on/off cycles in the -0.4 V to $+0.8$ V vs.

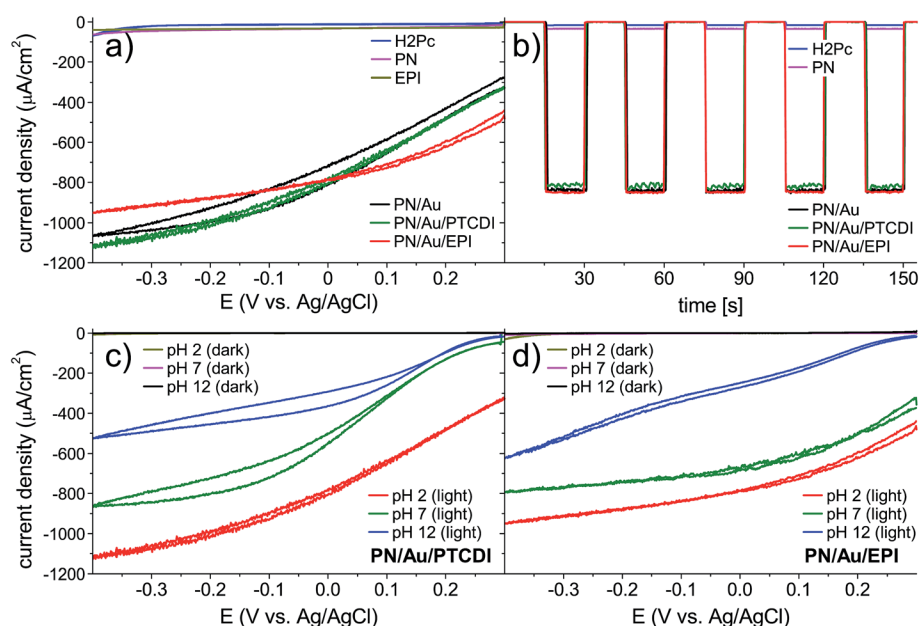


Fig. 2 (a) Cyclic voltammetry of the photocathodes at pH 2 under 100 mW cm^{-2} irradiation. As a reference, EPI and H₂Pc covered ITO substrates are prepared and measured. (b) Chronoamperometry of the photocathodes at pH 2 and 0 V vs. Ag/AgCl under pulsed (15 s) 100 mW cm^{-2} irradiation. (c and d) Comparison of cyclic voltammograms for the PN/Au/PTCDI and PN/Au/EPI photocathodes at pH 2, pH 7, and pH 12 in the dark and under 100 mW cm^{-2} irradiation.



Ag/AgCl range for PN/Au/PTCDI (Fig. 3a) and PN/Au/EPI (Fig. 3b). With these measurements we can estimate the onset potential of the photoelectrochemical process, and thus accurately determine the photovoltage generated by the device. The calculated onset potentials are shown in the insets in Fig. 3a and b. As expected, in both cases the highest onset potential (defined as the potential at which the photocurrent density is at least $10 \mu\text{A cm}^{-2}$) values were obtained at pH 2, being equal to 0.61 V and 0.68 V vs. Ag/AgCl for the PN/Au/PTCDI and PN/Au/EPI, respectively. As the obtained values are close to the theoretical 0.74 V vs. Ag/AgCl (assuming that the maximum photovoltage generated by the $\text{H}_2\text{Pc}/\text{PTCDI}$ PN junction is 550 mV,³⁸ the oxidation potential of the $2\text{H}^+ + 2\text{e}^- + \text{O}_2 \rightleftharpoons \text{H}_2\text{O}_2$ process is 0.19 V at pH 2 vs. Ag/AgCl⁴ and 0 V overpotential of oxygen reduction), it proves not only a judicious selection of the oxygen reduction catalysts used, but also the $2\text{e}^-/2\text{H}^+$ O_2 reduction mechanism itself. In the case of photoelectrochemical formation of hydrogen peroxide in acidic solution, there are two possible pathways of oxygen reduction leading to peroxide: direct $2\text{e}^-/2\text{H}^+$ reduction ($2\text{H}^+ + 2\text{e}^- + \text{O}_2 \rightleftharpoons \text{H}_2\text{O}_2$), or 1e^- reduction of oxygen to a protonated superoxide radical, which subsequently disproportionates to H_2O_2 ($\text{H}^+ + \text{e}^- + \text{O}_2 \rightleftharpoons \text{HO}_2^\cdot$ and then $2\text{HO}_2^\cdot \rightleftharpoons \text{H}_2\text{O}_2 + \text{O}_2$). Two-electron reduction, while thermodynamically favourable, may be kinetically more demanding than the single-electron pathway. As the oxidation potential of the protonated superoxide radical at pH 2 is -0.215 V vs. Ag/AgCl,³⁹ a photocathode for 1e^- reduction of oxygen to superoxide would not generate any photocurrent when the bias potential is more positive than 0.4 V vs. Ag/AgCl. Based on the obtained onset potential values, corroborated by the evidence of the faradaic yield measurements showing efficient H_2O_2 generation, we can conclude that the $2\text{e}^-/2\text{H}^+$ reduction mechanism of O_2 to H_2O_2 is the dominant pathway.

To provide additional evidence that our deduction of the $2\text{e}^-/2\text{H}^+$ mechanism is correct, we performed Koutecký–Levich analysis with a rotating disc electrode (RDE) allowing the determination of the number of electrons transferred per oxygen molecule. To avoid any possible issues with photocurrent stability (a reliable calculation requires very stable current), we simplified the system by measuring the electrocatalytic layer of 30 nm of PTCDI alone, which we deposited on the glassy carbon RDE surface. The high stability of the PTCDI

performance for the O_2 to H_2O_2 reduction was proven before.³¹ We conducted a series of linear sweep voltammetry scans with different rotation speeds in the oxygenated pH 2 electrolyte in the +0.4 V to -0.5 V vs. Ag/AgCl range (Fig. S2†). The details of the RDE experiment and Koutecký–Levich analysis can be found in the ESI.† The number of electrons transferred per oxygen molecule was calculated to be 2.03 at the -0.5 V vs. Ag/AgCl bias, which confirms the conclusion of the $2\text{e}^-/2\text{H}^+$ pathway considering the onset potential values.

Next, longer term photoelectrolysis experiments (6+ hours) were conducted with PN/Au/PTCDI and PN/Au/EPI systems and the faradaic efficiency of H_2O_2 production was checked. During these experiments, the electrolyte was constantly purged with moist O_2 gas and the catholyte was stirred. We found this procedure to be critical for maintaining a high oxygen reduction photocurrent (Fig. S3†). Both photoelectrodes, biased at 0 V vs. Ag/AgCl, showed a slight photocurrent decrease over time, and yet still retained 75% of their initial photocurrent after 6 h of photoelectrolysis at pH 2 (Fig. 4a and b). Within 6 h of photoelectrolysis, both PN/Au/PTCDI and PN/Au/EPI photocathodes showed good faradaic yield (86–62%, as shown in Fig. 4a and b); however, the values decreased over the course of the experiments. Previously, we observed the same dependence for the PTCDI on Au cathodes and it is related to the fact that a long electrolysis process results in the accumulation of H_2O_2 , whose concentration is comparable to the concentration of O_2 (approx. 1.3 mM under 1 atm). Under these conditions, H_2O_2 reduction to H_2O competes with the process of $\text{O}_2/\text{H}_2\text{O}_2$ synthesis and thus causes a decrease in the faradaic yield. For the same PTCDI on Au cathode it was also observed that the lower the current density, the higher the faradaic yield. This can be a good explanation for the lower faradaic yield of the PN/Au/EPI system in comparison to the previously reported EPI photocathodes. In that case, the faradaic yield was 96%; however, the current density was over 8 times lower than that for the PN/Au/EPI photocathode tested in this work.

Repetition of the experiment with the already 6 hour used samples showed that the performance loss is not reversible (Fig. 4a and b; green traces). As any physical damage to the layers (e.g. delamination or swelling) was not readily apparent, the performance loss could not be explained by the shrinking of the active area. Degradation of ITO used as a conducting

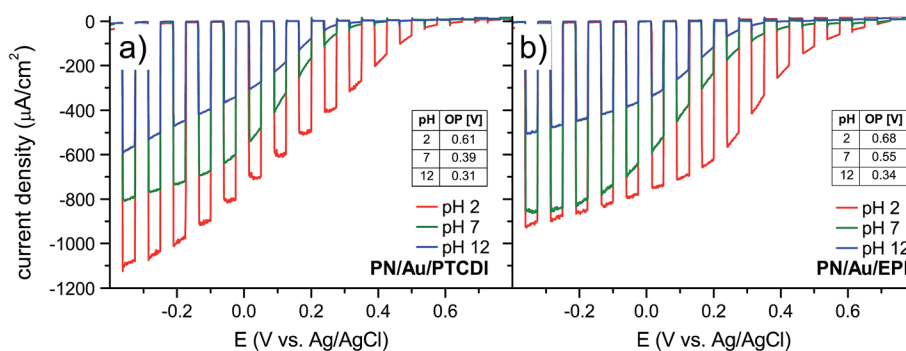


Fig. 3 Linear sweep voltammetry with 15 s light on/off cycles for (a) PN/Au/PTCDI and (b) PN/Au/EPI. Scans were measured at pH 2, pH 7, and pH 12 with 100 mW cm^{-2} irradiation. Values of onset potential (OP) at a given pH are shown in the inset tables.



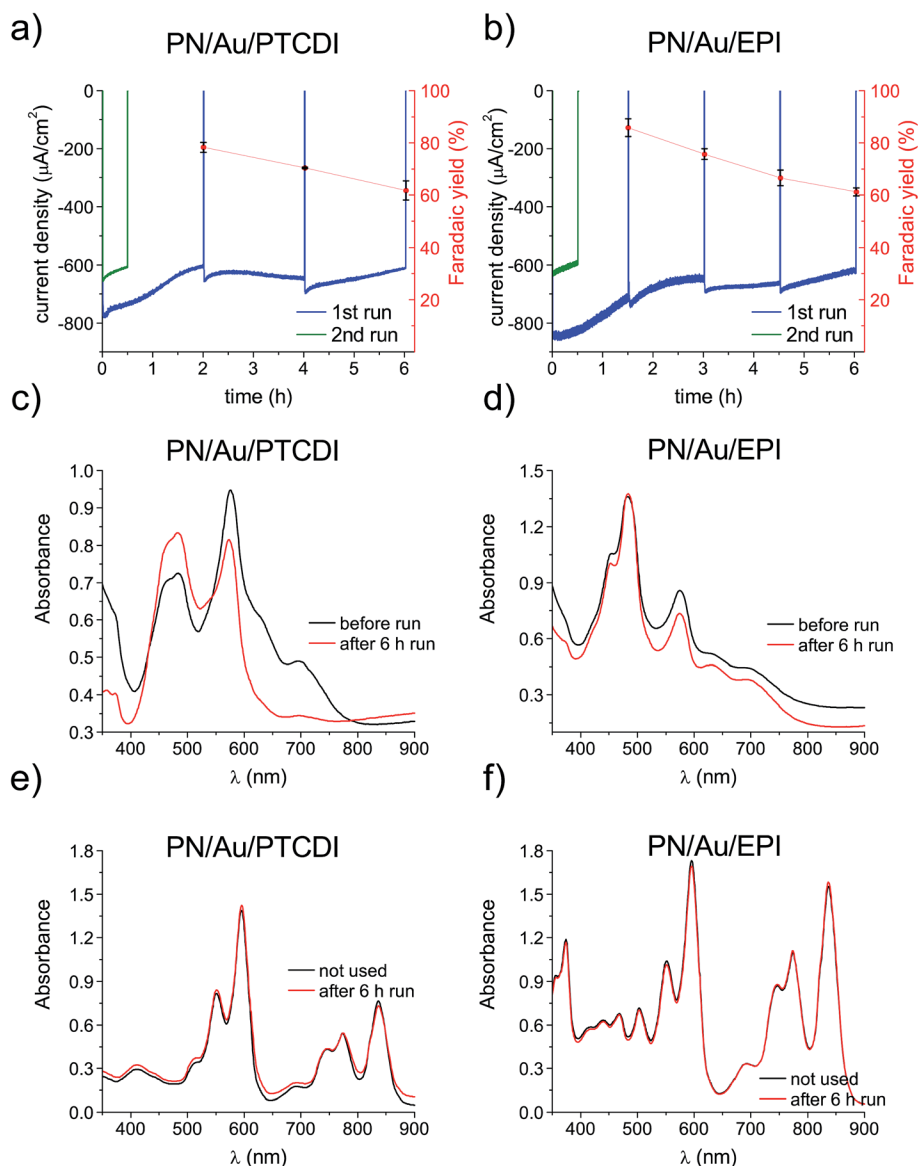


Fig. 4 Photoelectrolytic H_2O_2 evolution experiments for (a) PN/Au/PTCDI and (b) PN/Au/EPI photocathodes at pH 2, 0 V vs. Ag/AgCl bias, and under 100 mW cm^{-2} irradiation. The blue traces show the first 6 h run for the given photocathode while the green ones correspond to the second run. (c and d) Comparison of the UV-vis spectra for the respective photocathodes before and after 6 h of photoelectrolysis. (e and f) Comparison of the UV-vis spectra for the organic components of the same photocathodes dissolved in conc. H_2SO_4 after 6 h of photoelectrolysis with the corresponding spectra obtained for fresh devices. While optical absorption changes are obvious in the thin films, any optical changes are absent when the films are dissolved. This suggests that a morphological degradation and not a chemical degradation occurs.

substrate can also be excluded, as the same performance decrease was also observed when FTO and thin, transparent Au substrates were used. We compared SEM images of the samples before and after the long photoelectrolysis experiment to see if the observed phenomenon can be explained by the change in the catalyst layer morphology (Fig. S4†). However, in neither case had the morphology (shape and size of the nanocrystallites) changed obviously. That led to the conclusion that the drop in the photocathode performance may have been caused by a change in the crystalline structure of the organic pigment layers or irreversible chemical degradation of the multi-layered photoelectrocatalytic system. Organic pigments are widely known for their occurrence in different crystalline

forms, differing in their optical properties.⁴⁰ Polymorphic transition can be induced by many factors, such as solvent treatment,⁴¹ post deposition annealing⁴² or light exposure.⁴³ This can result in changes in optical properties and charge carrier mobilities and is likely in the case of our devices, operating under water conditions under constant illumination. Therefore, UV-vis spectra of the photocathodes before and after 6 h of photoelectrolysis were measured and compared (Fig. 4c and d). A significant change could be seen, especially for H_2Pc related peaks. This could be the result of the polymorphic transition, but could also be explained by chemical degradation. The latter seemed to be less likely, as in the case of chemical degradation of the layer deposited directly on the



conducting substrate, its chemical degradation would probably mean delamination of the whole multilayered system. The possibility of chemical degradation was excluded by measuring the optical absorption of the pigments following dissolution of the device layers in conc. H_2SO_4 . Many insoluble organic pigments can be dissolved in H_2SO_4 , as the strong acid protonates carbonyl moieties.⁴⁴ In the discussed case it can give a true picture of the chemical composition of the photocathodes without the influence of the polymorphic transitions. The UV-vis spectra of the H_2SO_4 dissolved cathodes show no change compared with the spectra of the corresponding solutions obtained for the unused samples. This proves that the photocathodes presented in this work are not affected by chemical degradation within 6 h of photoelectrolysis. This is an important finding in light of our previous studies,¹¹ confirming the hypothesis that the very same organic semiconductor, which is unstable as a photocatalyst even in the presence of a sacrificial electron donor, can be significantly more chemically stable after its deposition on the conductive substrate, when the applied bias facilitates efficient extraction of holes.

The UV-vis measurements of the photocathodes before and after the 6 h of photoelectrolysis demonstrated that the most probable explanation of the performance drop of the photocathodes is polymorphic transition of their constituents. However, the possibility of the problem with metastable PN interface morphology cannot be excluded. This is a common

issue in organic bulk heterojunction solar cells.⁴⁵ As described by Schaffer *et al.* with the example of a P3HT:PCBM based solar cell, the morphological degradation and performance worsening of the device during its operation is caused by the phase separation and growth of the domain size of the polymeric donor.⁴⁶ Although the photocathodes discussed herein, prepared by the vacuum evaporation process, are not typical bulk heterojunction structures, the interface morphology of the devices can also be crucial for their efficient performance. A thorough explanation of the changes leading to instability in these photocathode devices, supported by the structural investigation, will be provided in a forthcoming study.

The satisfactory performance of the devices operating at 0 V vs. Ag/AgCl at pH 2 encouraged us to check the possibility of their application in a nonbiased, 2-electrode system with a Pt counter electrode (Fig. 5). Unfortunately, upon irradiation, the photocurrent, low from the beginning, quickly vanished. We hypothesized that the process is limited by the relatively high potential of water oxidation at the Pt counter electrode and that the issue can be solved by changing the pH of the solution, as the reaction potential is pH dependent (*i.e.* 1.23 V at pH 0, 0.817 V at pH 7). To determine the optimum pH value for the 2-electrode photoelectrochemical cell, we ran the chronoamperometry experiment with pulsed light and a -0.5 V vs. Pt counter electrode bias, which was enough to register the photocurrent even for the pH 2 solution. As shown in Fig. 4b, in

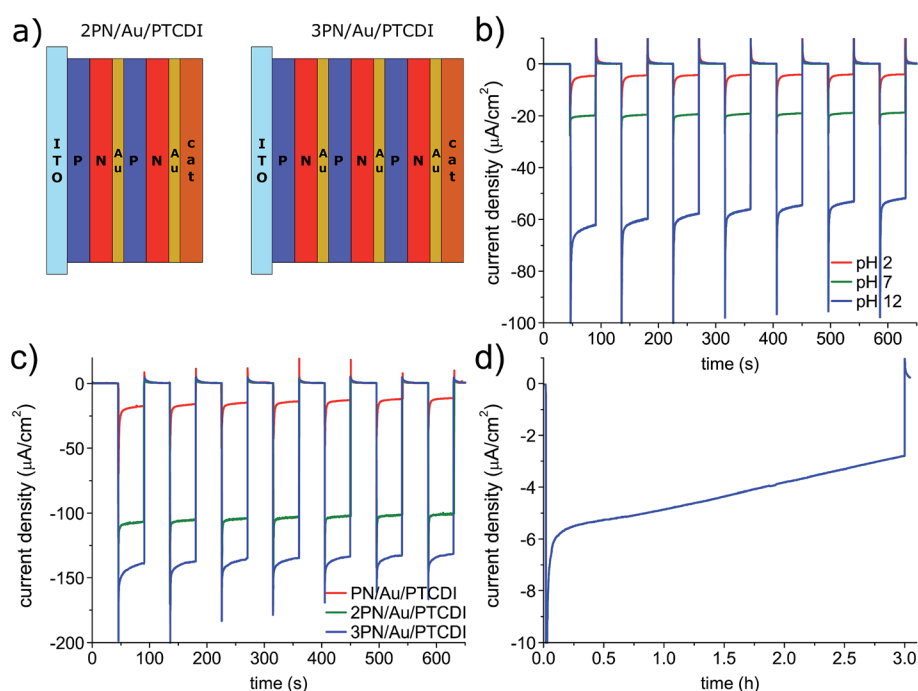


Fig. 5 (a) Structure of the tandem photocathodes. The optimum PN thickness was determined to be 30/30 nm; thicker layers prevent efficient light capture in the terminal PN junction in the 3 PN device, which worsens the performance. (b) The pH dependence for the PN/Au/PTCDI device operating in a 2-electrode arrangement at a constant bias of -0.5 V vs. a Pt counter electrode under pulsed (45 s) 100 mW cm^{-2} irradiation. In all cases, electrolyte with the same ionic strength was used (0.1 M). (c) Comparison of the tandem devices with different number of PN junctions operating in a 2-electrode arrangement at a constant bias of -0.5 V vs. a Pt counter electrode under pulsed (45 s) 100 mW cm^{-2} irradiation. The PN/Au/PTCDI sample used in this experiment has 30/30 nm PN junction thickness and was prepared only as a reference for the 2 and 3 PN devices. (d) The $I = f(t)$ dependence for a longer photoelectrolysis experiment with the 3 PN photocathode without external bias at pH 12.



contrast to the previously determined photocurrent dependence for the photocathodes operating at 0 V vs. Ag/AgCl in electrolytes of different pH, for the 2-electrode setup, as expected, at the same bias, the higher the pH the higher the photocurrent. Therefore, the photoelectrochemical cell operation is limited by water oxidation, and not the photocathodic process. Despite switching to the basic electrolyte, the photocurrent under non-biased conditions was still below 100 nA. It was clear that the photovoltage generated by the photoelectrode was too low. To address this issue, we fabricated the PN/Au/PTCDI tandem photocathodes with multiple PN junctions (Fig. 5a). The concept was inspired by previously published studies on so-called artificial leaves for photochemical hydrogen evolution – photovoltaic devices with multiple semiconductor layers which are able to generate a photovoltage high enough to run the water splitting reaction.^{47,48} We deposited the Au/PTCDI layers on top of the PN junction stacks with different number of junctions. As a recombination contact between the PN junctions, a transparent, thin Au layer (2 nm) was used in all cases. The performance of the devices with 1, 2, and 3 PN layers, operating in a 2 electrode setup at a -0.3 V bias vs. a Pt counter electrode, is shown in Fig. 5c. The 2PN/Au/PTCDI device gives an almost 3-fold photocurrent increase compared with the initial PN/Au/PTCDI design. The additional, third PN junction, gives a further rise in the performance and enables the possibility of running the photoelectrolysis process in a two-electrode setup without any external bias (Fig. 5d). Nevertheless, the device performance still needs to be improved, as the photocurrent is relatively low and unstable (over 50% drop within 3 h). However, the concept of tandems is viable, and is easily applicable in the case of evaporated thin films.

In summary, photocathodes with an organic semiconductor heterojunction and catalysts based on organic pigments were demonstrated as efficient devices for H₂O₂ photosynthesis. The photocurrent generated by the PN/Au/PTCDI and PN/Au/EPI devices at 0 V vs. Ag/AgCl is the highest ever reported for this process. The materials comprising the devices are chemically stable and do not apparently undergo any chemical degradation; however, their long-term performance is affected by morphological degradation. Though a long-standing belief that organic semiconductors are inherently photochemically unstable under oxygenated and aqueous conditions still exists, recent research has suggested that this is not necessarily the case. Crystalline pigments, such as those used here, with stable heteroatomic substituents and aromatic structures are known from the field of industrial colorants to show outstanding stability. Here we see that the organic materials do not chemically degrade, but rearrange morphologically, resulting in a decline in performance. Morphological changes such as donor/acceptor demixing have been implicated as the primary problem in organic heterojunction photovoltaics. It is therefore likely that the same issue needs to be addressed in organic photoelectrodes. This work proves that the discussed structures may be easily fabricated from cheap and abundant materials (such as the industrial pigments used in this work); however, further progress, addressing the issue of long-term stability and maximising the faradaic yield of the process, still needs to be

made. Another aspect of morphological optimisation is the utilization of a bulk heterojunction architecture created by coevaporation of donor and acceptor materials, or potentially finding solution-processable analogues which also allow such a heterojunction formation. Application of other semiconductors and reaction catalysts should be evaluated, as it could not only increase the long-term stability and the reaction selectivity, but also the device photovoltage, enabling possibility of efficient photoelectrolysis without external bias.

Conflicts of interest

The authors declare no conflicts of interest.

Acknowledgements

The authors are grateful for financial support from the Knut and Alice Wallenberg Foundation, especially from the Wallenberg Centre for Molecular Medicine at Linköping University, and Vinnova within the framework of Treearch.se.

References

- 1 R. S. Disselkamp, *Energy Fuels*, 2008, **22**, 2771–2774.
- 2 R. S. Disselkamp, *Int. J. Hydrogen Energy*, 2010, **35**, 1049–1053.
- 3 S. ichi Yamazaki, Z. Siroma, H. Senoh, T. Ioroi, N. Fujiwara and K. Yasuda, *J. Power Sources*, 2008, **178**, 20–25.
- 4 S. Fukuzumi and Y. Yamada, *ChemElectroChem*, 2016, **3**, 1978–1989.
- 5 T. R. Rubin, J. G. Calvert, G. T. Rankin and W. MacNevin, *J. Am. Chem. Soc.*, 1953, **75**, 2850–2853.
- 6 A. J. Hoffman, E. R. Carraway and M. R. Hoffmann, *Environ. Sci. Technol.*, 1994, **28**, 776–785.
- 7 J. R. Harbour, J. Tromp and M. L. Hair, *Can. J. Chem.*, 1985, **63**, 204–208.
- 8 R. E. Stephens, B. Ke and D. Trivich, *J. Phys. Chem.*, 1955, **59**, 966–969.
- 9 Y. Kofuji, Y. Isobe, Y. Shiraishi, H. Sakamoto, S. Tanaka, S. Ichikawa and T. Hirai, *J. Am. Chem. Soc.*, 2016, **138**, 10019–10025.
- 10 R. Wang, X. Zhang, F. Li, D. Cao, M. Pu, D. Han, J. Yang and X. Xiang, *J. Energy Chem.*, 2018, **27**, 343–350.
- 11 M. Gryszel, M. Sytnyk, M. Jakešová, G. Romanazzi, R. Gabrielsson, W. Heiss and E. D. Głowacki, *ACS Appl. Mater. Interfaces*, 2018, **10**, 13253–13257.
- 12 N. Kaynan, B. A. Berke, O. Hazut and R. Yerushalmi, *J. Mater. Chem. A*, 2014, **2**, 13822–13826.
- 13 T. Baran, S. Wojtyła, A. Vertova, A. Minguzzi and S. Rondinini, *J. Electroanal. Chem.*, 2018, **808**, 395–402.
- 14 A. Fujishima and K. Honda, *Nature*, 1972, **238**, 37–38.
- 15 A. Paracchino, V. Laporte, K. Sivula, M. Grätzel and E. Thimsen, *Nat. Mater.*, 2011, **10**, 456–461.
- 16 L. Li, L. Duan, F. Wen, C. Li, M. Wang, A. Hagfeldt and L. Sun, *Chem. Commun.*, 2012, **48**, 988–990.
- 17 J. D. Benck, S. C. Lee, K. D. Fong, J. Kibsgaard, R. Sinclair and T. F. Jaramillo, *Adv. Energy Mater.*, 2014, **4**(18), 1400739.



- 18 T. W. Kim and K.-S. Choi, *Science*, 2014, **343**, 990–994.
- 19 G. Wang, H. Wang, Y. Ling, Y. Tang, X. Yang, R. C. Fitzmorris, C. Wang, J. Z. Zhang and Y. Li, *Nano Lett.*, 2011, **11**, 3026–3033.
- 20 M. Jakešová, D. H. Apaydin, M. Sytnyk, K. Oppelt, W. Heiss, N. S. Sariciftci and E. D. Głowacki, *Adv. Funct. Mater.*, 2016, **26**, 5248–5254.
- 21 M. K. Węclawski, M. Jakešová, M. Charyton, N. Demitri, B. Koszarna, K. Oppelt, S. Sariciftci, D. T. Gryko and E. D. Głowacki, *J. Mater. Chem. A*, 2017, 20780–20788.
- 22 N. U. Day and C. C. Wamser, *J. Phys. Chem. C*, 2017, **121**, 11076–11082.
- 23 D. H. Apaydin, H. Seelajaroen, O. Pengsakul, P. Thamyongkit, N. S. Sariciftci, J. Kunze-Liebhusser and E. Portenkirchner, *ChemCatChem*, 2018, **10330**, 1793–1797.
- 24 L. Migliaccio, M. Gryszel, V. Derek, A. Pezzella and E. D. Głowacki, *Mater. Horiz.*, 2018, **5**, 984–990.
- 25 A. S. Konev, Y. Kayumov, M. P. Karushev and Y. V. Novoselova, *ChemElectroChem*, 2018, **5**, 1–6.
- 26 O. Jung, M. L. Pegis, Z. Wang, G. Banerjee, C. T. Nemes, W. L. Hoffeditz, J. T. Hupp, C. A. Schmittenmaer, G. W. Brudvig and J. M. Mayer, *J. Am. Chem. Soc.*, 2018, **140**, 4079–4084.
- 27 B. Seger, T. Pedersen, A. B. Laursen, P. C. K. Vesborg, O. Hansen and I. Chorkendorff, *J. Am. Chem. Soc.*, 2013, **135**, 1057–1064.
- 28 T. Bourgeteau, D. Tondelier, B. Geffroy, R. Brisse, S. Campidelli, R. Cornut and B. Jusselme, *J. Mater. Chem. A*, 2016, **4**, 4831–4839.
- 29 A. Ghadirzadeh, F. Fumagalli, A. Mezzetti, S. Bellani, L. Meda, M. R. Antognazza and F. Di Fonzo, *ChemPhotoChem*, 2018, **2**, 283–292.
- 30 D. Rand, M. Jakešová, G. Lubin, I. Vebráite, M. David-Pur, V. Derek, T. Cramer, N. S. Sariciftci, Y. Hanein and E. D. Głowacki, *Adv. Mater.*, 2018, **30**, 1707292.
- 31 M. Warczak, M. Gryszel, M. Jakešová, V. Derek and E. D. Głowacki, *Chem. Commun.*, 2018, **54**, 1960–1963.
- 32 Y. Yang, C. Dai, A. Fisher, Y. Shen and D. Cheng, *J. Phys.: Condens. Matter*, 2017, **29**, 365201.
- 33 N. S. K. Gowthaman, S. Shankar and S. Abraham John, *J. Electroanal. Chem.*, 2018, **812**, 37–44.
- 34 E. Pizzutilo, O. Kasian, C. H. Choi, S. Cherevko, G. J. Hutchings, K. J. J. Mayrhofer and S. J. Freakley, *Chem. Phys. Lett.*, 2017, **683**, 436–442.
- 35 Y. Sun, I. Sinev, W. Ju, A. Bergmann, S. Dresch, S. Köhl, C. Spöri, H. Schmies, H. Wang, D. Bernsmeier, B. Paul, R. Schmack, R. Kraehnert, B. Roldan Cuenya and P. Strasser, *ACS Catal.*, 2018, **8**, 2844–2856.
- 36 Z. Lu, G. Chen, S. Siahrostami, Z. Chen, K. Liu, J. Xie, L. Liao, T. Wu, D. Lin, Y. Liu, T. F. Jaramillo, J. K. Nørskov and Y. Cui, *Nat. Catal.*, 2018, **1**, 156–162.
- 37 H. W. Kim, M. B. Ross, N. Kornienko, L. Zhang, J. Guo, P. Yang and B. D. McCloskey, *Nat. Catal.*, 2018, **1**, 282–290.
- 38 P. Peumans, A. Yakimov and S. R. Forrest, *J. Appl. Phys.*, 2003, **93**(7), 3693–3723.
- 39 D. A. Armstrong, R. E. Huie, S. Lyman, W. H. Koppenol, G. Merényi, P. Neta, D. M. Stanbury, S. Steenken and P. Wardman, *BioInorg. React. Mech.*, 2013, **9**, 59–61.
- 40 G. Klebe, F. Graser, E. Hädicke and J. Berndt, *Acta Crystallogr., Sect. B: Struct. Sci.*, 1989, **45**, 69–77.
- 41 Q. Zhang, H. Chen, Y. Liu and D. Huang, *Dyes Pigm.*, 2004, **63**, 11–16.
- 42 S. M. Bayliss, S. Heutz, G. Rumbles and T. S. Jones, *Phys. Chem. Chem. Phys.*, 1999, **1**, 3673–3676.
- 43 L. Gaffo, M. J. S. P. Brasil, F. Cerdeira and W. C. Moreira, *Thin Solid Films*, 2005, **488**, 236–241.
- 44 Y. Nagao, *Prog. Org. Coat.*, 1997, **31**, 43–49.
- 45 P. Cheng and X. Zhan, *Chem. Soc. Rev.*, 2016, **45**, 2544–2582.
- 46 C. J. Schaffer, C. M. Palumbiny, M. A. Niedermeier, C. Jendrzewski, G. Santoro, S. V. Roth and P. Müller-Buschbaum, *Adv. Mater.*, 2013, **25**, 6760–6764.
- 47 S. Y. Reece, J. A. Hamel, K. Sung, T. D. Jarvi, A. J. Esswein, J. J. H. Pijpers and D. G. Nocera, *Science*, 2011, **334**, 645–648.
- 48 S. Esiner, R. E. M. Willems, A. Furlan, W. Li, M. M. Wienk and R. A. J. Janssen, *J. Mater. Chem. A*, 2015, **3**, 23936–23945.





Cite this: DOI: 10.1039/c9cc09215c

 Received 26th November 2019,
Accepted 2nd January 2020

DOI: 10.1039/c9cc09215c

rsc.li/chemcomm

Organic thin film photofaradaic pixels for on-demand electrochemistry in physiological conditions†

 Maciej Gryszel ^{ab} and Eric Daniel Głowacki ^{*abc}

We report ultrathin organic photovoltaic elements optimized to run photofaradaic reactions in biological conditions. We demonstrate concurrent oxygen reduction to hydrogen peroxide and glucose oxidation. The devices are powered by deep-red irradiation in the tissue transparency window. We utilize bilayers of phthalocyanine, acting as the light absorber, and perylene diimide, functioning as both electron-acceptor and the hydrogen peroxide evolution electrocatalyst. These heterojunction bilayers are stable when irradiated in simulated physiological conditions, producing photovoltages sufficient to simultaneously drive cathodic oxygen reduction to H₂O₂ and anodic oxidation of glucose. We find that optimization of the anode metal is critical for sustained photofaradaic reactivity. Our results demonstrate a robust “wet” thin film photovoltaic with potential for physiological applications where localized electrochemical manipulation is desired, in particular the delivery of reactive oxygen species.

Light-triggered production of reactive oxygen species (ROS) is central to photodynamic therapy, where generation of singlet oxygen is desired.¹ While delivery of ¹O₂ is well-established, recently the ROS species H₂O₂ has attracted attention as a signaling molecule effecting various (electro)physiological processes.^{2–4} Levels of H₂O₂ in the micromolar range, for instance, can regulate the gating of voltage-gated potassium channels which are critical to the behavior of excitable cells.⁵ Manipulation of local H₂O₂ also can be used to affect mitochondrial metabolic processes. The use of organic semiconducting nanoparticles as light absorbers to photogenerate ROS has already begun to gain traction in biophysical research.^{6–8} In our own research we have introduced aqueous organic dyes for photochemical ROS generation.⁹ The aim of this work is to

develop a solid-state photofaradaic device which can produce H₂O₂ *via* O₂ reduction, while consuming sacrificial electron donors available in physiological conditions. This device should operate in the tissue transparency window (roughly 620–800 nm). The great body of work on photocatalytic generation of H₂O₂ in aqueous conditions relies on higher energy photons.¹⁰ For this reason, here we use an organic heterojunction with broad absorption throughout the deep-red region. The metal-free phthalocyanine/*N,N'*-dimethylperylene-tetracarboxylic diimide (H₂Pc/PTCDI) materials system we have elaborated previously in our studies of organic electrolytic photocapacitors (OEPCs),^{11,12} photodiodes for the driving of electrophoretic ion pumps,¹³ and finally as photocathodes for O₂ reduction to H₂O₂.¹⁴ A salient feature emerging from these works is the remarkable stability of the H₂Pc/PTCDI donor/acceptor (PN) junction.¹² OEPC devices with a H₂Pc/PTCDI heterojunction operate in AC mode with short light impulses. Initial tests of long-term pulsing in artificial cerebrospinal fluid demonstrated that hydrogen peroxide forms in the solution.¹² Peroxide formation was only observed when the back contact of the device was gold. In the case where the back contact used was indium tin oxide (ITO), no detectable levels of peroxide were found. This can be rationalized by the fact that gold can support various faradaic reactions,¹⁵ while ITO has a large inert potential window.¹⁶ This finding points out that for net peroxide production, a photofaradaic cycle with a cathodic and anodic component must be supported. Here we detail how stable, DC photofaradaic devices can be produced for continuous H₂O₂ generation in biological environments.

We fabricated PN bilayers (30 + 30 nm) on semitransparent, evaporated gold layers (10 nm thickness). As a substrate for this and subsequent tests, we used Parylene-C. Parylene-C was chosen since it is a well-established ultrathin polymeric material for biocompatible implants.¹⁷ The PN bilayer serves as the charge generation layer: photogenerated excitons separate at the donor/acceptor interface, transferring electrons to the PTCDI layer. PTCDI is an established electrocatalyst for O₂ reduction to H₂O₂,¹⁸ and this PN charge generation layer we have previously optimized for photocathodes for H₂O₂ generation.¹⁴ Photogenerated holes,

^a Laboratory of Organic Electronics, ITN Campus Norrköping, Linköping University, Norrköping, Sweden. E-mail: eric.glowacki@liu.se

^b Wallenberg Centre for Molecular Medicine (WCMM) Linköping University, Linköping, Sweden

^c Warsaw University of Technology, Faculty of Chemistry, Warsaw, Poland

† Electronic supplementary information (ESI) available: Detailed experimental methods. See DOI: 10.1039/c9cc09215c



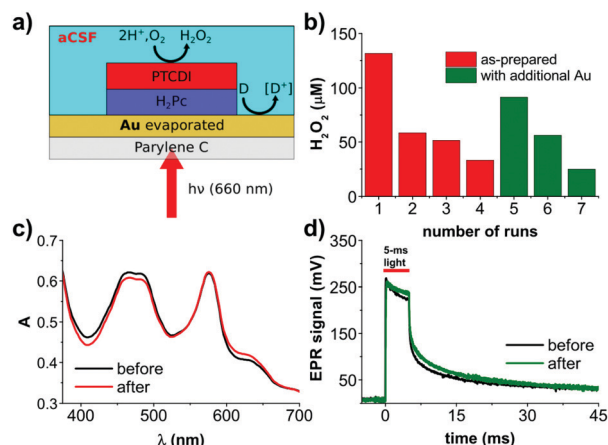


Fig. 1 Organic photofaradaic devices for H_2O_2 evolution. (a) Device structure schematic, comprising a Parylene-C 5 μm -thick foil, semitransparent layer of gold (10 nm, evaporated) and an organic PN junction, fabricated from organic pigments: H_2Pc (P type) and PTCDI (N type). Devices are fully immersed in aCSF electrolyte and irradiated with 660 nm light. (b) H_2O_2 concentrations measured in the electrolyte around the device in oxygen-containing aCSF solution under constant irradiation with red light (660 nm, 11 mW mm^{-2}). The chart presents final $[\text{H}_2\text{O}_2]$ at the end of each 30 min experiment. After each cycle, the electrolyte has been replaced with fresh solution. After the 4th experiment, the external layer of gold has been refreshed by thermal evaporation of additional 10 nm of Au. This series of experiments shows the crucial role of gold activity for the performance of the system. (c) Comparison of the UV-Vis spectra of the PN system, before and after the 4th experiment shows its photostability. (d) Electrical photo-response of the PN system before and after the 4th experiment shows stability of the photogenerated voltage.

meanwhile, are injected into the gold layer, where they can lead to oxidation of suitable electron donors in solution. For relevance to implantable devices in biomedical applications aimed at interfacing with the nervous system, we conducted experiments in artificial cerebrospinal fluid (aCSF). Following continuous irradiation with an LED emitting at 660 nm for 30 min, a concentration of 130 μM H_2O_2 was measured in the solution. Pictures of the experimental setup can be found in Fig. S1 (ESI \dagger). Repeating this experiment for several more 30 min cycles (same device, fresh electrolyte) led to rapid decrease in the amount of evolved H_2O_2 (Fig. 1b). We hypothesized that unfortunately the PN layers may be unstable under conditions of continuous high-intensity irradiation. We measured the UV-Vis spectrum of the used device, finding that in fact that spectrum was unchanged with respect to an as-fabricated device (Fig. 1c). Moreover, we registered the photovoltage using the transient electrophotoreponse method,¹¹ and found that the photovoltage and charging dynamics of the PN device were unchanged after the repeated runs (Fig. 1d). Therefore, the PN component itself appears to be stable and the origin of the H_2O_2 production drop-off must be something else. We suspected that the Au back contact may be the source of the problem. From work on OEPCs,¹² we knew that the back contact is critical to the overall capacitive *versus* faradaic performance of the device. We verified first that the Au layer was not degraded and of lower conductivity, it in fact had the same resistance as measured with a multimeter before and after. It led us to the hypothesis that the Au layer had,

at the microscopic level, lost its electrocatalytic properties. As a rapid empirical evidence that this may be the case, we evaporated a 10 nm layer of new gold on top of the part of the sample which was not covered by the PN junction, and measured a nearly threefold increase in the evolved H_2O_2 (Fig. 1b). This performance again declined with more subsequent runs – the Au was losing its catalytic properties. It was therefore clear that the PN layers provided stable operation, but faradaic performance of the gold back contact was the limitation to sustained faradaic behavior. Considering the photovoltage produced by the Au/PN device and the composition of the aCSF, it is clear that the only possible oxidizable species is glucose. We proceeded thus with the understanding that the back-contact material must be optimized with respect to stability as a glucose oxidizing electrocatalyst.

We therefore focused our attention on exploring potential electrocatalysts for glucose oxidation. Many examples exist in the literature concerning metallic catalysts based on Cu, Ag, Pd, Pt, or enzymes.¹⁹ In the case of our application, the catalyst must not only be highly stable in a chloride-containing electrolyte, but also should not catalyze the decomposition of or otherwise react with hydrogen peroxide. Cu or Ag do not have sufficient electrochemical stability to work in our device in the given conditions, while materials like Pt rapidly decompose H_2O_2 . We tested evaporated Pd films and found that they too decompose H_2O_2 . This led us to dig deeper into optimizing gold itself as a glucose oxidation catalyst. The nuances of glucose oxidation on gold surfaces are well-described in the literature, especially in relation to nonenzymatic amperometric glucose sensors.¹⁹ In many of such studies, gold is electrodeposited on top of an underlying conductor. We elected to pursue the same approach, and try electrodeposited gold layers around the PN pixel on preevaporated gold thin films. The thin evaporated gold under the PN pixel is necessary to maintain semitransparency. We attempted different gold electrodeposition conditions (Fig. S2, ESI \dagger), finding favorable conditions using HAuCl_4 as the precursor²⁰ and two-electrode potentiostatic deposition at -2 V *versus* the counter electrode. A comparison of results from different electrodeposition conditions, as well different evaporated and sputtered Au films, can be found in Fig. S2 (ESI \dagger). Fig. 2a illustrates this photofaradaic pixel modified with the optimal ring of electrodeposited gold. The performance of these modified devices was significantly higher in terms of peroxide yield, and the stability was likewise much better. In total, thirteen rounds of 30 minute irradiation experiments were performed, showing the enhanced performance stability afforded by the electrodeposited gold. After these repeated cycles, the UV-Vis absorption spectrum and the EPR photovoltage were recorded (Fig. 2c and d) and once again proved that the organic PN junction layers were undegraded. Scanning electron microscopy (SEM) of PN layers before and after the experiment likewise showed no significant changes in morphology, pinhole formation, *etc.* (Fig. 2d). Encouraged by the better performance afforded by electrodeposited gold layers, we tested a longer irradiation experiment, 180 min, and found that H_2O_2 rises to around 2000 μM , at which point it saturates. Such a peroxide saturation



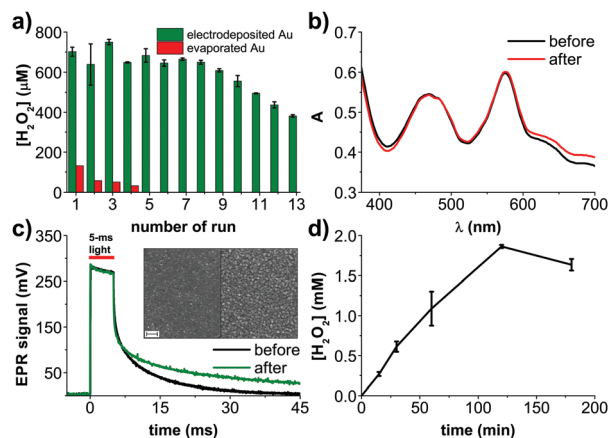


Fig. 2 Devices with electrodeposited Au anodes. (a) $[\text{H}_2\text{O}_2]$ produced by the device in oxygen-containing aCSF solution under constant irradiation with red light (660 nm , 11 mW mm^{-2}). The chart presents final $[\text{H}_2\text{O}_2]$ at the end of each, 30 min cycle. Compared with PN devices with evaporated Au, it shows not only much higher performance but also higher stability. (b) Comparison of the UV-Vis spectra of the PN system, before and after the 13th experiment. The PN layer is photostable. (c) Electrical photoresponse of the PN system before and after the 13th experiment, evidencing no decrease of the generated photovoltage. (c, inset) Comparison of SEM images of the PN structure before and after the 13th experiment. Shape and average size of the nanocrystalline PTCDI domains remains unchanged. Scale bar = 200 nm. (d) H_2O_2 photoevolution over 180 min, showing saturation of $[\text{H}_2\text{O}_2]$ after 2 h.

concentration can be rationalized considering the competitive process of H_2O_2 being further reduced to H_2O . This process begins to become efficient when the $[\text{H}_2\text{O}_2]$ and $[\text{O}_2]$ start to reach similar levels in the solution. In O_2 saturated solutions, where $[\text{O}_2]$ is around 1–2 mM, PTCDI as an electrocatalyst starts leveling off at an H_2O_2 equilibrium concentration of 20–30 mM.¹⁸ In ambient air as in the experiments done here, the $[\text{O}_2]$ is around 200–300 μM , therefore a saturated H_2O_2 concentration of 2 mM is reasonable. It should also be considered that glucose is present at 10 mM concentration, therefore by the end of this experiment it may also become a limiting reagent. Finally, the stability of H_2O_2 should be taken into account. We measured a background decomposition rate of roughly 500 nM min^{-1} under irradiation of the blank electrolyte alone. This rate was found not to be changed by presence of Au.

To better understand the role of the Au anode component of the photofaradaic pixel, we performed electrochemical measurements on the gold films alone. From CV scans of comparing electrodeposited Au films in aCSF with and without glucose, oxidation peaks resulting from the addition of glucose are clearly visible (Fig. 3a). In contrast, evaporated Au films are a poor electrocatalytic surface. The CV (Fig. 3b) shows roughly ten times lower anodic current, much less apparent peaks, and lower capacitive current on the backward scan when glucose is included in the solution, all together suggesting rapid poisoning of the catalytic surface even during the course of a single cycle. The poisoning of Au surfaces due to glucose oxidation is described in the literature.²¹ We tested stability and performance by performing chronoamperometry on the Au electrodes (Fig. 3c).

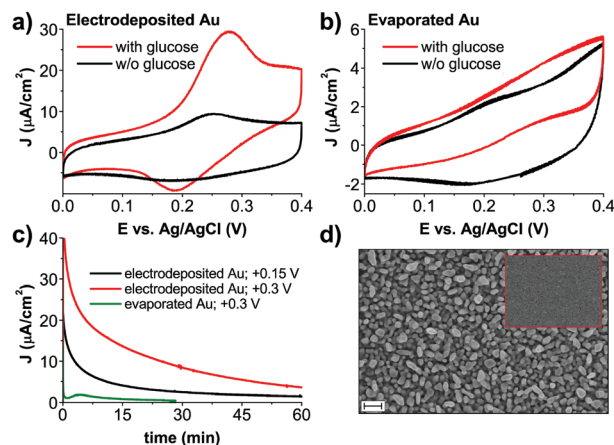


Fig. 3 Electrochemical characterization of different types of gold used for glucose oxidation. ((a) electrodeposited; and (b) evaporated) Comparison of CVs, obtained in aCSF with and without glucose. Glucose oxidation is clearly visible, with behavior in glucose-free conditions corresponding to the redox peak of Au in chloride-containing electrolyte.²² (c) Chronoamperometric stability test for aCSF with glucose. The solution has not been deoxygenated for consistency with conditions of photochemical H_2O_2 evolution. All values of applied potentials are given versus Ag/AgCl reference electrode (d) SEM image of electrodeposited Au before H_2O_2 photoevolution. During the course of the experiment morphology of gold does not change. For comparison, the inset shows a SEM of an evaporated gold electrode. Scale bar = 200 nm for both images.

Here again the much higher and sustained electrocatalytic performance of electrodeposited versus evaporated films is evidenced. A primary cause would appear to be simply the much higher electrochemical surface area of the electrodeposited gold films, apparent in SEM images (Fig. 3d).

Promising results with the improved back contact encouraged us to seek optimization of the cathodic side as well. From our earlier work on photocathodes for oxygen reduction we knew that electron-accepting Au contacts topped with an additional thin layer of PTCDI can increase photocathodic current significantly; or that vertical PN/PN tandems can boost performance as well.¹⁴ We hypothesized that these improvements would lead to higher photovoltages to provide greater overpotential to increase glucose oxidation. EPR measurements of improved PN structures confirm that voltage can be increased (Fig. S4a, ESI[†]). Irradiating these different samples showed that the structures optimized for higher voltage produce less H_2O_2 than the basic PN (Fig. S4b, ESI[†]). This can only be the case if the additional voltage is in fact resulting in reduction of O_2 all the way to H_2O , resulting in lower $[\text{H}_2\text{O}_2]$. This underscores an important aspect of these types of photofaradaic devices, which are electrically floating. One must consider to balance the anodic and cathodic performance to obtain the desired net faradaic reaction.

The result of our efforts is a free-standing photofaradaic unit on a thin plastic substrate, which demonstrates robustness in on-demand H_2O_2 generation. We have engineered the device in the direction of eventual biomedical devices operating in physiological conditions, focusing on glucose as a target electron donor. A critical message of our work is that that an



electrically-floating photovoltaic device must balance cathodic and anodic reactions to give the net sustained reaction. Simultaneous ROS production with local oxidation of glucose as the electron donor suggests this type of platform for combination chemodynamic/starvation therapy, an emerging targeted cancer treatment approach.²³ Future work should focus on evaluation of devices in biological *in vitro* and *in vivo* conditions, where it will be deployed for localized H₂O₂ delivery. This approach with light-actuation can enable many previously impossible experiments and eventually inspire new therapeutic directions as well.

The authors gratefully acknowledge financial support from the Knut and Alice Wallenberg Foundation, within the framework of the Wallenberg Centre for Molecular Medicine at Linköping University, as well as the Wallenberg Wood Science Centre 2.0; and the Swedish Research Council (Vetenskapsrådet, 2018-04505).

Conflicts of interest

There are no conflicts to declare.

Notes and references

- 1 *Photodynamic Therapy Methods and Protocols*, ed. C. J. Gomer, Humana Press, New York, 1998.
- 2 J. R. Stone and S. Yang, *Antioxidants Redox Signal.*, 2006, **8**, 243–270.
- 3 B. C. Dickinson and C. J. Chang, *Nat. Chem. Biol.*, 2011, **7**, 504–511.
- 4 R. Bretón-Romero and S. Lamas, *Redox Biol.*, 2014, **2**, 529–534.
- 5 N. Gamper, O. Zaika, Y. Li, P. Martin, C. C. Hernandez, M. R. Perez, A. Y. C. Wang, D. B. Jaffe and M. S. Shapiro, *EMBO J.*, 2006, **25**, 4996–5004.
- 6 M. Moros, A. Lewinska, G. Onorato, M. R. Antognazza, F. Di Maria, M. Blasio, G. Lanzani, A. Tino, M. Wnuk and C. Tortiglione, *MRS Commun.*, 2018, 1–8.
- 7 M. R. Antognazza, I. A. Aziz and F. Lodola, *Oxid. Med. Cell. Longev.*, 2019, 1–24.
- 8 F. Lodola, V. Rosti, G. Tullii, A. Desii, L. Tapella, P. Catarsi, D. Lim, F. Moccia and M. R. Antognazza, *Sci. Adv.*, 2019, **5**, eaav4620.
- 9 M. Gryszel, R. Rybakiewicz and E. D. Głowacki, *Adv. Sustainable Syst.*, 2019, **3**, 1900027.
- 10 S. Fukuzumi, Y. M. Lee and W. Nam, *Chem. – Eur. J.*, 2018, **24**, 5016–5031.
- 11 D. Rand, M. Jakešová, G. Lubin, I. Vebraite, M. David-Pur, V. Đerek, T. Cramer, N. S. Sariciftci, Y. Hanein and E. D. Głowacki, *Adv. Mater.*, 2018, **30**, 1707292.
- 12 M. Jakešová, M. S. Ejneby, V. Đerek, T. Schmidt, M. Gryszel, J. Brask, R. Schindl, D. T. Simon, M. Berggren, F. Elinder and E. D. Głowacki, *Sci. Adv.*, 2019, **5**, eaav5265.
- 13 M. Jakešová, T. A. Sjöström, V. Đerek, D. Poxson, M. Berggren, E. D. Głowacki and D. T. Simon, *npj Flex. Electron.*, 2019, **3**, 14.
- 14 M. Gryszel, A. Markov, M. Vagin and E. D. Głowacki, *J. Mater. Chem. A*, 2018, **6**, 24709–24716.
- 15 L. D. Burke and P. F. Nugent, *Gold Bull.*, 1998, **31**, 39–50.
- 16 J. D. Benck, B. A. Pinaud, Y. Gorlin and T. F. Jaramillo, *PLoS One*, 2014, **9**, e107942.
- 17 J. B. Fortin and T.-M. Lu, *Chemical Vapor Polymerization, The Growth and Properties of Parylene*, Springer Science + Business Media, New York, 1st edn, 2004.
- 18 M. Warczak, M. Gryszel, M. Jakešová, V. Đerek and E. D. Głowacki, *Chem. Commun.*, 2018, **54**, 1960–1963.
- 19 A. Brouzgou and P. Tsiakaras, *Top. Catal.*, 2015, **58**, 1311–1327.
- 20 T. M. Cheng, T. K. Huang, H. K. Lin, S. P. Tung, Y. L. Chen, C. Y. Lee and H. T. Chiu, *ACS Appl. Mater. Interfaces*, 2010, **2**, 2773–2780.
- 21 M. Tominaga, M. Nagashima, K. Nishiyama and I. Taniguchi, *Electrochem. Commun.*, 2007, **9**, 1892–1898.
- 22 L. D. Burke and P. F. Nugent, *Gold Bull.*, 1997, **30**, 43–53.
- 23 M. Chang, M. Wang, M. Wang, M. Shu, B. Ding, C. Li, M. Pang, S. Cui, Z. Hou and J. Lin, *Adv. Mater.*, 2019, **31**, 1905271.

